

Microkinetic modeling of Fischer-Tropsch synthesis on cobalt

Citation for published version (APA):

Zijlstra, B. (2020). *Microkinetic modeling of Fischer-Tropsch synthesis on cobalt*. [Phd Thesis 1 (Research TU/e / Graduation TU/e), Chemical Engineering and Chemistry]. Technische Universiteit Eindhoven.

Document status and date:

Published: 15/01/2020

Document Version:

Publisher's PDF, also known as Version of Record (includes final page, issue and volume numbers)

Please check the document version of this publication:

- A submitted manuscript is the version of the article upon submission and before peer-review. There can be important differences between the submitted version and the official published version of record. People interested in the research are advised to contact the author for the final version of the publication, or visit the DOI to the publisher's website.
- The final author version and the galley proof are versions of the publication after peer review.
- The final published version features the final layout of the paper including the volume, issue and page numbers.

[Link to publication](#)

General rights

Copyright and moral rights for the publications made accessible in the public portal are retained by the authors and/or other copyright owners and it is a condition of accessing publications that users recognise and abide by the legal requirements associated with these rights.

- Users may download and print one copy of any publication from the public portal for the purpose of private study or research.
- You may not further distribute the material or use it for any profit-making activity or commercial gain
- You may freely distribute the URL identifying the publication in the public portal.

If the publication is distributed under the terms of Article 25fa of the Dutch Copyright Act, indicated by the "Taverne" license above, please follow below link for the End User Agreement:

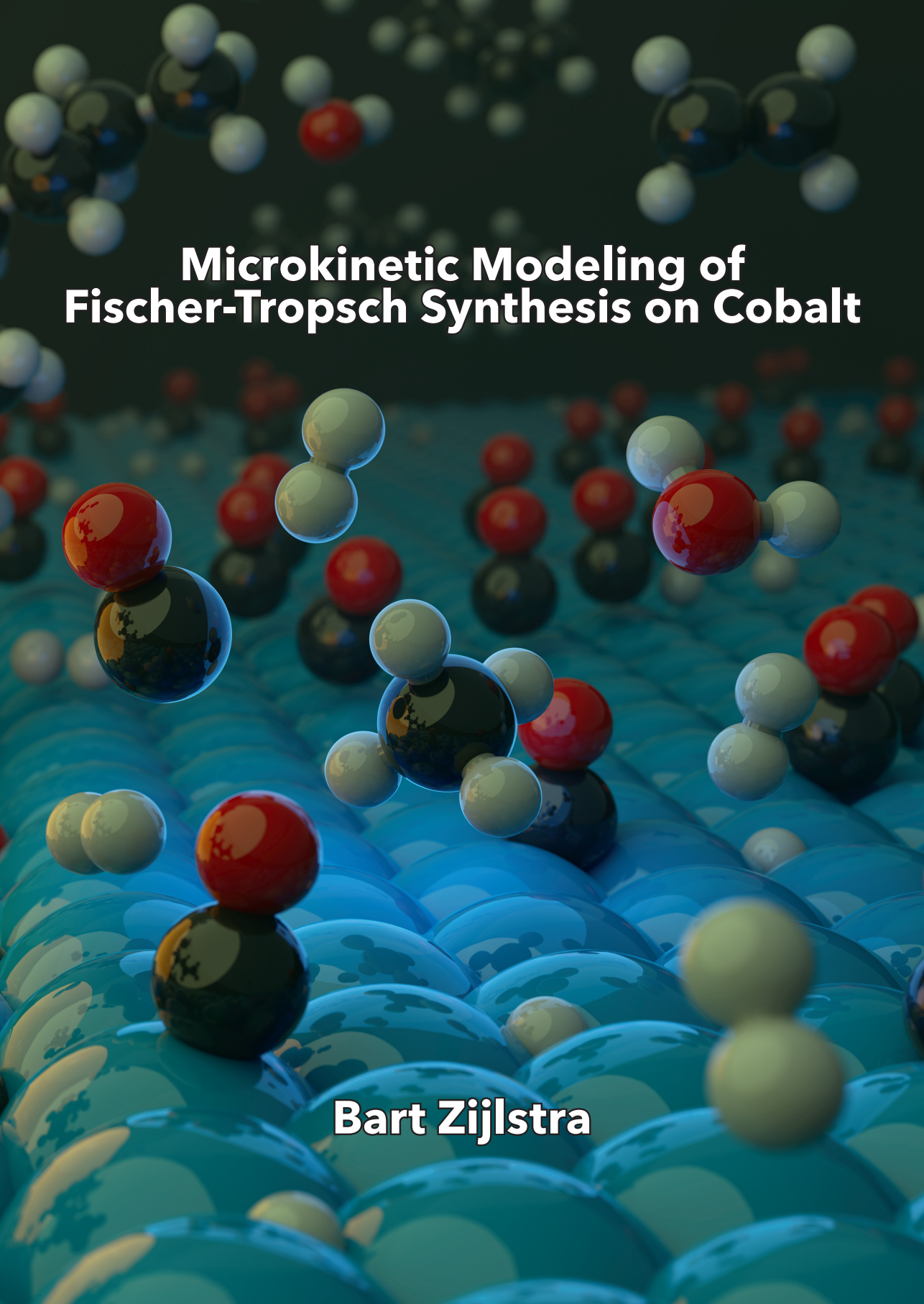
www.tue.nl/taverne

Take down policy

If you believe that this document breaches copyright please contact us at:

openaccess@tue.nl

providing details and we will investigate your claim.

A 3D molecular model illustrating the Fischer-Tropsch synthesis process on a cobalt surface. The cobalt surface is represented by a grid of blue spheres. Various molecules, including CO (red and white spheres), H2 (two white spheres), and H2O (red and white spheres), are shown interacting with the surface. The background is dark with blurred molecular models.

Microkinetic Modeling of Fischer-Tropsch Synthesis on Cobalt

Bart Zijlstra

MICROKINETIC MODELING OF FISCHER-TROPSCH SYNTHESIS ON COBALT

PROEFSCHRIFT

ter verkrijging van de graad van doctor aan de Technische Universiteit Eindhoven, op gezag van de rector magnificus prof.dr.ir. F.P.T. Baaijens, voor een commissie aangewezen door het College voor Promoties, in het openbaar te verdedigen op woensdag 15 januari 2020 om 16:00 uur

door

Bart Zijlstra

geboren te Roermond

Dit proefschrift is goedgekeurd door de promotoren en de samenstelling van de promotiecommissie is als volgt:

voorzitter: prof.dr.ir. J.C.M. van Hest
1^e promotor: prof.dr.ir. E.J.M. Hensen
copromotor: dr.ir. I.A.W. Filot
leden: prof.dr.ir. J.A.M. Kuipers
prof.dr. A. Urakawa (Technische Universiteit Delft)
dr.ir. B. Ensing (Universiteit van Amsterdam)
prof.dr.ir. M. van Sint Annaland
dr. G.L. Bezemer (Shell Global Solutions International B.V.)

Het onderzoek of ontwerp dat in dit proefschrift wordt beschreven is uitgevoerd in overeenstemming met de TU/e Gedragscode Wetenschapsbeoefening.

To my parents

Bart Zijlstra

Microkinetic Modeling of Fischer-Tropsch Synthesis on Cobalt

A catalogue record is available from the Eindhoven University of Technology Library

ISBN: 978-90-386-4956-6

Copyright © 2020 by Bart Zijlstra



The work described in this thesis has been carried out at the Inorganic Materials & Catalysis group at the Eindhoven University of Technology.



This work was made with financial support from Shell Global Solutions International B.V.



The Netherlands Organization for Scientific Research is acknowledged for providing access to computational resources.



This work was carried out on the Dutch national e-infrastructure with the support of SURF Cooperative.

Printed by: ProefschriftMaken

Cover design: Bart Zijlstra

CONTENTS

1	Introduction	1
1.1	The cost of carbon	1
1.2	History of Fischer-Tropsch synthesis	4
1.3	Catalysis	5
1.4	Mechanistic pathways in Fischer-Tropsch synthesis	9
1.5	Scope of this thesis	10
1.6	References	11
2	Theory and methods	15
2.1	Introduction	15
2.2	Reactions on surfaces	16
2.3	Transition state theory	20
2.4	Scaling relations	21
2.5	Density functional theory	22
2.6	Microkinetic modeling	27
2.7	References	30
3	Modeling mean-field lateral interactions on cobalt catalysts	33
3.1	Introduction	34
3.2	Computational methods	35
3.3	Results and discussion	36
3.4	Conclusions	61
3.5	References	62
4	Coverage effects in CO dissociation on metallic cobalt nanoparticles	65
4.1	Introduction	66
4.2	Computational methods	67
4.3	Results and discussion	68
4.4	Conclusions	80
4.5	References	80
	Appendix A	83

5	First-principles based microkinetic modeling of transient kinetics of CO hydrogenation on cobalt catalysts	85
5.1	Introduction	86
5.2	Computational methods	88
5.3	Results and discussion	91
5.4	Conclusions	100
5.5	References	101
	Appendix B	105
6	First-principles based microkinetic modeling of Fischer-Tropsch synthesis on cobalt	125
6.1	Introduction	126
6.2	Computational methods	128
6.3	Results and discussion	129
6.4	Conclusions	160
6.5	References	161
	Appendix C	165
	Appendix D	182
7	First-principles microkinetics simulations of electrochemical reduction of CO₂ over Cu catalysts	185
7.1	Introduction	186
7.2	Computational methods	188
7.3	Results and discussion	192
7.4	Conclusions	208
7.5	References	208
	Appendix E	213
	Summary	230
	Acknowledgments	234
	List of publications	239
	Curriculum Vitae	242

CHAPTER 1

INTRODUCTION

Contents

1.1	The cost of carbon	1
1.2	History of Fischer-Tropsch synthesis	4
1.3	Catalysis	5
1.3.1	Catalysts for the Fischer-Tropsch reaction	7
1.3.2	Catalyst design from first principles	8
1.4	Mechanistic pathways in Fischer-Tropsch synthesis	9
1.5	Scope of this thesis	10
1.6	References	11

1.1 The cost of carbon

The global energy consumption in 2040 is expected to increase by a quarter compared to 2018 [1]. Strong economic growth of developing countries is a main contributor to this increasing energy demand. Climate change due to anthropogenic greenhouse gas emissions is recognized as one of the most pressing societal challenges and, accordingly, is also high on the political agenda. Burning fossil resources releases CO₂ in the atmosphere, which is linked to global warming and climate change [2]. Therefore, it is pivotal to increase the share of energy supply with low CO₂ emissions such as renewable energy from wind and solar. Some scenarios predict, however, that natural gas, coal, petroleum oil and coal may still cover more than 70% of the energy demand by the year 2040. This is due to the relatively low price of fossil resources such as coal in some regions of the world, the increasing availability of unconventional natural gas resources (e.g. shale gas) and modern oil recovery technologies that allow retrieval of previously unobtainable reserves [3].

The traditional coupling between the natural gas and oil price is replaced by a reality where in different parts of the world different types of fossil feedstock may be advantageous. For example, the economic drivers for increasing domestic crude oil production levels have led to significant fluctuations in the oil price over the last decade. As shown in Figure 1.1, the price of Brent oil has dropped significantly from earlier highs, for a large part due to the

increased production of crude oil in the U.S. The Organization of the Petroleum Exporting Countries (OPEC) has since made attempts to stabilize the oil prices [4, 5]. Nevertheless, crude oil prices remain unpredictable and might stay relatively low in the coming decade. This could impede the transition to more sustainable alternatives, as more environmentally friendly energy technologies need to be economically competitive.

Still, the true cost of using carbonaceous resources lies in the impact on our climate through greenhouse-gas emissions. The Paris Agreement is one of the large non-economic driving forces towards a more sustainable energy infrastructure. Part of the implementation in this agreement is a carbon “budget” to keep the global temperature rise to below 1.5 °C as compared to pre-industrial levels. It is clear that only a relatively small part of all available fossil resources can be converted into CO₂ if we wish to stay below the 1.5 °C temperature rise.

To remain within the agreed carbon budget, our energy system needs to undergo a transition to low-carbon technologies. Solar and wind power are well-known renewable sources of clean electricity. Depending on local availability, hydropower is also an inexhaustive source of clean electricity. Other sources to generate low-carbon power are nuclear power, tidal power and geothermal power. Such clean electricity can replace combustion technologies in furnaces, boilers, and combustion engines. Together, these technologies could meet a large part of our future energy demands.

The limiting factor for transitioning to a fully electric infrastructure lies in the storage of energy. This storage issue is twofold, as energy must be stored both in- and outside of the electrical power grid. Grid energy storage is needed to deal with the intermittency of renewable sources like wind and solar. Large-scale storage can involve pumping large quantities of water to higher elevations so that electrical energy is converted into potential energy. Off-grid storage is important mainly for transportation purposes to cover the energy demand for mobility. Such storage technologies require high volumetric and gravimetric energy density. Batteries serve already as a storage medium for electric vehicles, but their performance in terms of energy density remains 1-2 orders of magnitude lower than conventional liquid fuels. Although a significant fraction of energy needs for mobility can probably be covered by electric vehicles, other sectors such as heavy duty transport and aviation will remain dependent on energy-dense fuels in the foreseeable future. This together with the increasing energy demand for mobility implies that the demand for liquid fuels will remain substantial in the coming decades, which at least in part should be covered by transportation fuels that do not contribute to net CO₂ emissions upon combustion.

One of the possible transition technologies is to produce CO₂-neutral liquid transportation fuels by the Fischer-Tropsch (FT) process [6]. A requirement is that the synthesis gas (syngas), a mixture of CO and H₂, is derived from renewable resources. For instance, biomass can be converted via gasification to syngas and via biomass-to-liquids (BTL) FT processes to transportation fuels with a lower CO₂ intensity than the use of fossil resources [7]. Waste streams are another source of syngas. Such an approach recycles part of the carbon used to make materials. However, we should realize that the amount of carbon used to make materials is much less than the amount of carbon used to generate energy. Accordingly,

closing the carbon cycle implies that CO_2 should be captured from the air, which has the additional benefit of decreasing the CO_2 content of the atmosphere. Direct air capture is heavily investigated but remains today a very expensive technology [8]. Nevertheless, CO_2 from air combined with CO_2 emissions from sectors that cannot easily decarbonize (steel, cement, lime industry) can be regarded as a building block for the production of transportation fuels. One route is to generate H_2 directly by water electrolysis using renewable energy. CO_2 can then be hydrogenated with renewable H_2 to obtain different hydrocarbon products. The simplest approach is to convert this mixture directly to CH_4 , which can be easily stored and transported via the existing natural gas grid. The underlying chemistry of this Sabatier reaction is akin to the chemistry of the FT reaction. Converting CO_2/H_2 to liquid transportation fuels is more challenging. The most obvious route is to first reduce CO_2 to CO via the reverse water-gas shift reaction, followed by conventional FT synthesis. On the other hand, there are also different routes possible. A recent study by Stanford University and Technical University of Denmark showed that CO_2 can be directly electrochemically converted into CO over ceria catalysts [9]. Although much basic research is devoted to the electrochemical reduction of CO_2 to products containing C–C bonds, the best performing systems can only produce ethylene as a valuable product.

Summarizing, FT technology is a practical technology, which in certain settings can be used to convert cheap feedstock such as methane or coal to liquid transportation fuels. An additional benefit is the low level of impurities in FT-derived fuels, which are more common in fuels derived from crude oil. The synthesis gas intermediate, which is fed to FT reactors, can in principle be derived from other renewable sources such as biomass. Ultimately, FT technology can play a significant role in reutilizing CO_2 captured directly from the air or CO_2 from irreducible sources, provided that a scalable technology for green H_2 production is developed.

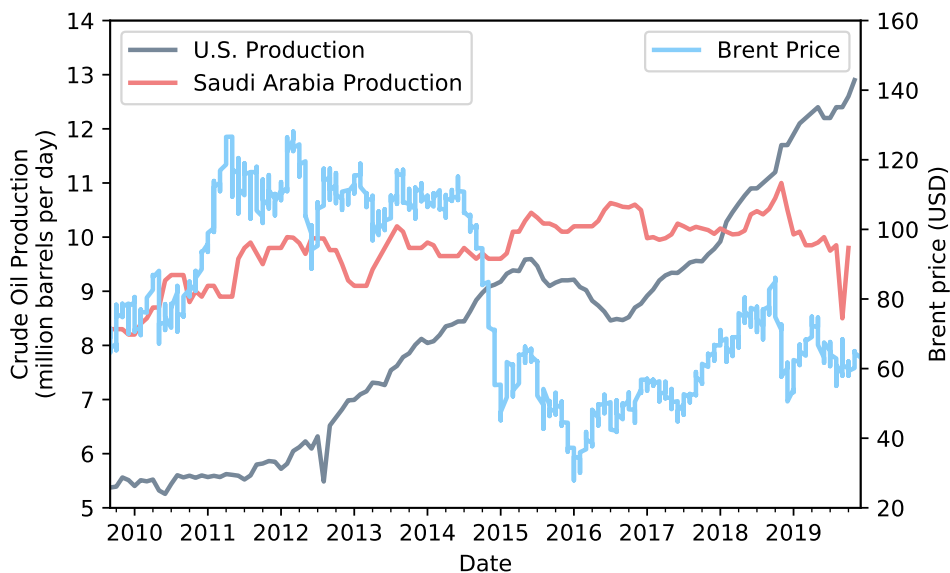
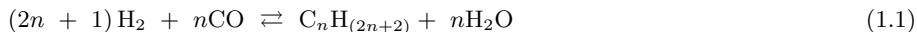


Figure 1.1: Crude oil production by the two largest producing countries as of 2019 and Brent crude prices price over the last 10 years [10].

1.2 History of Fischer-Tropsch synthesis

Fischer-Tropsch Synthesis (FTS) provides access to a range of valuable chemicals and fuels from two simple molecules, namely CO and H_2 . The overall process, which is often called GTL, CTL or BTL depending on the starting carbonaceous feedstock being Gas, Coal or Biomass, converts the feedstock to syngas [11], followed by the actual FT reaction in which syngas is converted into a range of hydrocarbon products in a polymerization-like reaction. The main products are long-chain hydrocarbons and water (Eq. 1.1). The oxygen from CO can also be incorporated in the hydrocarbon products, leading to oxygenates as a high value byproduct of the FT reaction. Depending on the catalyst and process conditions, also CO_2 can be formed which is usually disadvantageous. The preferred products of FT processes are typically linear n -paraffins and α -olefins, although internal olefins and branched hydrocarbons can also be formed [12]. Then the preferred product of oxygen removal is water. The overall reaction is given by:



The basis for the FT process dates back from the 1920s, when in the laboratories at the Kaiser Wilhelm Institute for Coal Research in Mülheim (Germany), Franz Fischer and Hans Tropsch developed the essential catalytic chemistry to convert syngas to hydrocarbons. Collaboration with the Ruhrchemie Company led to the development of a process and implementation in several plants reaching an annual capacity of 600,000 tonnes of liquid

Table 1.1: Large Fischer-Tropsch projects [16–19].

Project	Comple- tion	Country	Company	Feed- stock	Production (bbl/d)
Secunda	1984	S. Africa	Sasol	Coal	160 000
Mossgas	1993	S. Africa	PetroSA	NG	45 000
Bintulu	1993	Malaysia	Shell	NG	14 700
Oryx	2007	Qatar	Qatar Petroleum/Sasol	NG	34 000
Pearl	2012	Qatar	Shell	NG	140 000
Escravos	2014	Nigeria	Chevron/NNPC/Sasol	NG	34 000
Shenhua Ning Mei	2016	China	CHN Energy	Coal	100 000
Shenhua Xinjiang	2020+	China	CHN Energy	Coal	75 000
Oltin Yo'l	2020+	Uzbekistan	Sasol/Petronas/Uzbekneftegaz	NG	38 000
Lu'an CTL	2020+	China	Shanxi Lu'an	Coal	38 000
Yitai CTL	2020+	China	Meimeng Yitai/ Synfuels China	Coal	45 000

products between 1938 and 1945 [13, 14]. The need for liquid fuels from (brown) coal-derived syngas was borne from the German wartime efforts. Thereafter, oil became king, securing an abundant supply of liquid fuels that only needed to be refined. This meant that FT technology was not further developed as a commercial technology in the developed world. Nevertheless, most major oil companies and chemicals producers remained interested in the technology as a future technology when crude oil reserves were expected to decline [15]. Regained interest was for instance noted during and after the two oil crises in the 1970s. An exception was the development of coal-based FT technology in South Africa, for which again energy security was a major (political) driver. In this case, the availability of cheap domestic coal in combination with import restrictions on crude oil led to the development of large-scale coal-to-liquids processes by SASOL.

In recent years, other companies followed up on the successful coal-to-liquids applications in South Africa. Table 1.1 shows those large-scale applications of FT technology, including some that are still under development. Shell was the first company to commercialize cobalt-catalyzed gas-to-liquids in 1993 in Bintulu, Malaysia. Sasol developed their own cobalt-based technology and completed the Oryx project in Qatar in 2007. Also in Qatar, Shell finished construction of the Pearl GTL plant at the end of 2010. Reaching full capacity in 2012, the Pearl plant became the world's largest GTL facility with a production of 140,000 barrels of GTL products per day. Since then, Sasol has been involved in construction of the Escravos plant in Nigeria and the Oltin Yo'l plant in Uzbekistan. Completed in 2014, the Escravos plant is essentially a copy of the Oryx plant. Commissioning of the the Oltin Yo'l plant is expected in 2020. Plans to build a large GTL plant in Louisiana were abandoned due to the declined oil price in 2015. Meanwhile, China is on its way to become world's largest CTL producer. The current largest CTL project in China is the 2016 Shenhua Ning Mei project with a 100,000 barrel per day capacity. Under construction are among others the Shenhua Xinjiang, Lu'an CTL and Yitai CTL projects.

1.3 Catalysis

Many commercially applied chemical processes rely on catalysts. A catalyst lowers the overall reaction barrier for the process without changing the final energy of the completed

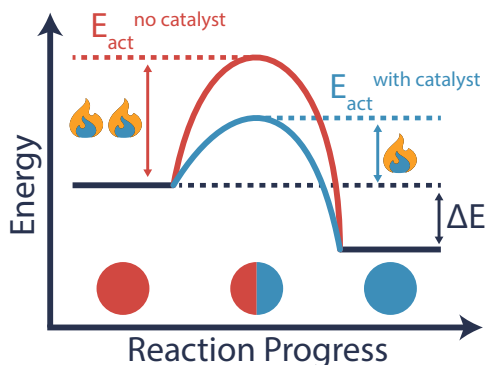


Figure 1.2: Simplified effect of adding a catalyst to a chemical conversion process.

reaction. An example of a catalytic vs. a non-catalytic reaction is depicted in Figure 1.2. Practical reactions consist of many more elementary reaction steps. In general, a catalyzed reaction can proceed at a lower temperature than the un-catalyzed one, although the total energy going in or out of the process is unchanged. Operating a chemical reaction at high temperatures is often undesired, due to safety issues, design constraints, or unwanted by-products. Therefore, low operating temperatures are usually preferred, requiring the use of a catalyst.

Catalysts are often described as accelerants of the chemical process that are not used up in the process. In practice, a catalyst usually undergoes some sort of change over time, which often leads to deactivation. This deactivation can be simply the loss of catalyst material due to leaching or attrition, but also involve more complex phenomena like structural changes or deposition of poisons at the surface [20].

In the absence of deactivating pathways, the active site on a catalyst cycles many times through a set of unique states. Each time such a cycle is completed the catalyst has made one ‘turnover’. Figure 1.3 depicts such a cycle, which starts with adsorption, is followed by reaction, and is completed by desorption of the product. The activity of a catalyst can be expressed by the turnover frequency (TOF), which is the number of turnovers per unit time.

The field of catalysis can be subdivided into heterogeneous catalysis, homogeneous catalysis, and bio- or enzymatic catalysis [21]. For a heterogeneously catalyzed system the reactants and products are in a different phase than the catalyst material. Usually the catalyst is a solid, while the reacting molecules are gasses or are in solution. Heterogeneous catalysts are usually the workhorse in the chemical industry, and are also the type of catalyst used for Fischer-Tropsch synthesis. For homogeneous catalysis both the catalyst material and the reactants are in the same phase. This can be both in the gas phase or, more commonly, both in solution. Bio-catalysis is catalysis by enzymes. These enzymes usually have very specific shapes that have been evolved over time to selectively break or form chemical bonds.

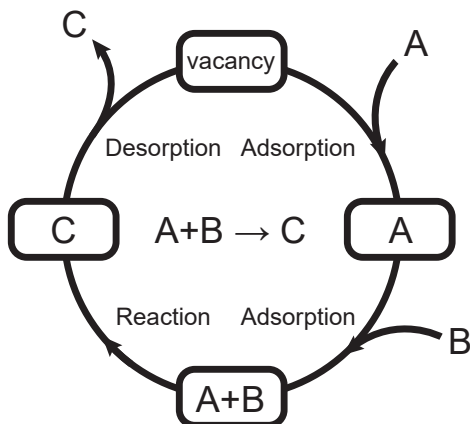


Figure 1.3: A simple catalytic cycle for the reaction of $A+B \rightarrow C$.

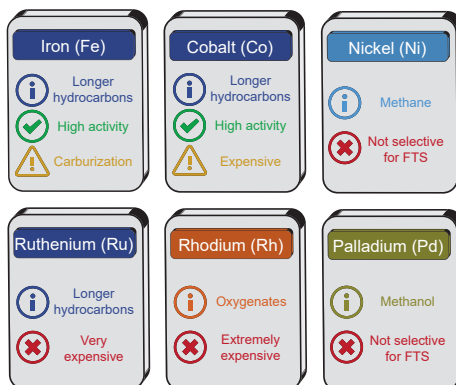


Figure 1.4: Transition metals that can be used for CO hydrogenation.

1.3.1 Catalysts for the Fischer-Tropsch reaction

Fischer-Tropsch synthesis can proceed over several transition metals. Iron, nickel, cobalt and ruthenium provide rates high enough for commercial application (Figure 1.4). Of these metals, nickel is not suitable for production of longer hydrocarbons [22], and ruthenium is too expensive [23]. The two remaining metals, iron and cobalt, are both applied industrially. Iron-based FT catalysts have as an advantage a low price compared to cobalt. One of the disadvantages of iron is stability. Oxidation or coke deposition cause iron-based FT catalysts to deactivate faster than cobalt. Cobalt is more stable due to a higher hydrogenation activity [13].

Because cobalt is significantly more expensive compared to iron, the surface area to volume ratio is increased by making the cobalt particles very small, i.e. between 1-100 nanometers. These nanoparticles are then usually deposited on a porous high surface area

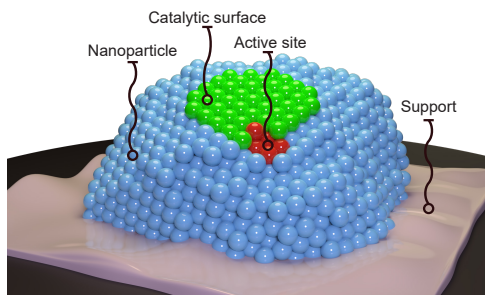


Figure 1.5: Schematic representation of a ~ 6 nm supported nanoparticle.

support [24]. The concept of a supported nanoparticle is depicted in Figure 1.5, indicating also the different length scales between an active site and a full nanoparticle.

1.3.2 Catalyst design from first principles

The design of heterogeneous catalysts from first principles remains passionately sought after. This formidable task hinges on fundamental understanding of catalytic action through molecular insight into the chain of elementary reaction steps proceeding on the surface of heterogeneous catalysts. The three paradigmatic laws of catalysis were formulated by Berzelius, Ostwald and Sabatier [25]. Of these, Sabatier's principle is most helpful for predicting the composition of optimum catalysts. Sabatier postulated that reaction complexes formed between the catalyst and the reactant should be neither too strong nor too weak. With the advent of modern quantum-chemical methods and increased computational power, this led to the formulation of scaling laws that link catalyst composition to performance [26–29]. The state of the art in computational catalysis is to explore the potential energy surface between reactants and products using density functional theory. Using Eyring's transition state theory [30], these data can be used to make predictions about conversion rates and product distribution by for instance microkinetics simulations [31, 32]. Such simulations are usually based on the assumption of a Langmuir surface characterized by one type of sites [33]. There are however many instances in heterogeneous catalysis that warrant an alternative Taylorian view of surface reactivity [34]. That is to say that catalysis occurs by uniquely active sites that are sometimes present only in very small numbers. Important examples are the hydrogenation of dinitrogen to ammonia (Haber-Bosch process) and the hydrogenation of carbon monoxide to liquid hydrocarbons (Fischer-Tropsch process). It remains unclear if and how low-reactive sites influence the ongoing catalytic reaction. While the importance of stepped sites is well accepted for the dissociation of dinitrogen [35], there remains considerable debate about the nature of active sites for carbon monoxide dissociation, which is an essential step in Fischer-Tropsch (FT) synthesis.

1.4 Mechanistic pathways in Fischer-Tropsch synthesis

Cobalt-based FTS is typically done at temperatures in the 200-240 °C range and pressures above 10 bars. Total CO conversion rates increase when operating FTS at higher temperatures. However, as the temperature increases, the selectivity of FT shifts towards shorter average chain lengths and ultimately methane. As FTS is kinetically controlled, this shift is not purely thermodynamic. Explaining this shift requires understanding of the fundamental mechanistic pathways leading to either methane or longer hydrocarbons.

Although many details about the Fischer-Tropsch process are known, there is an on-going debate in the literature about the molecular mechanism by which the monomeric species is incorporated in the growing chain [36]. Over the years of FT research two conflicting pathways have been proposed for chain propagation. Figure 1.6 depicts these two pathways, which are the carbide mechanism and the CO-insertion mechanism.

In the carbide mechanism, a $\text{CH}_{x(0-3)}$ intermediate is formed by scission of the C–O bond of carbon monoxide. This scission can be direct, i.e. not involving hydrogen, or H-assisted. The CH_x is then inserted into the growing chain. Then, new CO dissociation events have to occur to create more monomeric species. The CO-insertion mechanism starts with a single CO scission step, similar to the carbide mechanism. Then, the generated CH_x species couples to another CO forming an C_2 -oxygenate. C–O bond scission of this oxygenate then leads to a CH_xCH_y species. Further elongation of this C_2 species happens by insertion of a CO, followed by C–O bond scission. The main difference between the two mechanisms is thus the moment where C–O bond scission occurs.

A key aspect of this ongoing discussion is the role of lateral interactions on the usually crowded surfaces. In particular in the context of FT synthesis, high CO coverages encountered at reaction conditions are expected to substantially raise the barrier of CO dissociation [37, 38]. This would favor alternative pathways for CO dissociation and chain growth in the FT synthesis process.

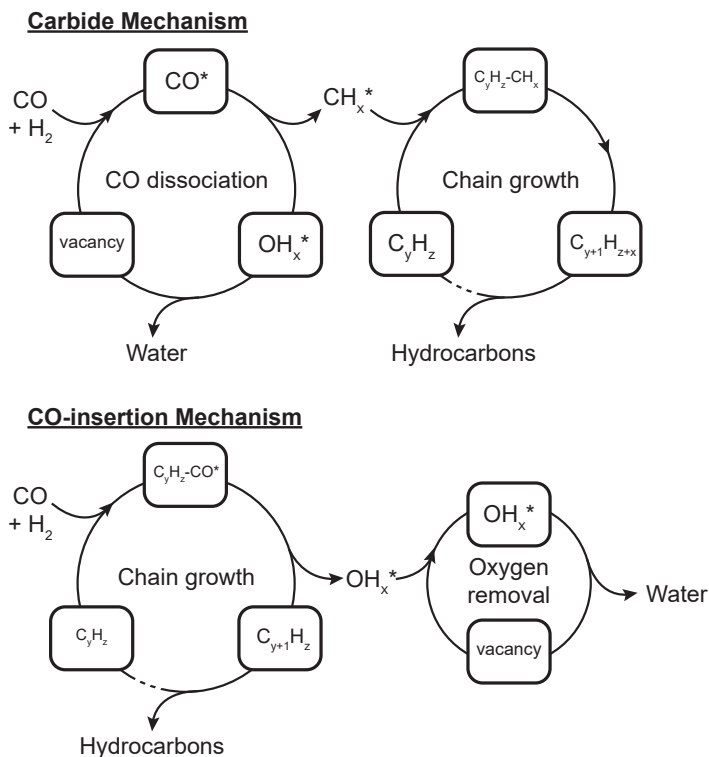


Figure 1.6: Comparison of the carbide and CO-insertion mechanisms. The difference between the two mechanisms is whether C–O bond scission happens before (carbide) or after (CO-insertion) C–C coupling.

1.5 Scope of this thesis

This thesis focuses on obtaining mechanistic understanding of Fischer-Tropsch synthesis on cobalt nanoparticles. The following chapters contain theoretical investigations and modeling of the FT reaction over two surfaces Co(0001) and Co(11 $\bar{2}$ 1). These two surfaces are models for terrace sites and step-edge sites, which are both exposed on real cobalt nanoparticles. Density functional theory (DFT) calculations will be discussed for the elementary reaction steps in the FT reaction. With first-principles based microkinetic modeling, the activity and selectivity of the FT reaction is then simulated. The results are discussed in the framework of other theoretical and experimental literature. The next chapters are organized as follows:

Chapter 2 of this thesis gives an overview of the computational methods used in this work and the theory behind them. A work flow is described that involves the definition of model surfaces of real catalysts, the identification of the most stable geometries of adsorbates and the transition states that separate adsorbed reactants and (adsorbed) products as well as microkinetics simulations that allow prediction of reaction rates, surface coverages and rate- and selectivity-controlling steps of complex reaction networks as those of the FT reaction.

Chapter 3 discusses the effect of lateral interactions on adsorbates on cobalt catalysts

relevant to the FT reaction. In particular, this chapter will show how the heat of adsorption of the reactants CO and H₂ decreases as a function of the surface coverage. Also, a method to incorporate these lateral interactions in a (mean-field) microkinetic model will be discussed.

Chapter 4 describes the influence of CO coverage on the CO dissociation reaction on stepped and planar cobalt surfaces, which is the most important step in the FT reaction. These effects will be discussed in the context of the ongoing debate regarding the locus of FT monomer formation.

Chapter 5 provides insight into the FT reaction by microkinetics simulations of methanation under steady-state and transient conditions. The emphasis in this work is on correlating the microscopic details of the elementary reaction steps underlying CO hydrogenation and common experimental observations for cobalt catalysts in the literature.

In Chapter 6, the chemokinetic network of CO hydrogenation to methane is expanded to include the formation of longer hydrocarbons. The chapter discusses the thermodynamic and kinetic aspects that finally determine not only the FT activity but also the FT selectivity. A key aspect discussed in this chapter is the interplay between terrace and step-edge sites on a cobalt nanoparticle. We also explored the hydrogenation of CO₂ in the context of making renewable liquid transportation fuels with FT chemistry.

Finally, Chapter 7 expands the scope of this work by addressing the microkinetics simulation of the electrochemical reduction of CO₂. The chapter will show how the effect of the electrochemical potential can be simulated for electrochemical CO₂ reduction over copper surfaces. An important aspect in this chapter is also the incorporation of mass-transport limitations through a diffusion layer.

1.6 References

- [1] U.S. Energy Information Administration, International Energy Outlook 2018, <https://www.eia.gov/outlooks/ieo/>.
- [2] I. Medhaug, M. B. Stolpe, E. M. Fischer, R. Knutti, *Nature* **2017**, *545*, 41.
- [3] A. Shah, R. Fishwick, J. Wood, G. Leeke, S. Rigby, M. Greaves, *Energy & Environmental Science* **2010**, *3*, 700–714.
- [4] E. Ansari, R. K. Kaufmann, *Nature Energy* **2019**, *4*, 321–328.
- [5] M. Bradshaw, T. Van de Graaf, R. Connolly, *Energy Strategy Reviews* **2019**, *26*, 100374.
- [6] G. P. Van Der Laan, A. A. C. M. Beenackers, *Catalysis Reviews* **1999**, *41*, 255–318.
- [7] E. van Steen, M. Claeys, *Chemical Engineering & Technology* **2008**, *31*, 655–666.
- [8] D. W. Keith, G. Holmes, D. St. Angelo, K. Heidel, *Joule* **2018**, *2*, 1573–1594.
- [9] T. L. Skafte, Z. Guan, M. L. Machala, C. B. Gopal, M. Monti, L. Martinez, E. Stamate, S. Sanna, J. A. Garrido Torres, E. J. Crumlin, M. García-Melchor, M. Bajdich, W. C. Chueh, C. Graves, *Nature Energy* **2019**, *4*, 846–855.
- [10] Macrotrends, Energy charts, <https://www.macrotrends.net/>.

- [11] J. R. Rostrup-Nielsen, *Catalysis Today* **2002**, *71*, 243–247.
- [12] M. E. Dry, *Catalysis Today* **1990**, *6*, 183–206.
- [13] M. E. Dry, *Catalysis Today* **2002**, *71*, 227–241.
- [14] H. Schulz, *Applied Catalysis A: General* **1999**, *186*, 3–12.
- [15] M. K. Hubbert, *Drilling and Production Practice American Petroleum Institute* **1956**, *95*.
- [16] V. Litvinenko, B. Meyer, *Syngas Production: Status and Potential for Implementation in Russian Industry*, Springer International Publishing, **2017**.
- [17] J. Xu, Y. Yang, Y.-W. Li, *Fuel* **2015**, *152*, 122–130.
- [18] J. M. Sánchez-Hervás, G. M. Moya, I. Ortiz-González in *New Trends in Coal Conversion*, (Eds.: I. Suárez-Ruiz, M. A. Diez, F. Rubiera), Woodhead Publishing, **2019**, pp. 175–202.
- [19] D. Leckel, *Energy & Fuels* **2009**, *23*, 2342–2358.
- [20] M. D. Argyle, C. H. Bartholomew, *Catalysts* **2015**, *5*, 145–269.
- [21] I. Chorkendorff, J. W. Niemantsverdriet, *Concepts of modern catalysis and kinetics*, Wiley-VCH Verlag, Weinheim, **2003**.
- [22] B. C. Enger, A. Holmen, *Catalysis Reviews* **2012**, *54*, 437–488.
- [23] Infomine, Metal prices, <http://www.infomine.com/investment/metal-prices/>.
- [24] E. Rytter, A. Holmen, *Catalysis Today* **2016**, *275*, 11–19.
- [25] R. A. van Santen, *Angew Chem Int Ed Engl* **2014**, *53*, 8618–20.
- [26] P. Ferrin, D. Simonetti, S. Kandoi, E. Kunkes, J. A. Dumesic, J. K. Norskov, M. Mavrikakis, *J Am Chem Soc* **2009**, *131*, 5809–15.
- [27] A. A. Latimer, A. R. Kulkarni, H. Aljama, J. H. Montoya, J. S. Yoo, C. Tsai, F. Abild-Pedersen, F. Studt, J. K. Nørskov, *Nature Materials* **2016**, *16*, 225.
- [28] J. K. Nørskov, T. Bligaard, J. Rossmeisl, C. H. Christensen, *Nat Chem* **2009**, *1*, 37–46.
- [29] R. A. van Santen, M. Neurock, S. G. Shetty, *Chemical Reviews* **2010**, *110*, 2005–2048.
- [30] H. Eyring, *Chemical Reviews* **1935**, *17*, 65–77.
- [31] I. A. Filot, R. A. van Santen, E. J. Hensen, *Angew Chem Int Ed Engl* **2014**, *53*, 12746–12750.
- [32] X. Liu, J. Xiao, H. Peng, X. Hong, K. Chan, J. K. Nørskov, *Nat Commun* **2017**, *8*, 15438.
- [33] I. Langmuir, *Transactions of the Faraday Society* **1922**, *17*, 621–621.
- [34] H. S. Taylor, *Proceedings of the Royal Society A: Mathematical Physical and Engineering Sciences* **1925**, *108*, 105–111.

- [35] K. Honkala, A. Hellman, I. N. Remediakis, A. Logadottir, A. Carlsson, S. Dahl, C. H. Christensen, J. K. Nørskov, *Science* **2005**, *307*, 555–558.
- [36] A. J. Markvoort, R. A. van Santen, P. A. Hilbers, E. J. Hensen, *Angew Chem Int Ed Engl* **2012**, *51*, 9015–9.
- [37] M. Zhuo, A. Borgna, M. Saeys, *Journal of Catalysis* **2013**, *297*, 217–226.
- [38] B. T. Loveless, C. Buda, M. Neurock, E. Iglesia, *J Am Chem Soc* **2013**, *135*, 6107–21.

CHAPTER 2

THEORY AND METHODS

Contents

2.1	Introduction	15
2.2	Reactions on surfaces	16
2.3	Transition state theory	20
2.4	Scaling relations	21
2.5	Density functional theory	22
2.6	Microkinetic modeling	27
2.7	References	30

2.1 Introduction

With the exponentially increased amount of computing power, previously intractable theoretical chemistry problems can now be solved in days, hours, or even minutes. This has led to the development of the field of computational chemistry, which applies computer simulations to solve chemical problems. Usually these problems pertain to finding the structure and properties of a particular molecular system. For catalysis, the quantity of interest is usually the rate of a chemical reaction.

In this work the rate of chemical reactions is predicted from theoretical chemistry methods and *ab initio* computations. The energetics of the catalytic system are determined with the use of Density Functional Theory (DFT). With this approach, each state of the catalyst, be it an empty catalyst, or a reaction event on a catalyst, is assigned an energy. Then, the energetic differences can be used in transition state theory to predict the rate constant of an elementary reaction step. These rate constants, in combination with an assumed mechanism, can then be used in a microkinetic modeling (MKM) approach to get macroscopic reaction rates [1].

2.2 Reactions on surfaces

Catalyst surfaces are able to lower the barrier for an elementary reaction step by forming chemical bonds with the reactants. These surface-adsorbate bonds lower the internal bond strengths in the adsorbate and thus reduce the stability of the reactants. Depending on the binding strength, a multi-atomic adsorbate can undergo either associative or dissociative adsorption.

Associative adsorption

The equilibrium reaction for associative adsorption of gas-phase component A on site * can be described as



where k_{A}^{+} is the rate constant for adsorption, k_{A}^{-} is the rate constant for desorption, and A^* is adsorbed A. The rate equation describing the change of the surface coverage θ_{A} is then

$$\frac{d\theta_{\text{A}}}{dt} = k_{\text{A}}^{+} P_{\text{A}} \theta_{*} - k_{\text{A}}^{-} \theta_{\text{A}} \quad (2.2)$$

where P_{A} is the dimensionless partial pressure of A corresponding to

$$P_{\text{A}} = \frac{p_{\text{A}}}{p_{\ominus}} \quad (2.3)$$

Then, if A is the only compound on the surface, the total sum of surface sites is

$$\theta_{\text{Total}} = 1 = \theta_{\text{A}} + \theta_{*} \quad (2.4)$$

Leading to,

$$\theta_{*} = 1 - \theta_{\text{A}} \quad (2.5)$$

Which can be used with

$$K_{\text{A}} = \frac{k_{\text{A}}^{+}}{k_{\text{A}}^{-}} \quad (2.6)$$

To describe the surface coverage θ_{A} under equilibrium as

$$\theta_{\text{A}} = K_{\text{A}} P_{\text{A}} \theta_{*} = K_{\text{A}} P_{\text{A}} (1 - \theta_{\text{A}}) \quad (2.7)$$

Rewriting this equation leads to,

$$\theta_{\text{A}} = \frac{K_{\text{A}} P_{\text{A}}}{1 + K_{\text{A}} P_{\text{A}}} \quad (2.8)$$

$$\theta_{*} = \frac{1}{1 + K_{\text{A}} P_{\text{A}}} \quad (2.9)$$

Associative adsorption + decomposition

For a monomolecular decomposition reaction of A the rate then depends on the rate constant k and the coverages via

$$r = k\theta_A\theta_* = \frac{k \cdot K_A P_A}{(1 + K_A P_A)^2} \quad (2.10)$$

Dissociative adsorption

The equilibrium reaction for dissociative adsorption of gas-phase component B_2 on site $*$ can be described as



where the rate equation describing the change of the surface coverage θ_B can be written as

$$\frac{d\theta_B}{dt} = k_{B_2}^+ P_{B_2} \theta_*^2 - k_{B_2}^- \theta_B^2 \quad (2.12)$$

Following the same procedure as for associative adsorption the coverages are

$$\theta_B = \frac{\sqrt{K_{B_2} P_{B_2}}}{1 + \sqrt{K_{B_2} P_{B_2}}} \quad (2.13)$$

$$\theta_* = \frac{1}{1 + \sqrt{K_{B_2} P_{B_2}}} \quad (2.14)$$

Competitive adsorption

If multiple components can adsorb to the surface then strong binding of one component can reduce the coverage of another component. This is called competitive adsorption. For example, in the case of associative adsorption of A and B following equation 2.1, and a conservation of sites of

$$\theta_{\text{Total}} = 1 = \theta_A + \theta_B + \theta_* \quad (2.15)$$

The coverages of A, B, and $*$ can be derived as

$$\theta_A = \frac{K_A P_A}{1 + K_A P_A + K_B P_B} \quad (2.16)$$

$$\theta_B = \frac{K_B P_B}{1 + K_A P_A + K_B P_B} \quad (2.17)$$

$$\theta_* = \frac{1}{1 + K_A P_A + K_B P_B} \quad (2.18)$$

2.2.1. Langmuir-Hinshelwood mechanism

Usually a reaction network is more complex than just a monomolecular decomposition reaction. For a bimolecular reaction the Langmuir-Hinshelwood (LH) mechanism can be used to predict the reaction rate. In this mechanism both reacting compounds have to adsorb to the surface before they can react. For example, for the association reaction of associatively adsorbed A and B to AB, the reaction network can be as follows:



The reaction rates then become

$$r_1 = k_1^+ P_A \theta_* - k_1^- \theta_A \quad (2.23)$$

$$r_2 = k_2^+ P_B \theta_* - k_2^- \theta_B \quad (2.24)$$

$$r_3 = k_3^+ \theta_A \theta_B - k_3^- \theta_{AB} \theta_* \quad (2.25)$$

$$r_4 = k_4^+ \theta_{AB} - k_4^- P_{AB} \theta_* \quad (2.26)$$

The evolution of the surface coverages over time can then be described by a set of ordinary differential equations (ODEs):

$$\frac{d\theta_A}{dt} = r_1 - r_3 \quad (2.27)$$

$$\frac{d\theta_B}{dt} = r_2 - r_3 \quad (2.28)$$

$$\frac{d\theta_{AB}}{dt} = r_3 - r_4 \quad (2.29)$$

$$\frac{d\theta_*}{dt} = r_3 + r_4 - r_1 - r_2 \quad (2.30)$$

This set can be solved numerically with microkinetic modeling. Alternatively, there are several assumptions that can be made to reduce the set of differential equations to a single rate equation [2]. First, if we assume that the system is in steady state, then the surface

coverage differentials approach zero. By assuming a rate determining step we can set the other reactions to be at quasi-equilibrium. Usually the quasi-equilibrium assumption is valid for adsorption and desorption steps. The rate determining step is often a surface reaction. In this case, setting reaction r_3 as rate determining results in the following overall rate:

$$r = r_3^+ - r_3^- = \frac{k_3^+ \cdot K_A P_A \cdot K_B P_B - k_3^- \cdot \frac{1}{K_{AB}} P_{AB}}{\left(1 + K_A P_A + K_B P_B + \frac{1}{K_{AB}} P_{AB}\right)^2} \quad (2.31)$$

$$= \frac{k_3^+ \cdot K_A P_A \cdot K_B P_B \cdot \left(1 - \frac{1}{K_3} \cdot \frac{1}{K_A P_A \cdot K_B P_B} \cdot \frac{1}{K_{AB}} P_{AB}\right)}{\left(1 + K_A P_A + K_B P_B + \frac{1}{K_{AB}} P_{AB}\right)^2} \quad (2.32)$$

$$= \frac{k_3^+ \cdot K_A P_A \cdot K_B P_B \cdot (1 - K_{EQ} \cdot P_{EQ})}{\left(1 + K_A P_A + K_B P_B + \frac{1}{K_{AB}} P_{AB}\right)^2} \quad (2.33)$$

With,

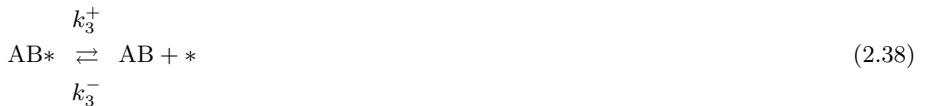
$$K_{EQ} = \frac{1}{K_3 K_A K_B K_{AB}} \quad (2.34)$$

$$P_{EQ} = \frac{P_{AB}}{P_A P_B} \quad (2.35)$$

From this state even more approximations can be made to simplify the system. The irreversible step approximation sets $K_{EQ} = 0$, so that the backward reaction term goes to zero. Alternatively, the zero-conversion approximation sets $P_{EQ} = 0$. This approximation has the same effect, with the additional benefit that the $\frac{1}{K_{AB}} P_{AB}$ term in the denominator of equation 2.33 drops out.

2.2.2. Eley-Rideal mechanism

The Eley-Rideal (ER) mechanism follows the same rules as the Langmuir-Hinshelwood model, with the exception that only one of the two reacting species has to adsorb to the surface. This often simplifies the kinetic network as one less species has to be taken into account for the surface coverage. For example, the association of A and B in an ER mechanism could be as follows:



With the second reaction as rate determining the rate can be described as:

$$r = \frac{k_2^+ \cdot K_A P_A \cdot P_B \cdot (1 - K_{\text{EQ}} \cdot P_{\text{EQ}})}{1 + K_A P_A + \frac{1}{K_{\text{AB}}} P_{\text{AB}}} \quad (2.39)$$

With,

$$K_{\text{EQ}} = \frac{1}{K_3 K_A K_{\text{AB}}} \quad (2.40)$$

$$P_{\text{EQ}} = \frac{P_{\text{AB}}}{P_A P_B} \quad (2.41)$$

Usually, the LH mechanism is more likely than the ER mechanism. For a reaction to occur directly from the gas phase a significant amount of entropy has to be lost for the impinging species. As a result, the rate of such a process is lower than via an adsorbed state in the LH mechanism.

2.3 Transition state theory

The previous section has shown how to relate the reaction rate r to partial pressures P , equilibrium constants K , and rate constants k . This section will show how K and k relate to differences in energy. For an elementary reaction step the equilibrium constant K can be related to the Gibbs free reaction heat:

$$K = \exp\left(\frac{-\Delta G}{RT}\right) = \exp\left(\frac{-(\Delta H - T\Delta S)}{RT}\right) = \frac{Q_{\text{FS}}}{Q_{\text{IS}}} \exp\left(\frac{-\Delta H}{RT}\right) \quad (2.42)$$

Here Q_{FS} and Q_{IS} represent the partition functions of the final and initial state respectively. Typically, the partition function Q is split into translational, vibrational, and rotational contributions

$$Q = q_{\text{trans}} \cdot q_{\text{vib}} \cdot q_{\text{rot}} \quad (2.43)$$

For a diatomic molecule these partition functions take the forms

$$q_{\text{trans}} \text{ (per dimension)} = \frac{L\sqrt{2\pi mk_{\text{B}}T}}{h} \quad (2.44)$$

$$q_{\text{vib}} \text{ (per vibration)} = \frac{1}{1 - \exp\left(\frac{-h\nu}{k_{\text{B}}T}\right)} \quad (2.45)$$

$$q_{\text{rot}} \text{ (in two dimensions)} = \frac{8\pi^2 I k_{\text{B}}T}{h^2} \quad (2.46)$$

The individual rate constants in forward and backward directions have empirically been linked to an exponential expression by Svante Arrhenius in 1889:

$$k = \nu \cdot \exp\left(\frac{-E_{\text{act}}}{RT}\right) \quad (2.47)$$

The equation as described by Transition state theory (TST) bears strong resemblance to this empirical Arrhenius equation. TST was developed independently by Henry Eyring, and by Meredith Gwynne Evans and Michael Polanyi [3–5]. It states:

$$k = \frac{k_{\text{B}}T}{h} \frac{Q_{\text{TS}\#}}{Q_{\text{IS}}} \exp\left(\frac{-E_{\text{act}}}{RT}\right) \quad (2.48)$$

The three underlying assumptions leading to this equation are:

- 1) The transition state is in thermal equilibrium with the initial state.
- 2) Going from the transition state to the final state is an irreversible process.
- 3) Crossing the transition state is done with a particular velocity or frequency.

2.4 Scaling relations

Despite the increases in computational power, computing reaction pathways is still a time-consuming process. For this reason, many studies regarding the theoretical screening of many model catalysts make use of scaling relations.

Already in the 1920s, Brønsted observed various relationships governing activity during acid and base catalysis. One such relationship is a proportionality between the catalytic constant and the strength constant of the acid or basic catalyst [6]. Evans and Polanyi generalized this relation for reaction barriers. This led to the ability to relate activation energies to the reaction energy by using the Brønsted–Evans–Polanyi (BEP) relationship

$$\delta E_{\text{act}} = \alpha \delta E_{\text{reac}} \quad (2.49)$$

where δE_{act} is the change in activation energy corresponding to a change of the reaction energy δE_{reac} . The linear scaling is determined by the constant α , which is based on the particular reaction type [7]. Generally, the α value for dissociation of π -bonds is close to 1, indicating a late transition state [8]. The lateness of a transition state is influenced by having more or less resemblance to either the initial or the final state.

An important requirement for BEP scaling is that the reactive environment for the transition state is similar between the scaled systems. For example, the BEP relation can be used to explain how reaction energy barriers change for the same active site on different transition metals. For dissociation reactions, the atomic binding energy in the final state is higher for transition metals to the upper left of the periodic table. The resulting negative value for δE_{reac} then leads to a lower dissociation barrier. An example of when the BEP relation breaks down is when a structure sensitive reaction is scaled to predict the barriers between different active site topologies, like terraces and step-edges.

The power of BEP scaling is that a transition state search does not have to be repeated if the energies of the electronically modified initial state and final state are known. An even more versatile scaling method is achieved by adding linear scaling between adsorbates [9]. In this way, it is possible to estimate the full potential energy diagram on the basis of only several chemisorption energies like C and O. Such a method is a useful tool for

screening new catalysts. Of course, as the resulting energy diagrams are only approximate, subsequent full DFT calculations are still necessary for the most interesting systems.

2.5 Density functional theory

Usually to goal of Density Functional Theory (DFT) is to get the ground state energies of a particular molecular system. From these energies, we can derive relative stabilities and reactiveness. In practice this means that we need to find solutions of the non-relativistic time-independent Schrödinger equation.

$$H |\Phi\rangle = E |\Phi\rangle \quad (2.50)$$

where H is a Hermitian operator called the Hamiltonian, $|\Phi\rangle$ is the wave function, and E is the energy. Only the simplest cases can be solved exactly. Therefore, the systems in this thesis can only be described by approximate solutions. This section will briefly go through some important aspects for finding ground state energies of molecular systems. A more in-depth introduction to the matter can be found in the book “*Modern quantum chemistry: introduction to advanced electronic structure theory*” by Szabó and Ostlund [10].

2.5.1. The Born-Oppenheimer Approximation

The ground state energy can be split into a number of contributions. A useful first distinction is the separation of energy contributions from the atom nuclei and from the electrons.

$$E_{\text{tot}} = E_{\text{elec}} + E_{\text{nuc1}} \quad (2.51)$$

Atom nuclei are much heavier than the electron around them. As such, the nuclei appear to be fixed in space from the perspective of the fast-moving electron. Therefore, a good approximation is to consider the electrons to be moving in the field of fixed nuclei. Although there is still an energy contribution from the nuclei, the nuclear repulsion can simply be added to the electronic problem as a constant.

$$E_{\text{tot}} = E_{\text{elec}} + \sum_{A=1}^M \sum_{B>A}^M \frac{Z_A Z_B}{R_{AB}} \quad (2.52)$$

This leaves the problem of solving the electronic Schrödinger equation.

$$H_{\text{elec}} \Phi = E_{\text{elec}} \Phi_{\text{elec}} \quad (2.53)$$

2.5.2. Hohenberg-Kohn

This section will closely follow the 1964 paper of Hohenberg and Kohn [11]. The example case is a collection of an arbitrary number of electrons enclosed in a large box. The electrons are moving under the influence of an external potential $v(\mathbf{r})$ and the mutual Coulomb

repulsion. The electronic Hamiltonian H has the following form:

$$H = T + V + U \quad (2.54)$$

Here the Hamiltonian is split into a kinetic part T , interactions with the external potential V , and the electron-electron interactions U . In atomic units these parts are:

$$T \equiv \frac{1}{2} \int \nabla \psi^*(\mathbf{r}) \nabla \psi(\mathbf{r}) d\mathbf{r} \quad (2.55)$$

$$V \equiv \int v(\mathbf{r}) \psi^*(\mathbf{r}) \psi(\mathbf{r}) d\mathbf{r} \quad (2.56)$$

$$U = \frac{1}{2} \int \int \frac{1}{|\mathbf{r} - \mathbf{r}'|} \psi^*(\mathbf{r}) \psi^*(\mathbf{r}') \psi(\mathbf{r}') \psi(\mathbf{r}) d\mathbf{r} d\mathbf{r}' \quad (2.57)$$

For a nondegenerate ground state Ψ we can denote the electronic density by

$$n(\mathbf{r}) \equiv (\Psi, \psi^*(\mathbf{r}) \psi(\mathbf{r}) \Psi) \quad (2.58)$$

which is a functional of $v(\mathbf{r})$. Hohenberg and Kohn showed by *reductio ad absurdum* that $v(\mathbf{r})$ is (to within a constant) a unique functional of $n(\mathbf{r})$. As such H is fixed by $v(\mathbf{r})$, and the ground state wave function is a unique functional of $n(\mathbf{r})$.

The kinetic and interaction energy in the Hamiltonian can be combined to define a universal functional, valid for any number of particles and any external potential:

$$F[n(\mathbf{r})] \equiv (\Psi, (T + U) \Psi) \quad (2.59)$$

For a given potential $v(\mathbf{r})$ this provides the energy functional

$$E_v[n(\mathbf{r})] \equiv \int v(\mathbf{r}) n(\mathbf{r}) d\mathbf{r} + F[n(\mathbf{r})]. \quad (2.60)$$

Minimization of this functional leads to the ground-state energy and density. The difficulty however, is that the universal functional $F[n(\mathbf{r})]$ is still unknown. For most purposes it is convenient to separate the classical Coulomb energy from $F[n(\mathbf{r})]$ to get

$$F[n(\mathbf{r})] = \frac{1}{2} \int \int \frac{n(\mathbf{r}) n(\mathbf{r}')}{|\mathbf{r} - \mathbf{r}'|} d\mathbf{r} d\mathbf{r}' + G[n(\mathbf{r})]. \quad (2.61)$$

In this new equation the term $G[n(\mathbf{r})]$ is still unknown, but smaller than $F[n(\mathbf{r})]$.

2.5.3. Kohn-Sham

This section continues from the $G[n(\mathbf{r})]$ term in the previous section, and will follow the 1965 paper of Kohn and Sham [12]. The term G is defined as

$$G[n] \equiv T_s[n] + E_{xc}[n] \quad (2.62)$$

Here $T_s[n]$ is the kinetic energy of a system of noninteracting electrons with density $n(\mathbf{r})$, and $E_{xc}[n]$ is defined as the exchange and correlation energy of an interacting system with

density $n(\mathbf{r})$. The energy functional $E_v[n(\mathbf{r})]$ has to be stationary when switching to the kinetic description of noninteracting electrons. Therefore, we can derive from it, subject to the condition

$$\int \delta n(\mathbf{r}) d\mathbf{r} = 0 \quad (2.63)$$

the equation

$$\int \delta n(\mathbf{r}) \left\{ \phi(\mathbf{r}) + \frac{\delta T_s[n]}{\delta n(\mathbf{r})} + v_{xc}(n(\mathbf{r})) \right\} d\mathbf{r} = 0; \quad (2.64)$$

Where

$$\phi(\mathbf{r}) = v(\mathbf{r}) + \int \frac{n(\mathbf{r}')}{|\mathbf{r} - \mathbf{r}'|} d\mathbf{r}' \quad (2.65)$$

and $v_{xc}(n)$ is the exact exchange and correlation contribution to the one-particle potential.

$$v_{xc}(n) \equiv \delta E_{xc}[n] / \delta n(\mathbf{r}) \quad (2.66)$$

For given ϕ and v_{xc} , the corresponding density can be found by solving the one-particle Schrödinger equation

$$\left\{ -\frac{1}{2} \nabla^2 + [\phi(\mathbf{r}) + v_{xc}(n(\mathbf{r}))] \right\} \psi_i(\mathbf{r}) = \epsilon_i \psi_i(\mathbf{r}) \quad (2.67)$$

and setting

$$n(\mathbf{r}) = \sum_{i=1}^N |\psi_i(\mathbf{r})|^2 \quad (2.68)$$

where N is the number of electrons.

These equations can be solved self-consistently with the following procedure: Make an initial guess for density $n(\mathbf{r})$. Next, find $\phi(\mathbf{r})$ and $v_{xc}(n)$. Finally, use $\phi(\mathbf{r})$ and $v_{xc}(n)$ to solve the Schrödinger equation and construct the new density.

As described in the previous section, minimization of the energy leads to real ground state. Therefore, the self-consistent procedure is repeated until a new iteration does not lead to a (significant) drop in total energy. The exact total energy is then given by

$$E = \sum_{i=1}^N \epsilon_i - \frac{1}{2} \iint \frac{n(\mathbf{r})n(\mathbf{r}')}{|\mathbf{r} - \mathbf{r}'|} d\mathbf{r}d\mathbf{r}' + E_{xc}[n] - \int v_{xc}(\mathbf{r})n(\mathbf{r})d\mathbf{r} \quad (2.69)$$

Unfortunately, directly applying this method is not trivial, as no DFT theory at this moment is possible to give an exact functional for $E_{xc}[n]$ and $v_{xc}(r)$. Fortunately, some very useful approximations have been developed.

2.5.3. Exchange-correlation energy approximations

Local-density approximation (LDA)

Two limiting cases exist with an exact value for $G[n]$. The first case is when the electron density is constant or sufficiently slowly varying. For this case, Hohenberg and Kohn have shown that

$$E_{xc}[n] = \int n(\mathbf{r})\epsilon_{xc}(n(\mathbf{r})) d\mathbf{r} \quad (2.70)$$

where $\epsilon_{xc}(n)$ is the exchange and correlation energy per electron of a uniform electron gas of density n . For cases outside the limit of slowly varying density the error scales with ∇^2 . The second case holds for systems with a high density. For very high electron densities the kinetic energy $T_s[n]$ tends to overrule the exchange and correlation energy. Even with varying density, $T_s[n]$ can be determined with no approximations.

For a chemical system of atoms and molecules the second case holds only near the atomic nucleus, as the electronic density there is high. Large parts of the charge distribution are slowly varying, and there the first case holds. However, at the outer shells of atoms and at overlap regions in molecules neither case applies. These strongly varying charge distributions make the LDA method unsuitable for most chemical systems, except for some bulk metal systems.

Although the LDA approximation can give good results for some bulk systems, it fails to properly describe magnetism. Therefore, Kohn and Sham extended the Hohenberg-Kohn theory with the local spin-density approximation (LSDA) approach. In this approach the ground-state energy not only a functional of the total electron density, but depends on both the charge densities of electrons with spin up (+) and spin down (-).

Generalized gradient approximation (GGA)

The search for sufficient chemical accuracy (~ 10 kJ/mol) led to gradient corrections on top of the already existing LDA theory. The exchange correlation can be expanded to include gradient corrections in the following form

$$E_{xc}[n] = \int n(\mathbf{r})\epsilon_{xc}(n)d\mathbf{r} + \int |\nabla n|^2 \epsilon_{xc}^{(2)}(n)d\mathbf{r} + \dots \quad (2.71)$$

where $\epsilon_{xc}^{(2)}$ is the exchange and correlation from the second term in the energy expansion in powers of the gradient operator.

In the early eighties Langreth and Mehl presented their Nonlocal Exchange-Correlation Energy Functional, reaching atomic total energies accurate to ~ 13 kJ/mol [13, 14]. Two GGA functionals popular in use are PW91 [15] and PBE [16–18]. The PBE functional was mainly developed as a simpler form and derivation of PW91. To achieve this, some correct but less important features from PW91 were sacrificed. Both GGA methods produce similar numerical results for many simple properties. However, some more exotic properties like monovacancy formation energies might deviate between the two [19]. In this thesis all calculations were performed using a PBE potential based on the pseudopotential approximation and the projector augmented-wave method (PAW).

Pseudopotentials

Electronic calculations usually require a large amount of computing power. One problem is the tremendous effort to evaluate every single electron contribution for systems of many electrons. Although these many electrons are replaced by an electron density in DFT, there are still very strong variations in the core region of atoms. This leads to a complex and computationally demanding potential in the Hamiltonian. In 1934 Hans G. A. Hellmann developed a pseudopotential to prevent this issue [20, 21]. Hellmann realized that the outer few (valence) electrons contribute the most to the chemical and physical properties of atoms. Although most computational time is spent on the complicated interactions between core electrons, these interactions do not provide much more chemical information. Hellmann therefore replaced these effects by a *Zusatzpotential*.

The less accurate pseudopotential method appeared to reproduce the results of all electron calculations surprisingly well, at only a fraction of the computational cost. In the early seventies Melius and Goddard III found that the pseudopotential, or effective potential method, was a reliable tool for attempting calculations on very large molecules [22, 23].

Projector augmented-wave (PAW) method

Generally, the wave functions in an electronic system are build out of linear combinations of certain basis functions. This is called a basis set, which can have many forms. An example of a basis set is a collection of atomic orbitals which can be combined to form molecular orbitals. Another type of basis set that is commonly used in DFT is a large amount of plane waves. The spatial resolution of the set of plane waves can be defined by a lower limit for the allowed wavelength. Usually this is done by setting a maximum wave energy. As the electron wave functions have strong fluctuations in the core region, the plane wave method is usually used together with pseudopotentials [24]. A generalization of that combination was shown in the 1994 article of Blöchl [25] on the projector augmented-wave (PAW) method.

In the Vienna Ab initio simulation package (VASP) [26–29], these potentials are provided as input including the exchange-correlation approximations. The software then generates a trial density for the given system and finds the pseudo (PS) wave functions to generate a new density. These PS wave functions then have to be converted back into all-electron (AE) wave functions to get correct chemical and physical properties. Although the exact conversion factors are again unknown, the PAW method provides augmented partial waves to use for this PS to AE conversion. As integration over multiple nuclei is computationally complex and expensive, the partial waves are made by summation over the one-center expansions. In this way, spherical symmetry can be applied and many computational expenses are saved. The PS wave function $|\tilde{\Psi}\rangle$ can be converted to the AE wave function $|\Psi\rangle$ by

$$|\Psi\rangle = |\tilde{\Psi}\rangle - \sum_i |\tilde{\psi}_i\rangle c_i + \sum_i |\psi_i\rangle c_i \quad (2.72)$$

where $|\tilde{\psi}_i\rangle$ and $|\psi_i\rangle$ are the PS and AE partial waves respectively. Projector functions $\langle \tilde{p}_i |$

are used to form a scalar product with the PS wave function to give the coefficients

$$c_i = \langle \tilde{p}_i | \tilde{\Psi} \rangle \quad (2.73)$$

The projector functions are such that the one-center PS expansion, within the augmentation zone, is identical to the PS wave function itself. Finally, the AE wavefunction is obtained from the PS wavefunction by

$$|\Psi\rangle = |\tilde{\Psi}\rangle - \sum_i \left(|\psi_i\rangle - |\tilde{\psi}_i\rangle \right) \langle \tilde{p}_i | \tilde{\Psi} \rangle. \quad (2.74)$$

2.5.4. Zero-point energy (ZPE) correction

The previous sections showed how to compute the quantum chemical ground state energy. However, even in the ground state a quantum mechanical system will have zero-point vibrations and a corresponding zero-point energy (ZPE) [30]. One way to obtain this ZPE is by computing the second derivatives of the energy with respect to the atomic positions. To obtain this Hessian matrix, the ions i and j are displaced along each Cartesian coordinate. The Hessian is then constructed from the curvature in the forces — which are the first derivatives of the energy — at the various perturbations. Although the Hessian should in principle be symmetric, usually the computed values are slightly asymmetric. The matrix can be re-symmetrized easily by setting

$$H_{i,j} = \frac{H_{i,j}^{\text{asym}} + H_{j,i}^{\text{asym}}}{2} \quad (2.75)$$

To get the vibrational normal modes the Hessian is mass-weighted according to the masses of displaced atoms i and j so that

$$H_{i,j}^m = \frac{H_{i,j}}{\sqrt{M_i * M_j}} \quad (2.76)$$

Diagonalization of $H_{i,j}^m$ then yields eigenvalues ε from which the vibrational frequencies can be calculated with

$$\nu_i = \frac{1}{2\pi c} \sqrt{\varepsilon_i} \quad (2.77)$$

Determining the ZPE correction is now simply doing a summation over all (real) frequencies. Also, the vibrational partition function can be calculated from these frequencies by

$$q_{\text{vib}} = \prod_i \frac{1}{1 - \exp\left(\frac{-\nu_i^{\text{real}}}{k_{\text{B}} T}\right)} \quad (2.78)$$

2.6 Microkinetic modeling

In the previous sections the concepts of Langmuir-Hinshelwood kinetics, transition state theory, and DFT have been discussed. Combined, these methods allow the construction of microkinetic models. Typically, DFT is used to determine energy barriers that are used in

transition state theory to predict reaction rate constants. These rate constants can be applied in a kinetic model by either reducing the reaction network through various approximations, or by numerically solving the entire set of differential equations. Microkinetic modeling (MKM) is the latter approach, by which reaction rates and surface coverages are integrated over time.

2.6.1. Ordinary differential equation (ODE) solving

The set of elementary reaction rates define the set of ordinary differential equations (ODEs). The initial gas and surface component concentrations are the boundary conditions for this set. A simple way of solving this set of ODEs numerically is to use the Euler method. For a system evolving over time with a step size of Δt , a new value $y_i(t + \Delta t)$ can be found from a known value $y_i(t)$ by using the differential:

$$y_i(t + \Delta t) \approx y_i(t) + \Delta t \cdot y_i'(t) \quad (2.79)$$

This (Forward) Euler method is explicit and the error increases as the step size increases. An alternative is the Backward Euler method where

$$y_i(t + \Delta t) \approx y_i(t) + \Delta t \cdot y_i'(t + \Delta t) \quad (2.80)$$

This method is implicit, as the derivative $y_i'(t + \Delta t)$ is unknown at time t , and has to be solved for. As a result, the computational costs of implicit methods are higher. An advantage of implicit methods is that they perform better for stiff systems. Stiffness is a phenomenon that is difficult to define in precise mathematical terms. Chemical systems are, in general, stiff systems. In this case, stiffness mostly arises from the fact that reaction rates can differ for multiple orders of magnitude. Unsuitable solving algorithms require very small step sizes to limit errors in such stiff systems. To prevent the high computational costs associated with these small step sizes, multiple methods exist specifically to handle stiff ODEs. The microkinetic modeling in this thesis has been done with a linear multistep backward differentiation formula method [31–34]. In principle this is an extension of the Backward Euler method, in which the step size can be increased by using the information of up to five previous steps.

2.6.1. Sensitivity analysis

From MKM we can find surface coverages and reaction rates under transient and steady-state conditions. By slightly altering input conditions like pressure and temperature, the system's sensitivity to these changes can be analyzed and related to experimental phenomena.

Reaction orders

Considering the reaction $A + B \rightleftharpoons C$, a possible parameterization of the rate is the power rate law:

$$r = k \cdot [A]^{n_A} \cdot [B]^{n_B} \cdot [C]^{n_C} \quad (2.81)$$

or

$$r = k \cdot P_A^{n_A} \cdot P_B^{n_B} \cdot P_C^{n_C} \quad (2.82)$$

where n_X is the reaction order of component X. These orders can be found by changing the partial pressure of X by small amounts and measuring the change in reaction rate. The reaction order in e.g. A can then be found from the following derivative:

$$n_A \equiv \frac{\partial \ln r^+}{\partial \ln [A]} = [A] \frac{\partial \ln r^+}{\partial [A]} \quad (2.83)$$

Apparent activation energy

The apparent activation energy follows from the sensitivity analysis for temperature:

$$E_{\text{act}^{\text{app}}} \equiv RT^2 \frac{\partial \ln r^+}{\partial T} \quad (2.84)$$

Degree of rate control methods

Often a single elementary reaction step is assumed as rate determining, with the other reactions in equilibrium. In reality this situation hardly ever occurs, and multiple steps are controlling the rate. The Degree of Rate Control (DRC) method can identify these steps [35].

For an elementary step i , the degree of rate control $X_{\text{RC},i}$ is defined as

$$X_{\text{RC},i} = \frac{k_i}{r} \left(\frac{\partial r}{\partial k_i} \right)_{k_{j \neq i}, K_i} = \left(\frac{\partial \ln r}{\partial \ln k_i} \right)_{k_{j \neq i}, K_i} \quad (2.85)$$

where only the rate constants of step i are changed. Equilibrium constant K_i is kept constant, so forward and backward k_i values are changed by equal factors. Essentially this method is changing the free energy of the transition state, thus either increasing or decreasing both forward and backward reaction barriers. A positive $X_{\text{RC},i}$ value implies that the overall reaction speeds up when lowering the barriers of step i . A negative $X_{\text{RC},i}$ value implies the reverse, that is, lowering the barriers of step i lowers the overall reaction rate. Summation over all reaction steps leads to conservation of the DRC:

$$\sum_i X_{\text{RC},i} = 1 \quad (2.86)$$

The same method can be applied to the reaction intermediates. This gives the thermodynamic degree of rate control $X_{\text{TRC},n}$ of intermediate n :

$$X_{\text{TRC},n} = \frac{1}{r} \left(\frac{\partial r}{\partial \left(\frac{-G_n^0}{RT} \right)} \right)_{G_{m \neq n}^0, G_i^{\text{TS}}} = \left(\frac{\partial \ln r}{\partial \left(\frac{-G_n^0}{RT} \right)} \right)_{G_{m \neq n}^0, G_i^{\text{TS}}} \quad (2.87)$$

Now a negative $X_{\text{TRC},n}$ value implies that the overall reaction slows down when stabilizing

an intermediate. Often, $X_{\text{TRC},n}$ can be linked to the coverage θ_n of intermediate n by

$$X_{\text{TRC},n} = -\sigma \cdot \theta_n \quad (2.88)$$

where σ is the average number of sites required in the rate limiting steps. Typically, this value varies between 1 and 2.

Analogous to the degree of rate control, the degree of selectivity control (DSC) [1, 36] can be defined by

$$X_{\text{SC},i,c} = \left(\frac{\partial \eta_c}{\partial \ln k_i} \right)_{k_{j \neq i}, K_i} \quad (2.89)$$

Where η_c is the selectivity to compound c . The corresponding sum-rule for the degree of selectivity control is

$$\sum_{i,c} X_{\text{SC},i,c} = 0 \quad (2.90)$$

2.7 References

- [1] I. A. W. Filot, *Introduction to microkinetic modeling*, Technische Universiteit Eindhoven, Eindhoven, **2018**.
- [2] I. Chorkendorff, J. W. Niemantsverdriet, *Concepts of modern catalysis and kinetics*, Wiley-VCH Verlag, Weinheim, **2003**.
- [3] H. Eyring, *The Journal of Chemical Physics* **1935**, *3*, 107–115.
- [4] H. Eyring, *Chemical Reviews* **1935**, *17*, 65–77.
- [5] S. Glasstone, K. Laidler, H. Eyring, *The Theory of Rate Processes: The Kinetics of Chemical Reactions, Viscosity, Diffusion and Electrochemical Phenomena*, McGraw-Hill Book Company, Incorporated, **1941**.
- [6] J. N. Bronsted, *Chemical Reviews* **1928**, *5*, 231–338.
- [7] M. G. Evans, M. Polanyi, *Transactions of the Faraday Society* **1938**, *34*, 11–24.
- [8] R. A. van Santen, M. Neurock, S. G. Shetty, *Chemical Reviews* **2010**, *110*, 2005–2048.
- [9] F. Abild-Pedersen, J. Greeley, F. Studt, J. Rossmeisl, T. R. Munter, P. G. Moses, E. Skúlason, T. Bligaard, J. K. Nørskov, *Physical Review Letters* **2007**, *99*, 016105.
- [10] A. Szabo, N. Ostlund, *Modern Quantum Chemistry: Introduction to Advanced Electronic Structure Theory*, Dover Publications, **1996**.
- [11] P. Hohenberg, W. Kohn, *Physical Review* **1964**, *136*, B864–B871.
- [12] W. Kohn, L. J. Sham, *Physical Review* **1965**, *140*, A1133–A1138.
- [13] D. C. Langreth, M. J. Mehl, *Physical Review Letters* **1981**, *47*, 446–450.
- [14] D. C. Langreth, M. J. Mehl, *Physical Review B* **1983**, *28*, 1809–1834.

- [15] J. P. Perdew, J. A. Chevary, S. H. Vosko, K. A. Jackson, M. R. Pederson, D. J. Singh, C. Fiolhais, *Physical Review B* **1992**, *46*, 6671–6687.
- [16] J. P. Perdew, K. Burke, M. Ernzerhof, *Physical Review Letters* **1996**, *77*, 3865–3868.
- [17] J. P. Perdew, K. Burke, M. Ernzerhof, *Physical Review Letters* **1997**, *78*, 1396–1396.
- [18] J. P. Perdew, K. Burke, Y. Wang, *Physical Review B* **1996**, *54*, 16533–16539.
- [19] A. E. Mattsson, R. Armiento, P. A. Schultz, T. R. Mattsson, *Physical Review B* **2006**, *73*, 195123.
- [20] H. Hellmann, *The Journal of Chemical Physics* **1935**, *3*, 61–61.
- [21] P. Schwerdtfeger, *ChemPhysChem* **2011**, *12*, 3143–3155.
- [22] L. R. Kahn, W. A. G. III, *The Journal of Chemical Physics* **1972**, *56*, 2685–2701.
- [23] C. F. Melius, W. A. Goddard, *Physical Review A* **1974**, *10*, 1528–1540.
- [24] D. R. Hamann, M. Schlüter, C. Chiang, *Physical Review Letters* **1979**, *43*, 1494–1497.
- [25] P. E. Blochl, *Phys Rev B Condens Matter* **1994**, *50*, 17953–17979.
- [26] G. Kresse, J. Hafner, *Physical Review B* **1993**, *47*, 558–561.
- [27] G. Kresse, J. Hafner, *Physical Review B* **1994**, *49*, 14251–14269.
- [28] G. Kresse, J. Furthmüller, *Computational Materials Science* **1996**, *6*, 15–50.
- [29] G. Kresse, J. Furthmüller, *Physical Review B* **1996**, *54*, 11169–11186.
- [30] A. Einstein, O. Stern, *Annalen der Physik* **1913**, *345*, 551–560.
- [31] B. Gough, *GNU Scientific Library Reference Manual - Third Edition*, Network Theory Ltd., **2009**, p. 592.
- [32] G. D. Byrne, A. C. Hindmarsh, *ACM Trans. Math. Softw.* **1975**, *1*, 71–96.
- [33] P. N. Brown, G. D. Byrne, A. C. Hindmarsh, *SIAM Journal on Scientific and Statistical Computing* **1989**, *10*, 1038–1051.
- [34] A. C. Hindmarsh, P. N. Brown, K. E. Grant, S. L. Lee, R. Serban, D. E. Shumaker, C. S. Woodward, *ACM Trans. Math. Softw.* **2005**, *31*, 363–396.
- [35] C. Stegelmann, A. Andreasen, C. T. Campbell, *Journal of the American Chemical Society* **2009**, *131*, 8077–8082.
- [36] C. Stegelmann, N. C. Schiødt, C. T. Campbell, P. Stoltze, *Journal of Catalysis* **2004**, *221*, 630–649.

CHAPTER 3

MODELING MEAN-FIELD LATERAL INTERACTIONS ON COBALT CATALYSTS

Contents

3.1	Introduction	34
3.2	Computational methods	35
3.3	Results and discussion	36
3.3.1	CO adsorption on Co(0001)	36
3.3.2	CO adsorption on Co(11 $\bar{2}$ 1)	43
3.3.3	CO adsorption on Co(0001) and Co(11 $\bar{2}$ 1) combined	48
3.3.4	N ₂ adsorption on Co(0001)	49
3.3.5	H ₂ activation on Co(0001) and Co(11 $\bar{2}$ 1)	50
3.3.6	H adsorption on Co(0001)	52
3.3.7	Stability of C, CH, O and OH on Co(0001)	52
3.3.8	Competitive adsorption on Co(0001)	56
3.3.9	A rigorous lateral interaction potential	58
3.3.10	A simplified thermodynamically consistent potential	59
3.3.11	Simulated temperature programmed desorption	60
3.4	Conclusions	61
3.5	References	62

Abstract

The surface coverage of nanoparticle catalysts is of significant influence on the mechanism of Fischer-Tropsch Synthesis (FTS). High coverages result in lateral interactions that change the stability of surface intermediates, which can significantly change both the activity as well as the selectivity of the overall reaction. Under Fischer-Tropsch conditions the CO coverage at the catalyst surface is expected to reach a saturation coverage well below unity as a result of such lateral interactions. To properly describe lateral interactions, we computed integral and differential adsorption heats for various FT intermediates. We found that, from the viewpoint of enthalpy, CO coverages above 6/9 ML are kinetically inaccessible, despite being thermodynamically allowed. At a relevant temperature of 500 K, we predict a

maximum CO coverage in the range of 0.32 ML - 0.55 ML, which is in good correspondence with experimental data. Importantly, we found that such lateral effects affect the coverage in a similar manner for a terrace and a step-edge surface, which can be explained by inter-adsorbate repulsion being the main contributing effect in interaction interactions. Adsorbed hydrogen was affected less by lateral interactions. The lateral interaction penalties of C and O were found to be comparable to that of CO. To model these effects, we proposed a rigorous lateral interaction potential satisfying thermodynamic consistency. To cope with the associated complexity of implementing such a potential in microkinetic modeling codes, we developed a simplified thermodynamically consistent potential. Mean-field microkinetics simulations using this potential can reproduce well the features of experimental temperature programmed desorption measurements.

3.1 Introduction

Three key aspects influencing the mechanism of Fischer-Tropsch Synthesis (FTS) are nanoparticle shape, size, and surface coverage [1–3]. Although the reaction energy network of the Fischer-Tropsch reaction can be determined with Density Functional Theory (DFT), these calculations usually do not include the effects of surface reconstruction or changing surface coverages. Exploration of the low coverage pathways for CO hydrogenation have already been done for rhodium and ruthenium surfaces, including the extension towards microkinetic modeling (MKM) [4–7]. However, lateral interactions are not explicitly included in these simulations.

The goal of this chapter is to study the effect of lateral interactions on two cobalt model surfaces, the Co(0001) surface and the Co(11 $\bar{2}$ 1) surface. These surfaces were chosen as Co(0001) is often used in experimental surface science studies [8, 9] and the Co(11 $\bar{2}$ 1) surface exposes step-edge sites that are highly active for CO dissociation [10]. The particular configuration of atoms in the Co(11 $\bar{2}$ 1) step-edge site is a perturbed arrangement of the classical B₅-site as referred to by Van Hardeveld and Hartog [11]. With a reported barrier of ~ 100 kJ/mol for direct CO dissociation this site is more active than e.g. the FCC Co(311) facet at ~ 150 kJ/mol [10]. If these sites are formed by surface reconstruction under FT conditions [3], it is likely that they contribute significantly to both FT activity and selectivity.

Under FT conditions the catalyst surface is expected to be filled for a large extent with CO. Surface science studies show that CO prefers to form a hexagonal pattern on cobalt terraces [12]. The question is how these structures develop at increasing coverages. The CO–CO separation is generally more than 4 Å for such a hexagonal arrangement at 1/3 monolayer (ML) coverage on cobalt. Therefore, at very low coverage, it is expected that lateral interactions are small and, due to dispersion interactions, might even be slightly attractive [13, 14]. At intermediate coverages the lateral interactions are expected to be more repulsive. On the one hand, the metallic surface becomes less reactive because the exposed surface atoms are already binding to other adsorbates. On the other hand, due to the decreasing CO–CO distance, the electrostatic repulsion between neighboring adsorbates

is expected to increase. As the electronic density around the adsorbates is of an exponential form, the lateral repulsion is expected to increase exponentially as well [15]. This suggests that the saturation coverage is limited by the amount of CO adsorbates per surface area, rather than by the amount of surface atoms per area [16]. This indicates that lateral interactions between the adsorbates play a dominant role and might explain the often negative reaction order for CO in the FTS process [17, 18].

Both experimental surface science data [8, 9] and DFT modeling [19, 20] of CO adsorption show that the CO saturation coverage for the Co(0001) surface is about 7/12 ML. Experimental steady-state isotopic transient kinetic analysis (SSITKA) data show that the CO coverage is between 0.4 ML and 0.6 ML under model FT conditions [16, 21, 22] in good agreement with extrapolated surface science data [9].

The literature contains various methods to deal with lateral interactions in kinetic modeling. Interactions can be fitted to computational adsorption energies at various coverages, to Monte-Carlo simulations, or to experimental desorption experiments [8, 23–28]. A quantitative *ab-initio* description of lateral interactions requires computational expenses combinatorial in the number of adsorbates and surface sites. Therefore, we mostly focused on the lateral interactions between adsorbates of the same species. The end of this chapter will then discuss the extension of these findings to co-coverage of unlike intermediates.

3.2 Computational methods

All quantum-chemical calculations were performed using a plane-wave density functional theory approach with the projector-augmented wave (PAW) method [29], as implemented in the Vienna ab initio simulation package (VASP) [30–33]. For exchange-correlation, the Perdew-Burke-Ernzerhof (PBE) functional was used [34]. The plane-wave basis set was limited to a 400 eV kinetic energy cut-off base. A gamma-centered Monkhorst-Pack 21 x 21 x 21 k-point mesh [35] was used for bulk hcp Co and a 5 x 5 x 1 k-point mesh for Co surface slabs. Calculations for molecular gas-phase references only employed the gamma point in a 10 x 10 x 10 Å³ cell. The Co lattice parameters for our calculations correspond to 2.49 Å, 2.49 Å and 4.03 Å for the *a*, *b* and *c* directions, respectively. For the Co(0001) surface, multiple unit cell expansions were constructed ranging from (2 x 2) to (4 x 4) unit cells. All Co(0001) surfaces were constructed with 5 atomic layers. The Co(11 $\bar{2}$ 1) surface was constructed from a (2 x 2) unit cell with 3 atomic layers (48 Co atoms per unit cell). Adsorbates on the Co(0001) surface slab were placed with mirror symmetry in the *ab*-plane to avoid spurious dipole-dipole interactions between neighboring unit cells. For the Co(11 $\bar{2}$ 1) surface slab, the adsorbates were placed using inversion symmetry. All atomic positions were optimized using the conjugate-gradient technique. We explored the dissociation pathway of associatively adsorbed H₂ with the climbing image nudged elastic band (cNEB) implementation [36–38]. The transition state (TS) was optimized using a quasi-Newton algorithm and was confirmed by the saddle point obtained from frequency calculation. Hessian matrices were calculated with the finite displacement technique in order to compute the zero-point energy (ZPE) corrections and vibrational partition functions for

all adsorbed species. The temperature programmed desorption simulations were carried out using the in-house developed MKMCXX code [6, 39].

3.3 Results and discussion

In this section two types of adsorption energies are discussed, which are presented as integral adsorption energy (average adsorption energy per adsorbate) and the differential adsorption energy. The average adsorption energy relates to the difference in stability of N adsorbates on a surface compared to the empty surface and all N adsorbates in the gas phase. Then, this energy difference is divided by the total number of adsorbates, giving the integral adsorption energy.

$$E_{\text{ads}}^{\text{int}} = \frac{\left(E_{N \cdot \text{adsorbate}}^{\text{surface}} - E_{\text{empty}}^{\text{surface}} - N \cdot E_{\text{adsorbate}}^{\text{gas}} \right)}{N} \quad (3.1)$$

$$E_{\text{ads}}^{\text{diff}} = E_{N \cdot \text{adsorbate}}^{\text{surface}} - E_{(N-1) \cdot \text{adsorbate}}^{\text{surface}} - 1 \cdot E_{\text{adsorbate}}^{\text{gas}} \quad (3.2)$$

The differential adsorption energy is incremental. Here, the energy difference is taken between the surface with N adsorbates compared to the surface with $N - 1$ adsorbates and one adsorbate in the gas phase. Changes in the integral adsorption energy are a good proxy to study the magnitude of lateral interactions. However, from a kinetic point of view the differential adsorption energy is more important, because it is this difference that determines the rate constant for desorption at a particular coverage.

3.3.1 CO adsorption on Co(0001)

We first determined stable CO configurations as a function of total CO coverage on the terrace Co(0001) surface. Figure 3.1 shows the geometries of the most stable configurations of CO on the (3×3) unit cell expansion. Comparison of the configurations at the different coverages shows that the most stable geometries are those where the CO adsorbates are well separated. That is, no two CO adsorbates will occupy vicinal sites, when there is room to alleviate repulsion by moving to a more distant site. The geometrically most favorable separation would be obtained by forming a symmetric hexagonal adsorption structure. As seen in Figure 3.1, full hexagonal symmetry is only present at $1/9$ ML, $3/9$ ML and $9/9$ ML. At the other coverages the adlayer structuring is constrained by the adsorption site lattice. The Co(0001) exposes three kinds of adsorption sites: top sites, bridge sites, and threefold-hollow sites. The latter sites can be subdivided again into fcc-hollow and hcp-hollow sites, depending on the underlying cobalt layer. For a fcc-hollow site no cobalt atom is directly below the site, while for an hcp-hollow site there is. Regardless of the site, adsorption of CO is strongest if it is positioned exactly above the site, rather than e.g. halfway between a bridge site and a threefold-hollow site. With the CO adsorbates constrained to these exact site positions it is not possible to form a fully hexagonally symmetric adlayer for every coverage.

By analyzing the site distributions, we find that CO preferentially adsorbs in threefold-

Table 3.1: Most stable configurations of CO adsorbates on the terrace (3 x 3) Co(0001) surface.

Coverage	Adsorption modes	Average E_{ads} (kJ/mol)	Differential E_{ads} (kJ/mol)
1/9 ML	FCC	-164	-164
2/9 ML	FCC	-161	-158
3/9 ML	FCC	-160	-159
4/9 ML	FCC + HCP	-154	-133
5/9 ML	FCC + HCP	-141	-91
6/9 ML	FCC + HCP	-131	-77
7/9 ML	FCC + HCP	-96	113
8/9 ML	HCP	-64	154
9/9 ML	HCP	-49	72

hollow sites. At low coverage CO adsorbates prefer to occupy the fcc-hollow site, while close to the full monolayer coverage the hcp-hollow site is preferred. This is in contrast to the top-adsorption mode, which is commonly observed in experiments [40]. However, the computed enthalpic difference in site preference is very small, e.g. top-adsorbed CO is only 1-3 kJ/mol less stable at a 1/3 ML CO coverage (Table 3.2). Overbinding and the incorrect site-preference prediction for CO have been frequently reported for GGA functionals like the PBE functional used here [41]. Although applying hybrid functionals like B3LYP [42] or methods like RPA [43] can in principle improve these results, the small differences observed in this study do not warrant the additional computational expenditure. The same holds for predicting the exact influence of lateral interactions. While there are various flavors of DFT functionals available, there is no universal one that can guarantee a highly accurate description of subtle coverage effects.

The adsorption energies corresponding to the most stable (3 x 3) configurations are presented in Table 3.1. As expected, higher CO coverage leads to a lower average CO adsorption strength, which is in line with both experimental findings [9] and theoretical studies using different DFT functionals [20, 44]. The average adsorption energy shows monotonically increasing (less negative) values, and at 9/9 ML the adsorption energy is -49 kJ/mol per CO. The differential energies increase more strongly with coverage, reaching positive values at a 6/9 ML coverage. The more pronounced increase in the differential energy can be understood by the fact that one additional adsorbate introduces additional lateral interactions between all other adsorbates. Interestingly, the differential adsorption energy decreases going from 8/9 ML to 9/9 ML. This is an anomaly of the constrained surface unit cell, as at 9/9 ML a more favorable fully hexagonally symmetric overlayer is formed. Nevertheless, the differential adsorption energy at this coverage is positive. This means that, although the average energy is still negative, there is no enthalpic driving force to go beyond 6/9 ML CO adsorption on Co(0001). Thus, coverages above 6/9 ML are kinetically inaccessible despite being thermodynamically allowed.

Assuming that 6/9 ML is the highest attainable coverage, there are only 7 (incl. 0 ML) discrete unique fractional coverages that the (3 x 3) Co(0001) surface can hold. Of course,

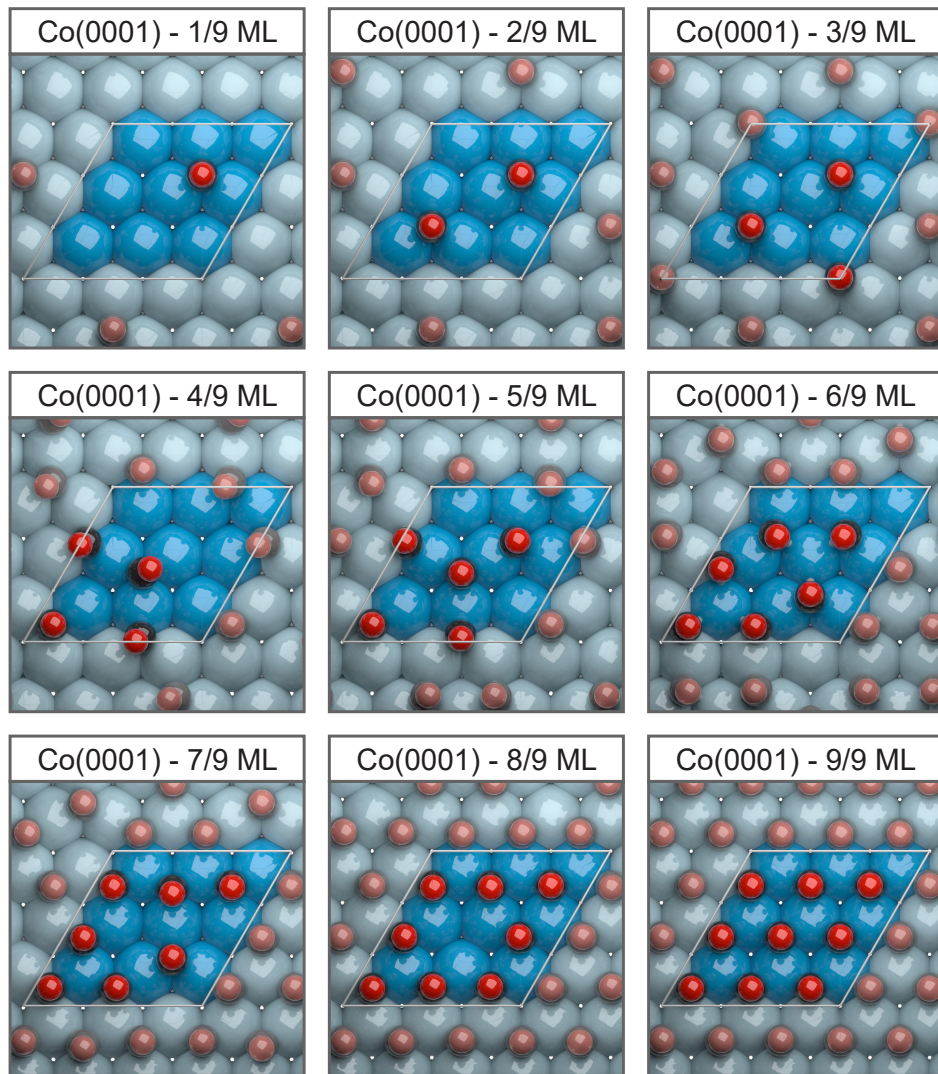


Figure 3.1: Most stable configurations of CO adsorbates on the terrace (3 x 3) Co(0001) surface.

the number of unique coverages on a much larger real catalyst surface is much larger and the complexity of e.g. a 6 nm cobalt nanoparticle significantly exceeds the limited cases that can be simulated with DFT calculations. Therefore, we opted for describing desorption barriers as a function of (continuous) coverage by a continuous mathematical function.

To obtain additional data for other unique coverages we computed the average adsorption energies for different ($n \times n$) expansions of the Co(0001) terrace. Because structures with maximal CO–CO separation are in general lower in energy, we specifically searched for such configurations on the different adsorption sites. The resulting energies are collected in Table 3.2. A general trend again is that the threefold-adsorption modes are favored over the top-adsorption mode. Nevertheless, given the accuracy of DFT, the differences are not very large. At 1.00 ML coverage the difference is about 40 kJ/mol per CO in favor of threefold-adsorption. However, the corresponding differential energies will be too high to ever observe such structures experimentally. At a more realistic coverage of 0.57 ML, the ($\sqrt{7} \times \sqrt{7}$) structure featuring both top- and bridge-adsorption modes has an average energy of -141 kJ/mol. This is the same energy as for the hcp-fcc structure at 0.56 ML on the (3×3) expansion. This indicates that a hexagonal arrangement of top and bridge modes can be as stable as a threefold arrangement. An equivalent 0.58 ML ($2\sqrt{3} \times 2\sqrt{3}$) top-bridge structure has an even lower average energy of -147 kJ/mol.

Table 3.2: Zero-point-energy corrected average adsorption energies and stretching frequencies for CO on the terrace Co(0001) surface at various ($n \times n$) expansions.

Coverage (ML)	Adsorbates per surface cobalt	Adsorption modes	Average E_{ads} (kJ/mol)	Highest C–O frequency (cm^{-1})
<u>Co(0001) – 2×2</u>				
0.25 ML	1 / 4	FCC	-165	1783
0.25 ML	1 / 4	HCP	-163	1770
0.25 ML	1 / 4	TOP	-159	1994
0.50 ML	2 / 4	FCC + HCP	-157	1883
0.50 ML	2 / 4	TOP + HCP	-131	2035
0.50 ML	2 / 4	TOP + FCC	-130	2032
0.75 ML	3 / 4	TOP + FCC + HCP	-120	2059
0.75 ML	3 / 4	HCP	-82	1939
0.75 ML	3 / 4	FCC	-80	1937
1.00 ML	4 / 4	HCP	-51	1983
1.00 ML	4 / 4	FCC	-50	1984
<u>Co(0001) – $\sqrt{7} \times \sqrt{7}$</u>				
0.14 ML	1 / 7	FCC	-166	1762
0.14 ML	1 / 7	HCP	-164	1740
0.14 ML	1 / 7	TOP	-156	1971
0.43 ML	3 / 7	TOP + FCC + HCP	-155	2002

0.57 ML	4 / 7	TOP + BRIDGE	-141	2022
<u>Co(0001) - 3 x 3</u>				
0.11 ML	1 / 9	FCC	-164	1755
0.11 ML	1 / 9	HCP	-161	1743
0.11 ML	1 / 9	TOP	-157	1972
0.11 ML	1 / 9	BRIDGE	-156	1789
0.22 ML	2 / 9	FCC	-161	1784
0.22 ML	2 / 9	HCP	-158	1769
0.22 ML	2 / 9	TOP	-155	1991
0.33 ML	3 / 9	FCC	-158	1807
0.33 ML	3 / 9	HCP	-156	1793
0.33 ML	3 / 9	TOP	-155	2009
0.44 ML	4 / 9	FCC + HCP	-154	1852
0.44 ML	4 / 9	TOP + BRIDGE	-150	2007
0.56 ML	5 / 9	FCC + HCP	-141	1910
0.56 ML	5 / 9	TOP + FCC + HCP	-122	2036
0.67 ML	6 / 9	FCC + HCP	-131	1941
0.67 ML	6 / 9	HCP	-96	1903
0.67 ML	6 / 9	FCC	-95	1913
0.67 ML	6 / 9	TOP	-75	2091
0.78 ML	7 / 9	FCC + HCP	-96	1945
0.78 ML	7 / 9	HCP	-80	1949
0.89 ML	8 / 9	HCP	-64	1964
1.00 ML	9 / 9	HCP	-49	1985
1.00 ML	9 / 9	FCC	-49	1985
1.00 ML	9 / 9	TOP	-9	2137
<u>Co(0001) - 2√3 x 2√3</u>				
0.58 ML	7 / 12	TOP + BRIDGE	-147	2017
<u>Co(0001) - 4 x 4</u>				
0.06 ML	1 / 16	FCC	-165	1745
0.06 ML	1 / 16	HCP	-163	1732
0.06 ML	1 / 16	TOP	-158	1963

Also shown in Table 3.2 are the stretching frequencies corresponding to the strongest C–O bond for each adsorption structure. Overall, the stretching frequencies increase with increasing CO coverage. Most stretching frequencies are below 2000 cm⁻¹, except for the systems containing top-adsorbed CO. These systems have higher stretching frequencies, in line with experimental results [45]. Figure 3.2 shows that the systems with top-adsorbed CO can be confidently identified from the high stretching frequency. We contribute these differences to changes in π -backdonation to the antibonding molecular orbital of CO [46]. When π -backdonation increases as CO is adsorbed in high coordination sites, the

additional weakening of the C–O bond can explain a lower stretching frequency compared to top-adsorbed CO. Furthermore, the increase in C–O bond stretching frequencies at higher coverage suggests that π -backdonation decreases for higher coverages. This can be understood in terms of the CO-coordinating cobalt surface atoms requiring to share their electron density with multiple CO adsorbates. Based on the changes in C–O stretching frequency, these effects appear to scale linearly with coverage. The adsorption energies on the other hand scale more pronouncedly with coverage than a linear dependence. We expect that the σ -bonding interactions will display similar scaling, and are not responsible for the higher than linear scaling for CO adsorption.

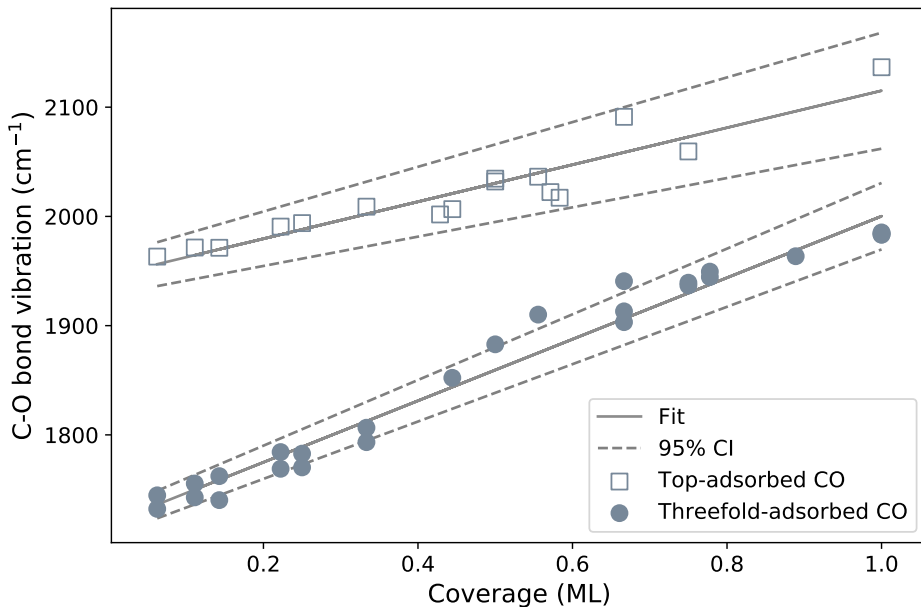


Figure 3.2: Strongest C–O bond vibrations for the various CO coverages on the terrace (3 x 3) Co(0001) surface. The configurations are separated into a set containing only systems with at least one top-adsorbed CO and a set containing only threefold-adsorbed CO.

To separate the linear and exponential coverage contributions to the adsorption energy of CO, we plotted all collected energies as a function of coverage in Figure 3.3 (left panel). We then selected for each unique coverage the most stable configuration (closed symbols) and performed nonlinear regression on these points. The equation used for the regression contains three parameters: a linear scaling factor A , an exponential scaling factor B , and a constant C .

$$E_{\text{ads}}^{\text{int}}(\text{kJ/mol}) = A \cdot \theta + \exp(B \cdot \theta) + C$$

For the set of CO adsorption energies on Co(0001), we found the following optimal values

with corresponding 95% confidence intervals:

$$A = 35 \pm 26, \quad B = 4.60 \pm 0.28, \quad C = -173 \pm 11, \quad (\text{kJ/mol})$$

The right panel of Figure 3.3 then shows the corresponding differential parametrization following

$$E_{\text{ads}}^{\text{diff}}(\text{kJ/mol}) = E_{\text{ads}}^{\text{int}} + \theta \frac{dE_{\text{ads}}^{\text{int}}}{d\theta} = E_{\text{ads}}^{\text{int}} + \theta (A + B \cdot \exp(B \cdot \theta))$$

For reference, the right panel of Figure 3.3 shows the differential data points corresponding to the (3 x 3) expansion. Except for the last data point, all values lie within the 95% confidence interval. As mentioned before, we attribute the lower position of the outlier to the formation of a favorable fully hexagonally symmetric overlayer at 9/9 ML. From the comparison between integral and differential adsorption energies it becomes clear that the latter is more sensitive to such effects. Without the smoothed parameterization of the integral adsorption energy it would have been difficult to assess whether the data point at 9/9 ML is an outlier. Note that ‘outlier’ in this context does not mean that the underlying DFT data is inaccurate. It merely indicates that the underlying DFT does not accurately relate to what happens on a real surface. A single adsorption event on a hypothetical periodic (3 x 3) cobalt surface contributes to a 0.11 ML increase in coverage. The same adsorption event on a (10 x 10) surface would contribute to only a 0.01 ML increment.

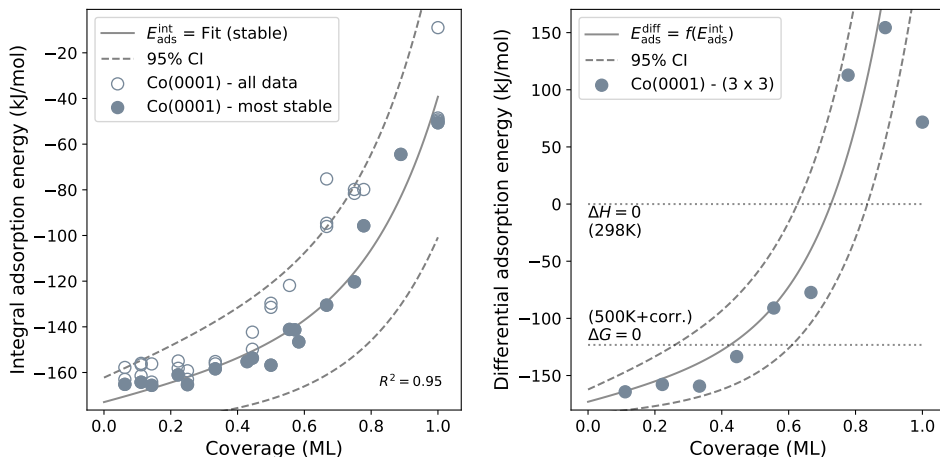


Figure 3.3: Zero-point energy corrected integral (left panel) and differential (right panel) heat of adsorption of CO on the flat Co(0001) surface as a function of CO coverage. The curve-fitting was performed on the most stable Co(0001) configurations.

Given the 95% confidence interval, the smoothed differential adsorption energy crosses zero between 0.63 ML and 0.84 ML. This range is the upper limit at which CO adsorption is favorable from the enthalpic point of view. In practice, the maximum attainable CO coverage will likely be lower, as these values are not yet corrected for overbinding and

entropic effects. We predict that overbinding corrections constitute to about +23 kJ/mol. At 500 K the temperature corrections for enthalpy and entropy are about +100 kJ/mol [47, 48]. Together these effects would shift the adsorption energies upwards resulting in a crossing of zero between 0.26 ML and 0.61 ML. This range is now much wider, because the shifted differential energies cross zero at a lower slope.

3.3.2 CO adsorption on Co(11 $\bar{2}$ 1)

In a similar way as for the terrace Co(0001) surface, we determined stable CO configurations as a function of total CO coverage on the stepped Co(11 $\bar{2}$ 1) surface. Important to note here is the way in which the total CO coverage can be defined on the stepped surface. In this section we use two different formats: fractional and decimal. We define the fractional ML coverage as the amount of CO adsorbates per 16 surface atoms in the (2 x 2) unit cell. However, not all exposed atoms on stepped surfaces are equivalent. Later in this chapter, we will compare the results for the stepped Co(11 $\bar{2}$ 1) surface to the terrace Co(0001) surface. Therefore, we defined the decimal ML coverages to be normalized to a 1 ML coverage for Co(0001). That is, we define 1.00 ML coverage on Co(11 $\bar{2}$ 1) as one CO per (1 x 1) Co(0001) surface area (5.38 Å²). In principle, this is analogous to the surface science approach of calibrating XPS signals to respective measurements for known patterns on flat terraces [49].

Figure 3.4 shows the geometries of the most stable configurations of CO on the (2 x 2) unit cell expansion. The adsorbed COs on the Co(11 $\bar{2}$ 1) surface undergo varying amounts of rotation towards the surface. For many of the adsorbates the oxygen atom is close to a cobalt surface atom, which indicates bonding interactions. This is in contrast to the Co(0001) adsorbates that are oriented perpendicular to the surface with minimal deviation. Even though the COs are oriented more anisotropically, structures reminiscent of close hexagonal packing are still visible. At low coverage, CO tends to preferentially bind with the carbon in a threefold-hollow pocket and the oxygen bonded to the cobalt atom protruding from the next step-edge. At higher coverages (> 8/16 ML), the COs tend to be positioned more in top and bridge positions.

The bonding positions were studied in more detail by a vibrational analysis. For each studied configuration we determined the strongest C–O bond vibration. Figure 3.5 shows the results for this analysis. The stable configurations can be grouped in two categories. The configurations with CO solely in the threefold-hollow adsorption sites show significantly lower vibrational frequencies as compared to the configurations with top- and bridge-adsorbed CO. At the lowest coverage (1/16 ML fractional; 0.07 ML decimal) we sampled six different configurations as shown in Figure 3.6. The lowest vibrational frequencies were found with the CO adsorbed in the B₅-site. This strong destabilization of the C–O bond is in line with the expected reactivity of the B₅-site towards CO dissociation. Furthermore, at an adsorption energy of -154 kJ/mol, this ‘pre-activated’ state is only 17 kJ/mol less favorable than the most stable configuration.

Table 3.3 presents the energies corresponding to the most stable configurations of CO at various coverages on the stepped Co(11 $\bar{2}$ 1) surface. At low coverage (1/16 ML), the binding strength of CO is ~6 kJ/mol stronger as compared to the low coverage (1/9 ML)

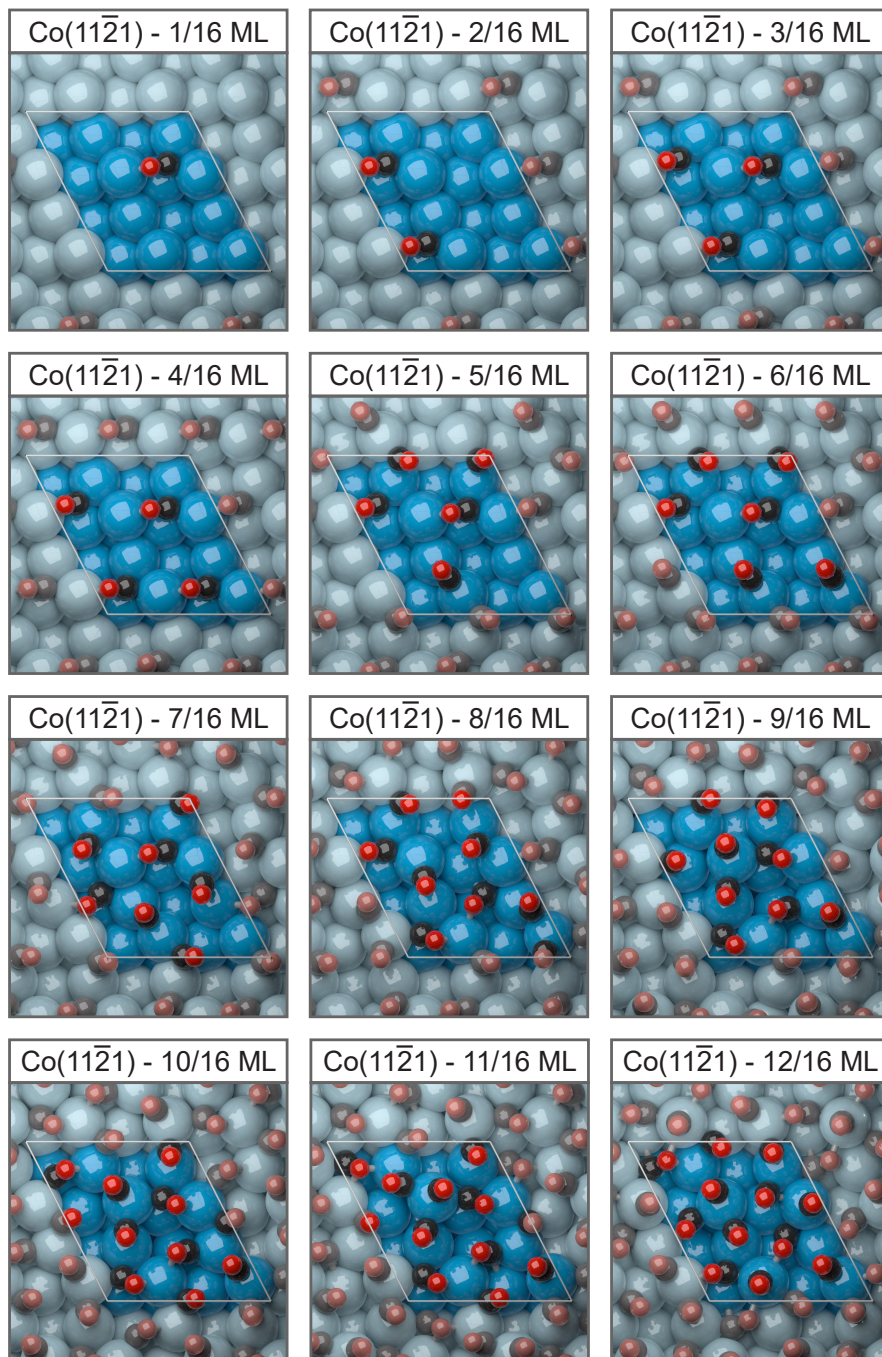


Figure 3.4: Most stable configurations of CO adsorbates on the stepped (2×2) $\text{Co}(11\bar{2}1)$ surface.

Table 3.3: Zero-point-energy corrected most stable adsorption energies for CO on the stepped (2 x 2) Co(11 $\bar{2}$ 1) surface.

Coverage	Average E_{ads} (kJ/mol)	Differential E_{ads} (kJ/mol)
1/16 ML	-171	-171
2/16 ML	-173	-175
3/16 ML	-170	-164
4/16 ML	-170	-170
5/16 ML	-165	-145
6/16 ML	-163	-155
7/16 ML	-154	-100
8/16 ML	-145	-77
9/16 ML	-129	-2
10/16 ML	-116	-1
11/16 ML	-100	62
12/16 ML	-85	75

on the Co(0001) surface. The destabilization of additional adsorbates is also less per 1/16 ML increment, although this is mostly because the increments are smaller. The differential adsorption energies are close to zero for 9/16 ML and 10/16 ML. For 11/16 ML and beyond the differential adsorption energies strongly exceed zero. We analyzed this data following the same procedure as for the Co(0001) surface. The resulting fit is shown in Figure 3.7. We found the following optimal values with corresponding 95% confidence intervals:

$$E_{\text{ads}}^{\text{int}} = A \cdot \theta + \exp(B \cdot \theta) + C, \quad E_{\text{ads}}^{\text{diff}} = E_{\text{ads}}^{\text{int}} + \theta (A + B \cdot \exp(B \cdot \theta))$$

$$A = 32 \pm 23, \quad B = 4.81 \pm 0.30, \quad C = -179 \pm 8, \quad (\text{kJ/mol})$$

Given the 95% confidence interval, the uncorrected enthalpic differential adsorption energy crosses zero between 0.63 ML and 0.80 ML. This range drops to 0.32 ML - 0.59 ML by including overbinding corrections and temperature corrections at 500 K for both enthalpy and entropy.

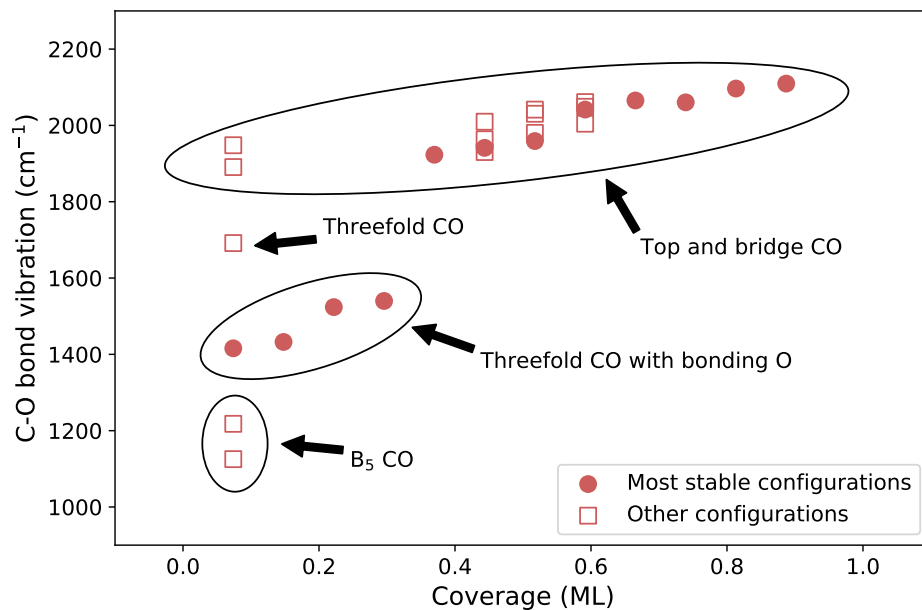


Figure 3.5: Strongest C–O bond vibrations for the various CO coverages on the stepped (3×3) $\text{Co}(11\bar{2}1)$ surface.

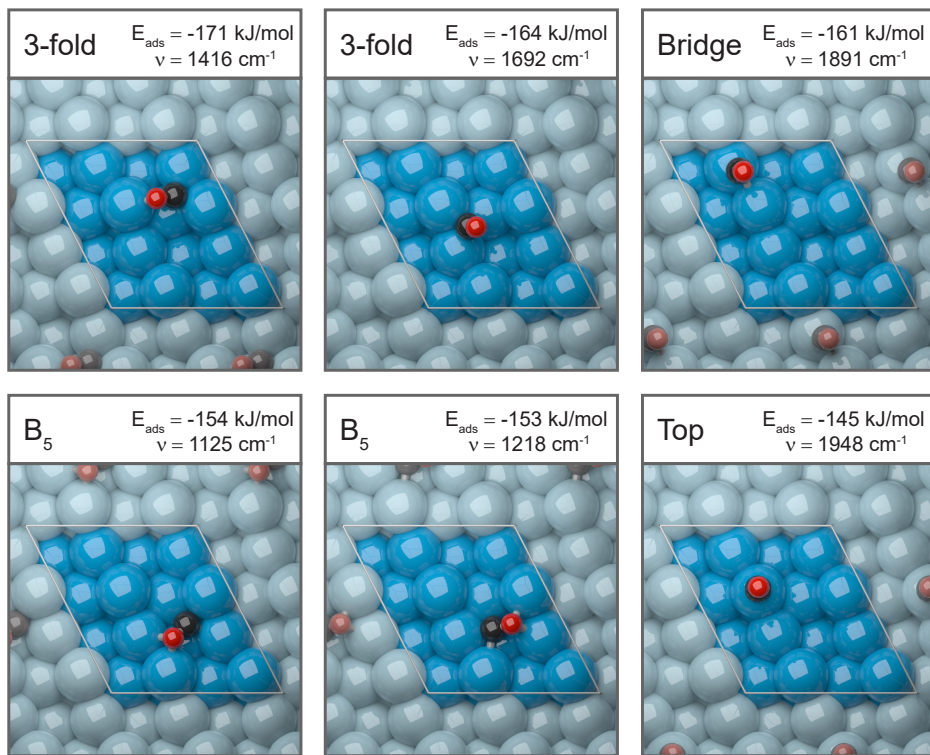


Figure 3.6: Adsorption configurations of 1/16 ML CO on the stepped (2 x 2) Co(11 $\bar{2}$ 1) surface.

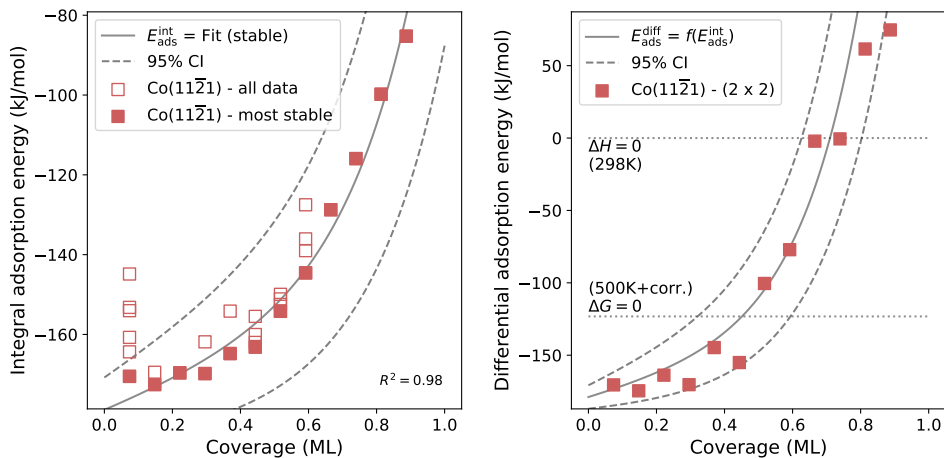


Figure 3.7: Zero-point energy corrected integral (left panel) and differential (right panel) heat of adsorption of CO on the stepped Co(11 $\bar{2}$ 1) surface as a function of CO coverage. The fractional CO coverage of the Co(11 $\bar{2}$ 1) is normalized to the Co(0001) area. The curve-fitting was performed on the most stable Co(11 $\bar{2}$ 1) configurations.

3.3.3 CO adsorption on Co(0001) and Co(11 $\bar{2}$ 1) combined

The previous sections showed the fitted adsorption energies of Co(0001) and Co(11 $\bar{2}$ 1) as a function of coverage. We found that the determined fit parameters for the two surfaces are within each other's 95% confidence intervals. This suggests that the coverage effects are, statistically speaking, independent of the surface. We therefore combined the two datasets and performed regression on the combined set of most stable configurations. The resulting fit is shown in Figure 3.8, for which we found the following optimal values and corresponding 95% confidence intervals:

$$E_{\text{ads}}^{\text{int}} = A \cdot \theta + \exp(B \cdot \theta) + C, \quad E_{\text{ads}}^{\text{diff}} = E_{\text{ads}}^{\text{int}} + \theta (A + B \cdot \exp(B \cdot \theta))$$

$$A = 36 \pm 17, \quad B = 4.64 \pm 0.20, \quad C = -176 \pm 7, \quad (\text{kJ/mol})$$

Given the 95% confidence interval, the uncorrected enthalpic differential adsorption energy crosses zero between 0.66 ML and 0.80 ML. This range drops to 0.32 ML - 0.55 ML by including overbinding corrections and temperature corrections at 500 K for both enthalpy and entropy.

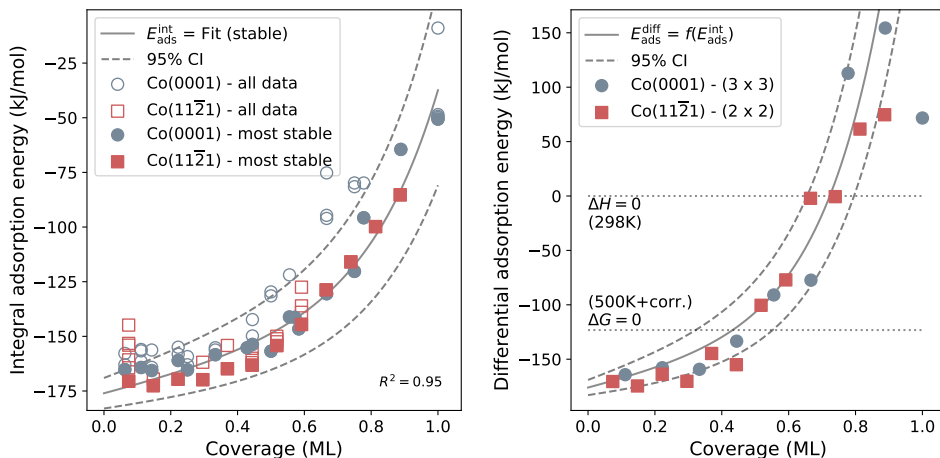


Figure 3.8: Zero-point energy corrected integral (left panel) and differential (right panel) heat of adsorption of CO on the flat Co(0001) surface (○) and on the stepped Co(11 $\bar{2}$ 1) surface (□) as a function of CO coverage. The fractional CO coverage of the Co(11 $\bar{2}$ 1) is normalized to the Co(0001) area. The curve-fitting was performed on the combined sets of most stable Co(0001) and Co(11 $\bar{2}$ 1) configurations (closed symbols).

Based on these results we conclude that the dominant lateral interaction effect is exponential in form, and that this effect is similar for the two surfaces. This is convenient, because it allows us to approximate lateral interaction effects on the stepped surface from calculated contributions on the terrace surface.

3.3.4 N₂ adsorption on Co(0001)

For CO we found that the dominant lateral interactions at high coverage are exponential in form. Therefore, we hypothesize that the lateral interactions are mostly caused by intermolecular repulsion, rather than through deactivation of the metal atoms in the surface. If this hypothesis is correct, then a similar diatomic species should give the same exponential trend. N₂ is similar to CO in the sense that these molecules are isoelectronic and N₂ shares a similar molecular orbital diagram. However, the reactivity of N₂ is much lower compared to CO. As such, we expect that any metal deactivation effects upon CO adsorption, if present, should be lower in the case of N₂. Then, a significantly different N₂ adsorption trend as a function of coverage could indicate a strong contribution of such effects on CO adsorption.

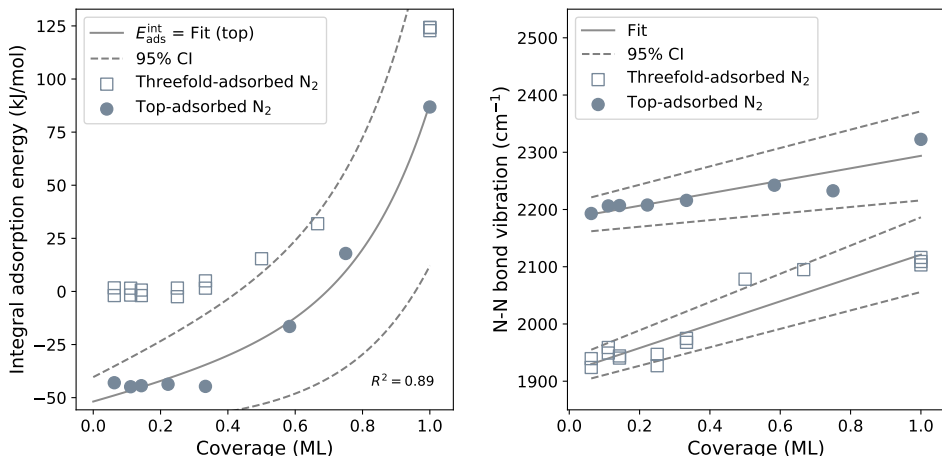


Figure 3.9: Zero-point energy corrected integral heat of adsorption (left panel) and strongest N–N bond vibrations (right panel) for the various N₂ coverages on the flat Co(0001) surface. The curve-fitting was performed on the top-adsorbed N₂ configurations.

We performed optimization and vibrational analysis of various N₂ coverages on the flat Co(0001) surface. In this analysis we considered vertically aligned N₂ on top sites and threefold-hollow sites. The corresponding integral adsorption energies and strongest N–N bond vibrations are shown in Figure 3.9. The top-adsorbed N₂ configurations are clearly more favorable compared to the threefold-adsorbed configurations. Like the C–O bond vibration, the N–N bond vibration is stronger for the top-adsorbed configurations. As expected, the most stable configurations are significantly less strongly bound to the surface than CO. We fitted the top-adsorbed N₂ configurations using the same procedure as for CO, and we found the following optimal values and corresponding 95% confidence intervals:

$$E_{\text{ads}}^{\text{int}} = A \cdot \theta + \exp(B \cdot \theta) + C$$

$$A = 41 \pm 35, \quad B = 4.61 \pm 0.35, \quad C = -52 \pm 12, \quad (\text{kJ/mol})$$

The linear term A of 41 ± 35 has an overlapping 95% confidence interval with the linear term of CO (36 ± 17 for the combined case). As the mean-value for this parameter has not decreased, there is no direct evidence that the linear lateral interaction contribution has decreased for N₂. However, the uncertainty in this parameter has increased to 85% from 47% for CO. This difference suggests that the linear parameter can probably be removed from the regression procedure without a large impact on the goodness of fit. The confidence intervals for exponential parameter B are also overlapping between N₂ and CO adsorption. However, here the uncertainty is only 8% (4% for CO). From this, we conclude that the lateral interactions of N₂ and CO can be described with the same exponential relation.

3.3.5 H₂ activation on Co(0001) and Co(11 $\bar{2}$ 1)

Given the strength of the C–O and N–N bonds we assumed that the adsorption of CO and N₂ proceeds associatively. H₂ on the other hand can adsorb on transition metal clusters through a dissociative pathway, directly forming two H* species [50]. Such a dissociative pathway can be activated, depending on the stability of the adsorbate and the reactivity of the metal. For H₂ on transition metals this dissociative adsorption barrier is usually assumed to be small compared to the desorption barrier [26]. To verify the validity of this assumption we first adsorbed H₂ associatively on both terrace Co(0001) and stepped Co(11 $\bar{2}$ 1). We then performed a transition state search using the climbing image nudged elastic band (cNEB) method. The corresponding transition state geometries are shown in Figure 3.10. These geometries show that dissociation occurs mostly a single surface cobalt atom.

Figure 3.11 shows the comparison of the activated associative pathway with the assumed non-activated dissociative pathway. Molecular adsorption of H₂ is favorable from the enthalpic point of view on both the terrace and the stepped surface. However, molecular adsorption is unfavorable in terms of the Gibbs free energy at 493.15 K. For the forward Gibbs free adsorption barrier, we assumed the loss of one translational degree of freedom in the direction perpendicular to the surface. From the adsorbed H₂* state the dissociation is barrier-less on Co(0001), while on the Co(11 $\bar{2}$ 1) surface the process is activated with an enthalpic barrier of about 7 kJ/mol. The corresponding transition state energy is lower than the entropic barrier for H₂ adsorption. From this, we conclude that the dissociative adsorption of H₂ can be properly described with the assumption of a zero-enthalpy barrier.

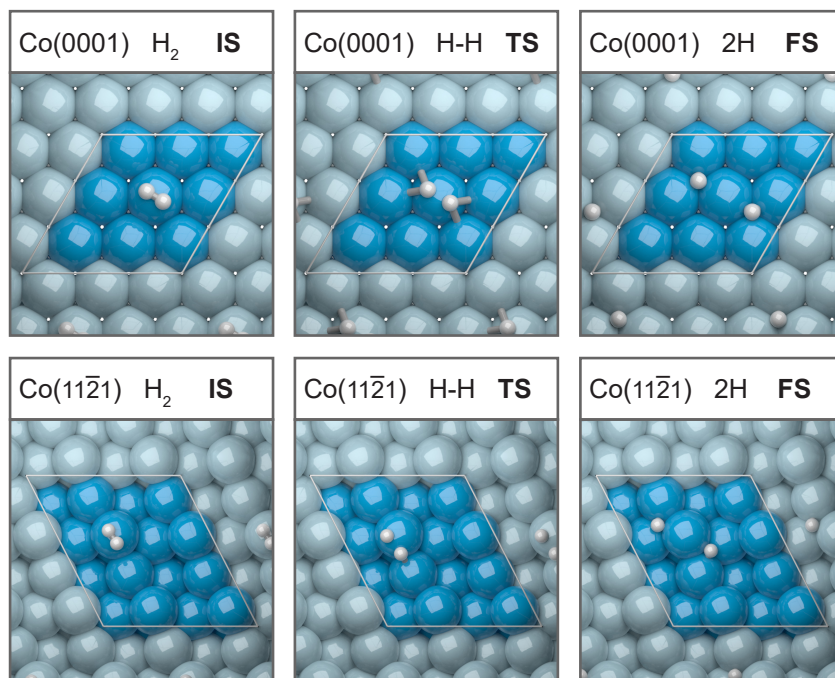


Figure 3.10: Initial state (IS), transition state (TS), and final state (FS) geometries for H_2 dissociation on $\text{Co}(0001)$ and $\text{Co}(11\bar{2}1)$ surfaces at low coverages of $1/9$ ML and $1/16$ ML respectively.

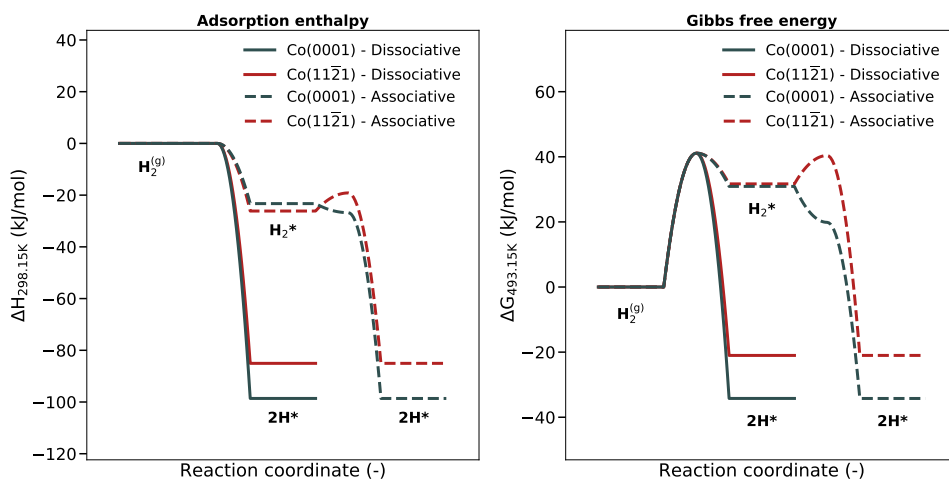


Figure 3.11: Comparison of the associative and dissociative pathways for H_2 adsorption on $\text{Co}(0001)$ and $\text{Co}(11\bar{2}1)$ at low coverage ($1/9$ ML and $1/16$ ML respectively). The left panel shows the enthalpic energy difference at 298.15 K. The right panel shows the Gibbs free energy at 493.15 K.

3.3.6 H adsorption on Co(0001)

To explore the effect of hydrogen coverage on its adsorption we computed adsorption energies of hydrogen at different H coverages. We assumed dissociative H₂ adsorption and defined the integral adsorption energy with respect to molecular hydrogen. That is, the fitted energies in Figure 3.12 correspond to two times the adsorption heat of H*. We found the following optimal values and corresponding 95% confidence intervals:

$$E_{\text{ads}}^{\text{int}} = A \cdot \theta + \exp(B \cdot \theta) + C, \quad E_{\text{ads}}^{\text{diff}} = E_{\text{ads}}^{\text{int}} + \theta (A + B \cdot \exp(B \cdot \theta))$$

$$A = 17 \pm 12, \quad B = 1.97 \pm 1.46, \quad C = -101 \pm 3, \quad (\text{kJ/mol})$$

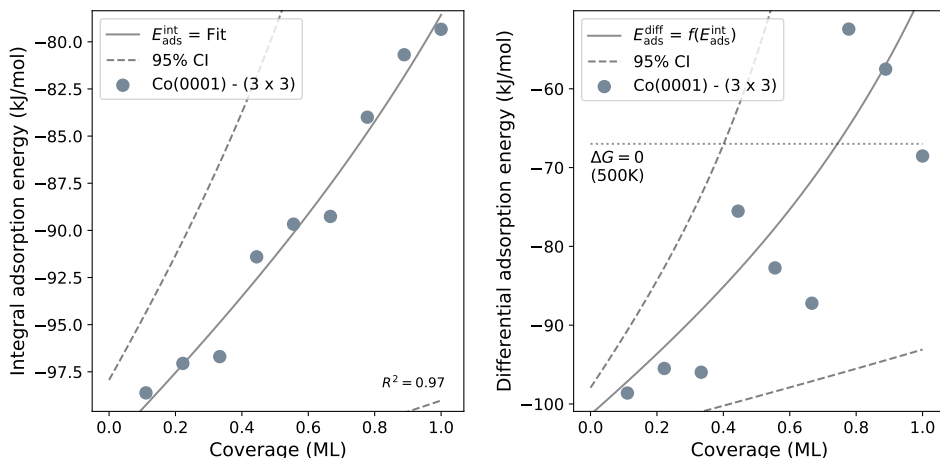


Figure 3.12: Zero-point energy corrected integral (left panel) and differential (right panel) heat of adsorption of H₂ on the flat Co(0001) surface as a function of H coverage.

As observed for the adsorption of N₂, the linear lateral interaction term A has a large uncertainty. In contrast, for H₂ also the exponential term B has a large relative uncertainty of 74%. Likely, this uncertainty is caused by the much lower effect of lateral interactions between hydrogen species. Even for a fully exponential relation, the trend may seem linear for the low interaction region. Nevertheless, the derived differential energy still becomes positive after correcting for the loss of H₂ gas phase entropy at 500 K. This would suggest that a full monolayer coverage of H atoms is not favorable at 500 K. However, the exact maximum coverage is uncertain given the accuracy of DFT and the limitations in the fit.

3.3.7 Stability of C, CH, O and OH on Co(0001)

The most important lateral interaction corrections for a microkinetic model pertain to the adsorption and desorption reactions. In the case of CO hydrogenation, especially the CO adsorption equilibrium is important. Without lateral interactions, the surface is expected to

be fully covered with CO, as it is the strongest binding reactant. As CO–CO interactions are added to the model, the CO coverage will drop. Then, other species may populate the surface, including but not limited to C, CH, O, and OH. These species will likely have similar lateral interaction effects on CO. To get a measure of these lateral interactions we determined the difference in stability of these species due to their own coverage. We took the CO methanation process as reference to derive these stabilities. For example, the stability of one atomic C relates to the adsorption of one molecule of CO. Then, the adsorbed CO dissociates and the oxygen is removed as H₂O using one molecule of H₂.

$$E_C^{\text{int}} = \frac{\left(E_{N \cdot C}^{\text{surface}} - E_{\text{empty}}^{\text{surface}} - N \cdot \left(E_{\text{CO}}^{\text{gas}} + E_{\text{H}_2}^{\text{gas}} - E_{\text{H}_2\text{O}}^{\text{gas}} \right) \right)}{N}$$

The resulting data and fits are shown in Figure 3.13, for which we found the following optimal values and corresponding 95% confidence intervals:

$$E_{\text{ads}}^{\text{int}} = A \cdot \theta + \exp(B \cdot \theta) + C$$

C),	$A = 103 \pm 28,$	$B = 4.00 \pm 0.43,$	$C = -86 \pm 11,$	(kJ/mol)
CH),	$A = 9 \pm 24,$	$B = 3.70 \pm 0.53,$	$C = -139 \pm 9,$	(kJ/mol)
O),	$A = 93 \pm 29,$	$B = 3.36 \pm 0.92,$	$C = -274 \pm 11,$	(kJ/mol)
OH),	$A = 99 \pm 52,$	$B = 3.76 \pm 1.07,$	$C = -288 \pm 19,$	(kJ/mol)

Compared to CO, the optimal values for exponential parameter B are lower. Except for CH, the linear terms A are larger than for CO. These species are expected to have stronger metal-adsorbate binding following the bond-order conservation principles [51]. This means that the surface deactivation effect from high adsorbate coverages should be larger as compared to CO. The higher linear terms seem to reflect this, although the relatively wide confidence intervals indicate that that it is difficult to differentiate between the linear and exponential effects.

For C (Figure 3.13a), we found that C–C coupling occurred at 7/9 ML and 8/9 ML, leading to reconstruction of the cobalt surface. This coupling and reconstruction led to an increase in stability as compared to the expected trend as a function of carbon coverage. The corresponding dimerized and trimerized carbon species are shown in Figure 3.14. Whether these structures can be formed under reaction conditions will depend on kinetic limitations.

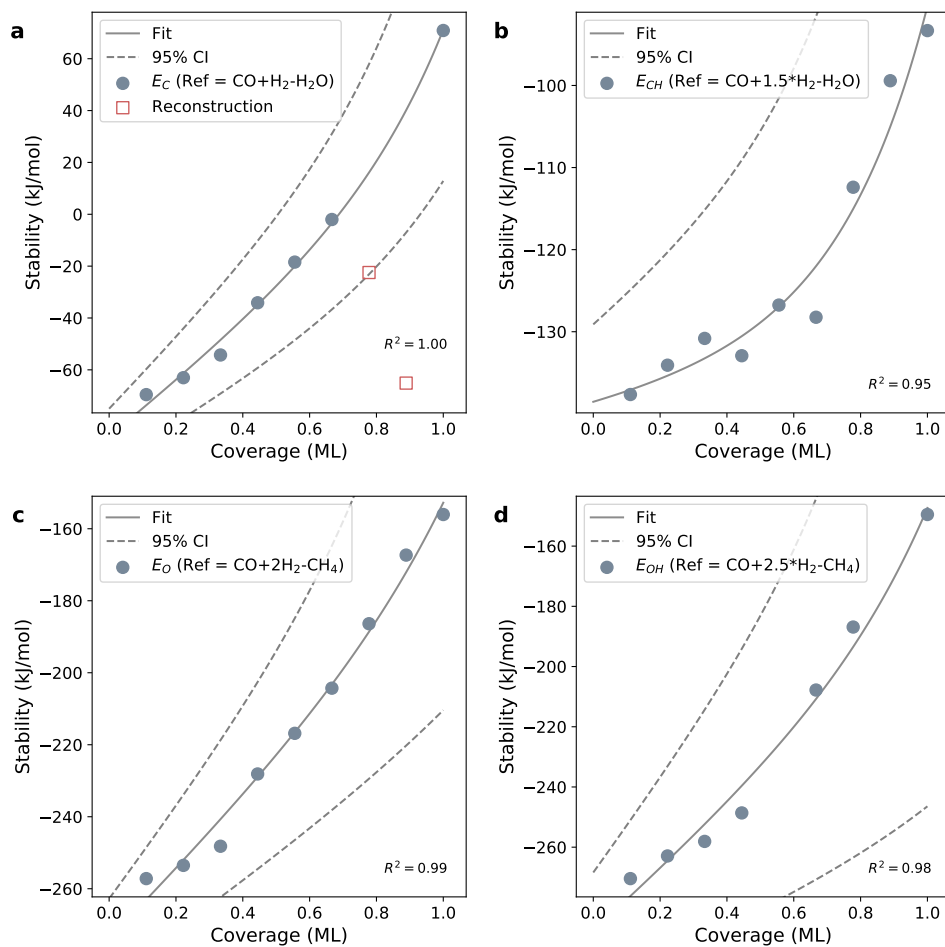


Figure 3.13: Zero-point energy corrected enthalpic stabilities of a) C*, b) CH*, c) O*, d) OH*.

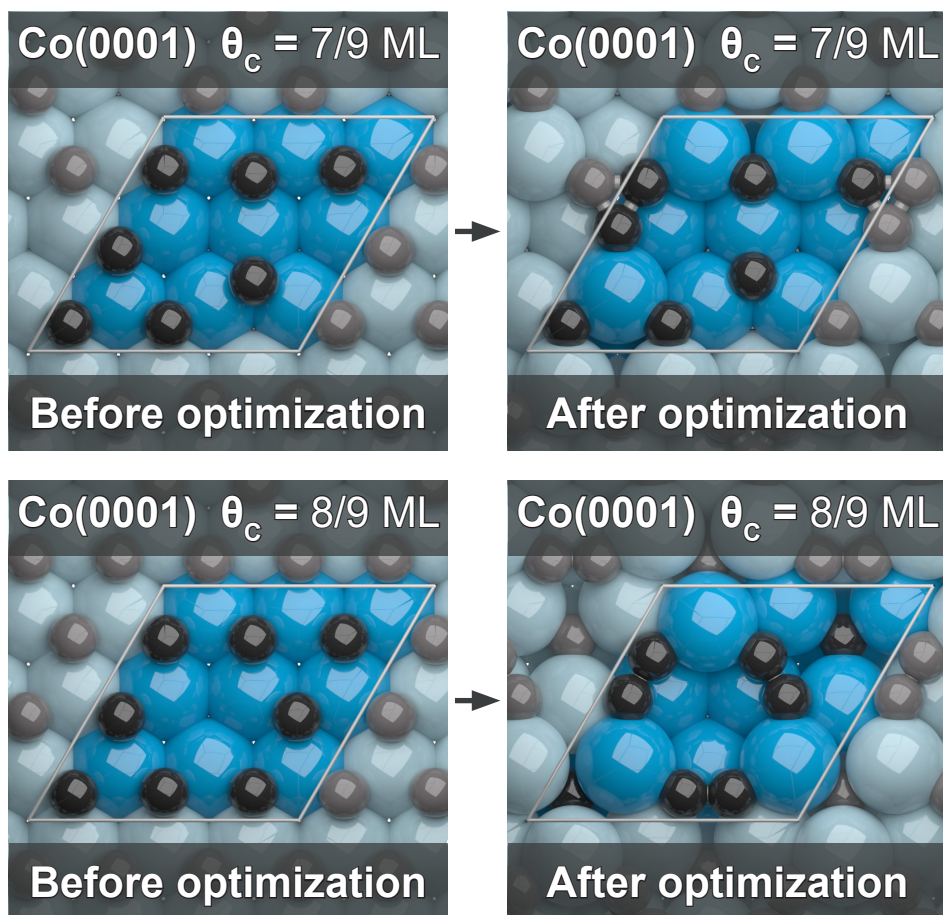


Figure 3.14: Geometries of 7/9 ML and 8/9 ML carbon on Co(0001) before and after geometric optimization. Dimerization and trimerization of the carbon atoms occurred during the optimization procedure.

3.3.8 Competitive adsorption on Co(0001)

The previous sections of this chapter showed the homogeneous lateral interaction effects between like species. For CO–CO interactions we found an exponentially increasing repulsion limiting the coverage at 500 K to around 0.55 ML. We found that H–H repulsion interactions were much lower. On Co(0001), the difference in integral adsorption energy between 1 ML CO and the most stable configuration is 115 kJ/mol. For H₂ this difference is only 19 kJ/mol. For C, CH, O, and OH these differences are 140, 44, 101, and 121 kJ/mol respectively. The similar total repulsion at 1 ML of CO, C, O, and OH suggests that competitive adsorption of these species might yield similar results. Because the underlying interactions might be of different natures, we investigated the co-adsorption of CO with C, O, and H. We compare these states with homogeneous CO–CO repulsion at the same coverage. The optimized geometries of the studied systems are shown in Figure 3.15, and the corresponding CO adsorption energies are provided in Table 3.4.

At 3/9 ML coverage the substitution of a CO with C or O causes only a 5-8 kJ/mol destabilization of the remaining CO adsorbates. In the extreme case of 9/9 ML coverage, the substitution leads to a relative stabilization of CO rather than a destabilization. For oxygen this difference is 19 kJ/mol compared to the case of a full monolayer of CO. Carbon co-coverage seems to be more favorable, given the 47 kJ/mol difference. However, as visible in Figure 3.15, the cobalt surface has undergone some reconstruction for this state. We contribute part of the difference to the more favorable binding state of carbon in the reconstructed surface. As this high coverage of 9/9 ML will not be achieved in practice, we assume that such reconstruction is likely inaccessible. As such, we conclude that co-adsorption of C and O results in roughly similar lateral interactions as for homogeneous CO–CO repulsion. Then, with co-adsorbed hydrogen, the repulsion decreases significantly. The average CO adsorption energy for a 6/9 ML hcp-coverage is -96 kJ/mol (Table 3.1). Adding 3/9 ML of hydrogen increases this energy by only 10 kJ/mol to -86 kJ/mol, which is a 90 kJ/mol difference compared to the +4 kJ/mol reached by co-adsorbing 3/9 ML CO.

Table 3.4: Average CO adsorption energies on Co(0001) with co-adsorbed carbon, oxygen, and hydrogen.

Total coverage	Adsorbed species (on 3 x 3)	Co-adsorbed species (on 3 x 3)	Adsorption mode of CO	Adsorption mode of C/O/H	Average E_{ads} CO (kJ/mol)
3/9 ML	2 CO	1 CO	FCC	-	-155
3/9 ML	2 CO	1 CO	HCP	-	-154
3/9 ML	2 CO	1 CO	TOP	-	-154
3/9 ML	2 CO	1 C	TOP	HCP	-146
3/9 ML	2 CO	1 O	TOP	HCP	-149
9/9 ML	6 CO	3 CO	HCP	-	4
9/9 ML	6 CO	3 C	HCP	HCP	-56
9/9 ML	6 CO	3 O	HCP	HCP	-28
9/9 ML	6 CO	3 H	HCP	HCP	-86

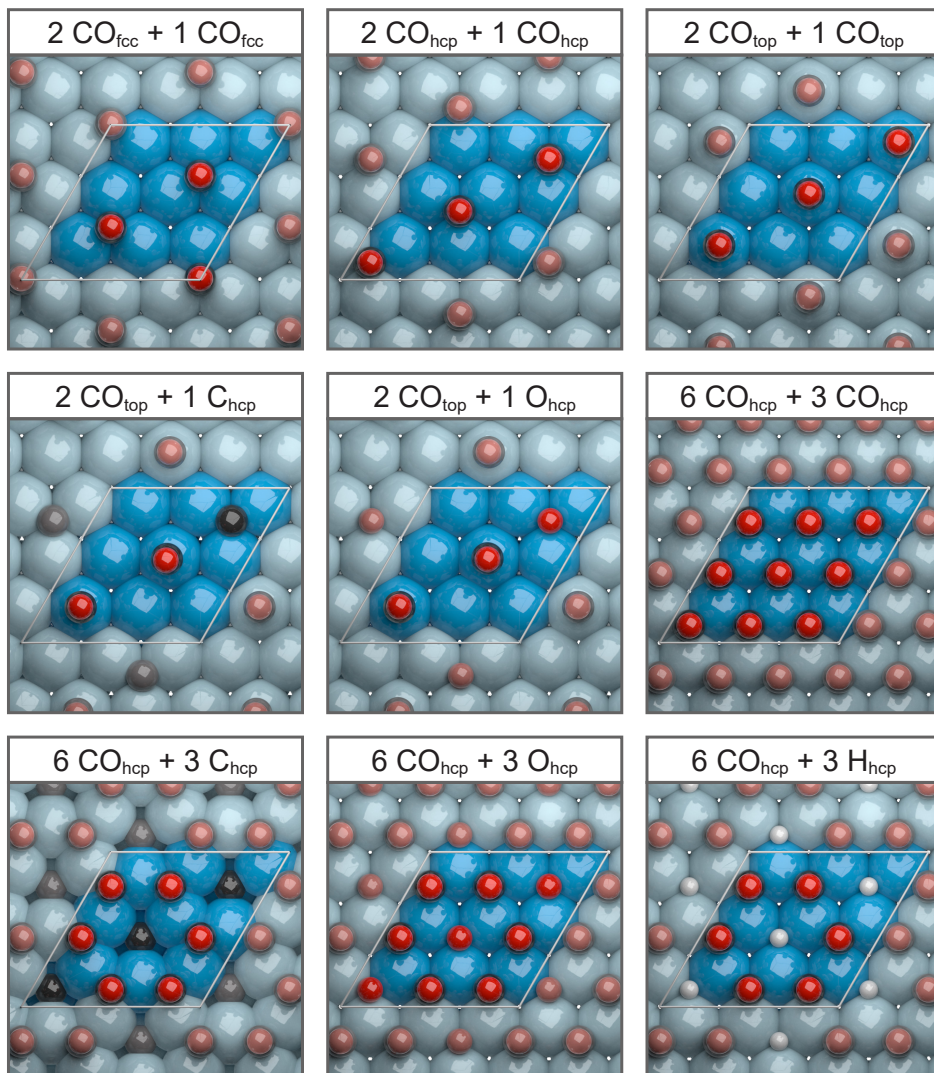


Figure 3.15: Configurations of CO on Co(0001) with co-adsorbed carbon, oxygen, and hydrogen.

3.3.9 A rigorous lateral interaction potential

A catalyst does not change the overall thermodynamics of a chemical reaction. Therefore, the inclusion of lateral interactions in a mean-field microkinetic model ideally should not alter the thermodynamics of the total model. The parameterizations for the adsorption energies as function of the composition of the adsorbed layer as discussed above can be used for developing a thermodynamically consistent potential. We start by assuming a total Gibbs free lateral energy G_{lat} that is the summation over all contributions E_i^{lat} by the separate species i on the surface scaled by the coverage θ_i of that species:

$$G_{\text{lat}} = \sum_i \theta_i E_i^{\text{lat}} \quad (3.3)$$

Here E_i^{lat} (in kJ/mol) is the lateral interaction component of the integral adsorption energy such that

$$E_i^{\text{lat}} = \sum_i A_i \theta_i + \epsilon \cdot \exp \left(\sum_j B_j \theta_j Z_{ij} \right) - 1 \quad (3.4)$$

In this equation A_i is the linear repulsion factor (kJ/mol), B_j is the exponential repulsion factor (dimensionless), Z_{ij} is the cross term (dimensionless) for intercomponent interactions, and ϵ is a dimensional correction factor of 1 kJ/mol. The cross term Z_{ij} is unity in the case that $i = j$, which signifies homogeneous repulsion between like species. For heterogeneous repulsion when $i \neq j$, the Z_{ij} term can have values other than unity.

The lateral interaction potential evolves as a function of time through elementary reaction steps occurring on the catalyst surface. The derivative of the interaction potential to time can be written as

$$\frac{\partial G_{\text{lat}}}{\partial t} = \sum_i \frac{\partial G_{\text{lat}}}{\partial \theta_i} \cdot \frac{\partial \theta_i}{\partial t} = \vec{\mu} \cdot \vec{\theta} \quad (3.5)$$

Here $\vec{\mu}$ is an infinitesimal change in the lateral interaction potential by an infinitesimal change in the surface coverages. For each species i this term evaluates to

$$\mu_i = \frac{\partial G_{\text{lat}}}{\partial \theta_i} = E_i^{\text{lat}} + \theta_T \left(A_i + B_i Z_{ij} \cdot \epsilon \cdot \exp \left(\sum_j B_j \theta_j Z_{ij} \right) \right) \quad (3.6)$$

Here, θ_T is the total surface concentration

$$\theta_T = \sum_{\alpha} \theta_{\alpha} = 1 - \theta_* \quad (3.7)$$

Modifying the elementary reaction steps can then be done by modifying the rate constants with a BEP-like coefficient β as follows

$$k_{\text{forw}}^{\text{lat}} = k_{\text{forw}}^0 \cdot \exp \left(\beta \frac{\mu_{\text{FS}} - \mu_{\text{IS}}}{RT} \right) \quad (3.8)$$

$$k_{\text{back}}^{\text{lat}} = k_{\text{back}}^0 \cdot \exp\left(\left(1 - \beta\right) \frac{\mu_{\text{FS}} - \mu_{\text{IS}}}{RT}\right) \quad (3.9)$$

The difficulty with this approach is that the lateral interaction parameters A_i and B_i must be known for every species on the surface. Furthermore, every combination of species has a cross term Z_{ij} that needs to be known. Based on the results of the previous sections, we predict that the cross terms between CO, C, and O are close to unity. Deviations below unity are expected for interactions between those species and hydrogen.

3.3.10 A simplified thermodynamically consistent potential

A rigorous approach to lateral interaction requires large computational expenses to determine all interaction parameters and cross terms. For the complete set of possible intermediates in the Fischer-Tropsch process this procedure becomes intractable. To incorporate the most important effects we constructed a simplified lateral interaction potential in our mean-field microkinetic code.

One of the important constraints for such a potential is again that it should not alter the thermodynamics of the total model. To achieve this, we again start by defining the total potential G_{lat} as

$$G_{\text{lat}} = \sum_i \theta_i E_i^{\text{lat}} \quad (3.10)$$

Now, the individual lateral penalties E_i^{lat} are derived on a per-atom basis. For example, the lateral interaction penalty for CH_4 is determined by the penalty of one carbon atom and four hydrogen atoms.

$$E_{\text{CH}_4}^{\text{lat}} = E_{\text{C}}^{\text{lat}} + 4E_{\text{H}}^{\text{lat}} \quad (3.11)$$

In the previous sections we performed nonlinear regression to model the combined effect of linear and exponential contributions. Especially for CO the exponential effect seemed to dominate. At low coverage the adsorption energy is relatively constant, and at high coverage the repulsion strongly increases. To easily include both homogeneous and heterogeneous repulsion we make the lateral interaction penalty an exponential function of the total lateral coverage θ_{lat} . Scaling of the penalty for different atomic contributions is then done through a pre-factor $E_x^{\theta=1}$, which is the lateral penalty at $\theta_{\text{lat}} = 1$.

$$E_x^{\text{lat}} = E_x^{\theta=1} \times \frac{\left(101^{\theta_{\text{lat}}} - 1\right)}{100} \quad (3.12)$$

A value of $\theta_{\text{lat}} = 0$ will result in a lateral penalty of zero. The steepness of the lateral penalty function increases for higher values of θ_{lat} , and values of $\theta_{\text{lat}} > 1$ will correspondingly lead to exponentially increasing repulsion above $E_x^{\theta=1}$.

We then assume that all surface species contribute equally to the lateral interaction coverage except for hydrogen. Furthermore, we allow for remapping of the lateral interaction coverage to another coverage range through parameters θ_{LB} and θ_{UB} . The resulting

expression for θ_{lat} is then

$$\theta_{\text{lat}} = \frac{(\theta_{\text{total}} - \theta_* - 0.5 \cdot \theta_H) - \theta_{\text{LB}}}{\theta_{\text{UB}} - \theta_{\text{LB}}}, \quad \text{with } \theta_{\text{lat}} \geq 0 \quad (3.13)$$

For example, setting $\theta_{\text{LB}} = 0.25$ ML and $\theta_{\text{UB}} = 0.75$ ML scales the lateral interaction coverage such that the lateral penalty is always zero below a coverage of 0.25 ML. The penalty then increases exponentially, reaching $E_x^{\theta=1}$ at e.g. 0.75 ML CO*, or 0.5 ML CO* and 0.5 ML H*.

3.3.11 Simulated temperature programmed desorption

With the simplified thermodynamically consistent potential we can transiently modify the adsorption energies during the time integration of a microkinetics simulation. This means that, in addition to steady-state simulations, the microkinetic modeling code can be used to simulate temperature-programmed desorption (TPD) experiments [23]. We used the latter approach to compare simulated TPD spectra to experimental references. Figure 3.16 shows simulated thermal desorption curves for CO and H₂ adsorbed on Co(0001) and Co(11 $\bar{2}$ 1). In this case we set θ_{LB} and θ_{UB} to 0.25 ML and 0.75 ML respectively, and used $E_{\text{CO}}^{\theta=1}$ and $E_{\text{H}}^{\theta=1}$ penalties of 120 kJ/mol and 15 kJ/mol respectively. The temperature was ramped from -80 °C to 200 °C at a rate of 1 °C s⁻¹.

We will first consider the desorption of CO on the two different surfaces. The initial CO coverage was set to 0.33 ML in both cases. Desorption starts at 77 °C and 102 °C for Co(0001) and Co(11 $\bar{2}$ 1), respectively. The maximum desorption rate for the step-edge surface is higher (155 °C) than for the terrace surface (137 °C), consistent with the slightly higher CO adsorption energy on Co(11 $\bar{2}$ 1) as found earlier in this chapter. Next we consider the desorption of 0.5 ML of hydrogen. As hydrogen atoms are more strongly bound on the Co(0001) surface, thermal desorption of H₂ is delayed on the terrace in comparison to the stepped surface. Without co-adsorption of CO the maximum desorption rates of hydrogen are found at 1 °C for the step-edge surface and 44 °C for the terrace surface. The thermal desorption peak maxima for CO and H₂ on the Co(0001) surface correspond well with experimental spectra found in the literature [8, 9]. We could also reproduce the increased rate of H₂ desorption upon co-adsorption of 0.33 ML CO found by Weststrate and Niemantsverdriet [52]. Although no TPD data for the Co(11 $\bar{2}$ 1) surface could be found in the literature, experimental and theoretical evidence shows a lower temperature TPD peak for hydrogen on defect sites [26].

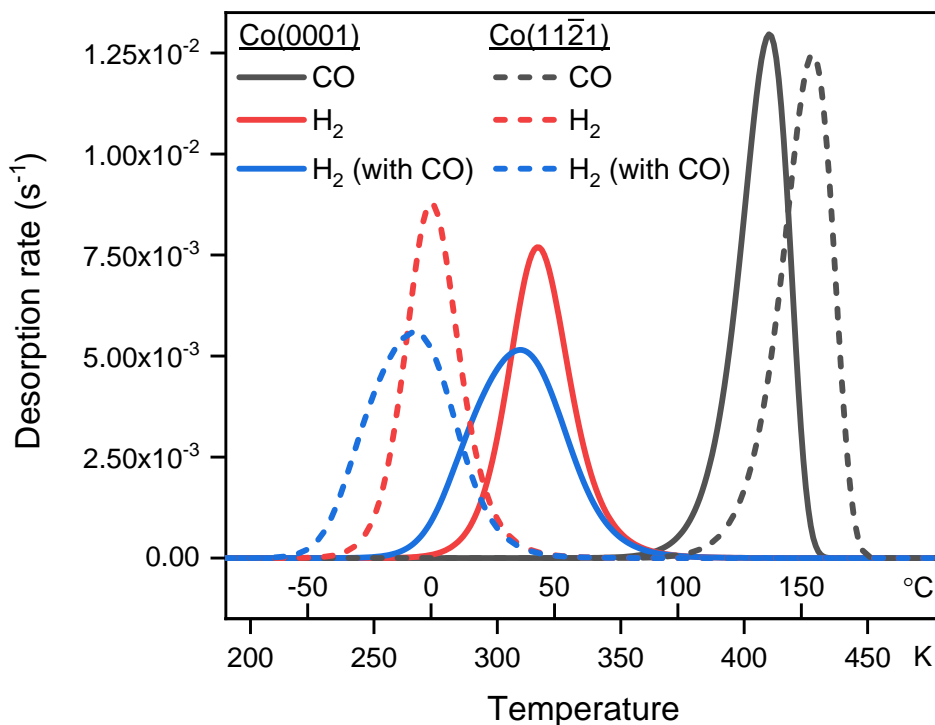


Figure 3.16: Microkinetics simulations of temperature programmed desorption of (i) 0.33 ML CO*, (ii) 0.5 ML H*, and (iii) 0.5 ML H* with 0.33 ML co-adsorbed CO* from (solid lines) Co(0001) and (dashed lines) Co(11 $\bar{2}$ 1).

3.4 Conclusions

Under Fischer-Tropsch conditions the CO coverage on the catalyst surface is expected to reach a saturation coverage well below unity as a result of lateral interactions. To properly describe these lateral interactions, we computed integral and differential adsorption heats for various FT intermediates. The nonlinear regression results show that the adsorption heats can be described as a combined linear and exponential function of coverage. For CO adsorption we find that a fully hexagonally symmetric adlayer is preferred, indicating that inter-adsorbate repulsion is the main lateral interaction effect. A vibrational analysis of the various structures shows that top-adsorbed CO has a larger C–O bond vibration frequency compared to other bonding modes. While both top-adsorbed and threefold-adsorbed frequencies increase linearly as a function of coverage, the difference between the two remains large enough to deduce the bonding mode. A similar result was found for N₂ adsorption. Comparison of CO adsorption between the terrace Co(0001) and stepped Co(11 $\bar{2}$ 1) surfaces shows that the dominant lateral interaction effect is exponential in form, and that this effect is similar for the two surfaces. We conclude that the saturation coverage in this case is determined by the CO–CO distance. Hydrogen adsorption was found to occur through a dissociative pathway without an overall enthalpic barrier. Adsorbed hydrogen

atoms show lower lateral interaction, while the lateral interaction penalties of C and O were found to be comparable to CO. We proposed a rigorous lateral interaction potential satisfying thermodynamic consistency with the disadvantage of computational complexity. Finally, we provide a more versatile simplified thermodynamically consistent potential that we could apply to simulate a temperature programmed desorption experiment. We found that we could reproduce both the desorption peak maxima for CO and H₂, and the increased rate of H₂ desorption due to lateral interaction.

3.5 References

- [1] Q. Zhang, W. Deng, Y. Wang, *Journal of Energy Chemistry* **2013**, *22*, 27–38.
- [2] L. A. Richard, P. Moreau, S. Rugmini, F. Daly, *Applied Catalysis A: General* **2013**, *464-465*, 200–206.
- [3] J. Wilson, C. de Groot, *The Journal of Physical Chemistry* **1995**, *99*, 7860–7866.
- [4] I. A. W. Filot, S. G. Shetty, E. J. M. Hensen, R. A. van Santen, *Journal of Physical Chemistry C* **2011**, *115*, 14204–14212.
- [5] I. A. W. Filot, R. J. P. Broos, J. P. M. van Rijn, G. J. H. A. van Heugten, R. A. van Santen, E. J. M. Hensen, *ACS Catalysis* **2015**, *5*, 5453–5467.
- [6] I. A. Filot, R. A. van Santen, E. J. Hensen, *Angew Chem Int Ed Engl* **2014**, *53*, 12746–12750.
- [7] I. A. W. Filot, B. Zijlstra, R. J. P. Broos, W. Chen, R. Pestman, E. J. M. Hensen, *Faraday Discussions* **2017**, *197*, 153–164.
- [8] J. Lahtinen, J. Vaari, K. Kauraala, *Surface Science* **1998**, *418*, 502–510.
- [9] C. J. Weststrate, J. van de Loosdrecht, J. W. Niemantsverdriet, *Journal of Catalysis* **2016**, *342*, 1–16.
- [10] J. X. Liu, H. Y. Su, D. P. Sun, B. Y. Zhang, W. X. Li, *J Am Chem Soc* **2013**, *135*, 16284–7.
- [11] R. Van Hardeveld, F. Hartog, *Surface Science* **1969**, *15*, 189–230.
- [12] G. A. Beitel, A. Laskov, H. Oosterbeek, E. W. Kuipers, *The Journal of Physical Chemistry* **1996**, *100*, 12494–12502.
- [13] A. Mikhailov, G. Ertl, *Chemical Physics Letters* **1995**, *238*, 104–109.
- [14] M. Golze, M. Grunze, W. Hirschwald, *Vacuum* **1981**, *31*, 697–703.
- [15] J. K. Badenhop, F. Weinhold, *The Journal of Chemical Physics* **1997**, *107*, 5406–5421.
- [16] H. Papp, *Surface Science* **1983**, *129*, 205–218.
- [17] W. Chen, I. A. W. Filot, R. Pestman, E. J. M. Hensen, *ACS Catalysis* **2017**, *7*, 8061–8071.
- [18] I. C. Yates, C. N. Satterfield, *Energy & Fuels* **1991**, *5*, 168–173.

- [19] M. Zhuo, A. Borgna, M. Saeys, *Journal of Catalysis* **2013**, *297*, 217–226.
- [20] G. T. K. K. Gunasooriya, A. P. van Bavel, H. P. C. E. Kuipers, M. Saeys, *Surface Science* **2015**, *642*, L6–L10.
- [21] J. Yang, V. Frøseth, D. Chen, A. Holmen, *Surface Science* **2016**, *648*, 67–73.
- [22] J. P. den Breejen, P. B. Radstake, G. L. Bezemer, J. H. Bitter, V. Frøseth, A. Holmen, K. P. de Jong, *J Am Chem Soc* **2009**, *131*, 7197–203.
- [23] P. van Helden, J.-A. v. d. Berg, M. A. Petersen, W. Janse van Rensburg, I. M. Ciobîcă, J. van de Loosdrecht, *Faraday Discussions* **2017**, *197*, 117–151.
- [24] A. P. v. Bavel, M. J. P. Hopstaken, D. Curulla, J. W. Niemantsverdriet, J. J. Lukkien, P. A. J. Hilbers, *The Journal of Chemical Physics* **2003**, *119*, 524–532.
- [25] S. E. Mason, I. Grinberg, A. M. Rappe, *The Journal of Physical Chemistry B* **2006**, *110*, 3816–3822.
- [26] P. van Helden, J.-A. van den Berg, C. J. Weststrate, *ACS Catalysis* **2012**, *2*, 1097–1107.
- [27] K. Liao, V. Fiorin, D. S. D. Gunn, S. J. Jenkins, D. A. King, *Physical Chemistry Chemical Physics* **2013**, *15*, 4059–4065.
- [28] N. Yang, A. J. Medford, X. Liu, F. Studt, T. Bligaard, S. F. Bent, J. K. Nørskov, *Journal of the American Chemical Society* **2016**, *138*, 3705–3714.
- [29] P. E. Blochl, *Phys Rev B Condens Matter* **1994**, *50*, 17953–17979.
- [30] G. Kresse, J. Hafner, *Physical Review B* **1993**, *47*, 558–561.
- [31] G. Kresse, J. Hafner, *Physical Review B* **1994**, *49*, 14251–14269.
- [32] G. Kresse, J. Furthmüller, *Computational Materials Science* **1996**, *6*, 15–50.
- [33] G. Kresse, J. Furthmüller, *Physical Review B* **1996**, *54*, 11169–11186.
- [34] J. P. Perdew, K. Burke, M. Ernzerhof, *Physical Review Letters* **1996**, *77*, 3865–3868.
- [35] H. J. Monkhorst, J. D. Pack, *Physical Review B* **1976**, *13*, 5188–5192.
- [36] G. Mills, H. Jónsson, G. K. Schenter, *Surface Science* **1995**, *324*, 305–337.
- [37] G. Henkelman, B. P. Uberuaga, H. Jonsson, *Journal of Chemical Physics* **2000**, *113*, 9901–9904.
- [38] G. Henkelman, H. Jónsson, *The Journal of Chemical Physics* **2000**, *113*, 9978–9985.
- [39] I. A. W. Filot, B. Zijlstra, E. J. M. Hensen, MKMCXX, a C++ program for constructing microkinetic models, <http://www.mkmcxx.nl/>.
- [40] J. Lahtinen, J. Vaari, K. Kauraala, E. A. Soares, M. A. Van Hove, *Surface Science* **2000**, *448*, 269–278.
- [41] P. J. Feibelman, B. Hammer, J. K. Nørskov, F. Wagner, M. Scheffler, R. Stumpf, R. Watwe, J. Dumesic, *Journal of Physical Chemistry B* **2001**, *105*, 4018–4025.

- [42] A. Gil, A. Clotet, J. M. Ricart, G. Kresse, M. García-Hernández, N. Rösch, P. Sautet, *Surface Science* **2003**, *530*, 71–87.
- [43] L. Schimka, J. Harl, A. Stroppa, A. Grüneis, M. Marsman, F. Mittendorfer, G. Kresse, *Nature Materials* **2010**, *9*, 741.
- [44] L. C. Grabow, B. Hvolbæk, J. K. Nørskov, *Topics in Catalysis* **2010**, *53*, 298–310.
- [45] W. Chen, B. Zijlstra, I. A. W. Filot, R. Pestman, E. J. M. Hensen, *ChemCatChem* **2018**, *10*, 136–140.
- [46] G. Blyholder, *The Journal of Physical Chemistry* **1964**, *68*, 2772–2777.
- [47] C. H. Shomate, *The Journal of Physical Chemistry* **1954**, *58*, 368–372.
- [48] *Journal of Physical and Chemical Reference Data* **1982**, *11*, 695–940.
- [49] F. Tao, S. Dag, L.-W. Wang, Z. Liu, D. R. Butcher, H. Bluhm, M. Salmeron, G. A. Somorjai, *Science* **2010**, *327*, 850–853.
- [50] I. Swart, F. M. F. de Groot, B. M. Weckhuysen, P. Gruene, G. Meijer, A. Fielicke, *The Journal of Physical Chemistry A* **2008**, *112*, 1139–1149.
- [51] E. Shustorovich, H. Sellers, *Surface Science Reports* **1998**, *31*, 1–119.
- [52] C. J. Weststrate, J. W. Niemantsverdriet, *Faraday Discussions* **2017**, *197*, 101–116.

CHAPTER 4

COVERAGE EFFECTS IN CO DISSOCIATION ON METALLIC COBALT NANOPARTICLES

Contents

4.1	Introduction	66
4.2	Computational methods	67
4.3	Results and discussion	68
4.3.1	Direct and hydrogen-assisted CO dissociation at low coverage	68
4.3.2	Dissociation barrier as a function of coverage	71
4.3.3	Bond order analysis	74
4.3.4	Electrostatic potential	76
4.4	Conclusions	80
4.5	References	80
	Appendix A	83

Abstract

The active site of CO dissociation on a cobalt nanoparticle, relevant to the Fischer-Tropsch reaction, can be computed directly using density functional theory. We investigated the direct and H-assisted CO dissociation pathways at low coverage. While the H-assisted HCO-pathway is preferred on the terrace Co(0001) surface, the corresponding overall barrier of 182 kJ/mol is too high to produce FT monomers at rates comparable to experimental turnovers. The direct CO dissociation step on the stepped Co(11 $\bar{2}$ 1) surface has a much lower barrier of 100 kJ/mol, supporting the hypothesis that step-edge sites are the active sites of CO dissociation in the FT reaction. We then investigated how the activation barrier for direct CO dissociation depends on CO coverage for step-edge and terrace cobalt sites. Whereas on terrace sites increasing coverage results in a substantial increase of the direct CO dissociation barrier, we find that this barrier is nearly independent of CO coverage for the step-edge sites on corrugated surfaces. A detailed electronic analysis shows that this difference is due to the flexibility of the adsorbed layer, minimizing Pauli repulsion during the carbon-oxygen bond dissociation reaction on the step-edge site.

4.1 Introduction

It is of significant fundamental and practical interest to understand the molecular details underlying Fischer-Tropsch (FT) synthesis catalyzed by metal nanoparticles [1–4]. CO dissociation is a crucial elementary reaction step within the FT mechanism. Depending on catalyst choice and reaction conditions, the CO dissociation step can significantly control the overall reaction rate [5]. A prerequisite for obtaining long-chain hydrocarbons is a high supply rate of C_1 monomers [6–9]. A common view is that low-barrier CO dissociation needs step-edge sites, which can explain the experimentally observed strong structure sensitivity of the FT reaction [10]. Optimum FT catalysts comprise Co nanoparticles with a size of about 6 nm, because smaller particles cannot accommodate a sufficient amount of step-edge sites [11–13]. Typical activation barriers for direct CO dissociation computed by density functional theory (DFT) are in the range of 100–150 kJ/mol for most stepped Co surfaces [14, 15]. Lower barriers are reported for Ru surfaces [16, 17]. These values should be contrasted with barriers higher than 200 kJ/mol for direct dissociation of CO on close-packed surfaces. H-assisted CO dissociation pathways have also been explored [16–19]. Although barriers for C–O bond cleavage in adsorbed HCO, H_2CO and HCOH intermediates are lower than for adsorbed CO, these hydrogenated surface intermediates are typically much less stable [20, 21]. Therefore, overall barriers for H-assisted CO dissociation are usually higher than those for direct CO dissociation on step-edge sites. For example, Pilot et al. found a direct CO dissociation barrier of 173 kJ/mol on Rh(211), while the overall barriers via HCO and COH are 263 kJ/mol and 275 kJ/mol respectively [22]. Shetty et al. report an overall barrier for HCO dissociation on Ru(11 $\bar{2}$ 1) of 120 kJ/mol, whereas the direct CO scission is only 65 kJ/mol on the same site [17]. Liu et al. concluded that FCC cobalt catalysts and HPC cobalt terraces prefer the H-assisted route (125 kJ/mol on Co(110)), while corrugated HCP cobalt catalysts have remarkably higher intrinsic activity via a preferred direct dissociation route (103 kJ/mol on Co(11 $\bar{2}$ 1)) [15, 23].

Although all these studies suggest a FT mechanism dominated by direct CO dissociation, significant changes in reaction kinetics can be expected due to carbon induced deactivation [24–26] and lateral interactions from high surface coverage [27–29]. As both effects could block facile pathways for direct CO dissociation, the mechanism is expected to shift to a H-assisted mechanism. CO-scrambling experiments, however, contradict this [30]. Relevant scrambling rates on a cobalt FT catalyst were found to be fast, even without hydrogen. Moreover, it has been demonstrated that carbon deposition on a cobalt FT catalyst occurs mainly on terrace surfaces and, at low concentrations, it does not affect FT activity [2]. This implies that C atoms generated on step-edge sites are involved in chain-growth reactions and, therefore, do not block the step-edge sites.

Chapter 3 of this thesis has described the CO saturation coverages for the cobalt surfaces, which are expected to be no higher than 0.6 ML under relevant FT conditions. However, Loveless et al. showed by DFT modeling that a higher than 1 ML CO coverage is possible on a cluster of 201 Ru atoms [28]. For such a cluster, the CO dissociation barrier on a (1 $\bar{1}$ 05) step-edge site with a CO coverage of 1.07 ML is close to 150 kJ/mol, much higher than the barrier on a Ru(11 $\bar{2}$ 1) step-edge at low coverage. Thus, a high coverage might lead

to an increased CO dissociation barrier. Neurock and Iglesia alternatively emphasized the role of H- and also H₂O-promoted pathways for CO dissociation on the terrace surfaces that dominate nanoparticles [29, 31, 32]. A critique on these works mentions that the high coverage possible on a Ru₂₀₁ cluster is mainly due to the expansion and restructuring of the relatively small cluster [33]. A further concern is that the chosen step-edge site has only a low reactivity. We computed the activation barrier for CO dissociation on a similar Co($\bar{1}\bar{1}05$) surface at low coverage (see Appendix A). The resulting value of 151 kJ/mol is substantially higher than CO dissociation on a Co($11\bar{2}1$) step-edge, indeed showing that the particular step-edge geometry used in the work of Neurock and Iglesia is not very favorable for CO dissociation. High CO coverages are expected to destabilize adsorbed hydrogen, which might lower the barrier for HCO formation and as a result the HCO pathway may compete with direct CO scission. However, the HCO compound itself is also destabilized by high CO coverages, which counteracts the decrease in the HCO formation barrier. Su et al. considered the effect of a 7/12 ML CO coverage on the FT mechanism on Co(0001) and found that steric hindrance contributes to additional repulsive interactions on HCO compared to CO [34]. From this data we infer that these two effects will lead to an overall barrier for HCO formation and dissociation largely independent of CO coverage. Thus, a remaining question is whether direct CO dissociation over reactive cobalt step-edges also maintains a low barrier at a coverage around 0.6 ML, which is expected under practical FT conditions.

4.2 Computational methods

All quantum-chemical calculations were performed using a plane-wave density functional theory approach with the projector-augmented wave (PAW) method [35], as implemented in the Vienna ab initio simulation package (VASP) [36–39]. For exchange-correlation, the Perdew-Burke-Ernzerhof (PBE) functional was used [40]. The plane-wave basis set was limited to a 400 eV kinetic energy cut-off base. A gamma-centered Monkhorst-Pack 21 x 21 x 21 k-point mesh [41] was used for bulk HCP Co, and a 5 x 5 x 1 k-point mesh for Co surface slabs. Calculations for molecular references in the gas phase only employed the gamma point in a 10 x 10 x 10 Å³ cell. We used Co(0001) and Co($11\bar{2}1$) as model surfaces for the terrace sites and step-edges on cobalt nanoparticles. The latter step-edge sites can describe the high reactivity of B₅-sites [15]. The Co lattice parameters for our calculations correspond to 2.49 Å, 2.49 Å and 4.03 Å for the *a*, *b* and *c* directions respectively. The Co(0001) surface was constructed from a (3 x 3) unit cell with 5 atomic layers, which corresponds to 45 Co atoms per unit cell. The Co($11\bar{2}1$) surface was constructed from a (2 x 2) unit cell with 3 atomic layers (48 Co atoms per unit cell). Adsorbates on the Co(0001) surface slab were placed with mirror symmetry in the *ab*-plane to avoid spurious dipole-dipole interactions between neighboring unit cells. For the Co($11\bar{2}1$) surface slab, the adsorbates were placed using inversion symmetry. All atomic positions were optimized using the conjugate-gradient technique. We explored reaction paths with the climbing image nudged elastic band (cNEB) implementation [42–44]. The transition states (TS)

were optimized using a quasi-Newton algorithm and were confirmed by the saddle points obtained from frequency calculations. The Hessian matrices were calculated with the finite displacement technique. The corresponding vibrations were also used to compute the zero-point energy (ZPE) corrections and vibrational partition functions for all adsorbed species and transition states. The surface integral for determining the electrostatic potential was calculated using the 23rd order (i.e. 194-point) Lebedev quadrature [45] and the values for the electrostatic potential at the Lebedev sampling points were calculated from the scalar grid using trilinear interpolation.

4.3 Results and discussion

As systematic computational data of coverage-dependent CO dissociation were lacking, we determined activation barriers for this elementary reaction step for low-reactive Co(0001) and high-reactive stepped Co(11 $\bar{2}$ 1) surfaces using DFT as a function of coverage. Different from the uniform planar Co(0001) surface, the Co(11 $\bar{2}$ 1) surface contains a two-dimensional array of step-edge sites comprised of a reactive pocket consisting of 5 cobalt atoms (B₅-site following the notation of Van Harvelde and Hartog [46]). The low coverage pathways will be discussed first, including the hydrogen assisted pathways. Then, the reaction profile of direct CO scission as a function of CO coverage will be investigated in more detail. Finally, we will discuss the coverage effects through analysis of the bond orders and the electrostatic potential along the reaction coordinate.

4.3.1 Direct and hydrogen-assisted CO dissociation at low coverage

The direct and hydrogen-assisted CO dissociation pathways were computed at 0.11 ML coverage for the Co(0001) surface and 0.07 ML coverage for the Co(11 $\bar{2}$ 1) surface. Figure 4.1 shows the most favorable transition states for the C–O bond scission in CO, COH, HCO, H₂CO, HCOH, and H₂COH on the two surfaces. For the Co(0001) surface, we found that the bonding mode of the carbon atom with the cobalt surface changes from a threefold mode to a bridged mode upon hydrogenation of the carbon. While the oxygen atom is in bridged position for the un-hydrogenated CO transition state, it moves to the center of the threefold site upon hydrogenation of the carbon atom. In the transition states of HCOH and H₂COH the oxygen atom moves to a top adsorbed position. This suggests that the hydrogenated species are less strongly bound to the cobalt surface. For the Co(11 $\bar{2}$ 1) surface, we see a similar effect for the H₂CO, HCOH, and H₂COH transition states.

The elementary reaction step barriers for the C–O bond scission steps are presented in Table 4.1. As expected, the scission of hydrogenated intermediates like COH and HCO is more facile as compared to direct CO dissociation on the same surface. For the terrace Co(0001) surface the lowest barrier is found for the H₂COH scission. This elementary reaction step has a barrier of 45 kJ/mol, while the direct pathway requires overcoming a barrier of 225 kJ/mol. For the more reactive stepped Co(11 $\bar{2}$ 1) surface the direct pathway is only 100 kJ/mol, in line with the work of Liu [15]. The lowest barrier on the stepped surface is found for the COH scission, which has a barrier of only 18 kJ/mol.

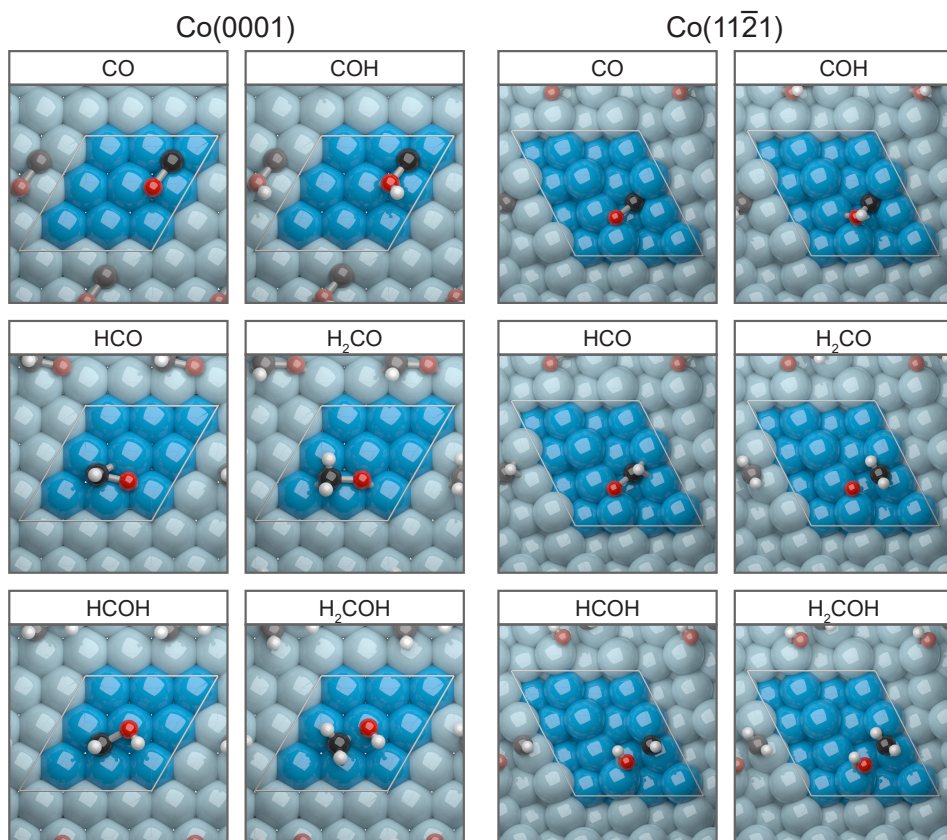


Figure 4.1: Configurations of the C–O bond scission transition states on the terrace (3 x 3) Co(0001) surface (left) and the stepped (2 x 2) Co(11 $\bar{2}$ 1) surface (right).

As the low barriers for the hydrogenated intermediates are mostly a consequence of their lower stability, we also determined the overall barriers for the CO dissociation process, i.e. including the hydrogenation of the CO adsorbate. For this we first determined the barriers of the hydrogenation steps as shown in Table 4.2. For the Co(0001) surface the initial hydrogenation step of CO to COH or HCO has a forward barrier of 175 kJ/mol and 127 kJ/mol respectively. Hence, the overall barrier for dissociation of those species cannot be lower than these barriers. Likewise, the overall barrier for COH scission on the stepped Co(11 $\bar{2}$ 1) surface is much higher than 18 kJ/mol given the 209 kJ/mol hydrogenation step of CO to COH. In fact, a lower pathway is possible via CO \rightarrow HCO \rightarrow HCOH \rightarrow COH \rightarrow C + OH. Nevertheless, this pathway still requires an overall barrier of 191 kJ/mol to reach the HCOH state. Table 4.3 shows that the lowest hydrogen-assisted pathway is the HCO pathway on the Co(11 $\bar{2}$ 1) surface with an overall barrier of 151 kJ/mol. The lowest overall pathway on the Co(0001) surface is the HCO dissociation pathway with an overall barrier of 182 kJ/mol. Qi et al [47]. also found that the lowest dissociation pathway on Co(0001) goes via the HCO intermediate and that the overall barrier for HCOH is higher than for HCO

Table 4.1: Elementary reaction step barriers for the C–O bond scission reactions on Co(0001) and Co(11 $\bar{2}$ 1). All barriers are corrected for the zero point energy and are referenced to the most stable surface intermediates.

Elementary reaction	Co(0001)		Co(11 $\bar{2}$ 1)	
	E_{act} forward (kJ/mol)	E_{act} backward (kJ/mol)	E_{act} forward (kJ/mol)	E_{act} backward (kJ/mol)
$\text{CO}^* + * \rightleftharpoons \text{C}^* + \text{O}^*$	225	158	100	102
$\text{COH}^* + * \rightleftharpoons \text{C}^* + \text{OH}^*$	149	145	18	116
$\text{HCO}^* + * \rightleftharpoons \text{CH}^* + \text{O}^*$	63	135	82	133
$\text{H}_2\text{CO}^* + * \rightleftharpoons \text{CH}_2^* + \text{O}^*$	59	126	62	145
$\text{HCOH}^* + * \rightleftharpoons \text{CH}^* + \text{OH}^*$	62	149	56	175
$\text{H}_2\text{COH}^* + * \rightleftharpoons \text{CH}_2^* + \text{OH}^*$	45	134	37	159

Table 4.2: Elementary reaction step barriers for the CO hydrogenation reactions on Co(0001) and Co(11 $\bar{2}$ 1). All barriers are corrected for the zero point energy and are referenced to the most stable surface intermediates.

Elementary reaction	Co(0001)		Co(11 $\bar{2}$ 1)	
	E_{act} forward (kJ/mol)	E_{act} backward (kJ/mol)	E_{act} forward (kJ/mol)	E_{act} backward (kJ/mol)
$\text{CO}^* + \text{H}^* \rightleftharpoons \text{COH}^* + *$	175	77	209	100
$\text{CO}^* + \text{H}^* \rightleftharpoons \text{HCO}^* + *$	127	7	69	-1
$\text{HCO}^* + \text{H}^* \rightleftharpoons \text{H}_2\text{CO}^* + *$	43	10	64	12
$\text{HCO}^* + \text{H}^* \rightleftharpoons \text{HCOH}^* + *$	102	51	122	42
$\text{COH}^* + \text{H}^* \rightleftharpoons \text{HCOH}^* + *$	68	-5	70	29
$\text{HCOH}^* + \text{H}^* \rightleftharpoons \text{H}_2\text{COH}^* + *$	65	25	54	30
$\text{H}_2\text{CO}^* + \text{H}^* \rightleftharpoons \text{H}_2\text{COH}^* + *$	96	38	87	35

dissociation. However, these authors argue based on SSITKA results and kinetic isotope effects (KIE) that dissociation of HCOH and not HCO is responsible for CH_4 formation. We expect such a pathway to be unlikely, given the high overall barrier of 233 kJ/mol as presented here. Furthermore, SSITKA and KIE results can also be explained by the involvement of hydrogen in the termination of hydrocarbon species and removal of oxygen as water. These effects will be discussed in more detail in Chapter 5. Altogether, our results clearly show that direct CO dissociation on the B_5 -site of the stepped Co(11 $\bar{2}$ 1) surface is at least 51 kJ/mol more favorable than the lowest hydrogen-assisted pathway. The transition state for this reaction is reached by first migrating CO from its most stable adsorption site to the B_5 -site, where it is less stable by 17 kJ/mol. From this state, dissociation can occur with a barrier of 83 kJ/mol, giving a combined activation barrier of 100 kJ/mol, which is sufficiently low to maintain a high rate of monomer formation [6–9].

Table 4.3: Overall barriers for the C–O bond scission pathways on Co(0001) and Co(11 $\bar{2}$ 1). All barriers are corrected for the zero point energy and are referenced to the most stable surface intermediates.

Species	Dissociation pathway	Co(0001)	Co(11 $\bar{2}$ 1)
		E_{act} (kJ/mol)	E_{act} (kJ/mol)
CO	direct	225	100
COH	CO \rightarrow COH	247	209
COH	CO \rightarrow HCO \rightarrow HCOH \rightarrow COH	247	191
HCO	CO \rightarrow HCO	182	151
HCOH	CO \rightarrow COH \rightarrow HCOH	233	209
HCOH	CO \rightarrow HCO \rightarrow HCOH	233	206
H ₂ CO	CO \rightarrow HCO \rightarrow H ₂ CO	212	184
H ₂ CO	CO \rightarrow COH \rightarrow HCOH \rightarrow H ₂ COH \rightarrow H ₂ CO	249	209
H ₂ CO	CO \rightarrow HCO \rightarrow HCOH \rightarrow H ₂ COH \rightarrow H ₂ CO	249	209
H ₂ COH	CO \rightarrow COH \rightarrow HCOH \rightarrow H ₂ COH	256	210
H ₂ COH	CO \rightarrow HCO \rightarrow HCOH \rightarrow H ₂ COH	256	210
H ₂ COH	CO \rightarrow HCO \rightarrow H ₂ CO \rightarrow H ₂ COH	256	210

4.3.2 Dissociation barrier as a function of coverage

Based on the insight that direct CO scission is the most favorable low coverage pathway, we computed dissociation barriers at CO coverages up to 0.59 ML and 0.67 ML on the stepped Co(11 $\bar{2}$ 1) and close-packed Co(0001) surfaces, respectively. Figures 4.2 and 4.3 depict the most favorable transition states for the Co(11 $\bar{2}$ 1) and Co(0001) surfaces. The transition states at higher CO coverage are similar in nature to those determined at the low coverages of 0.07 ML and 0.11 ML. As also found in Chapter 3, the additional CO adsorbates are oriented in different directions on the stepped surface as compared to nearly perpendicular orientation to the surface for the terrace model.

Table 4.4: Zero-point-energy corrected differential adsorption energies for CO and reaction barriers for direct CO dissociation on the stepped (2 x 2) Co(11 $\bar{2}$ 1) surface. Forward barriers are referenced to either the most stable adsorption configuration, or to the local pre-activated initial state. Backward barriers are referenced to the co-adsorbed state of C and O after dissociation.

Coverage	Forward E_{act}	Forward E_{act}	Backward E_{act}
	(kJ/mol) IS = most stable	(kJ/mol) IS = local	(kJ/mol)
0.07 ML	100	83	97
0.15 ML	93	80	99
0.22 ML	100	86	100
0.30 ML	114	79	88
0.37 ML	107	85	78
0.44 ML	96	81	80
0.52 ML	88	88	72
0.59 ML	98	90	85

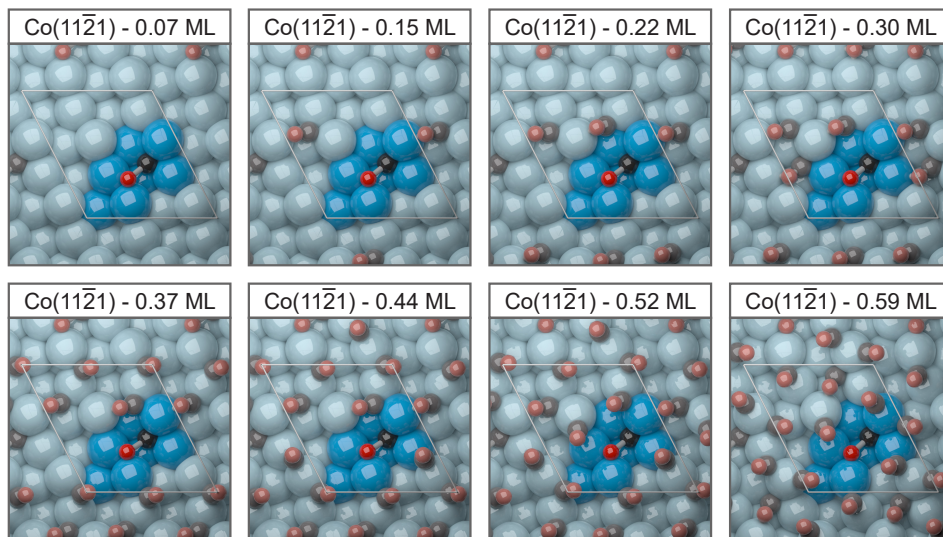


Figure 4.2: Top surface views of the most favorable CO dissociation pathways on CO-covered Co(11 $\bar{2}$ 1).

The corresponding activation barriers for CO dissociation on the Co(11 $\bar{2}$ 1) and Co(0001) surfaces are given in Table 4.4 and Table 4.5, respectively. We will first discuss the barriers on the stepped Co(11 $\bar{2}$ 1) surface. The forward dissociation barriers as referenced to the most stable adsorption configuration range from 88 kJ/mol to 114 kJ/mol. There is no clear trend as a function of coverage, because the lowest barrier is found for 0.52 ML and the low 0.07 ML coverage barrier of 100 kJ/mol is roughly in the middle of the range. The second column of forward barriers in Table 4 provides the barriers as referenced to the local pre-activated initial state. This means that an additional reorientation may be necessary from the most stable adsorption configuration. This is mostly the case for the Co(11 $\bar{2}$ 1) surface, as a properly located vacancy is needed, and the dissociating CO molecule

Table 4.5: Zero-point-energy corrected differential adsorption energies for CO and reaction barriers for direct CO dissociation on the terrace (3 x 3) Co(0001) surface. Forward barriers are referenced to either the most stable adsorption configuration, or to the local initial state. Backward barriers are referenced to the co-adsorbed state of C and O after dissociation.

Coverage	Forward E_{act} (kJ/mol) IS = most stable	Forward E_{act} (kJ/mol) IS = local	Backward E_{act} (kJ/mol)
0.11 ML	225	225	134
0.22 ML	239	239	140
0.33 ML	227	227	110
0.44 ML	259	259	117
0.56 ML	258	253	108
0.67 ML	318	269	108

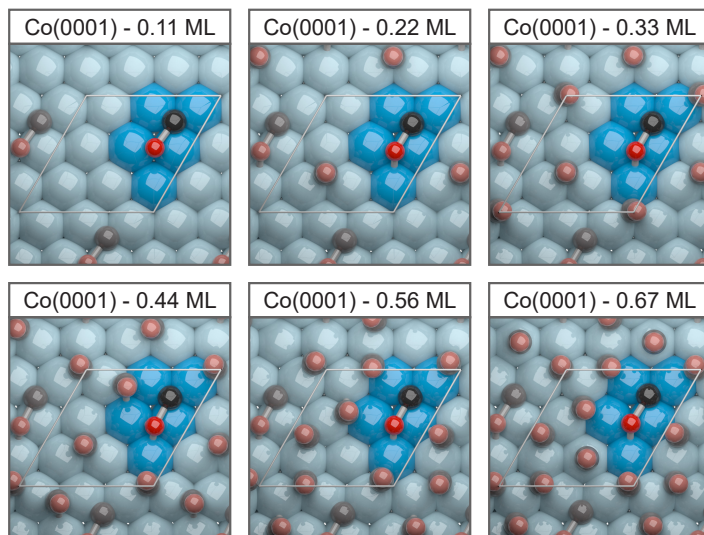


Figure 4.3: Top surface views of the most favorable CO dissociation pathways on CO-covered Co(0001).

is for most coverages more stable with the carbon atom in a three-fold adsorption site. For example, at 0.07 ML the difference pertains to the 17 kJ/mol migration of CO from the most stable adsorption state to the adsorption mode in the B_5 -site. The actual forward barriers as referenced to the local pre-activated initial state are in the 79-90 kJ/mol range, which is an even smaller range than the range of the barriers referenced to the most stable adsorption configuration. Also in this case there is no real trend with coverage. The spread in the backward barriers is larger with values between 72 kJ/mol and 100 kJ/mol. In this case the lowest three coverages have the highest backward barriers, while the coverages at 0.30 ML and higher have 10-20 kJ/mol lower barriers. The important corollary is that the CO dissociation barrier on the Co($1\bar{1}\bar{2}1$) surface does not appreciably depend on the CO coverage.

Next, we will discuss the coverage dependence of the dissociation barriers on the terrace Co(0001) surface (Table 4.5). Although the low coverage barrier is already very high, we found that the dissociation barrier increases further with coverage, in contrast to the stepped surface. At 0.33 ML, the forward dissociation barrier is only 2 kJ/mol higher than at a coverage of 0.11 ML. The backward barrier is 24 kJ/mol lower, which indicates that the reaction heat is more endothermic. For coverages of 0.44 ML and higher the backward barrier remains similar in magnitude as compared to 0.33 ML. For these coverages the forward barrier increases strongly. At 0.67 ML the dissociation barrier from the most stable state is increased by 93 kJ/mol as compared to a coverage of 0.11 ML.

Thus, whereas on a terrace cobalt surface a higher CO coverage leads to the expected increase of the activation barrier for CO dissociation, this reaction is hardly affected by CO co-adsorbates on the step-edge site. To understand the underlying origin of this difference,

we performed nudged elastic band calculations of the transition states with a larger number of images along the reaction coordinate. Figure 4.4a and 4.4b show the resulting potential energy surfaces as a function of the C–O distance, which is used here as the reaction coordinate. The energy profiles are relative to the electronic energy of the local initial state. On the Co(11 $\bar{2}$ 1) surface, the heat of reaction shifts from exothermic at low CO coverage to endothermic at high CO coverage, which is due to the stronger lateral interactions of the adsorbed C and O atoms compared to adsorbed CO at higher coverage. On the Co(0001) surface, the heat of reaction is already endothermic at low coverage, and additional CO co-adsorbates further increase the endothermicity. Apart from the differences in barrier height, the two potential energy surfaces have different shapes. For the stepped Co(11 $\bar{2}$ 1) surface, the profile has a shoulder at a carbon-oxygen distance of 3.5 Å. This metastable state resembles the final state, but has the oxygen atom adsorbed in a bridge position rather than in a threefold one. The potential energy surface of the terrace Co(0001) surface, on the other hand, shows additional curvature close to the initial state. A further analysis shows that CO undergoes a rotation towards the surface which increases the energy by 100 kJ/mol without leading to a significant increase in the carbon-oxygen distance. Likely, this rotation contributes to the height of the barrier and the pronounced coverage effect.

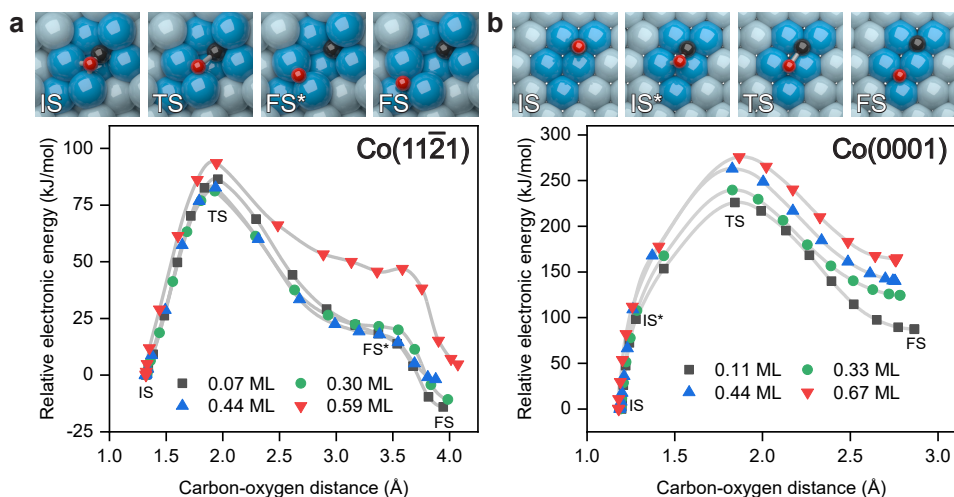


Figure 4.4: Potential energy surfaces of CO dissociation as a function of the reaction coordinate (C–O bond distance) for (a) Co(11 $\bar{2}$ 1) and (b) Co(0001): The top panels show the initial state (IS), the transition state (TS) and the final state (FS) for CO dissociation at the lowest CO coverage. FS* is a metastable state with the O atom bridge-bonded. IS* is the state after rotation of the CO without significantly increasing the C–O distance.

4.3.3 Bond order analysis

We analyzed the potential energy surfaces in more detail by studying the electronic structure along the dissociation pathway. As discussed in the previous chapter, the influence of co-adsorbates could originate from through-space electron-electron repulsion with the

dissociating CO molecule and from a decreased reactivity of surface metal atoms due to metal valence electron sharing between the dissociating molecule and co-adsorbates. We addressed the latter aspect by computing bond orders along the reaction coordinate during dissociation using the recently introduced DDEC6 atomic population analysis, which allows accurate charge partitioning to assign net atomic charges [48].

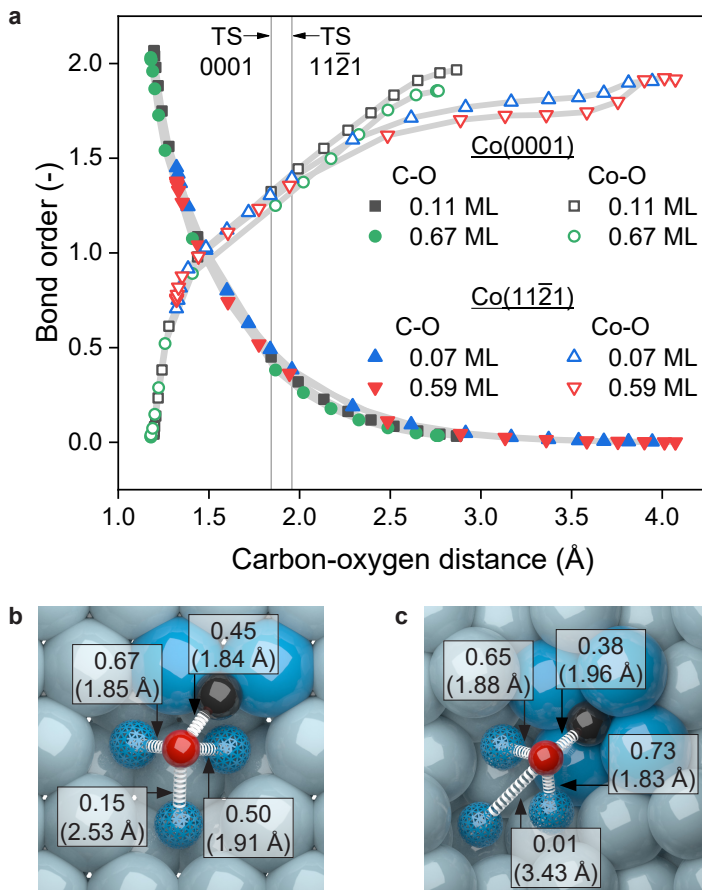


Figure 4.5: Bond orders determined by a DDEC6 atomic population analysis for CO dissociation on Co(11 $\bar{2}$ 1) and Co(0001) at low and high coverage. The filled symbols in panel (a) represent the bond orders between the dissociating carbon-oxygen pair, the open symbols the cumulative bond order of the dissociating oxygen atom with the three cobalt atoms to which the oxygen binds to in the final state. The locations of the two transition states are also indicated. Panels (b) and (c) show the individual bond orders and atom-atom distances at low coverage for the transition state on Co(0001) and Co(11 $\bar{2}$ 1), respectively. The cobalt atoms accommodating the oxygen atom are shown with smaller spheres for improved clarity.

Figure 4.5 shows the bond orders of the dissociating CO molecule and the Co-O bonds, along the reaction coordinate. The C-O bond order starts around 2.0 on the Co(0001) surface, while the C-O bond on Co(11 $\bar{2}$ 1) is already elongated and starts at 1.5 (bond order

in free CO is 2.5). The bond orders then decrease to a value close to zero in the final state. Strikingly, the changes in the C–O bond order do not depend on the CO coverage. Similarly, we find that the Co–O bond orders increase in a very similar manner for the two investigated surfaces along the reaction coordinate. Only at the highest CO coverage, the Co–O bond order is slightly lower in comparison to lower coverage. From these trends, we can infer that the sharing of valence electrons of the Co surface atoms involved in binding the C and O atoms is not strongly affected by CO co-adsorbates and, therefore, cannot account for the stronger CO coverage dependence of CO dissociation on the Co(0001) surface.

4.3.4 Electrostatic potential

To better understand the way through-space electron-electron repulsion from CO co-adsorbates affects the activation barrier, we aimed for analyzing the Hartree potential along the reaction coordinate of C–O bond dissociation. The Hartree potential (V_{Hartree}) is defined as the electrostatic potential resulting from the electron charge density. This potential is repulsive and larger values relate to regions of stronger coulombic repulsion. In the VASP implementation of DFT the Hartree potential cannot be separated from the attractive electron-ion potential (V_{ion}). The combined potential is negative, wherein values closer to zero relate to regions less favorable for inserting electron density of nearby atoms. Accordingly, we sampled the combined Hartree and electron-ion potential ($V_{\text{Hartree}} + V_{\text{ion}}$, hereafter called $V_{\text{electrostatic}}$) on a sphere with 0.75 Å radius positioned concentric to the O atom of the dissociating CO molecule. We first focus on the differences for the two surfaces before discussing the coverage effects. Figure 7 shows that $V_{\text{electrostatic}}$ increases for all reaction pathways considered during the stretching of the C–O bond. This increase is mainly due to the decreasing electron-ion attraction when the C–O bond is elongated. Notably, there is a very steep increase of the electrostatic potential along the reaction coordinate for the Co(0001) surface, which corresponds to the bending of the CO molecule towards the surface. Comparison of the two cases shows that — as habitually assumed — the energy needed to bend the adsorbed CO molecule makes up a large part of the CO dissociation barrier difference between terrace and stepped surfaces. In the B₅-site on the Co(11 $\bar{2}$ 1) surface, the CO molecule is already pre-activated. After the transition state $V_{\text{electrostatic}}$ becomes more negative for the Co(0001) surface, whereas there is a plateau for the Co(11 $\bar{2}$ 1) surface. Inspection of the C–O bond dissociation pathways shows that the decrease is due to migration of the O atom from two-fold adsorption to the final three-fold adsorption site. The plateau for the Co(11 $\bar{2}$ 1) surface corresponds to the migration of the O atom over the bridge site from one side of the step to the other side before the energy is lowered by movement into the three-fold adsorption site. The final C–O bond distance after dissociation is longer for the Co(11 $\bar{2}$ 1) surface because of the different geometry of the step edge.

Next, we consider the effect of co-adsorbates. The findings above imply that the changes in the electrostatic potential brought about by co-adsorbates should predominantly be the result of variations in the electron-electron repulsion. Figure 4.6 shows that the electron-electron repulsion for CO dissociation on Co(0001) is significantly stronger at a high CO coverage. The corresponding data for Co(11 $\bar{2}$ 1) surprisingly show that the electron-electron

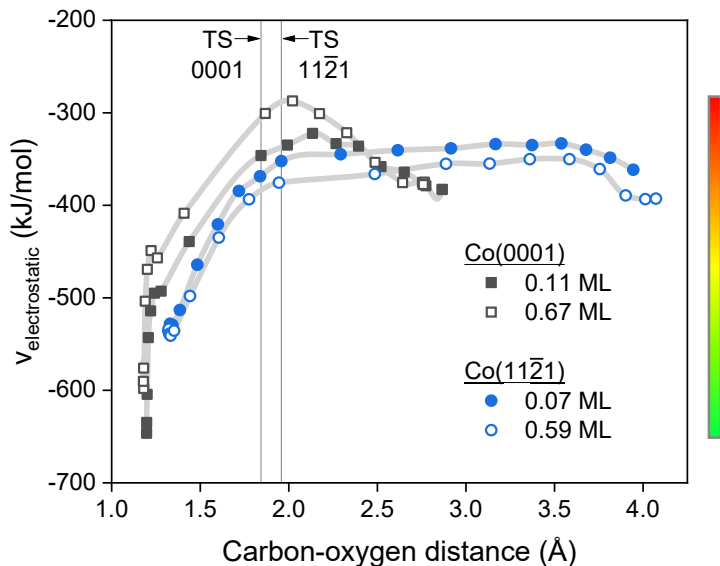


Figure 4.6: The electrostatic potential ($V_{\text{electrostatic}}$, a combination of the electron-ion and the Hartree potential) along the CO dissociation pathway on the Co(11 $\bar{2}$ 1) and Co(0001) surfaces at low and high CO coverage. The electrostatic potential was sampled on a sphere with 0.75 Å radius positioned concentric to the O atom of the dissociating CO molecule. The color bar indicates the range of electrostatic values corresponding to the colors in Figure 4.7c and Figure 4.8c.

repulsion at higher coverage is not increased due to co-adsorbates. These very different trends can well explain why CO bond dissociation is nearly unaffected by CO co-adsorbates at the step-edge site. The configurations of the various states during the dissociation reaction at high coverage are shown in Figure 4.7 and Figure 4.8 for the Co(11 $\bar{2}$ 1) and Co(0001) surfaces respectively. Analyzing the geometries along the reaction pathway, the possibility of CO co-adsorbates to reorient at the step-edge site stands out over the rigid configuration of the adsorbed layer observed for the Co(0001) terrace at high CO coverage. The reorientation of the adsorbed layer at the step-edge site results in nearly similar electrostatic potentials at low and high coverage, both for the initial and the transition state. On Co(0001), this only holds for the final state. The reason is that in this case the oxygen atom obtained by CO dissociation is significantly closer to the surface than the oxygen atoms of the co-adsorbed CO. Another possible effect is that the CO co-adsorbates withdraw electron density from the two cobalt atoms at the top of the step-edge site, resulting in a larger cobalt-cobalt distance. This distance is 2.47 Å at low coverage and increases to 2.58 Å at high coverage, which can explain the reduced energy for the O atom to cross the bridged site.

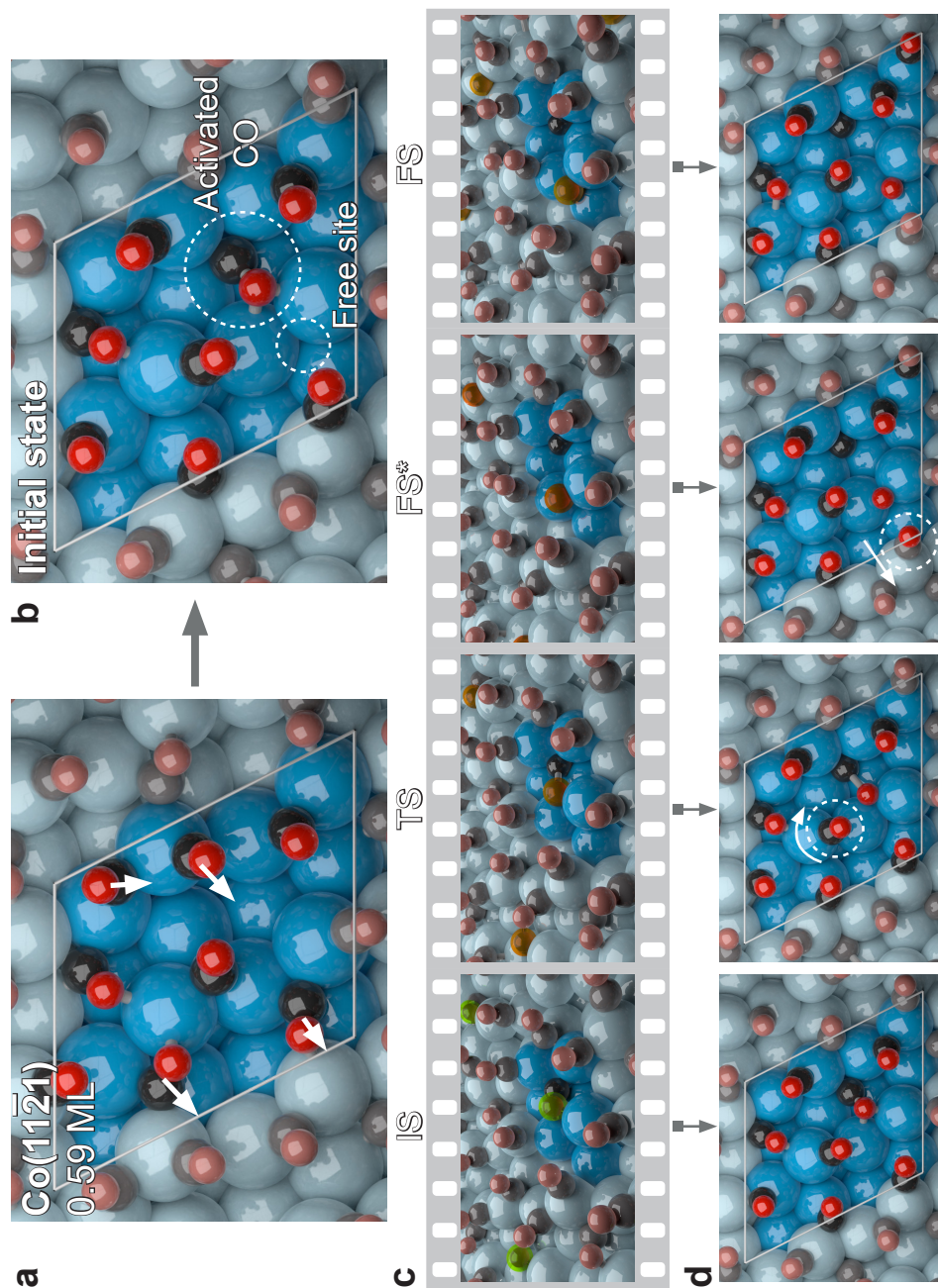


Figure 4.7: Configurations of CO dissociation on Co(111̄21) at 0.59 ML: (a) most stable adsorption configuration at 0.59 ML; (b) local initial state for dissociation of CO; (c) states during the dissociation with the color-coded value of the electrostatic potential on the O atom; (d) top-down view of the same states.

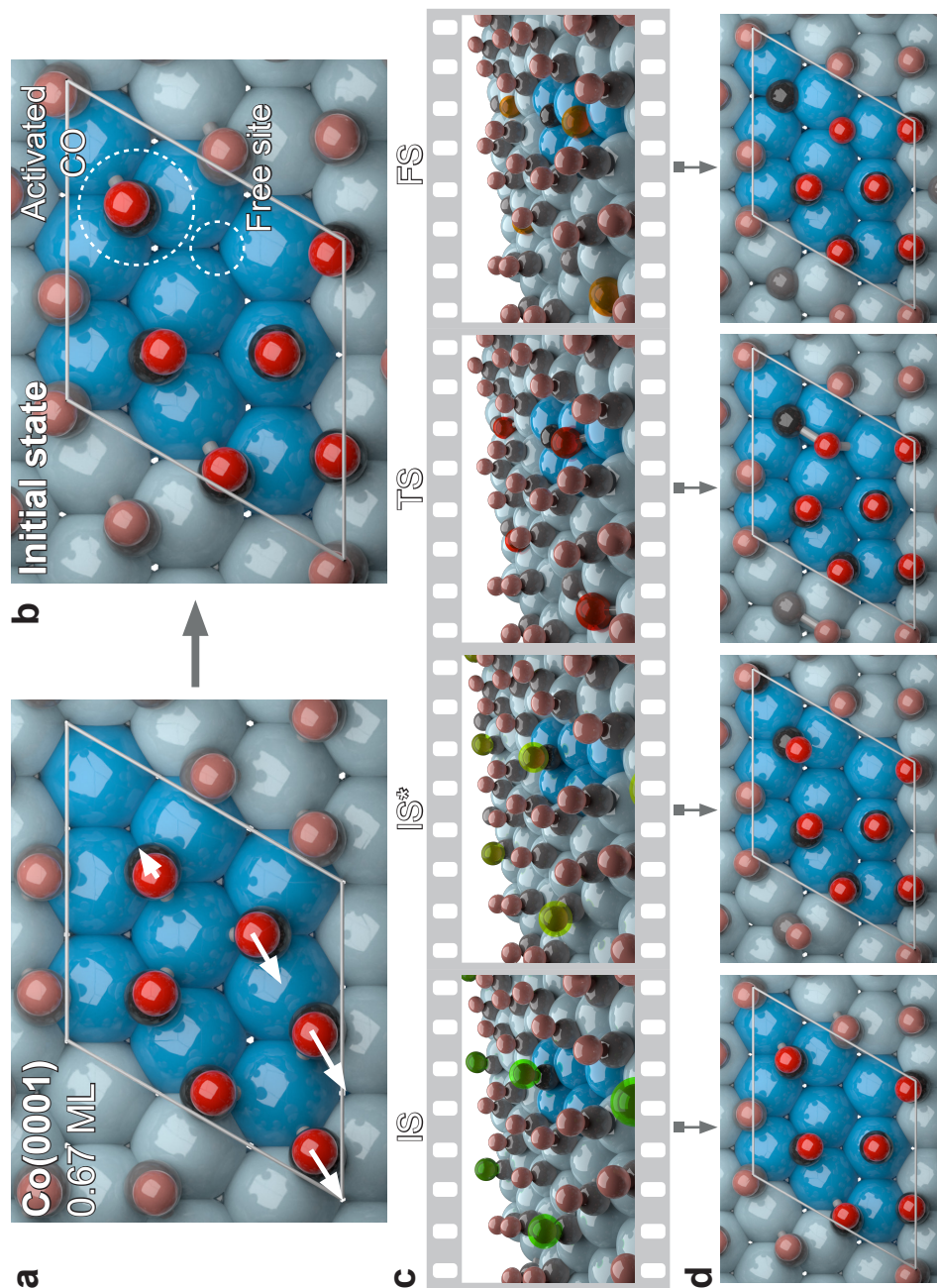


Figure 4.8: Configurations of CO dissociation on Co(0001) at 0.67 ML: (a) most stable adsorption configuration at 0.67 ML; (b) local initial state for dissociation of CO; (c) states during the dissociation with the color-coded value of the electrostatic potential on the O atom; (d) top-down view of the same states.

4.4 Conclusions

DFT-computed reaction barriers show that CH_x formation in FT synthesis likely proceeds through a direct CO scission pathway. The reaction energetics show that this pathway needs step-edge sites and has a high activation barrier on terraces. An important result is that step-edge sites remain highly active for direct CO dissociation at the high CO coverages relevant to practical FT synthesis. To the contrary, the further reduced rate of direct CO scission on terrace sites suggests that the much slower dissociation on those sites will proceed through a hydrogen-assisted pathway. We investigated the electronic structure along the direct CO dissociation pathway on step-edge and terrace cobalt surfaces. We find that the sharing of valence electrons of the cobalt surface atoms involved in binding the C and O atoms is not strongly affected by CO co-adsorbates and, therefore, cannot account for the differences in CO coverage dependence. A detailed analysis of the electronic structure around the dissociating oxygen atom reveals significant differences of the electrostatic potential on the oxygen atom of the dissociating CO molecule between the two surfaces. The higher flexibility of the adsorbed CO layer on the corrugated stepped surface weakens lateral interactions and explains the lower dissociation barrier compared to the terrace surface that has a more rigid CO adsorbed layer.

4.5 References

- [1] G. P. Van Der Laan, A. A. C. M. Beenackers, *Catalysis Reviews* **1999**, *41*, 255–318.
- [2] W. Chen, T. F. Kimpel, Y. Song, F. K. Chiang, B. Zijlstra, R. Pestman, P. Wang, E. J. M. Hensen, *ACS Catalysis* **2018**, *8*, 1580–1590.
- [3] X. Sun, A. I. O. Suarez, M. Meijerink, T. van Deelen, S. Ould-Chikh, J. Zecevic, K. P. de Jong, F. Kapteijn, J. Gascon, *Nature Communications* **2017**, *8*, 1680.
- [4] V. Navarro, M. A. van Spronsen, J. W. Frenken, *Nat Chem* **2016**, *8*, 929–34.
- [5] I. A. Filot, R. A. van Santen, E. J. Hensen, *Angew Chem Int Ed Engl* **2014**, *53*, 12746–12750.
- [6] S. G. Shetty, I. M. Ciobica, E. J. Hensen, R. A. van Santen, *Chem Commun (Camb)* **2011**, *47*, 9822–4.
- [7] W. Chen, I. A. W. Filot, R. Pestman, E. J. M. Hensen, *ACS Catalysis* **2017**, *7*, 8061–8071.
- [8] Z.-P. Liu, P. Hu, *Journal of the American Chemical Society* **2002**, *124*, 11568–11569.
- [9] Q. Ge, M. Neurock, H. A. Wright, N. Srinivasan, *The Journal of Physical Chemistry B* **2002**, *106*, 2826–2829.
- [10] X. Y. Quek, I. A. Filot, R. Pestman, R. A. van Santen, V. Petkov, E. J. Hensen, *Chem Commun (Camb)* **2014**, *50*, 6005–8.
- [11] G. L. Bezemer, J. H. Bitter, H. P. Kuipers, H. Oosterbeek, J. E. Holewijn, X. Xu, F. Kapteijn, A. J. van Dillen, K. P. de Jong, *J Am Chem Soc* **2006**, *128*, 3956–64.

- [12] P. van Helden, I. M. Ciobîcă, R. L. J. Coetzer, *Catalysis Today* **2016**, *261*, 48–59.
- [13] D. A. J. M. Ligthart, I. A. W. Filot, A. A. H. Almutairi, E. J. M. Hensen, *Catalysis Communications* **2016**, *77*, 5–8.
- [14] M. A. Petersen, J. A. van den Berg, I. M. Ciobica, P. van Helden, *ACS Catalysis* **2017**, *7*, 1984–1992.
- [15] J. X. Liu, H. Y. Su, D. P. Sun, B. Y. Zhang, W. X. Li, *J Am Chem Soc* **2013**, *135*, 16284–7.
- [16] I. A. W. Filot, R. A. van Santen, E. J. M. Hensen, *Catal. Sci. Technol.* **2014**, *4*, 3129–3140.
- [17] S. Shetty, A. P. Jansen, R. A. van Santen, *J Am Chem Soc* **2009**, *131*, 12874–5.
- [18] P. van Helden, J.-A. van den Berg, I. M. Ciobîcă, *Catalysis Science & Technology* **2012**, *2*, 491–494.
- [19] M. Ojeda, R. Nabar, A. U. Nilekar, A. Ishikawa, M. Mavrikakis, E. Iglesia, *Journal of Catalysis* **2010**, *272*, 287–297.
- [20] Y.-H. Zhao, J.-X. Liu, H.-Y. Su, K. Sun, W.-X. Li, *ChemCatChem* **2014**, *6*, 1755–1762.
- [21] S. Shetty, R. A. van Santen, *Phys Chem Chem Phys* **2010**, *12*, 6330–2.
- [22] I. A. W. Filot, R. J. P. Broos, J. P. M. van Rijn, G. J. H. A. van Heugten, R. A. van Santen, E. J. M. Hensen, *ACS Catalysis* **2015**, *5*, 5453–5467.
- [23] J.-X. Liu, H.-Y. Su, W.-X. Li, *Catalysis Today* **2013**, *215*, 36–42.
- [24] D. J. Moodley, J. van de Loosdrecht, A. M. Saib, M. J. Overett, A. K. Datye, J. W. Niemantsverdriet, *Applied Catalysis A: General* **2009**, *354*, 102–110.
- [25] K. Fei Tan, J. Xu, J. Chang, A. Borgna, M. Saeys, *Journal of Catalysis* **2010**, *274*, 121–129.
- [26] S. B. Vendelbo, M. Johansson, D. J. Mowbray, M. P. Andersson, F. Abild-Pedersen, J. H. Nielsen, J. K. Norskov, I. Chorkendorff, *Topics in Catalysis* **2010**, *53*, 357–364.
- [27] M. Zhuo, A. Borgna, M. Saeys, *Journal of Catalysis* **2013**, *297*, 217–226.
- [28] B. T. Loveless, C. Buda, M. Neurock, E. Iglesia, *J Am Chem Soc* **2013**, *135*, 6107–21.
- [29] D. Hibbitts, E. Dybeck, T. Lawlor, M. Neurock, E. Iglesia, *Journal of Catalysis* **2016**, *337*, 91–101.
- [30] W. Chen, B. Zijlstra, I. A. W. Filot, R. Pestman, E. J. M. Hensen, *ChemCatChem* **2018**, *10*, 136–140.
- [31] J. Liu, D. Hibbitts, E. Iglesia, *J Am Chem Soc* **2017**, *139*, 11789–11802.
- [32] D. D. Hibbitts, B. T. Loveless, M. Neurock, E. Iglesia, *Angew Chem Int Ed Engl* **2013**, *52*, 12273–8.

- [33] H. Niemantsverdriet, P. van Helden, E. Hensen, D. Lennon, K. Holt, G. Hutchings, M. Bowker, R. Catlow, M. Shoji, L. Jewell, M. Claeys, J. Hayward, N. Coville, N. Fischer, A. Roldan, E. Redekop, T. Gambu, L. Deeplal, T. P. O. Mkhwanazi, K. J. Weststrate, D. Bahnemann, M. Neurock, H. Schulz, D. Ma, S. Kondrat, P. Collier, A. K. Gupta, A. Corma, P. Akomeah, E. Iglesia, E. van Steen, N. de Leeuw, M. Wolf, T. van Heerden, *Faraday Discuss* **2017**, *197*, 165–205.
- [34] H.-Y. Su, Y. Zhao, J.-X. Liu, K. Sun, W.-X. Li, *Catalysis Science & Technology* **2017**, *7*, 2967–2977.
- [35] P. E. Blochl, *Phys Rev B Condens Matter* **1994**, *50*, 17953–17979.
- [36] G. Kresse, J. Hafner, *Physical Review B* **1993**, *47*, 558–561.
- [37] G. Kresse, J. Hafner, *Physical Review B* **1994**, *49*, 14251–14269.
- [38] G. Kresse, J. Furthmüller, *Computational Materials Science* **1996**, *6*, 15–50.
- [39] G. Kresse, J. Furthmüller, *Physical Review B* **1996**, *54*, 11169–11186.
- [40] J. P. Perdew, K. Burke, M. Ernzerhof, *Physical Review Letters* **1996**, *77*, 3865–3868.
- [41] H. J. Monkhorst, J. D. Pack, *Physical Review B* **1976**, *13*, 5188–5192.
- [42] G. Mills, H. Jónsson, G. K. Schenter, *Surface Science* **1995**, *324*, 305–337.
- [43] G. Henkelman, B. P. Uberuaga, H. Jónsson, *Journal of Chemical Physics* **2000**, *113*, 9901–9904.
- [44] G. Henkelman, H. Jónsson, *The Journal of Chemical Physics* **2000**, *113*, 9978–9985.
- [45] K. Atkinson, W. Han in *Spherical Harmonics and Approximations on the Unit Sphere: An Introduction*. Lecture Notes in Mathematics, vol 2044. Springer Berlin Heidelberg, Berlin, Heidelberg, **2012**, Chapter Numerical Quadrature, pp. 165–210.
- [46] R. Van Hardeveld, F. Hartog, *Surface Science* **1969**, *15*, 189–230.
- [47] Y. Qi, J. Yang, X. Duan, Y.-A. Zhu, D. Chen, A. Holmen, *Catalysis Science & Technology* **2014**, *4*, 3534–3543.
- [48] T. A. Manz, *Rsc Advances* **2017**, *7*, 45552–45581.

Appendix A

Table A1: Zero-point-energy corrected adsorption energy for CO and reaction barriers for direct CO dissociation on the stepped (1 x 2) Co(1 $\bar{1}$ 05) surface. Forward barriers are referenced to the most stable adsorption configuration. Backward barriers are referenced to the co-adsorbed state of C and O after dissociation.

Elementary reaction	Forward Eact (kJ/mol)	Backward Eact (kJ/mol)
CO + * \rightleftharpoons CO* (Figure A1a)	-	175
CO* + * \rightleftharpoons C* + O* (Figure A1b)	144	133
CO* + * \rightleftharpoons C* + O* (Figure A1c)	152	134
CO* + * \rightleftharpoons C* + O* (Figure A1d)	151	56

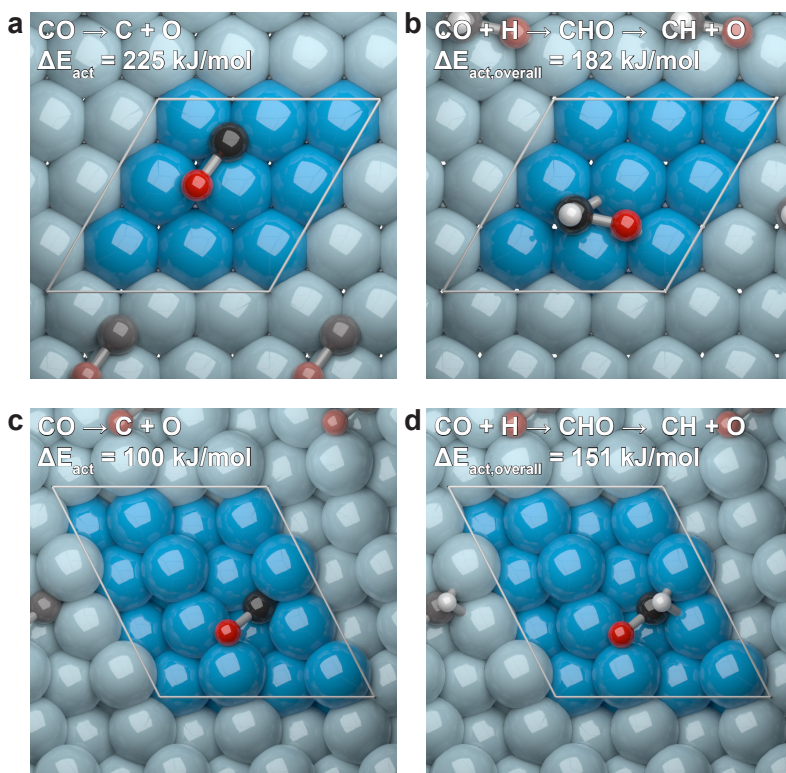


Figure A1: Configurations of initial and transition states on the stepped (1 x 2) Co(1 $\bar{1}$ 05) surface. (a) Most stable adsorption mode of CO. (b) Transition state for direct CO dissociation with the oxygen going up the step. (c) Transition state for direct CO dissociation with the oxygen going down the step. (d) Transition state for direct CO dissociation on the other B₅ step-edge site. For clarity the cell has been translated along its length by half a unit vector.

CHAPTER 5

FIRST-PRINCIPLES BASED MICROKINETIC MODELING OF TRANSIENT KINETICS OF CO HYDROGENATION ON COBALT CATALYSTS

Contents

5.1	Introduction	86
5.2	Computational methods	88
5.3	Results and discussion	91
5.3.1	Elementary reaction step barriers for carbon and oxygen removal	91
5.3.2	Steady-state methanation	92
5.3.3	Chemical and isotopic transients of methanation	95
5.3.4	CO scrambling	99
5.4	Conclusions	100
5.5	References	101
	Appendix B	105

Abstract

Computational efforts towards a fundamental understanding of the underlying mechanistic pathways in synthesis gas conversion processes such as Fischer-Tropsch synthesis are exemplary for the developments in heterogeneous catalysis. Advances in transient kinetic analysis methods contribute to unraveling complex reaction pathways over nanoparticle surfaces. Tracing the activity and selectivity of Fischer-Tropsch catalysts to the individual events occurring at the active site remains difficult with experimental techniques. Here we provide simulations of transient kinetics at the scale of the active site by making use of the reaction energetics for CO hydrogenation to methane on stepped and terrace cobalt

surfaces that are suitable models for cobalt FT nanoparticle catalysts. We investigate the hydrogen-deuterium kinetic isotope effect and simulate common steady-state and chemical isotopic transients. Comparison to experimental literature leads to important mechanistic insights. Direct CO dissociation is the main pathway for breaking the C–O bond and it occurs exclusively on step-edge sites. While the experimentally observed hydrogen-deuterium kinetic isotopic effect is often used as evidence for H-assisted CO dissociation, we show that hydrogenation of C and O as partly rate-controlling steps provides an alternative explanation. The simulations of the chemical transients provide significant insight into the importance of the changing surface coverages that strongly affect the reaction rate. The reversibility of CO dissociation on cobalt step-edges is evident from simulations of $^{12}\text{C}^{16}\text{O}/^{13}\text{C}^{18}\text{O}$ scrambling being in good agreement with experimental data.

5.1 Introduction

Gas-to-liquid processes like Fischer-Tropsch (FT) synthesis comprise alternative pathways from carbonaceous feedstock towards clean fuels and chemicals [1, 2]. Considerable efforts have already been made to gain a deep understanding of the operation of relevant catalysts for the hydrogenation of carbon monoxide. While from the practical side catalysts are optimized with respect to mass and heat transport [3], catalyst attrition [4], and catalyst deactivation at high conversion [5], the focus at the fundamental level is on resolving the complex chemo-kinetic mechanism that occurs at the surface of supported metal nanoparticle catalysts.

The FT reaction is a chain reaction involving CH_x species as monomers. Unique initiation, propagation and termination rates lead to varying hydrocarbon product distributions on cobalt [6], ruthenium [7], and iron carbides [8]. For cobalt and ruthenium based catalysts, the initiation and propagation steps that give rise to the formation of long-chain hydrocarbons are usually assumed to proceed via the carbide mechanism [9–12], i.e. the carbon-oxygen bond is broken prior to carbon-carbon coupling. However, the exact bond breaking mechanism remains heavily debated. The high activity of step-edge sites towards direct scission of π -bonds is widely accepted [13–18], but the availability of such sites under CO hydrogenation conditions has been called into question due to carbon deposition [19–21] and lateral interactions [22–24]. Accordingly, hydrogen-assisted CO scission is often proposed as the dominant pathway in FT synthesis [17, 25–27].

Chapter 4 of this thesis has demonstrated using density functional theory (DFT) calculations that a direct CO scission pathway requires step-edge sites. An important finding is that these step-edge sites remain highly active at a typical CO coverage encountered under practical FT synthesis. Thus, hydrogen is not directly required for CO dissociation. Rather, carbon and oxygen removal steps could explain the empirically observed hydrogen partial pressure dependency of CO hydrogenation rates [28].

Chemical and isotopic transient kinetic experiments provide a powerful means to compare such mechanistic proposals [29–31]. Biloen and Sachtler [9] investigated surface intermediates with steady-state isotopic transient kinetic analysis (SSITKA) to develop their arguments

in favor of the carbide mechanism. To the contrary, Kruse and coworkers proposed the importance of oxygenated intermediates to interpret chemical transient kinetic analysis (CTKA) measurements and emphasized CO insertion as the main growth mechanism [32, 33]. The groups of Holmen and De Jong used these methods to determine CO coverages and found that CO residence times appeared independent of size for cobalt particles larger than 6 nm [34–37]. Although these results indicate a reduced FT activity below 6 nm, the precise mechanism of chain growth on optimum particles remains a topic of controversy. Further insight can for instance be obtained through isotopic substitution of hydrogen with deuterium to determine kinetic isotope effects (KIE) [38]. A strong KIE in experiments using H₂ (r_H) and D₂ (r_D) can indicate a strong involvement of hydrogen in the controlling reaction steps of the mechanism. Inverse KIE ratios of r_H/r_D in the range of 0.7-0.8 have been associated with H-assisted CO dissociation routes [39, 40]. However, such conclusions usually hinge on assumed rate-controlling steps, specifically CO dissociation in the work of the Holmen group. Hydrogen is also needed for termination of hydrocarbon species and removal of oxygen as water. Any rate control in these steps will therefore also influence the measured KIE ratios, regardless of the CO activation pathway. Unfortunately, experimental observations are usually a convolution of parallel pathways on different active sites. As such, direct deduction of the degree of rate control from experimental data is challenging [41, 42]. Nevertheless, substantial efforts have been made to obtain this kind of information, predominantly by correlating predictions from microkinetics simulations to experimental data [43–51]. The consensus of these works is that catalytic activity is difficult to generalize using idealized models of isolated surface sites. More realistic descriptions of FT kinetics require a multi-site model that allows multiple reaction pathways. A specialized computer code developed for dealing with the complexity of SSITKA experiments has also been described in the literature as a realistic model leads to many options for isotopic compositions [52]. A salient result from the latter study is that the transient modeling results suggest a similar reaction mechanism over FCC and HCP cobalt with mainly differences in the number of active sites.

This chapter reports on the development of a microkinetic model to complement experimental transient studies of CO hydrogenation. The microkinetics simulations utilize a continuous stirred-tank reactor (CSTR) model to allow a changing gas-phase composition over time and all intermediates are explicitly labeled to follow isotopic changes. In this study all relevant elementary reaction steps are included from synthesis gas as a feedstock to methane, water, and carbon dioxide products. The reaction constants are computed from differences in energies and configurations of the reaction intermediates and transition states determined by DFT. The mechanistic trends in this study were found to be insensitive to both the site ratio and to the reaction barrier for migration between the different sites. Migration reactions between these sites are included to explain the results of site blocking experiments [53, 54]. Simulated steady-state methanation with hydrogen and deuterium predicts KIE ratios close to the experimental values and point to step-edges as the active site for CO dissociation. Simulated isotopic and chemical transients then show the relevance of coverage effects, further unraveling the initiation pathway in FT synthesis over cobalt nanoparticles.

5.2 Computational methods

All quantum-chemical calculations were performed using a plane-wave density functional theory approach with the projector-augmented wave (PAW) method [55], as implemented in the Vienna ab initio simulation package (VASP) [56–59]. For exchange-correlation, the Perdew-Burke-Ernzerhof (PBE) functional was used [60]. The plane-wave basis set was limited to a 400 eV kinetic energy cut-off base. A gamma-centered Monkhorst-Pack $21 \times 21 \times 21$ k-point mesh [61] was used for bulk HCP Co, and a $5 \times 5 \times 1$ k-point mesh for Co surface slabs. Calculations for molecular references in the gas phase only employed the gamma point in a $10 \times 10 \times 10 \text{ \AA}^3$ cell. We used Co(0001) and Co(11 $\bar{2}$ 1) as model surfaces for the terrace sites and step-edges on cobalt nanoparticles. These surfaces were chosen as Co(0001) is often used in experimental surface science studies [62, 63] and the Co(11 $\bar{2}$ 1) surface exposes step-edge sites that are highly active for CO dissociation [15]. The particular configuration of atoms in the Co(11 $\bar{2}$ 1) step-edge site is a perturbed arrangement of the classical B₅-site as referred to by Van Hardeveld and Hartog [13]. With a barrier of 100 kJ/mol for direct CO dissociation this site is more active than e.g. the FCC Co(311) facet at ~ 150 kJ/mol [15]. If these sites are formed by surface reconstruction under FT conditions [64], it is likely that they contribute significantly to both FT activity and selectivity. The Co lattice parameters for our calculations correspond to 2.49 Å, 2.49 Å and 4.03 Å for the *a*, *b* and *c* directions respectively. The Co(0001) surface was constructed from a (3 x 3) unit cell with 5 atomic layers, which corresponds to 45 Co atoms per unit cell. The Co(11 $\bar{2}$ 1) surface was constructed from a (2 x 2) unit cell with 3 atomic layers (48 Co atoms per unit cell). All reactions were performed in the low coverage limit. Adsorbates on the Co(0001) surface slab were placed with mirror symmetry in the *ab*-plane to avoid spurious dipole-dipole interactions between neighboring unit cells. For the Co(11 $\bar{2}$ 1) surface slab the adsorbates were placed using inversion symmetry. All atomic positions were optimized using the conjugate-gradient technique. We explored reaction paths with the climbing image nudged elastic band (cNEB) implementation [65–67]. The transition states (TS) were optimized using a quasi-Newton algorithm and were confirmed by the saddle points obtained from frequency calculations. The Hessian matrices were calculated with the finite displacement technique. The corresponding vibrations were also used to compute the zero point energy (ZPE) corrections and vibrational partition functions for all adsorbed species and transition states. The effect of deuterium substitution on elementary reaction steps was included by re-calculating all ZPE corrections and partition functions after changing the atomic mass of hydrogen in the Hessian matrix from one to two. We neglected the much smaller effect of using ¹³C and ¹⁸O isotopes on the ZPE.

The microkinetics simulations were carried out using the in-house developed MKMCXX code [68, 69], which has been extensively employed in previous works to investigate CO hydrogenation on rhodium and ruthenium surfaces in the zero conversion limit [68, 70, 71]. In this work, we implemented these simulations in an isobaric and isothermal CSTR model assuming that the gases behave ideally. Gas-phase concentrations C_i were determined according to Eq. (5.1), where r_i is the production or consumption of species *i* on a single

active site.

$$V \frac{dC_i}{dt} = F_i^{\text{in}} - F_i^{\text{out}} + N_{\text{sites}} \times r_i \quad (5.1)$$

The flow rates F_i^{in} at the reactor entrance were chosen to obtain a residence time of 1 s at differential conditions. The reactor was operated at isobaric conditions. We varied the number of active sites N_{sites} such that a CO conversion of ca. 10% was achieved at each temperature. This conversion was chosen to allow for comparison to experimental kinetic data for cobalt determined under differential conditions [43, 44]. A sensitivity analysis of the microkinetic model to changes in the CO conversion can be found in Appendix B. We assumed non-activated adsorption and used the Hertz-Knudsen equation [72] to describe the forward rate constant of adsorption (Eq. (5.2)).

$$k_{\text{ads}} = \frac{PA}{\sqrt{2\pi mk_{\text{B}}T}} \quad (5.2)$$

The surface area A was set to 5.38 \AA^2 , the area of a (1 x 1) unit cell of Co(0001). A dimensionless gas activity $a_{\text{gas}} = \frac{P}{P^\ominus}$ was used in which P^\ominus is a reference pressure of 1 atm upon calculating the adsorption rate with Eq. (5.3).

$$r_{\text{ads}}^{\text{surf}} = \frac{N_{\text{surf}}}{N_{\text{total}}} \times \left(\theta_{\text{*}}^{\text{surf}}\right)^n \times a_{\text{gas}} \times k_{\text{ads}}^{\text{surf}} \quad (5.3)$$

Here $r_{\text{ads}}^{\text{surf}}$ reflects the rate of adsorption on a particular surface site with abundance $\frac{N_{\text{surf}}}{N_{\text{total}}}$, $\theta_{\text{*}}^{\text{surf}}$ is the fractional amount of free sites and n is one for associative and two for dissociative adsorption. The underlying assumption for this adsorption rate is that the adsorbing molecule loses one translational degree of freedom when going from the gas phase to the transition state for adsorption. Following the concept of microscopic reversibility, the rate constant for desorption can be approximated from the enthalpy of desorption and the entropy gain of two translational degrees of freedom and all rotational degrees of freedom. For the enthalpy of adsorption we used the zero point energy corrected adsorption heat as computed by DFT. We applied a correction for the over-binding of CO, which is a known issue with DFT [73–75]. Adsorption energies were chosen such that enthalpy changes of methanation and water-gas shift reactions correspond to tabulated data at 298.15 K [76]. For this purpose, we corrected the adsorption energies (ΔH_{ads}) of CO and CO₂ by +22.72 kJ/mol and -17.88 kJ/mol, respectively ($\Delta H_{\text{ads}}^{\text{corr}}$). The desorption rate constant and desorption rate are then described by Eq. (5.4) and Eq. (5.5).

$$k_{\text{des}} = \frac{k_{\text{ads}}}{K_{\text{eq}}} = \frac{PA}{\sqrt{2\pi mk_{\text{B}}T}} \frac{\exp\left(\frac{S_{\text{gas}}}{R}\right)}{q_{\text{vib,ads}}} \exp\left(\frac{\Delta H_{\text{ads}}^{\text{corr}} - H_{\text{gas}}^{298.15 \rightarrow T} + E_{\text{lat}}}{RT}\right) \quad (5.4)$$

$$r_{\text{des}}^{\text{surf}} = \frac{N_{\text{surf}}}{N_{\text{total}}} \times \left(\theta_{\text{ads}}^{\text{surf}}\right)^n \times k_{\text{des}}^{\text{surf}} \quad (5.5)$$

As entropy is especially important for predicting accurate adsorption and desorption rates, we incorporated gas-phase entropies S_{gas} from thermodynamic tables [77], and also included temperature corrections for the enthalpy $H_{\text{gas}}^{298.15 \rightarrow T}$ using the Shomate equation [78]. The

$q_{\text{vib,ads}}$ term was introduced because not all gas-phase entropy is lost in the adsorption step. Vibrational entropy in the adsorbed state remains in the form of bond vibrations and hindered translational and rotational motion. A further correction (E_{lat}) was added to the rate of desorption to take into account the lateral interactions as discussed in Chapter 3. In short, the correction applied here reflects the qualitative effect of lateral interactions on the differential adsorption energies. The most important aspect is that the adsorption energy is relatively constant at low coverage and that the lateral repulsion increases steeply at high coverage. The overall thermodynamics of the microkinetic model are preserved by defining a lateral correction on a per-atom basis with the penalty of species x corresponding to Eq. (5.6) and Eq. (5.7).

$$E_x^{\text{lat}} = E_x^{\theta=1} \times \frac{(101^{\theta_{\text{lat}}} - 1)}{100} \quad (5.6)$$

$$\theta_{\text{lat}} = \frac{(\theta_{\text{total}} - \theta_* - 0.5 \cdot \theta_{\text{H}}) - \theta_{\text{LB}}}{\theta_{\text{UB}} - \theta_{\text{LB}}} \quad \text{with } \theta_{\text{lat}} \geq 0 \quad (5.7)$$

We used lateral interaction parameters of $E_{\text{C}}^{\theta=1} = E_{\text{O}}^{\theta=1} = 4 \times E_{\text{H}}^{\theta=1} = 60 \text{ kJ/mol}$, $\theta_{\text{LB}} = 0.25 \text{ ML}$, and $\theta_{\text{UB}} = 0.75 \text{ ML}$. These parameters prevent CO coverages in our simulations that are physically unrealistic, e.g. coverages above 0.6 ML at 240 °C. We assumed that all surface species contribute equally to the lateral interaction potential with the exception of hydrogen. We considered that treating hydrogen equally would overestimate the lateral repulsion considering its relatively small size. However, totally removing its contribution is likely an underestimation. Therefore, we subtract from the total coverage the fraction of empty sites and half of the hydrogen coverage. A sensitivity analysis of this parameter (Appendix B) shows that the model trends do not change with respect to this choice.

The rate constants of the elementary surface reactions were determined using the Eyring equation, which is shown in Eq. (5.8).

$$k_{\text{surf}} = \frac{k_{\text{B}}T}{h} \frac{Q^\ddagger}{Q} \exp\left(\frac{-\Delta E_{\text{act}}^{\text{zpe}}}{k_{\text{B}}T}\right) \quad (5.8)$$

The $\Delta E_{\text{act}}^{\text{zpe}}$ term reflects the ZPE corrected enthalpy difference between the transition state and the initial or final state. Entropic contributions to the rate constants are included in the $\frac{Q^\ddagger}{Q}$ term. These ratios are available in the Appendix B and were calculated according to Eq. (5.9), where ε_i is the i -th eigenvalue of the Hessian.

$$Q = \prod_i \frac{1}{1 - \exp\left(\frac{-\varepsilon_i}{k_{\text{B}}T}\right)} \quad (5.9)$$

Eq. (10) is then used to compute reaction rates based on θ_i as the coverage of species i and ν_i as the stoichiometric coefficient of species i .

$$r_{\text{surf}} = k_{\text{surf}} \prod_i \theta_i^{\nu_i, \text{surf}} \quad (5.10)$$

The ordinary differential equations for each surface component are then defined by Eq.

(5.11).

$$\frac{d\theta_i}{dt} = \sum_j v_{i,j} r_j \quad (5.11)$$

The complex surface of cobalt nanoparticles is approximated by a mean field of terrace and step-edge sites in a 10:1 ratio. This site ratio is a conservative estimate of the abundance of step-edge sites on FCC cobalt nanoparticles of 6-8 nm [79]. As actual site compositions might differ we performed a sensitivity analysis of this parameter, which can be found in Appendix B.

5.3 Results and discussion

Constructing a microkinetic model of the methanation reaction entails computing the activation barriers for CO bond dissociation, oxygen removal, and carbon hydrogenation. In Chapter 4 we discussed direct and hydrogen assisted CO dissociation pathways. Here, we present the carbon and oxygen removal pathways leading to CH₄, H₂O, and CO₂. We discuss the microkinetic modeling results of steady state methanation using both hydrogen- and deuterium-based syngas and describe transient results obtained from simulating SSITKA and CTKA switches. Finally, we show the findings from simulated CO scrambling experiments.

5.3.1 Elementary reaction step barriers for carbon and oxygen removal

We first investigated the reaction energetics of the methanation reaction (excluding CO bond dissociation) on the two cobalt surfaces by DFT calculations. The transition states relevant to CH₄, H₂O, and CO₂ formation are depicted in Figure 5.1. The corresponding (zero-point energy corrected) forward and backward activation barriers are listed in Table 5.1. CH₄ is formed by hydrogenation of CH_x intermediates formed after CO bond dissociation. Of these, the final hydrogenation step of the CH₃ intermediate has the highest barrier with a value of 101 kJ/mol on the terrace Co(0001) surface and a value of 76 kJ/mol on the stepped Co(11 $\bar{2}$ 1) surface. Most of the hydrogenation reactions are endothermic, so the overall barrier for CH₄ formation will be determined by the energy of the transition state for the final hydrogenation step relative to the energy of C and H. On the stepped surface both the final transition state and the initial adsorbed C are more stable. This results in similar overall barriers on both surfaces. These overall barriers from C to CH₄ are 119 kJ/mol and 120 kJ/mol for the Co(0001) and Co(11 $\bar{2}$ 1) surfaces respectively. O atoms are removed as water or carbon dioxide. H₂O is formed by sequential hydrogenation of O to H₂O, having overall barriers of 175 kJ/mol on Co(0001) and 135 kJ/mol on Co(11 $\bar{2}$ 1), respectively. We also considered the OH+OH proton shuffling reaction, which has lower overall barriers of 157 kJ/mol and 101 kJ/mol for the Co(0001) and Co(11 $\bar{2}$ 1) surfaces respectively. CO₂ can be formed by oxidation of adsorbed CO with an O adsorbate. With barriers of 137 kJ/mol and 127 kJ/mol, this step is easier than sequential hydrogenation of oxygen, but not as favorable as proton shuffling on the step-edge site. Rate control of one of these removal pathways is likely, given that the overall barriers are higher than the

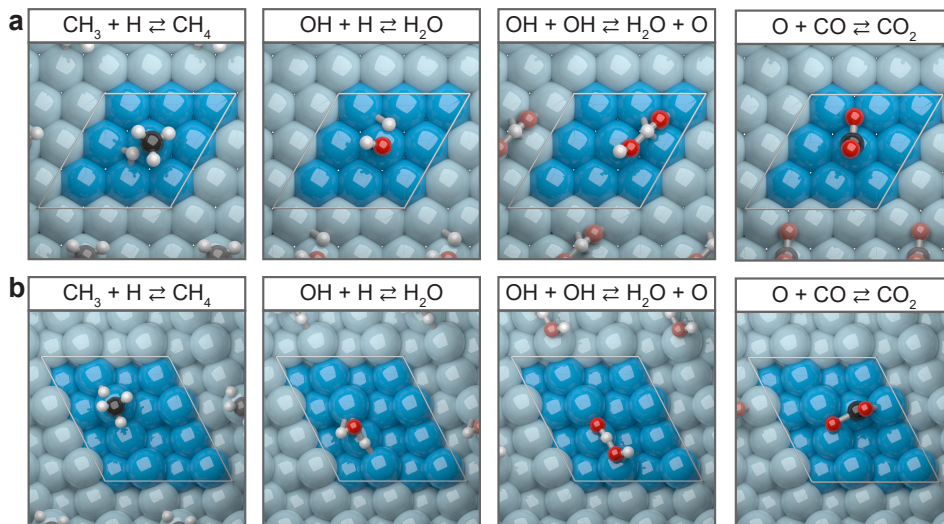


Figure 5.1: Configurations of the transition states for CH_4 , H_2O , and CO_2 formation on (a) the terrace (3×3) $\text{Co}(0001)$ surface and (b) the stepped (2×2) $\text{Co}(11\bar{2}1)$ surface.

100 kJ/mol barrier found for direct CO dissociation. The exact contributions will depend strongly on the surface coverages of the intermediates.

The barriers for the desorption of the CH_4 , H_2O , and CO_2 products are given in Table 5.2, in which we also provide the desorption barriers for reactants CO and H_2 . Important to note here is that we corrected the desorption barriers of CO and CO_2 by -22.72 kJ/mol and $+17.88$ kJ/mol, respectively. This corrects for over-binding of CO and ensures that the total methanation and water-gas-shift reaction heats correspond to tabulated data.

5.3.2 Steady-state methanation

Figure 5.2 shows the results of microkinetics simulations of steady-state CO hydrogenation under methanation conditions. The reaction temperature was varied between 220 °C and 260 °C, while the pressures of CO and H_2 were set to 45 mbar and 450 mbar, respectively. These conditions were chosen, because they were also used in an isotopic transient kinetic study on a Co/SiO_2 catalyst [44]. In the modeling, we ignored the formation of higher hydrocarbons through C–C bond formation. This assumption is reasonable for the relatively high H_2/CO ratios employed in these simulations. We used a two-site model composed of step-edge and terrace sites present in a 1:10 ratio and further assumed that migration between the surfaces was fast (20 kJ/mol barriers from terraces to step-edges). The site ratio is a conservative estimate of the abundance of step-edge sites at optimum particles [79]. In practice, this ratio will depend strongly on the nanoparticle size, support, and the way the cobalt nanoparticle catalyst is prepared and activated. Moreover, real nanoparticles will expose a wider range of surface topologies than considered here with different reactivities. Turnover frequencies (TOF) vary between ~ 0.2 s^{-1} and ~ 2 s^{-1} in the explored temperature

Table 5.1: Elementary reaction step barriers for carbon and oxygen removal on Co(0001) and Co(11 $\bar{2}$ 1). All barriers are corrected for the zero point energy and are referenced to the most stable surface intermediates. Enthalpic desorption barriers for species involved in the methanation of synthesis gas on Co(0001) and Co(11 $\bar{2}$ 1). All barriers are corrected for the zero point energy.

Elementary reaction	Co(0001)		Co(11 $\bar{2}$ 1)	
	E_{act} forward (kJ/mol)	E_{act} backward (kJ/mol)	E_{act} forward (kJ/mol)	E_{act} backward (kJ/mol)
$\text{C}^* + \text{H}^* \rightleftharpoons \text{CH}^* + *$	71	90	65	44
$\text{CH}^* + \text{H}^* \rightleftharpoons \text{CH}_2^* + *$	52	14	47	26
$\text{CH}_2^* + \text{H}^* \rightleftharpoons \text{CH}_3^* + *$	51	52	41	38
$\text{CH}_3^* + \text{H}^* \rightleftharpoons \text{CH}_4^* + *$	101	83	76	61
$\text{O}^* + \text{H}^* \rightleftharpoons \text{OH}^* + *$	121	85	89	77
$\text{OH}^* + \text{H}^* \rightleftharpoons \text{H}_2\text{O}^* + *$	139	72	123	55
$\text{OH}^* + \text{OH}^* \rightleftharpoons \text{H}_2\text{O}^* + \text{O}^*$	47	17	49	-7
$\text{O}^* + \text{CO}^* \rightleftharpoons \text{CO}_2^* + *$	137	30	127	84

Table 5.2: Elementary reaction step barriers for carbon and oxygen removal on Co(0001) and Co(11 $\bar{2}$ 1). All barriers are corrected for the zero point energy and are referenced to the most stable surface intermediates. Enthalpic desorption barriers for species involved in the methanation of synthesis gas on Co(0001) and Co(11 $\bar{2}$ 1). All barriers are corrected for the zero point energy.

Elementary reaction	Co(0001)	Co(11 $\bar{2}$ 1)
	Desorption barrier (kJ/mol)	Desorption barrier (kJ/mol)
$\text{CO} + * \rightleftharpoons \text{CO}^*$	142	148
$\text{H}_2 + 2* \rightleftharpoons 2\text{H}^*$	99	85
$\text{CH}_4 + * \rightleftharpoons \text{CH}_4^*$	2	6
$\text{H}_2\text{O} + * \rightleftharpoons \text{H}_2\text{O}^*$	24	53
$\text{CO}_2 + * \rightleftharpoons \text{CO}_2^*$	22	112

range. These TOFs are an order of magnitude higher than experimentally observed rates [34, 44], likely because only a fraction of all surface sites on real nanoparticles are active in FT synthesis. We find higher steady-state CO coverages on the stepped surface than on the terrace surface, while the reverse holds for the H coverage. Given the abundance of terrace sites, we find that the predicted CO coverage of 0.32 ML compares well with the CO coverage of 0.25 ML as determined by an experimental SSITKA study for Co/SiO₂ under the same reaction conditions [44]. The CH_x coverage at the step-edge sites is 20%, which renders an overall CH_x coverage of about 2%, comparing favorably with the CH_x coverage of 5% as experimentally determined. These results are also in correspondence with experimental results at a lower temperature of 210 °C that predict a CO coverage around 0.4 ML and a CH_x coverage of 5-10% [34]. The H coverages around 0.2 ML on step-edge sites and 0.6 ML on terrace sites correspond well with microkinetic results of FCC cobalt [48]. Under the given conditions, the simulations predict that oxygen derived from CO

dissociation is predominantly removed in the form of water. The CO₂ selectivity is very low (in the 0.1-0.3% range).

Analysis of the reaction network shows that the main reaction channel for CO conversion involves direct C–O bond dissociation on step-edge sites. A degree of rate control (DRC) analysis identifies CO dissociation as the dominant rate-controlling step, especially at low temperature. The other rate-controlling steps are the final hydrogenation step of CH₃ to CH₄ on both step-edge and terrace sites and the first hydrogenation step of atomic oxygen to OH on the step-edge sites. The DRC values of these hydrogenation steps become more rate-controlling at higher temperature. Apparent activation energies for methane formation are in the range of 90-110 kJ/mol. These results are qualitatively in good agreement with the experimental kinetic studies of Chen et al. [43, 44]. These authors contended that hydrogenation reactions significantly control the reaction rate at 260 °C, while the rate is increasingly controlled by CO dissociation with decreasing reaction temperature. This is mainly due to the lower availability of free sites with decreasing temperature. These vacancies are needed for CO dissociation. Our simulations show that CO bond dissociation and O removal as water occur on step-edge sites, while methane is formed both on step-edge and terrace sites. Careful inspection of the individual reactions in the mechanism shows that methane formation on terrace sites is due to migration of CH₃ from step-edge to terrace sites. The migration of C, CH and CH₂ is not observed, likely because these intermediates bind much stronger to the surface. The contribution of terrace sites to the formation of methane increases with reaction temperature, indicating increased rates of migration. Modeling results on FCC cobalt also show high rates of migration and indicate that the migrated CH_x species might also be involved in coupling reactions [48].

We also investigated the KIE of CO hydrogenation by replacing hydrogen with deuterium in the feed. A KIE of unity means that $r_H = r_D$, while deviations from unity are caused by kinetically relevant steps in which making or breaking of bonds with H are involved. Usually, KIE are more pronounced (deviate more from unity) at lower temperature. For a reaction involving hydrogen both normal KIE ($r_H > r_D$) and inverse KIE ($r_H/r_D < 1$) can be observed. In our simulations, an inverse KIE was computed with values between 0.8 and 0.9, close to the values found in experimental literature [38, 40]. Note that in our simulations the effect of a lower methane selectivity with decreasing temperature (due to a higher chain-growth probability) is not included. In the experimental literature, the occurrence of an inverse KIE has led to contradictory conclusions. While earlier works on ruthenium [80] and rhodium [81] assumed a direct CO dissociation mechanism, more recent works on cobalt infer that CO dissociation occurs in an H-assisted manner [39, 40]. From our simulations, we conclude that also for cobalt the inverse KIE can best be explained by rate-controlling hydrogenation reactions in addition to (direct) CO dissociation. As follows from Figure 5.2a, the amount of free sites increases after replacing hydrogen with deuterium. As CO dissociation substantially controls the reaction rate, an increase in free sites also increases the rate of CO dissociation and therefore the overall reaction rate. Accordingly, the KIE towards methane is proportional to the increase in the amount of free sites with a deuterium-containing feed. This can also explain the apparent inverse KIE with respect to

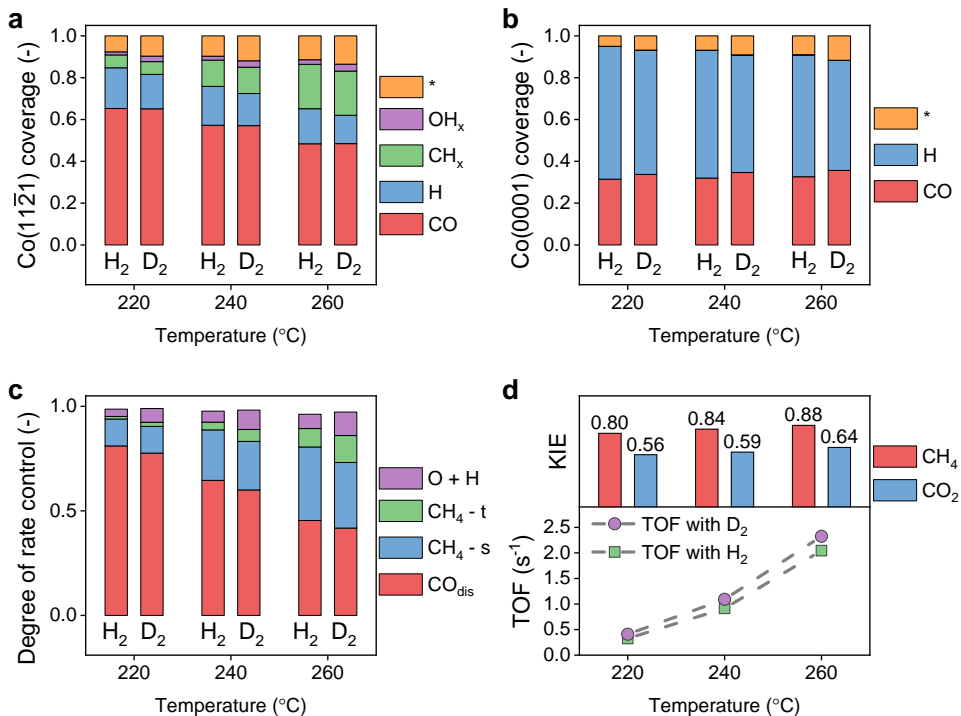


Figure 5.2: Microkinetics simulations of CO hydrogenation at $T = 220/240/260$ °C, $p_{\text{H}_2/\text{D}_2} = 450$ mbar, $p_{\text{CO}} = 45$ mbar. (a) Steady-state coverages on the Co(112̄1) step-edge sites. (b) Steady-state coverages on the Co(0001) terrace sites. (c) Degree of rate control for CO consumption. (d) Turnover frequencies for CO consumption and corresponding kinetic isotope effects (KIE, $r_{\text{H}}/r_{\text{D}}$) for CH_4 and CO_2 production.

CO_2 . As more oxygen atoms are formed by CO dissociation with a deuterium-containing feed when more free sites are available, the CO_2 formation rate also increases despite the oxygen hydrogenation step not depending on the free sites. This shows the importance of a proper knowledge of the composition of the adsorbed layer.

5.3.3 Chemical and isotopic transients of methanation

Understanding the experimental response to (isotopic) kinetic switches is challenging. This problem is aggravated when more than one elementary reaction step controls the overall reaction rate. For CO hydrogenation these steps are CO dissociation and hydrogenation steps to CH_4 and H_2O . In this work, we use our simulations to understand the response to different CTKA and SSITKA switches using our kinetic model for a cobalt catalyst. For this purpose, the kinetic models were implemented in a continuous stirred-tank reactor (CSTR) model. This means that the reactor is free from concentration and temperature gradients and that mass transport limitations are not considered. The residence time (i.e. the ratio of the reactor volume and the flow rate) in the CSTR is 1 s (no correction applied

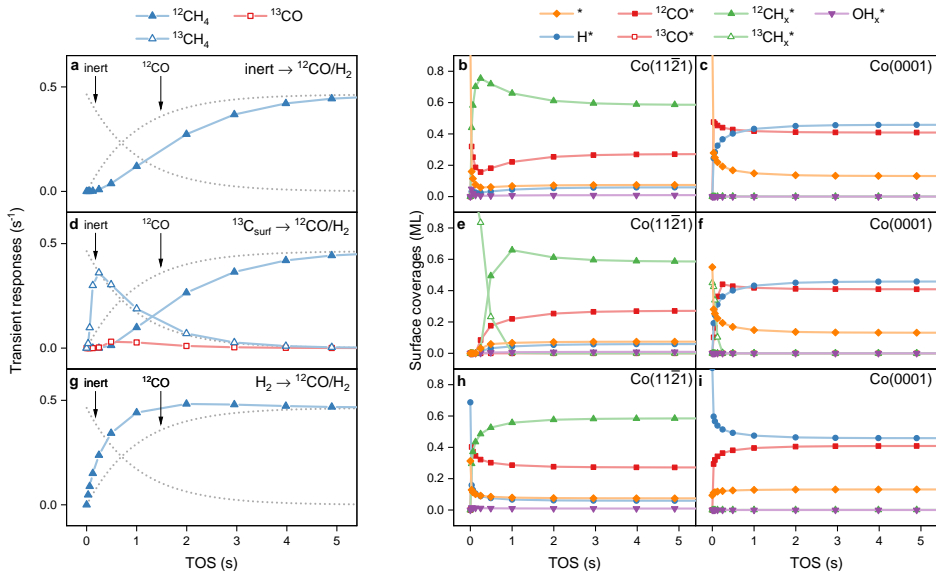


Figure 5.3: Microkinetics simulations of transient switches at $T = 260$ °C, $p_{\text{H}_2} = 200$ mbar, $p_{\text{CO}} = 200$ mbar. The inert and CO responses are normalized to the steady-state CH_4 production. Transient responses and surface coverages are shown for: (a-c) inert \rightarrow $^{12}\text{CO}/\text{H}_2$ over an initially empty surface; (d-f) inert \rightarrow $^{12}\text{CO}/\text{H}_2$ for a surface pre-covered with 0.5 ML ^{13}C ; (g-i) $\text{H}_2 \rightarrow$ $^{12}\text{CO}/\text{H}_2$. Panels (a, d, g) indicate the transient responses. Surface coverages on the Co(11 $\bar{2}$ 1) step-edge sites are shown in (b, e, h). Surface coverages on the Co(0001) terrace sites are shown in (c, f, i).

to the transients). The following sections will discuss the effects of CTKA, SSITKA, and CO scrambling experiments. The temperatures and pressure used for these simulations were chosen for comparison to the work of Chen et al. [43, 44, 82]. We will first discuss the forward CTKA responses from a feed without CO to syngas at a low H_2/CO ratio of unity. Then we will describe the CTKA and SSITKA transients using a higher H_2/CO ratio of 10. Finally, we show the results of CO scrambling at a H_2/CO ratio of 2.

Normalized transient responses of CO and methane over an initially empty surface (inert \rightarrow $^{12}\text{CO}/\text{H}_2$) are shown in Figure 5.3a. Methane production is delayed compared to the increase of the CO amount leaving the reactor. These trends are in qualitative agreement with experimental observations for Co/SiO₂ [44]. Initially, CO dissociation is fast on the empty surface. C hydrogenation cannot keep up with the rate of C deposition because of the lowered H coverage. We have chosen a relatively low H_2/CO ratio of unity to emphasize this effect. Figures 5.4b and 5.4c show the surface coverages during the transient for the step-edge and terrace sites, respectively. Consistent with the finding that CO dissociates preferentially at the step-edge sites, we find a rapid build-up of CH_x species on these sites. The predominant species is atomic carbon. The CH_x coverage on the Co(0001) terrace is very low and this surface is predominantly covered by CO and H. The composition of the adsorbed layer on the terrace sites is mostly determined by the adsorption-desorption equilibria of CO and H_2 . These simulations show that CO dissociation predominantly takes

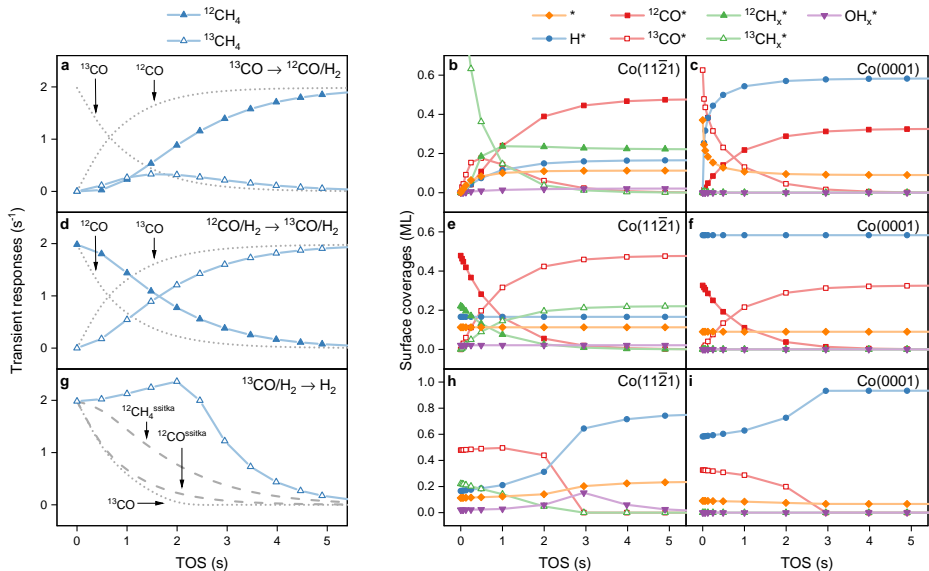


Figure 5.4: Microkinetics simulations of transient switches at $T = 260$ °C, $p_{\text{H}_2} = 450$ mbar, $p_{\text{CO}} = 45$ mbar. The CO responses are normalized to the steady-state CH_4 production. Transient responses and surface coverages are shown for: (a-c) $^{13}\text{CO} \rightarrow ^{12}\text{CO}/\text{H}_2$; (d-f) $^{12}\text{CO}/\text{H}_2 \rightarrow ^{13}\text{CO}/\text{H}_2$; (g-i) $^{13}\text{CO}/\text{H}_2 \rightarrow \text{H}_2$. Panels (a, d, g) indicate the transient responses. Surface coverages on the Co(11 $\bar{2}$ 1) step-edge sites are shown in (b, e, h). Surface coverages on the Co(0001) terrace sites are shown in (c, f, i).

place at the step-edge sites and that the composition of the surface adsorbed layer on the two surfaces is completely different. Pre-covering both surfaces with labeled carbon (^{13}C) leads to a similar delay of $^{12}\text{CH}_4$ for a $^{13}\text{C}_{\text{surf}} \rightarrow ^{12}\text{CO}/\text{H}_2$ switch (Figure 5.3d). To the contrary, labeled methane ($^{13}\text{CH}_4$) produced from pre-deposited carbon shows a very small delay with respect to the introduction of H_2 . The difference between $^{12}\text{CH}_4$ and $^{13}\text{CH}_4$ formation is mainly due to the limited amount of surface vacancies available for ^{12}CO dissociation. Surface coverages at the step-edge site as shown in Figure 5.3e confirm that ^{13}C is quickly replaced by ^{12}C derived from dissociating ^{12}CO upon creating these vacancies. Interestingly, we also observe the formation of a small amount of ^{13}CO , which is due to the recombination of oxygen derived from ^{12}CO dissociation with ^{13}C on the surface. The formation rate of ^{13}CO is one order of magnitude lower than that of $^{13}\text{CH}_4$ and also slightly delayed. This result is in keeping with the notion that CO dissociation is reversible on a Co/SiO₂ catalyst [82]. Figure 5.3g shows the responses to a $\text{H}_2 \rightarrow ^{12}\text{CO}/\text{H}_2$ switch. CH_4 is not delayed compared to CO when starting from a H-covered surface. This shows that the slight delay in $^{12}\text{CH}_4$ formation in Figure 5.3d compared to CO evolution is due to the lack of H atoms on the surface. It emphasizes the critical role of H atoms in the formation of hydrocarbon products. Figures 5.3h and 5.3i show that the additional hydrogen prevents the overshoot of CH_x coverage following from Figure 5.3b. Finally, it may be noted that the steady-state coverages in all three cases in Figure 5.3 are the same as expected.

Figure 5.4 shows the responses following transient switches using a higher H_2/CO ratio of 10. C_{2+} selectivity is low for real systems at these conditions, justifying the absence of chain lengthening in our simulations. As a consequence, the surfaces contain more H and less CO and CH_x species compared to the simulations shown in Figure 5.3. A $^{13}\text{CO} \rightarrow ^{12}\text{CO}/\text{H}_2$ switch (Figure 5.4a) results in simultaneous production of $^{12}\text{CH}_4$ and $^{13}\text{CH}_4$, immediately after the switch. The initial $^{13}\text{CH}_4$ originates from carbon deposited before the switch through disproportionation of ^{13}CO into $^{13}\text{CO}_2$ and ^{13}C . This $^{13}\text{CH}_x$ removal generates vacancies for competitive adsorption of newly introduced ^{12}CO and ^{13}CO still present in the reactor. The newly formed CH_x species follow the isotopic ratio of the gas composition because the rates of CO ad- and desorption are higher than the conversion rate of adsorbed CO to CH_4 . After a few seconds on stream the ratio of $^{13}\text{CH}_4/^{12}\text{CH}_4$ is comparable to the $^{12}\text{CH}_4/^{13}\text{CH}_4$ ratio shown for the SSITKA switch ($^{12}\text{CO}/\text{H}_2 \rightarrow ^{13}\text{CO}/\text{H}_2$) in Figure 5.4d. Still, the total methane yield directly after the forward transient is lower than at steady-state conditions due to the initially lower hydrogen coverage (Figure 5.4b-c). The opposite effect can be seen in Figure 5.4g, where the backward transient from synthesis gas to hydrogen ($^{13}\text{CO}/\text{H}_2 \rightarrow \text{H}_2$) is simulated. A significant amount of “extra-methane” is produced compared to the SSITKA switch. “Extra methane” is defined as the additional amount of methane obtained during this switch compared to the methane produced during a SSITKA switch. This “extra-methane” has also been observed experimentally [44, 83, 84]. Its origin can be appreciated from the surface coverages during the transient, which are shown in Figure 5.4h-i. Notably, the absence of ^{13}CO in the feed first leads to a decrease of the CH_x coverage. The freed sites are then predominantly occupied by H atoms, which can explain the increased rate of CH_4 formation. Interestingly, the ^{13}CO coverage on the step-edge sites also increases slightly. This is primarily due to a lower CO desorption rate when the lateral interactions become weaker with less CH_x on the surface. The corresponding shift in the adsorption equilibrium of CO, the higher H coverage and the higher amount of vacancies result in a maximum rate at 2 s on stream. This maximum rate is higher than the steady-state rate before the switch. After this time, the CO coverages on both surface decrease rapidly as does the CH_4 formation rate. These simulations indicate that the most important cause of an increased CH_4 formation rate is a higher H coverage.

These results are in qualitative agreement with the CTKA measurements reported by Chen et al. [44] and Kruse and co-workers [85]. We calculated that the amount of “extra methane” formed in the simulation in Figure 5.4h is about 3.5 ML. This is due to adsorption on free sites and reaction of CO present in the (CSTR) gas-phase hold-up. This result shows that CO conversion in a CTKA $\text{CO}/\text{H}_2 \rightarrow \text{H}_2$ experiment carried out in a CSTR is not limited to CO adsorbed on the surface. Due to the broad residence time distribution in a CSTR, also gas-phase CO is converted in addition to CO initially present on the cobalt surface. Thus, one cannot draw conclusions on the composition of the surface adsorbed layer under steady-state conditions when a CTKA is carried out in a CSTR or other non-ideal reactors with a residence time distribution. We therefore surmise that the “extra methane” in the experiments carried out in Kruse’s group, leading to the claim of the presence of multiple adsorbed layers under FT conditions, might have to do with a non-ideal behavior

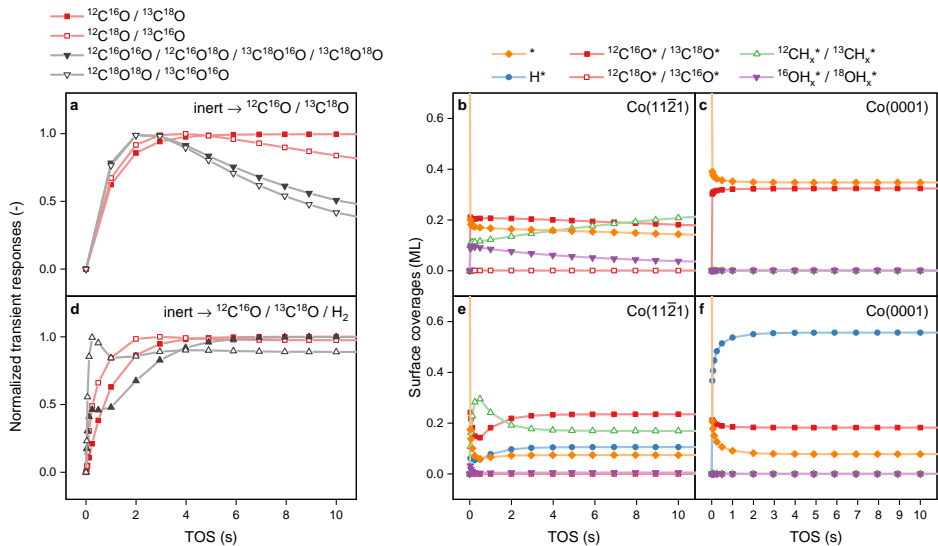


Figure 5.5: Microkinetics simulations of CO scrambling at $T = 220$ °C, $p_{\text{H}_2} = 180$ mbar, $p_{^{12}\text{C}^{16}\text{O}} = 45$ mbar, $p_{^{13}\text{C}^{18}\text{O}} = 45$ mbar. Normalized transient responses and surface coverages are shown for: (a-c) inert \rightarrow $^{12}\text{C}^{16}\text{O} / ^{13}\text{C}^{18}\text{O}$; (d-f) inert \rightarrow $^{12}\text{C}^{16}\text{O} / ^{13}\text{C}^{18}\text{O} / \text{H}_2$. Panels (a, d) indicate the transient responses. Surface coverages on the Co(11 $\bar{2}$ 1) step-edge sites are shown in (b, e). Surface coverages on the Co(0001) terrace sites are shown in (c, f).

of the used reactor. Such an effect is absent when a plug-flow reactor is used in which in the ideal case there is no residence time distribution. This can provide an explanation for the different result obtained in the work of Chen et al., who observed that the amount of “extra methane” determined by CTKA corresponds very closely to the CO coverage determined by SSITKA [44]. In such case readsorption of CO and a high enough reactivity of the surface for methanation are key to the complete conversion of surface adsorbed CO to methane.

5.3.4 CO scrambling

Intrigued by the reversibility of CO dissociation revealed by the results in Figure 5.3d, we also modeled the isotopic scrambling experiment by Chen et al. [82]. For this purpose, simulations were carried out using a $^{12}\text{C}^{16}\text{O} / ^{13}\text{C}^{18}\text{O}$ mixture in the absence and presence of H₂. The H₂/CO ratio was kept at 2. Figure 5.5a shows that the scrambling response without H₂ quickly reaches a maximum after a few seconds on stream and then decreases with time. At the same time both labeled and unlabeled CO₂ is produced. While oxygen is removed as CO₂, carbon is accumulating at the surface (Figure 5.5b). This leads to a strong decrease in the scrambling activity after about 3 s. To the contrary, when hydrogen is added to the isotopic reaction mixture, the scrambling activity is retained (Figure 5.5d). This is because C is removed as methane in this case. Figure 5.6a shows the data obtained in the presence of H₂. Initially, the CO scrambling rate is higher than CH₄ production, after which

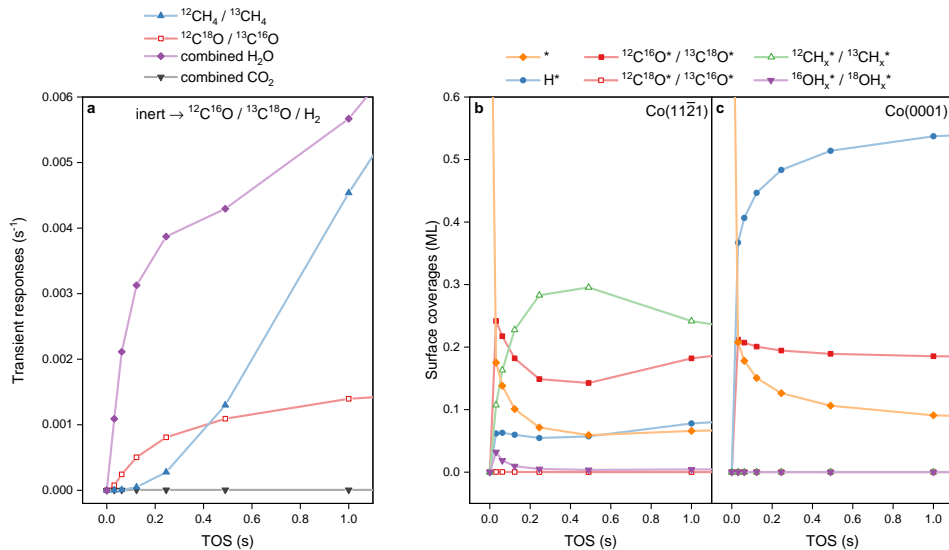


Figure 5.6: Microkinetics simulation of CO scrambling at $T = 220$ °C, $p_{\text{H}_2} = 180$ mbar, $p_{^{12}\text{C}^{16}\text{O}} = 45$ mbar, $p_{^{13}\text{C}^{18}\text{O}} = 45$ mbar. Transient responses are shown for: (a) inert \rightarrow $^{12}\text{C}^{16}\text{O} / ^{13}\text{C}^{18}\text{O} / \text{H}_2$. Surface coverages on the Co(11 $\bar{2}$ 1) step-edge sites are shown in (b). Surface coverages on the Co(0001) terrace sites are shown in (c).

the CH_x coverage (Figure 5.6b) reaches a maximum at 0.5 s. Although $^{12}\text{C}^{18}\text{O}^{18}\text{O}$ and $^{13}\text{C}^{16}\text{O}^{16}\text{O}$ are formed in our simulations, their absolute rates of formation are almost three orders of magnitude lower than that of other CO₂ isotopes. This can be explained by the fact that other CO₂ isotopes can be formed by reacting unscrambled CO with atomic oxygen. Formation of $^{12}\text{C}^{18}\text{O}^{18}\text{O}$ and $^{13}\text{C}^{16}\text{O}^{16}\text{O}$ needs scrambled CO to recombine with atomic oxygen, which has a much lower probability. This effect is enhanced because the scrambling rate is limited by the low oxygen coverage in the simulations. For scrambling with the addition of hydrogen, only during the initial 0.2 s a significant amount of atomic oxygen is available (Figure 5.6a). We also found that the higher oxygen coverages without hydrogen resulted in a one order of magnitude higher maximum scrambling activity compared to scrambling with hydrogen. This is another example of the importance of the composition of the surface adsorbed layer in determining the kinetics of CO hydrogenation.

5.4 Conclusions

Microkinetics simulations of transient kinetics for a cobalt nanoparticle model surface display strong evidence for CH_x formation through a direct CO scission pathway. Computed reaction energetics show that this pathway needs step-edge sites and does not take place on terraces. The kinetic isotope effect for the hydrogenation of CO to methane is consistent with experimental data. Partial rate control in the hydrogenation steps of C and O shows that these observations do not require involving H-assisted CO dissociation. The simulations

of the transients provide significant insight into the surface kinetics of CO hydrogenation. We conclude that CO scission on an empty surface is initially very fast after which the overall rate is limited by carbon hydrogenation. This conclusion is strengthened by the observed reversibility of CO dissociation that is evident from simulations of $^{12}\text{C}^{16}\text{O}/^{13}\text{C}^{18}\text{O}$ scrambling. This indicates an approach to a steady-state surface coverage where CO dissociation and CH_x termination compete. “Extra-methane” produced after switching from synthesis gas to hydrogen represents a case in which the composition of the surface adsorbed layer changes in such a way that methanation is favored. Notably, the lower CH_x coverage results in a higher H coverage and decreases the CO adsorption energy, resulting in a lower rate of CO desorption. Readsorption of CO results in the rapid consumption of most of the CO on the step-edge sites and conversion to methane. In the next chapter, carbon-carbon formation reactions will be included, which are expected to slightly affect the surface composition of the step-edge sites, suppressing CH_4 formation in favor of longer hydrocarbons.

5.5 References

- [1] M. E. Dry, *Catalysis Today* **1990**, *6*, 183–206.
- [2] M. E. Dry, *Catalysis Today* **2002**, *71*, 227–241.
- [3] M. Lualdi, S. Lögdberg, G. Di Carlo, S. Järås, M. Boutonnet, A. M. Venezia, E. A. Blekkan, A. Holmen, *Topics in Catalysis* **2011**, *54*, 1175.
- [4] B. C. Enger, Å.-L. Fossan, Ø. Borg, E. Rytter, A. Holmen, *Journal of Catalysis* **2011**, *284*, 9–22.
- [5] M. Wolf, H. Kotzé, N. Fischer, M. Claeys, *Faraday Discussions* **2017**, *197*, 243–268.
- [6] E. Iglesia, *Applied Catalysis A: General* **1997**, *161*, 59–78.
- [7] D. L. King, *Journal of Catalysis* **1978**, *51*, 386–397.
- [8] B. H. Davis, *Catalysis Today* **2009**, *141*, 25–33.
- [9] P. Biloen, J. N. Helle, F. G. A. van den Berg, W. M. H. Sachtler, *Journal of Catalysis* **1983**, *81*, 450–463.
- [10] P. Biloen, J. N. Helle, W. M. H. Sachtler, *Journal of Catalysis* **1979**, *58*, 95–107.
- [11] R. A. van Santen, A. J. Markvoort, I. A. W. Filot, M. M. Ghouri, E. J. M. Hensen, *Physical Chemistry Chemical Physics* **2013**, *15*, 17038–17063.
- [12] I. A. W. Filot, R. A. van Santen, E. J. M. Hensen, *Catal. Sci. Technol.* **2014**, *4*, 3129–3140.
- [13] R. Van Hardeveld, F. Hartog, *Surface Science* **1969**, *15*, 189–230.
- [14] R. van Hardeveld, A. van Montfoort, *Surface Science* **1966**, *4*, 396–430.
- [15] J. X. Liu, H. Y. Su, D. P. Sun, B. Y. Zhang, W. X. Li, *J Am Chem Soc* **2013**, *135*, 16284–7.

- [16] I. A. W. Filot, S. G. Shetty, E. J. M. Hensen, R. A. van Santen, *Journal of Physical Chemistry C* **2011**, *115*, 14204–14212.
- [17] S. Shetty, A. P. Jansen, R. A. van Santen, *J Am Chem Soc* **2009**, *131*, 12874–5.
- [18] X. Y. Quek, I. A. Filot, R. Pestman, R. A. van Santen, V. Petkov, E. J. Hensen, *Chem Commun (Camb)* **2014**, *50*, 6005–8.
- [19] D. J. Moodley, J. van de Loosdrecht, A. M. Saib, M. J. Overett, A. K. Datye, J. W. Niemantsverdriet, *Applied Catalysis A: General* **2009**, *354*, 102–110.
- [20] K. Fei Tan, J. Xu, J. Chang, A. Borgna, M. Saeys, *Journal of Catalysis* **2010**, *274*, 121–129.
- [21] S. B. Vendelbo, M. Johansson, D. J. Mowbray, M. P. Andersson, F. Abild-Pedersen, J. H. Nielsen, J. K. Nørskov, I. Chorkendorff, *Topics in Catalysis* **2010**, *53*, 357–364.
- [22] M. Zhuo, A. Borgna, M. Saeys, *Journal of Catalysis* **2013**, *297*, 217–226.
- [23] B. T. Loveless, C. Buda, M. Neurock, E. Iglesia, *J Am Chem Soc* **2013**, *135*, 6107–21.
- [24] D. Hibbitts, E. Dybeck, T. Lawlor, M. Neurock, E. Iglesia, *Journal of Catalysis* **2016**, *337*, 91–101.
- [25] P. van Helden, J.-A. van den Berg, I. M. Ciobică, *Catalysis Science & Technology* **2012**, *2*, 491–494.
- [26] M. Ojeda, R. Nabar, A. U. Nilekar, A. Ishikawa, M. Mavrikakis, E. Iglesia, *Journal of Catalysis* **2010**, *272*, 287–297.
- [27] M. P. Andersson, F. Abild-Pedersen, I. N. Remediakis, T. Bligaard, G. Jones, J. Engbæk, O. Lytken, S. Horch, J. H. Nielsen, J. Sehested, *Journal of Catalysis* **2008**, *255*, 6–19.
- [28] I. C. Yates, C. N. Satterfield, *Energy & Fuels* **1991**, *5*, 168–173.
- [29] C. Ledesma, J. Yang, D. Chen, A. Holmen, *ACS Catalysis* **2014**, *4*, 4527–4547.
- [30] S. L. Shannon, J. G. Goodwin, *Chemical Reviews* **1995**, *95*, 677–695.
- [31] H. A. J. van Dijk, J. H. B. J. Hoebink, J. C. Schouten, *Chemical Engineering Science* **2001**, *56*, 1211–1219.
- [32] J. Schweicher, A. Bundhoo, A. Frennet, N. Kruse, H. Daly, F. C. Meunier, *The Journal of Physical Chemistry C* **2010**, *114*, 2248–2255.
- [33] A. Bundhoo, J. Schweicher, A. Frennet, N. Kruse, *The Journal of Physical Chemistry C* **2009**, *113*, 10731–10739.
- [34] J. P. den Breejen, P. B. Radstake, G. L. Bezemer, J. H. Bitter, V. Frøseth, A. Holmen, K. P. de Jong, *J Am Chem Soc* **2009**, *131*, 7197–203.
- [35] V. Frøseth, A. Holmen, *Topics in Catalysis* **2007**, *45*, 45–50.
- [36] J. Xie, J. Yang, A. I. Dugulan, A. Holmen, D. Chen, K. P. de Jong, M. J. Louwerse, *ACS Catalysis* **2016**, *6*, 3147–3157.
- [37] J. Yang, V. Frøseth, D. Chen, A. Holmen, *Surface Science* **2016**, *648*, 67–73.

- [38] G. Jacobs, B. H. Davis, *Catalysis Science & Technology* **2014**, *4*, 3927–3944.
- [39] M. Ojeda, A. Li, R. Nabar, A. U. Nilekar, M. Mavrikakis, E. Iglesia, *The Journal of Physical Chemistry C* **2010**, *114*, 19761–19770.
- [40] Y. Qi, J. Yang, X. Duan, Y.-A. Zhu, D. Chen, A. Holmen, *Catalysis Science & Technology* **2014**, *4*, 3534–3543.
- [41] S. Kozuch, S. Shaik, *The Journal of Physical Chemistry A* **2008**, *112*, 6032–6041.
- [42] C. Stegelmann, A. Andreasen, C. T. Campbell, *Journal of the American Chemical Society* **2009**, *131*, 8077–8082.
- [43] W. Chen, I. A. W. Filot, R. Pestman, E. J. M. Hensen, *ACS Catalysis* **2017**, *7*, 8061–8071.
- [44] W. Chen, R. Pestman, B. Zijlstra, I. A. W. Filot, E. J. M. Hensen, *ACS Catalysis* **2017**, *7*, 8050–8060.
- [45] R. Carrasquillo-Flores, J. M. R. Gallo, K. Hahn, J. A. Dumesic, M. Mavrikakis, *ChemCatChem* **2013**, *5*, 3690–3699.
- [46] C. J. Heard, C. Hu, M. Skoglundh, D. Creaser, H. Grönbeck, *ACS Catalysis* **2016**, *6*, 3277–3286.
- [47] M. K. Sabbe, G. Canduela-Rodriguez, J.-F. Joly, M.-F. Reyniers, G. B. Marin, *Catalysis Science & Technology* **2017**, *7*, 5267–5283.
- [48] P. van Helden, J.-A. v. d. Berg, M. A. Petersen, W. Janse van Rensburg, I. M. Ciobîcă, J. van de Loosdrecht, *Faraday Discussions* **2017**, *197*, 117–151.
- [49] T. L. Wind, H. Falsig, J. Sehested, P. G. Moses, T. T. M. Nguyen, *Journal of Catalysis* **2016**, *342*, 105–116.
- [50] N. Yang, A. J. Medford, X. Liu, F. Studt, T. Bligaard, S. F. Bent, J. K. Nørskov, *Journal of the American Chemical Society* **2016**, *138*, 3705–3714.
- [51] P. van Helden, J.-A. van den Berg, R. L. J. Coetzer, *Industrial & Engineering Chemistry Research* **2012**, *51*, 6631–6640.
- [52] E. Rebmann, P. Fongarland, V. Lecocq, F. Diehl, Y. Schuurman, *Catalysis Today* **2016**, *275*, 20–26.
- [53] W. Chen, R. Pestman, F.-K. Chiang, E. J. M. Hensen, *Journal of Catalysis* **2018**, *366*, 107–114.
- [54] J. C. Kelzenberg, T. S. King, *Journal of Catalysis* **1990**, *126*, 421–433.
- [55] P. E. Blochl, *Phys Rev B Condens Matter* **1994**, *50*, 17953–17979.
- [56] G. Kresse, J. Hafner, *Physical Review B* **1993**, *47*, 558–561.
- [57] G. Kresse, J. Hafner, *Physical Review B* **1994**, *49*, 14251–14269.
- [58] G. Kresse, J. Furthmüller, *Computational Materials Science* **1996**, *6*, 15–50.
- [59] G. Kresse, J. Furthmüller, *Physical Review B* **1996**, *54*, 11169–11186.

- [60] J. P. Perdew, K. Burke, M. Ernzerhof, *Physical Review Letters* **1996**, *77*, 3865–3868.
- [61] H. J. Monkhorst, J. D. Pack, *Physical Review B* **1976**, *13*, 5188–5192.
- [62] J. Lahtinen, J. Vaari, K. Kaurala, *Surface Science* **1998**, *418*, 502–510.
- [63] C. J. Weststrate, J. van de Loosdrecht, J. W. Niemantsverdriet, *Journal of Catalysis* **2016**, *342*, 1–16.
- [64] J. Wilson, C. de Groot, *The Journal of Physical Chemistry* **1995**, *99*, 7860–7866.
- [65] G. Mills, H. Jónsson, G. K. Schenter, *Surface Science* **1995**, *324*, 305–337.
- [66] G. Henkelman, B. P. Uberuaga, H. Jonsson, *Journal of Chemical Physics* **2000**, *113*, 9901–9904.
- [67] G. Henkelman, H. Jónsson, *The Journal of Chemical Physics* **2000**, *113*, 9978–9985.
- [68] I. A. Filot, R. A. van Santen, E. J. Hensen, *Angew Chem Int Ed Engl* **2014**, *53*, 12746–12750.
- [69] I. A. W. Filot, B. Zijlstra, E. J. M. Hensen, MKMCXX, a C++ program for constructing microkinetic models, <http://www.mkmcxx.nl/>.
- [70] I. A. W. Filot, R. J. P. Broos, J. P. M. van Rijn, G. J. H. A. van Heugten, R. A. van Santen, E. J. M. Hensen, *ACS Catalysis* **2015**, *5*, 5453–5467.
- [71] I. A. W. Filot, B. Zijlstra, R. J. P. Broos, W. Chen, R. Pestman, E. J. M. Hensen, *Faraday Discussions* **2017**, *197*, 153–164.
- [72] B. V. L’vov, *Reaction Kinetics Mechanisms and Catalysis* **2015**, *116*, 1–18.
- [73] P. J. Feibelman, B. Hammer, J. K. Nørskov, F. Wagner, M. Scheffler, R. Stumpf, R. Watwe, J. Dumesic, *Journal of Physical Chemistry B* **2001**, *105*, 4018–4025.
- [74] F. Abild-Pedersen, M. P. Andersson, *Surface Science* **2007**, *601*, 1747–1753.
- [75] S. E. Mason, I. Grinberg, A. M. Rappe, *Physical Review B* **2004**, *69*, 161401.
- [76] J. Xu, G. F. Froment, *AIChE Journal* **1989**, *35*, 88–96.
- [77] *Journal of Physical and Chemical Reference Data* **1982**, *11*, 695–940.
- [78] C. H. Shomate, *The Journal of Physical Chemistry* **1954**, *58*, 368–372.
- [79] P. van Helden, I. M. Ciobică, R. L. J. Coetzer, *Catalysis Today* **2016**, *261*, 48–59.
- [80] C. S. Kellner, A. T. Bell, *Journal of Catalysis* **1981**, *67*, 175–185.
- [81] M. A. Logan, G. A. Somorjai, *Journal of Catalysis* **1985**, *95*, 317–320.
- [82] W. Chen, B. Zijlstra, I. A. W. Filot, R. Pestman, E. J. M. Hensen, *ChemCatChem* **2018**, *10*, 136–140.
- [83] H. Matsumoto, C. O. Bennett, *Journal of Catalysis* **1978**, *53*, 331–344.
- [84] W. T. Ralston, G. Melaet, T. Saephan, G. A. Somorjai, *Angewandte Chemie International Edition* **2017**, *56*, 7415–7419.
- [85] N. Kruse, J. Schweicher, A. Bundhoo, A. Frennet, T. Visart de Bocarmé, *Topics in Catalysis* **2008**, *48*, 145–152.

Appendix B

- Table B1. Reaction barriers on Co(0001) and Co(11 $\bar{2}$ 1).
- Table B2. Vibrational partition function ratios at 493.15 K.
- Table B3. Vibrational partition function ratios at 513.15 K.
- Table B4. Vibrational partition function ratios at 533.15 K.
- Table B5. KIE adjusted reaction barriers on Co(0001) and Co(11 $\bar{2}$ 1).
- Table B6. KIE adjusted vibrational partition function ratios at 493.15 K.
- Table B7. KIE adjusted vibrational partition function ratios at 513.15 K.
- Table B8. KIE adjusted vibrational partition function ratios at 533.15 K.
- Table B9. Migration barriers and vibrational partition functions.
- Figure B1. Free energy surface
- Figure B2. Reaction network analysis
- Figure B3. Model sensitivity to conversion
- Figure B4. Model sensitivity to site ratio
- Figure B5. Model sensitivity to migration barrier
- Figure B6. Model sensitivity to excluding hydrogen from lateral coverage
- Figure B7. Model sensitivity to lateral penalty of C
- Figure B8. Model sensitivity to lateral penalty of O
- Figure B9. Model sensitivity to lateral penalty of H
- Figure B10. Model sensitivity to combined lateral penalty of C+O+H

Table B1: Elementary reaction step barriers for methanation of synthesis gas on Co(0001) and Co(11 $\bar{2}$ 1). All barriers are zero-point energy corrected and are given with reference to the most stable surface intermediates.

Elementary reaction	Co(0001)		Co(11 $\bar{2}$ 1)	
	E_{act} forward (kJ/mol)	E_{act} backward (kJ/mol)	E_{act} forward (kJ/mol)	E_{act} backward (kJ/mol)
CO + * \rightleftharpoons CO*	-	141.53	-	147.79
H ₂ + 2* \rightleftharpoons 2H*	-	98.62	-	85.05
CH ₄ + * \rightleftharpoons CH ₄ *	-	2.13	-	6.32
H ₂ O + * \rightleftharpoons H ₂ O*	-	23.94	-	52.90
CO ₂ + * \rightleftharpoons CO ₂ *	-	21.75	-	111.81
CO* + H* \rightleftharpoons COH* + *	174.99	76.95	208.74	99.96
CO* + H* \rightleftharpoons CHO* + *	126.78	7.39	68.52	-0.92
CHO* + H* \rightleftharpoons CH ₂ O* + *	43.04	10.02	64.21	11.96
CHO* + H* \rightleftharpoons CHOH* + *	101.69	50.60	121.74	41.79
COH* + H* \rightleftharpoons CHOH* + *	67.65	-4.80	69.75	29.14
CHOH* + H* \rightleftharpoons CH ₂ OH* + *	64.98	24.70	53.74	29.68
CH ₂ O* + H* \rightleftharpoons CH ₂ OH* + *	96.27	37.91	87.09	35.33
C* + H* \rightleftharpoons CH* + *	71.00	89.53	64.61	44.30
CH* + H* \rightleftharpoons CH ₂ * + *	51.73	14.13	47.39	26.35
CH ₂ * + H* \rightleftharpoons CH ₃ * + *	50.53	51.89	40.76	38.16
CH ₃ * + H* \rightleftharpoons CH ₄ * + *	100.96	82.92	76.31	61.11
CO* + * \rightleftharpoons C* + O*	224.80	158.39	99.86	102.03
COH* + * \rightleftharpoons C* + OH*	149.42	144.73	17.59	116.15
CHO* + * \rightleftharpoons CH* + O*	63.01	134.52	82.01	133.32
CH ₂ O* + * \rightleftharpoons CH ₂ * + O*	59.47	126.40	62.49	145.01
CHOH* + * \rightleftharpoons CH* + OH*	62.32	148.61	56.17	175.03
CH ₂ OH* + * \rightleftharpoons CH ₂ * + OH*	44.86	133.82	36.88	158.75
O* + H* \rightleftharpoons OH* + *	120.90	84.57	89.08	76.67
OH* + H* \rightleftharpoons H ₂ O* + *	138.82	72.18	123.05	54.89
OH* + OH* \rightleftharpoons H ₂ O* + O*	47.26	16.95	48.87	-6.89
CO* + O* \rightleftharpoons CO ₂ * + *	137.38	30.47	126.74	83.52

Table B2: Ratios of vibrational partition functions at 493.15 K derived from frequency analysis used to calculate the pre-exponential factors in the rate equations for methanation of synthesis gas on Co(0001) and Co(11 $\bar{2}$ 1). For thermodynamic consistency we have set Q_{TS} and Q_{IS} of adsorption steps to equal unity.

Elementary reaction	Co(0001) at 493.15 K		Co(11 $\bar{2}$ 1) at 493.15 K	
	$Q_{\text{TS}}/Q_{\text{IS}}$	$Q_{\text{TS}}/Q_{\text{FS}}$	$Q_{\text{TS}}/Q_{\text{IS}}$	$Q_{\text{TS}}/Q_{\text{FS}}$
$\text{CO} + * \rightleftharpoons \text{CO}^*$	-	1.26×10^{-2}	-	4.28×10^{-2}
$\text{H}_2 + 2* \rightleftharpoons 2\text{H}^*$	-	6.78×10^{-1}	-	6.21×10^{-1}
$\text{CH}_4 + * \rightleftharpoons \text{CH}_4^*$	-	3.97×10^{-4}	-	1.67×10^{-4}
$\text{H}_2\text{O} + * \rightleftharpoons \text{H}_2\text{O}^*$	-	6.99×10^{-4}	-	6.04×10^{-3}
$\text{CO}_2 + * \rightleftharpoons \text{CO}_2^*$	-	3.41×10^{-3}	-	7.37×10^{-3}
$\text{CO}^* + \text{H}^* \rightleftharpoons \text{COH}^* + *$	4.41×10^{-1}	1.57	3.07	1.39
$\text{CO}^* + \text{H}^* \rightleftharpoons \text{CHO}^* + *$	7.26×10^{-1}	2.10	1.11	9.06×10^{-1}
$\text{CHO}^* + \text{H}^* \rightleftharpoons \text{CH}_2\text{O}^* + *$	8.47×10^{-1}	8.13×10^{-1}	1.02	1.19
$\text{CHO}^* + \text{H}^* \rightleftharpoons \text{CHOH}^* + *$	2.05	7.20×10^{-1}	1.78	5.94×10^{-1}
$\text{COH}^* + \text{H}^* \rightleftharpoons \text{CHOH}^* + *$	1.56	4.47×10^{-1}	5.98×10^{-1}	3.60×10^{-1}
$\text{CHOH}^* + \text{H}^* \rightleftharpoons \text{CH}_2\text{OH}^* + *$	1.12	5.84×10^{-1}	8.94×10^{-1}	8.51×10^{-1}
$\text{CH}_2\text{O}^* + \text{H}^* \rightleftharpoons \text{CH}_2\text{OH}^* + *$	1.89	3.62×10^{-1}	3.13	8.51×10^{-1}
$\text{C}^* + \text{H}^* \rightleftharpoons \text{CH}^* + *$	4.25	3.05	8.56×10^{-1}	6.55×10^{-1}
$\text{CH}^* + \text{H}^* \rightleftharpoons \text{CH}_2^* + *$	1.48	7.58×10^{-1}	1.06	4.51×10^{-1}
$\text{CH}_2^* + \text{H}^* \rightleftharpoons \text{CH}_3^* + *$	1.46	8.25×10^{-1}	8.46×10^{-1}	3.29×10^{-1}
$\text{CH}_3^* + \text{H}^* \rightleftharpoons \text{CH}_4^* + *$	3.24×10^1	2.86×10^{-1}	1.13	9.18×10^{-3}
$\text{CO}^* + * \rightleftharpoons \text{C}^* + \text{O}^*$	9.56×10^{-2}	1.17	2.71×10^{-1}	7.59×10^{-1}
$\text{COH}^* + * \rightleftharpoons \text{C}^* + \text{OH}^*$	9.79×10^{-1}	1.44	3.67×10^{-1}	7.86×10^{-1}
$\text{CHO}^* + * \rightleftharpoons \text{CH}^* + \text{O}^*$	4.58×10^{-1}	1.39	4.53×10^{-1}	1.19
$\text{CH}_2\text{O}^* + * \rightleftharpoons \text{CH}_2^* + \text{O}^*$	5.00×10^{-1}	8.08×10^{-1}	6.26×10^{-1}	6.02×10^{-1}
$\text{CHOH}^* + * \rightleftharpoons \text{CH}^* + \text{OH}^*$	7.58×10^{-1}	2.79	3.18×10^{-1}	8.67×10^{-1}
$\text{CH}_2\text{OH}^* + * \rightleftharpoons \text{CH}_2^* + \text{OH}^*$	1.57×10^{-1}	5.69×10^{-1}	6.84×10^{-1}	8.35×10^{-1}
$\text{O}^* + \text{H}^* \rightleftharpoons \text{OH}^* + *$	1.08	4.65×10^{-1}	1.26	4.36×10^{-1}
$\text{OH}^* + \text{H}^* \rightleftharpoons \text{H}_2\text{O}^* + *$	1.98	1.46×10^{-2}	1.69	1.67×10^{-1}
$\text{OH}^* + \text{OH}^* \rightleftharpoons \text{H}_2\text{O}^* + \text{O}^*$	2.63	4.53×10^{-2}	1.11	3.16×10^{-1}
$\text{CO}^* + \text{O}^* \rightleftharpoons \text{CO}_2^* + *$	7.01×10^{-1}	5.82×10^{-1}	1.78	1.07

Table B3: Ratios of vibrational partition functions at 513.15 K derived from frequency analysis used to calculate the pre-exponential factors in the rate equations for methanation of synthesis gas on Co(0001) and Co(11 $\bar{2}$ 1). For thermodynamic consistency we have set Q_{TS} and Q_{IS} of adsorption steps to equal unity.

Elementary reaction	Co(0001) at 513.15 K		Co(11 $\bar{2}$ 1) at 513.15 K	
	Q_{TS}/Q_{IS}	Q_{TS}/Q_{FS}	Q_{TS}/Q_{IS}	Q_{TS}/Q_{FS}
$\text{CO} + * \rightleftharpoons \text{CO}^*$	-	1.08×10^{-2}	-	3.74×10^{-2}
$\text{H}_2 + 2* \rightleftharpoons 2\text{H}^*$	-	6.48×10^{-1}	-	5.90×10^{-1}
$\text{CH}_4 + * \rightleftharpoons \text{CH}_4^*$	-	3.37×10^{-4}	-	1.36×10^{-4}
$\text{H}_2\text{O} + * \rightleftharpoons \text{H}_2\text{O}^*$	-	5.83×10^{-4}	-	5.13×10^{-3}
$\text{CO}_2 + * \rightleftharpoons \text{CO}_2^*$	-	3.06×10^{-3}	-	6.13×10^{-3}
$\text{CO}^* + \text{H}^* \rightleftharpoons \text{COH}^* + *$	4.35×10^{-1}	1.60	3.09	1.38
$\text{CO}^* + \text{H}^* \rightleftharpoons \text{CHO}^* + *$	7.07×10^{-1}	2.09	1.10	9.01×10^{-1}
$\text{CHO}^* + \text{H}^* \rightleftharpoons \text{CH}_2\text{O}^* + *$	8.37×10^{-1}	8.09×10^{-1}	1.01	1.18
$\text{CHO}^* + \text{H}^* \rightleftharpoons \text{CHOH}^* + *$	2.06	7.15×10^{-1}	1.79	5.96×10^{-1}
$\text{COH}^* + \text{H}^* \rightleftharpoons \text{CHOH}^* + *$	1.59	4.41×10^{-1}	5.89×10^{-1}	3.58×10^{-1}
$\text{CHOH}^* + \text{H}^* \rightleftharpoons \text{CH}_2\text{OH}^* + *$	1.11	5.74×10^{-1}	8.84×10^{-1}	8.35×10^{-1}
$\text{CH}_2\text{O}^* + \text{H}^* \rightleftharpoons \text{CH}_2\text{OH}^* + *$	1.91	3.54×10^{-1}	3.16	8.47×10^{-1}
$\text{C}^* + \text{H}^* \rightleftharpoons \text{CH}^* + *$	4.31	3.05	8.46×10^{-1}	6.41×10^{-1}
$\text{CH}^* + \text{H}^* \rightleftharpoons \text{CH}_2^* + *$	1.48	7.47×10^{-1}	1.05	4.40×10^{-1}
$\text{CH}_2^* + \text{H}^* \rightleftharpoons \text{CH}_3^* + *$	1.46	8.20×10^{-1}	8.29×10^{-1}	3.21×10^{-1}
$\text{CH}_3^* + \text{H}^* \rightleftharpoons \text{CH}_4^* + *$	3.30×10^1	2.94×10^{-1}	1.09	8.68×10^{-3}
$\text{CO}^* + * \rightleftharpoons \text{C}^* + \text{O}^*$	9.16×10^{-2}	1.16	2.63×10^{-1}	7.46×10^{-1}
$\text{COH}^* + * \rightleftharpoons \text{C}^* + \text{OH}^*$	9.93×10^{-1}	1.43	3.60×10^{-1}	7.75×10^{-1}
$\text{CHO}^* + * \rightleftharpoons \text{CH}^* + \text{O}^*$	4.49×10^{-1}	1.36	4.48×10^{-1}	1.18
$\text{CH}_2\text{O}^* + * \rightleftharpoons \text{CH}_2^* + \text{O}^*$	4.94×10^{-1}	7.86×10^{-1}	6.21×10^{-1}	5.86×10^{-1}
$\text{CHOH}^* + * \rightleftharpoons \text{CH}^* + \text{OH}^*$	7.49×10^{-1}	2.74	3.17×10^{-1}	8.51×10^{-1}
$\text{CH}_2\text{OH}^* + * \rightleftharpoons \text{CH}_2^* + \text{OH}^*$	1.51×10^{-1}	5.39×10^{-1}	6.80×10^{-1}	8.13×10^{-1}
$\text{O}^* + \text{H}^* \rightleftharpoons \text{OH}^* + *$	1.07	4.46×10^{-1}	1.26	4.28×10^{-1}
$\text{OH}^* + \text{H}^* \rightleftharpoons \text{H}_2\text{O}^* + *$	1.95	1.37×10^{-2}	1.69	1.61×10^{-1}
$\text{OH}^* + \text{OH}^* \rightleftharpoons \text{H}_2\text{O}^* + \text{O}^*$	2.55	4.28×10^{-2}	1.08	3.04×10^{-1}
$\text{CO}^* + \text{O}^* \rightleftharpoons \text{CO}_2^* + *$	6.80×10^{-1}	6.26×10^{-1}	1.75	1.07

Table B4: Ratios of vibrational partition functions at 533.15 K derived from frequency analysis used to calculate the pre-exponential factors in the rate equations for methanation of synthesis gas on Co(0001) and Co(11 $\bar{2}$ 1). For thermodynamic consistency we have set Q_{TS} and Q_{IS} of adsorption steps to equal unity.

Elementary reaction	Co(0001) at 533.15 K		Co(11 $\bar{2}$ 1) at 533.15 K	
	Q_{TS}/Q_{IS}	Q_{TS}/Q_{FS}	Q_{TS}/Q_{IS}	Q_{TS}/Q_{FS}
CO + * \rightleftharpoons CO*	-	9.37×10^{-3}	-	3.28×10^{-2}
H ₂ + 2* \rightleftharpoons 2H*	-	6.18×10^{-1}	-	5.61×10^{-1}
CH ₄ + * \rightleftharpoons CH ₄ *	-	2.87×10^{-4}	-	1.11×10^{-4}
H ₂ O + * \rightleftharpoons H ₂ O*	-	4.88×10^{-4}	-	4.37×10^{-3}
CO ₂ + * \rightleftharpoons CO ₂ *	-	2.75×10^{-3}	-	5.12×10^{-3}
CO* + H* \rightleftharpoons COH* + *	4.30×10^{-1}	1.63	3.10	1.38
CO* + H* \rightleftharpoons CHO* + *	6.89×10^{-1}	2.07	1.09	8.96×10^{-1}
CHO* + H* \rightleftharpoons CH ₂ O* + *	8.27×10^{-1}	8.04×10^{-1}	9.95×10^{-1}	1.17
CHO* + H* \rightleftharpoons CHOH* + *	2.08	7.10×10^{-1}	1.80	5.98×10^{-1}
COH* + H* \rightleftharpoons CHOH* + *	1.61	4.36×10^{-1}	5.80×10^{-1}	3.56×10^{-1}
CHOH* + H* \rightleftharpoons CH ₂ OH* + *	1.10	5.64×10^{-1}	8.74×10^{-1}	8.20×10^{-1}
CH ₂ O* + H* \rightleftharpoons CH ₂ OH* + *	1.92	3.48×10^{-1}	3.19	8.43×10^{-1}
C* + H* \rightleftharpoons CH* + *	4.37	3.06	8.35×10^{-1}	6.28×10^{-1}
CH* + H* \rightleftharpoons CH ₂ * + *	1.47	7.36×10^{-1}	1.04	4.30×10^{-1}
CH ₂ * + H* \rightleftharpoons CH ₃ * + *	1.46	8.14×10^{-1}	8.13×10^{-1}	3.14×10^{-1}
CH ₃ * + H* \rightleftharpoons CH ₄ * + *	3.34×10^1	3.01×10^{-1}	1.06	8.24×10^{-3}
CO* + * \rightleftharpoons C* + O*	8.79×10^{-2}	1.15	2.55×10^{-1}	7.34×10^{-1}
COH* + * \rightleftharpoons C* + OH*	1.01	1.41	3.54×10^{-1}	7.65×10^{-1}
CHO* + * \rightleftharpoons CH* + O*	4.41×10^{-1}	1.34	4.43×10^{-1}	1.17
CH ₂ O* + * \rightleftharpoons CH ₂ * + O*	4.89×10^{-1}	7.65×10^{-1}	6.16×10^{-1}	5.71×10^{-1}
CHOH* + * \rightleftharpoons CH* + OH*	7.40×10^{-1}	2.70	3.15×10^{-1}	8.35×10^{-1}
CH ₂ OH* + * \rightleftharpoons CH ₂ * + OH*	1.45×10^{-1}	5.12×10^{-1}	6.75×10^{-1}	7.91×10^{-1}
O* + H* \rightleftharpoons OH* + *	1.05	4.30×10^{-1}	1.26	4.20×10^{-1}
OH* + H* \rightleftharpoons H ₂ O* + *	1.92	1.29×10^{-2}	1.68	1.57×10^{-1}
OH* + OH* \rightleftharpoons H ₂ O* + O*	2.47	4.06×10^{-2}	1.05	2.93×10^{-1}
CO* + O* \rightleftharpoons CO ₂ * + *	6.59×10^{-1}	6.72×10^{-1}	1.71	1.06

Table B5: Kinetic isotope effect adjusted elementary reaction step barriers for methanation of synthesis gas on Co(0001) and Co(11 $\bar{2}$ 1). All barriers are zero point energy corrected and are given with reference to the most stable surface intermediates.

Elementary reaction	Co(0001)		Co(11 $\bar{2}$ 1)	
	E_{act} forward (kJ/mol)	E_{act} backward (kJ/mol)	E_{act} forward (kJ/mol)	E_{act} backward (kJ/mol)
CO + * \rightleftharpoons CO*	-	141.53	-	147.79
D ₂ + 2* \rightleftharpoons 2D*	-	100.68	-	86.68
CD ₄ + * \rightleftharpoons CD ₄ *	-	1.96	-	6.15
D ₂ O + * \rightleftharpoons D ₂ O*	-	24.73	-	54.01
CO ₂ + * \rightleftharpoons CO ₂ *	-	21.75	-	111.81
CO* + D* \rightleftharpoons COD* + *	177.26	81.82	210.64	104.96
CO* + D* \rightleftharpoons CDO* + *	125.10	8.37	69.27	1.46
CDO* + D* \rightleftharpoons CD ₂ O* + *	43.66	13.32	64.25	15.81
CDO* + D* \rightleftharpoons CDOD* + *	104.88	56.09	123.17	48.25
COD* + D* \rightleftharpoons CDOD* + *	67.53	-2.55	70.02	32.97
CDOD* + D* \rightleftharpoons CD ₂ OD* + *	65.16	28.55	54.25	32.59
CD ₂ O* + D* \rightleftharpoons CD ₂ OD* + *	98.62	43.56	89.64	41.51
C* + D* \rightleftharpoons CD* + *	72.83	93.31	65.82	47.65
CD* + D* \rightleftharpoons CD ₂ * + *	52.39	16.47	47.76	28.81
CD ₂ * + D* \rightleftharpoons CD ₃ * + *	51.23	55.90	40.48	41.53
CD ₃ * + D* \rightleftharpoons CD ₄ * + *	101.23	86.57	76.61	64.76
CO* + * \rightleftharpoons C* + O*	224.80	158.39	99.86	102.03
COD* + * \rightleftharpoons C* + OD*	149.52	144.85	17.95	116.58
CDO* + * \rightleftharpoons CD* + O*	63.07	133.88	82.23	134.05
CD ₂ O* + * \rightleftharpoons CD ₂ * + O*	59.87	125.11	63.28	144.59
CDOD* + * \rightleftharpoons CD* + OD*	61.91	147.80	57.39	174.91
CD ₂ OD* + * \rightleftharpoons CD ₂ * + OD*	46.30	132.88	37.87	158.09
O* + D* \rightleftharpoons OD* + *	123.11	89.40	90.82	81.59
OD* + D* \rightleftharpoons D ₂ O* + *	141.50	77.96	124.18	59.32
OD* + OD* \rightleftharpoons D ₂ O* + O*	49.63	19.80	52.39	-3.24
CO* + O* \rightleftharpoons CO ₂ * + *	137.38	30.47	126.74	83.52

Table B6: Kinetic isotope effect adjusted ratios of vibrational partition functions at 493.15 K derived from frequency analysis used to calculate the pre-exponential factors in the rate equations for methanation of synthesis gas on Co(0001) and Co(11 $\bar{2}$ 1). For thermodynamic consistency we have set Q_{TS} and Q_{IS} of adsorption steps to equal unity.

Elementary reaction	Co(0001) at 493.15 K		Co(11 $\bar{2}$ 1) at 493.15 K	
	Q_{TS}/Q_{IS}	Q_{TS}/Q_{FS}	Q_{TS}/Q_{IS}	Q_{TS}/Q_{FS}
CO + * \rightleftharpoons CO*	-	1.26×10^{-2}	-	4.28×10^{-2}
D ₂ + 2* \rightleftharpoons 2D*	-	4.05×10^{-1}	-	3.54×10^{-1}
CD ₄ + * \rightleftharpoons CD ₄ *	-	1.72×10^{-4}	-	4.80×10^{-5}
D ₂ O + * \rightleftharpoons D ₂ O*	-	3.01×10^{-4}	-	2.92×10^{-3}
CO ₂ + * \rightleftharpoons CO ₂ *	-	3.41×10^{-3}	-	7.37×10^{-3}
CO* + D* \rightleftharpoons COD* + *	4.59×10^{-1}	1.80	3.09	1.26
CO* + D* \rightleftharpoons CDO* + *	7.33×10^{-1}	2.13	1.09	8.94×10^{-1}
CDO* + D* \rightleftharpoons CD ₂ O* + *	7.90×10^{-1}	8.10×10^{-1}	9.52×10^{-1}	1.16
CDO* + D* \rightleftharpoons CDOD* + *	2.09	6.95×10^{-1}	1.79	6.18×10^{-1}
COD* + D* \rightleftharpoons CDOD* + *	1.92	4.71×10^{-1}	5.76×10^{-1}	3.99×10^{-1}
CDOD* + D* \rightleftharpoons CD ₂ OD* + *	1.05	5.47×10^{-1}	8.26×10^{-1}	7.54×10^{-1}
CD ₂ O* + D* \rightleftharpoons CD ₂ OD* + *	1.95	3.28×10^{-1}	3.30	8.57×10^{-1}
C* + D* \rightleftharpoons CD* + *	4.62	3.12	7.76×10^{-1}	5.85×10^{-1}
CD* + D* \rightleftharpoons CD ₂ * + *	1.43	6.96×10^{-1}	9.75×10^{-1}	3.98×10^{-1}
CD ₂ * + D* \rightleftharpoons CD ₃ * + *	1.41	8.16×10^{-1}	7.47×10^{-1}	2.90×10^{-1}
CD ₃ * + D* \rightleftharpoons CD ₄ * + *	3.48×10^1	4.07×10^{-1}	8.20×10^{-1}	6.32×10^{-3}
CO* + * \rightleftharpoons C* + O*	9.56×10^{-2}	1.17	2.71×10^{-1}	7.59×10^{-1}
COD* + * \rightleftharpoons C* + OD*	1.16	1.35	3.63×10^{-1}	8.03×10^{-1}
CDO* + * \rightleftharpoons CD* + O*	4.61×10^{-1}	1.31	4.81×10^{-1}	1.23
CD ₂ O* + * \rightleftharpoons CD ₂ * + O*	5.30×10^{-1}	7.15×10^{-1}	6.72×10^{-1}	5.79×10^{-1}
CDOD* + * \rightleftharpoons CD* + OD*	7.78×10^{-1}	2.48	3.63×10^{-1}	8.77×10^{-1}
CD ₂ OD* + * \rightleftharpoons CD ₂ * + OD*	1.60×10^{-1}	4.78×10^{-1}	7.29×10^{-1}	7.85×10^{-1}
O* + D* \rightleftharpoons OD* + *	8.80×10^{-1}	3.28×10^{-1}	1.20	3.89×10^{-1}
OD* + D* \rightleftharpoons D ₂ O* + *	1.71	1.05×10^{-2}	1.53	1.36×10^{-1}
OD* + OD* \rightleftharpoons D ₂ O* + O*	2.00	3.28×10^{-2}	9.38×10^{-1}	2.58×10^{-1}
CO* + O* \rightleftharpoons CO ₂ * + *	7.01×10^{-1}	5.82×10^{-1}	1.78	1.07

Table B7: Kinetic isotope effect adjusted ratios of vibrational partition functions at 513.15 K derived from frequency analysis used to calculate the pre-exponential factors in the rate equations for methanation of synthesis gas on Co(0001) and Co(11 $\bar{2}$ 1). For thermodynamic consistency we have set Q_{TS} and Q_{IS} of adsorption steps to equal unity.

Elementary reaction	Co(0001) at 513.15 K		Co(11 $\bar{2}$ 1) at 513.15 K	
	Q_{TS}/Q_{IS}	Q_{TS}/Q_{FS}	Q_{TS}/Q_{IS}	Q_{TS}/Q_{FS}
$\text{CO} + * \rightleftharpoons \text{CO}^*$	-	1.08×10^{-2}	-	3.74×10^{-2}
$\text{D}_2 + 2* \rightleftharpoons 2\text{D}^*$	-	3.75×10^{-1}	-	3.26×10^{-1}
$\text{CD}_4 + * \rightleftharpoons \text{CD}_4^*$	-	1.43×10^{-4}	-	3.80×10^{-5}
$\text{D}_2\text{O} + * \rightleftharpoons \text{D}_2\text{O}^*$	-	2.47×10^{-4}	-	2.44×10^{-3}
$\text{CO}_2 + * \rightleftharpoons \text{CO}_2^*$	-	3.06×10^{-3}	-	6.13×10^{-3}
$\text{CO}^* + \text{D}^* \rightleftharpoons \text{COD}^* + *$	4.50×10^{-1}	1.85	3.08	1.26
$\text{CO}^* + \text{D}^* \rightleftharpoons \text{CDO}^* + *$	7.09×10^{-1}	2.11	1.07	8.87×10^{-1}
$\text{CDO}^* + \text{D}^* \rightleftharpoons \text{CD}_2\text{O}^* + *$	7.74×10^{-1}	8.04×10^{-1}	9.33×10^{-1}	1.15
$\text{CDO}^* + \text{D}^* \rightleftharpoons \text{CDOD}^* + *$	2.10	6.91×10^{-1}	1.79	6.21×10^{-1}
$\text{COD}^* + \text{D}^* \rightleftharpoons \text{CDOD}^* + *$	1.94	4.64×10^{-1}	5.64×10^{-1}	3.95×10^{-1}
$\text{CDOD}^* + \text{D}^* \rightleftharpoons \text{CD}_2\text{OD}^* + *$	1.03	5.37×10^{-1}	8.10×10^{-1}	7.40×10^{-1}
$\text{CD}_2\text{O}^* + \text{D}^* \rightleftharpoons \text{CD}_2\text{OD}^* + *$	1.95	3.22×10^{-1}	3.32	8.54×10^{-1}
$\text{C}^* + \text{D}^* \rightleftharpoons \text{CD}^* + *$	4.63	3.11	7.62×10^{-1}	5.72×10^{-1}
$\text{CD}^* + \text{D}^* \rightleftharpoons \text{CD}_2^* + *$	1.41	6.83×10^{-1}	9.58×10^{-1}	3.87×10^{-1}
$\text{CD}_2^* + \text{D}^* \rightleftharpoons \text{CD}_3^* + *$	1.40	8.09×10^{-1}	7.26×10^{-1}	2.84×10^{-1}
$\text{CD}_3^* + \text{D}^* \rightleftharpoons \text{CD}_4^* + *$	3.49×10^1	4.23×10^{-1}	7.85×10^{-1}	6.01×10^{-3}
$\text{CO}^* + * \rightleftharpoons \text{C}^* + \text{O}^*$	9.16×10^{-2}	1.16	2.63×10^{-1}	7.46×10^{-1}
$\text{COD}^* + * \rightleftharpoons \text{C}^* + \text{OD}^*$	1.18	1.33	3.57×10^{-1}	7.91×10^{-1}
$\text{CDO}^* + * \rightleftharpoons \text{CD}^* + \text{O}^*$	4.53×10^{-1}	1.29	4.75×10^{-1}	1.22
$\text{CD}_2\text{O}^* + * \rightleftharpoons \text{CD}_2^* + \text{O}^*$	5.25×10^{-1}	6.97×10^{-1}	6.67×10^{-1}	5.64×10^{-1}
$\text{CDOD}^* + * \rightleftharpoons \text{CD}^* + \text{OD}^*$	7.71×10^{-1}	2.44	3.62×10^{-1}	8.59×10^{-1}
$\text{CD}_2\text{OD}^* + * \rightleftharpoons \text{CD}_2^* + \text{OD}^*$	1.54×10^{-1}	4.53×10^{-1}	7.27×10^{-1}	7.63×10^{-1}
$\text{O}^* + \text{D}^* \rightleftharpoons \text{OD}^* + *$	8.56×10^{-1}	3.13×10^{-1}	1.19	3.82×10^{-1}
$\text{OD}^* + \text{D}^* \rightleftharpoons \text{D}_2\text{O}^* + *$	1.67	9.87×10^{-3}	1.51	1.32×10^{-1}
$\text{OD}^* + \text{OD}^* \rightleftharpoons \text{D}_2\text{O}^* + \text{O}^*$	1.94	3.12×10^{-2}	9.11×10^{-1}	2.49×10^{-1}
$\text{CO}^* + \text{O}^* \rightleftharpoons \text{CO}_2^* + *$	6.80×10^{-1}	6.26×10^{-1}	1.75	1.07

Table B8: Kinetic isotope effect adjusted ratios of vibrational partition functions at 533.15 K derived from frequency analysis used to calculate the pre-exponential factors in the rate equations for methanation of synthesis gas on Co(0001) and Co(11 $\bar{2}$ 1). For thermodynamic consistency we have set Q_{TS} and Q_{IS} of adsorption steps to equal unity.

Elementary reaction	Co(0001) at 533.15 K		Co(11 $\bar{2}$ 1) at 533.15 K	
	Q_{TS}/Q_{IS}	Q_{TS}/Q_{FS}	Q_{TS}/Q_{IS}	Q_{TS}/Q_{FS}
CO + * \rightleftharpoons CO*	-	9.37×10^{-3}	-	3.28×10^{-2}
D ₂ + 2* \rightleftharpoons 2D*	-	3.47×10^{-1}	-	3.00×10^{-1}
CD ₄ + * \rightleftharpoons CD ₄ *	-	1.19×10^{-4}	-	3.10×10^{-5}
D ₂ O + * \rightleftharpoons D ₂ O*	-	2.05×10^{-4}	-	2.05×10^{-3}
CO ₂ + * \rightleftharpoons CO ₂ *	-	2.75×10^{-3}	-	5.12×10^{-3}
CO* + D* \rightleftharpoons COD* + *	4.42×10^{-1}	1.89	3.08	1.26
CO* + D* \rightleftharpoons CDO* + *	6.86×10^{-1}	2.09	1.05	8.80×10^{-1}
CDO* + D* \rightleftharpoons CD ₂ O* + *	7.59×10^{-1}	7.97×10^{-1}	9.14×10^{-1}	1.14
CDO* + D* \rightleftharpoons CDOD* + *	2.10	6.87×10^{-1}	1.79	6.23×10^{-1}
COD* + D* \rightleftharpoons CDOD* + *	1.96	4.57×10^{-1}	5.52×10^{-1}	3.92×10^{-1}
CDOD* + D* \rightleftharpoons CD ₂ OD* + *	1.01	5.28×10^{-1}	7.94×10^{-1}	7.27×10^{-1}
CD ₂ O* + D* \rightleftharpoons CD ₂ OD* + *	1.95	3.17×10^{-1}	3.33	8.52×10^{-1}
C* + D* \rightleftharpoons CD* + *	4.65	3.10	7.49×10^{-1}	5.60×10^{-1}
CD* + D* \rightleftharpoons CD ₂ * + *	1.40	6.70×10^{-1}	9.41×10^{-1}	3.78×10^{-1}
CD ₂ * + D* \rightleftharpoons CD ₃ * + *	1.38	8.02×10^{-1}	7.06×10^{-1}	2.78×10^{-1}
CD ₃ * + D* \rightleftharpoons CD ₄ * + *	3.49×10^1	4.38×10^{-1}	7.52×10^{-1}	5.73×10^{-3}
CO* + * \rightleftharpoons C* + O*	8.79×10^{-2}	1.15	2.55×10^{-1}	7.34×10^{-1}
COD* + * \rightleftharpoons C* + OD*	1.20	1.32	3.51×10^{-1}	7.80×10^{-1}
CDO* + * \rightleftharpoons CD* + O*	4.45×10^{-1}	1.27	4.69×10^{-1}	1.21
CD ₂ O* + * \rightleftharpoons CD ₂ * + O*	5.20×10^{-1}	6.79×10^{-1}	6.63×10^{-1}	5.50×10^{-1}
CDOD* + * \rightleftharpoons CD* + OD*	7.63×10^{-1}	2.40	3.60×10^{-1}	8.42×10^{-1}
CD ₂ OD* + * \rightleftharpoons CD ₂ * + OD*	1.49×10^{-1}	4.31×10^{-1}	7.24×10^{-1}	7.42×10^{-1}
O* + D* \rightleftharpoons OD* + *	8.34×10^{-1}	3.00×10^{-1}	1.19	3.75×10^{-1}
OD* + D* \rightleftharpoons D ₂ O* + *	1.63	9.33×10^{-3}	1.50	1.29×10^{-1}
OD* + OD* \rightleftharpoons D ₂ O* + O*	1.88	2.98×10^{-2}	8.85×10^{-1}	2.41×10^{-1}
CO* + O* \rightleftharpoons CO ₂ * + *	6.59×10^{-1}	6.72×10^{-1}	1.71	1.06

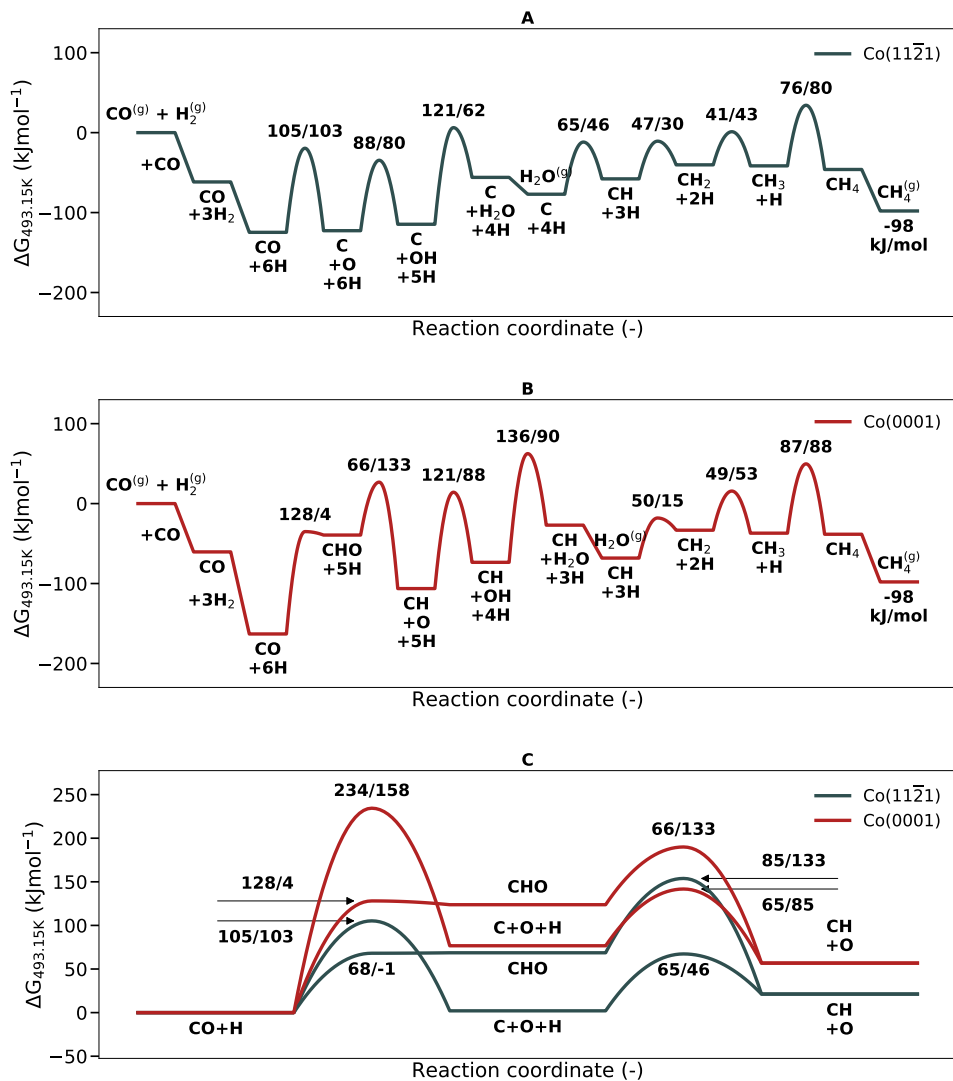


Figure B1: Free energy surfaces for methanation at 493.15 K. a) CO to CH $_4$ on Co(11 $\bar{2}$ 1); b) CO to CH $_4$ on Co(0001); c) Comparison of CH formation via direct CO dissociation or through the CHO intermediate on both surfaces.

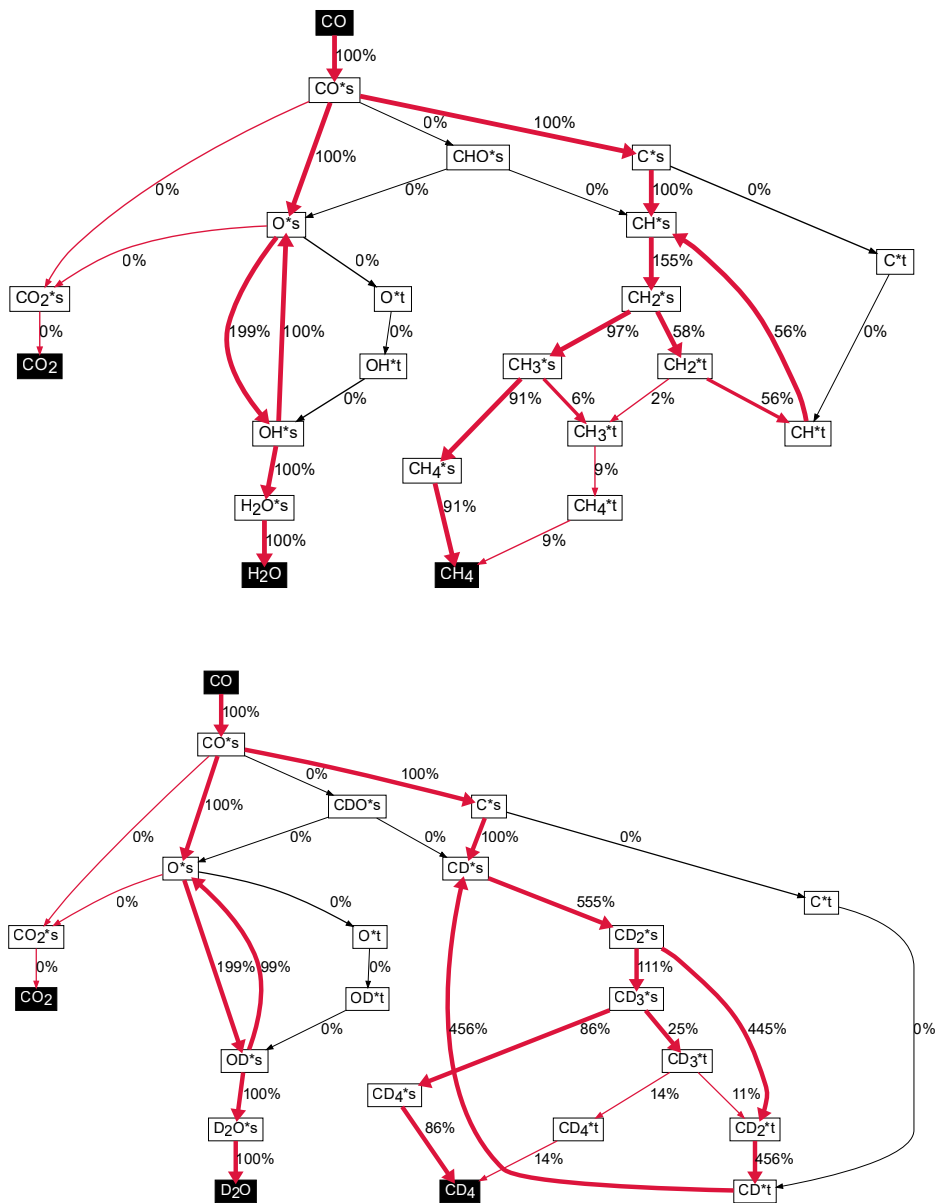


Figure B2: Reaction network analysis at 493.15 K. The top network shows the normalized fluxes for a syngas mixture of $\text{H}_2/\text{CO} = 450/45$ mbar. The bottom network shows the normalized fluxes for the corresponding deuterium feed.

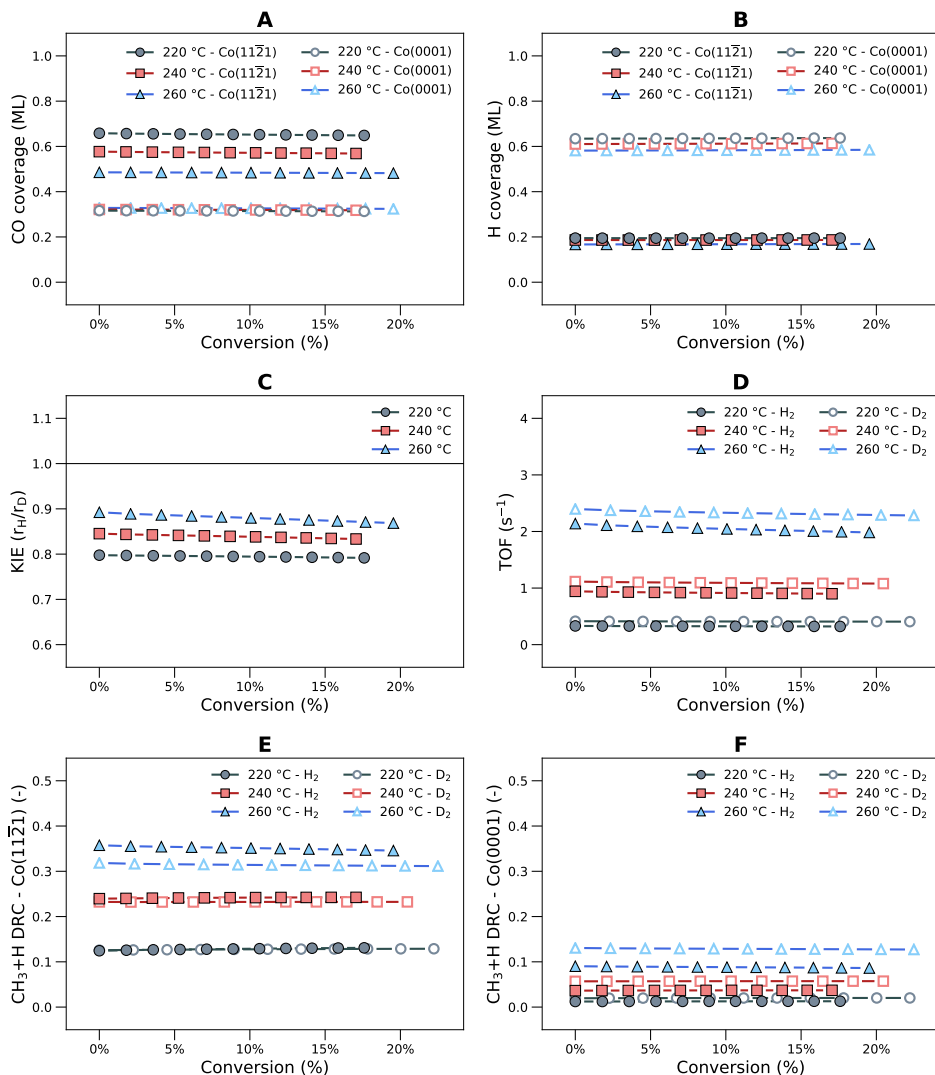


Figure B3: Sensitivity of the microkinetic modeling results at $H_2/CO = 450/45$ mbar as a function of conversion. a) CO coverage on both the stepped Co(11 $\bar{1}$ 21) surface and the terrace Co(0001) surface; b) H coverage; c) Kinetic isotope effect for CO conversion (The data point is plotted at the conversion of the respective hydrogen feed); d) TOF of CO conversion for both a hydrogen and a deuterium feed; e) Degree of rate control for the final hydrogenation step on the stepped Co(11 $\bar{1}$ 21) surface; f) Degree of rate control for the final hydrogenation step on the terrace Co(0001) surface.

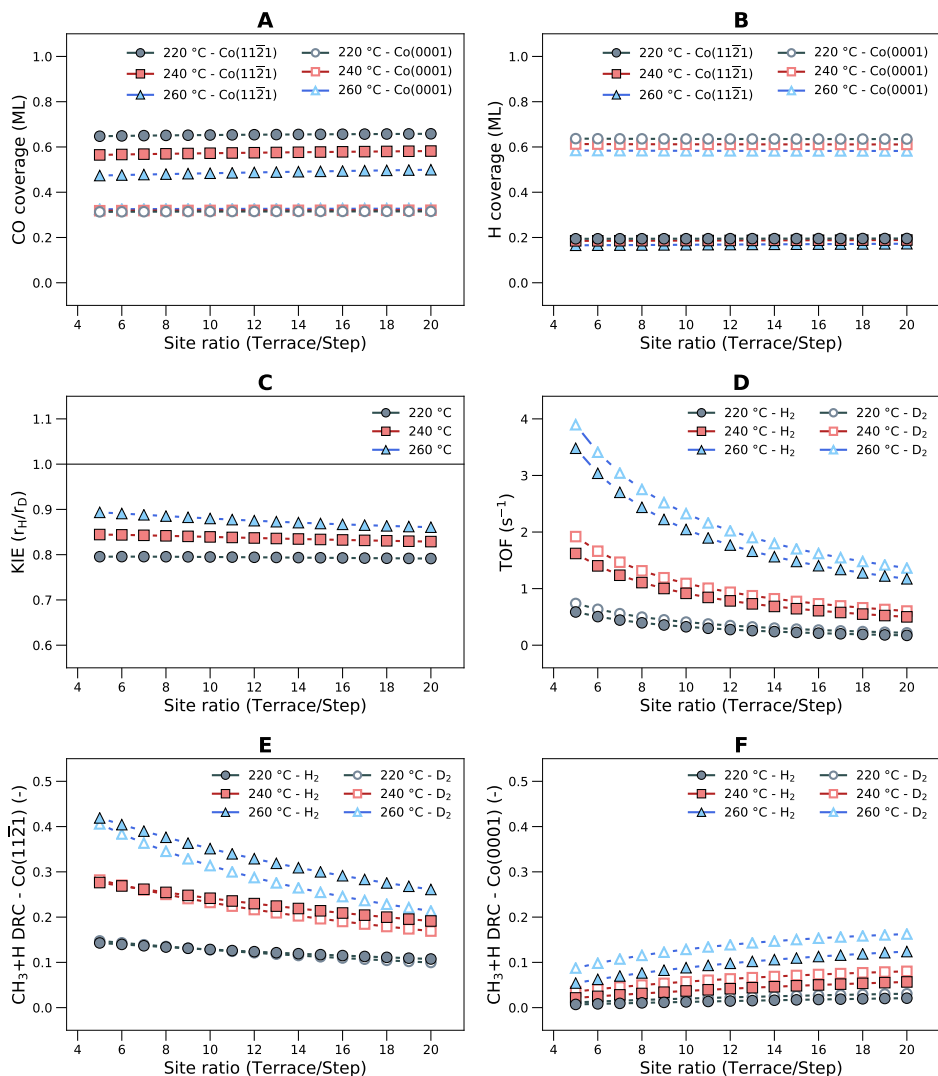


Figure B4: Sensitivity of the microkinetic modeling results at $H_2/CO = 450/45$ mbar as a function of the terrace/step site ratio. a) CO coverage on both the stepped $Co(11\bar{2}1)$ surface and the terrace $Co(0001)$ surface; b) H coverage; c) Kinetic isotope effect for CO conversion; d) TOF of CO conversion for both a hydrogen and a deuterium feed; e) Degree of rate control for the final hydrogenation step on the stepped $Co(11\bar{2}1)$ surface; f) Degree of rate control for the final hydrogenation step on the terrace $Co(0001)$ surface.

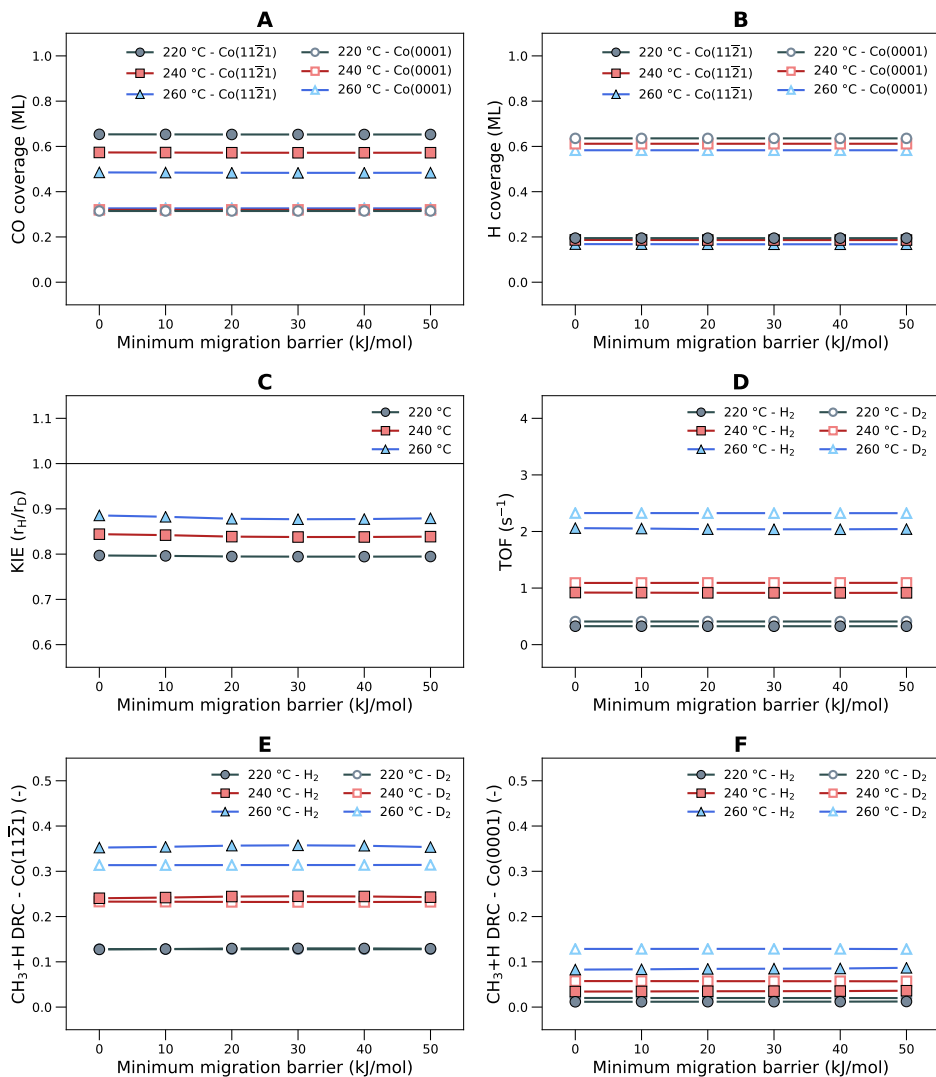


Figure B5: Sensitivity of the microkinetic modeling results at $H_2/CO = 450/45$ mbar as a function of the minimum migration barrier of CH_x species between the terrace and the stepped surface. a) CO coverage on both the stepped Co(111̄1) surface and the terrace Co(0001) surface; b) H coverage; c) Kinetic isotope effect for CO conversion; d) TOF of CO conversion for both a hydrogen and a deuterium feed; e) Degree of rate control for the final hydrogenation step on the stepped Co(111̄1) surface; f) Degree of rate control for the final hydrogenation step on the terrace Co(0001) surface.

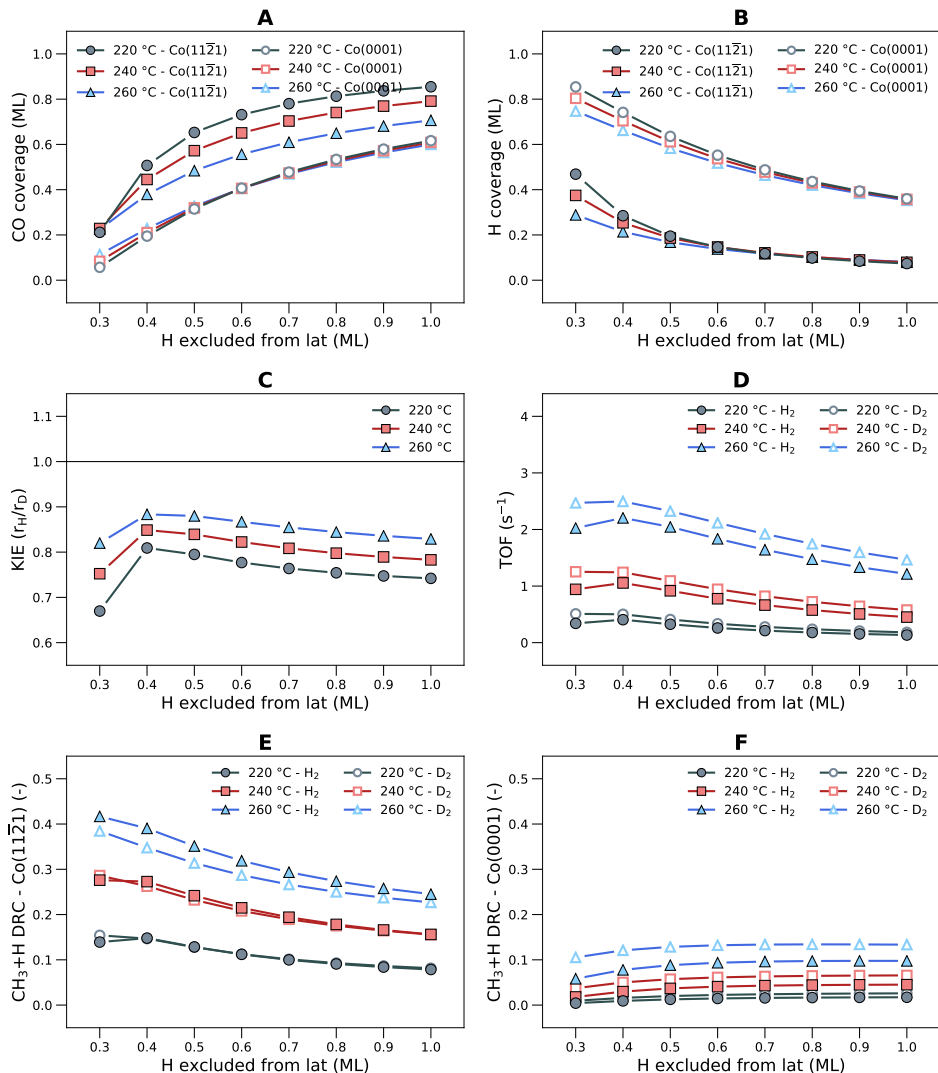


Figure B6: Sensitivity of the microkinetic modeling results at $\text{H}_2/\text{CO} = 450/45$ mbar as a function of the amount of H coverage that is excluded from the lateral coverage. a) CO coverage on both the stepped $\text{Co}(11\bar{1})$ surface and the terrace $\text{Co}(0001)$ surface; b) H coverage; c) Kinetic isotope effect for CO conversion; d) TOF of CO conversion for both a hydrogen and a deuterium feed; e) Degree of rate control for the final hydrogenation step on the stepped $\text{Co}(11\bar{1})$ surface; f) Degree of rate control for the final hydrogenation step on the terrace $\text{Co}(0001)$ surface.

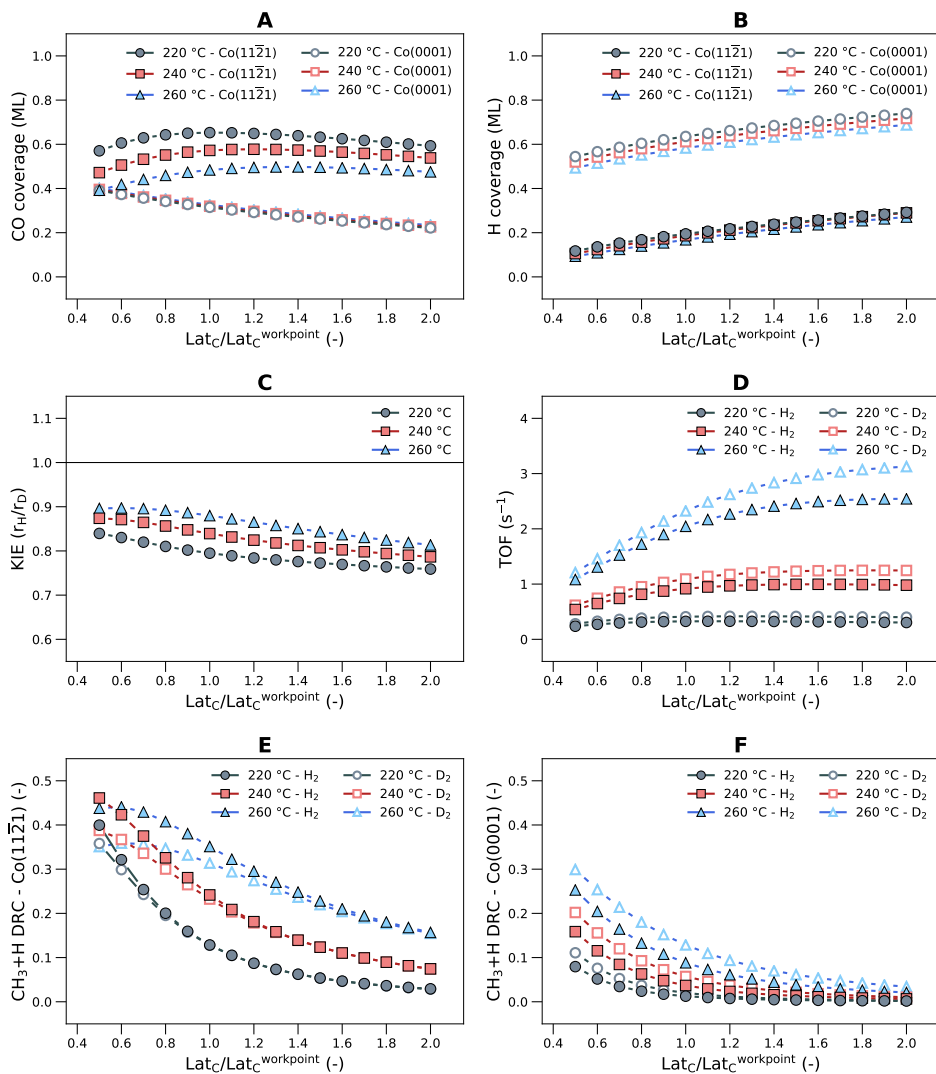


Figure B7: Sensitivity of the microkinetic modeling results at $\text{H}_2/\text{CO} = 450/45$ mbar as a function of the lateral interaction penalty per C atom. a) CO coverage on both the stepped $\text{Co}(11\bar{1}1)$ surface and the terrace $\text{Co}(0001)$ surface; b) H coverage; c) Kinetic isotope effect for CO conversion; d) TOF of CO conversion for both a hydrogen and a deuterium feed; e) Degree of rate control for the final hydrogenation step on the stepped $\text{Co}(11\bar{1}1)$ surface; f) Degree of rate control for the final hydrogenation step on the terrace $\text{Co}(0001)$ surface.

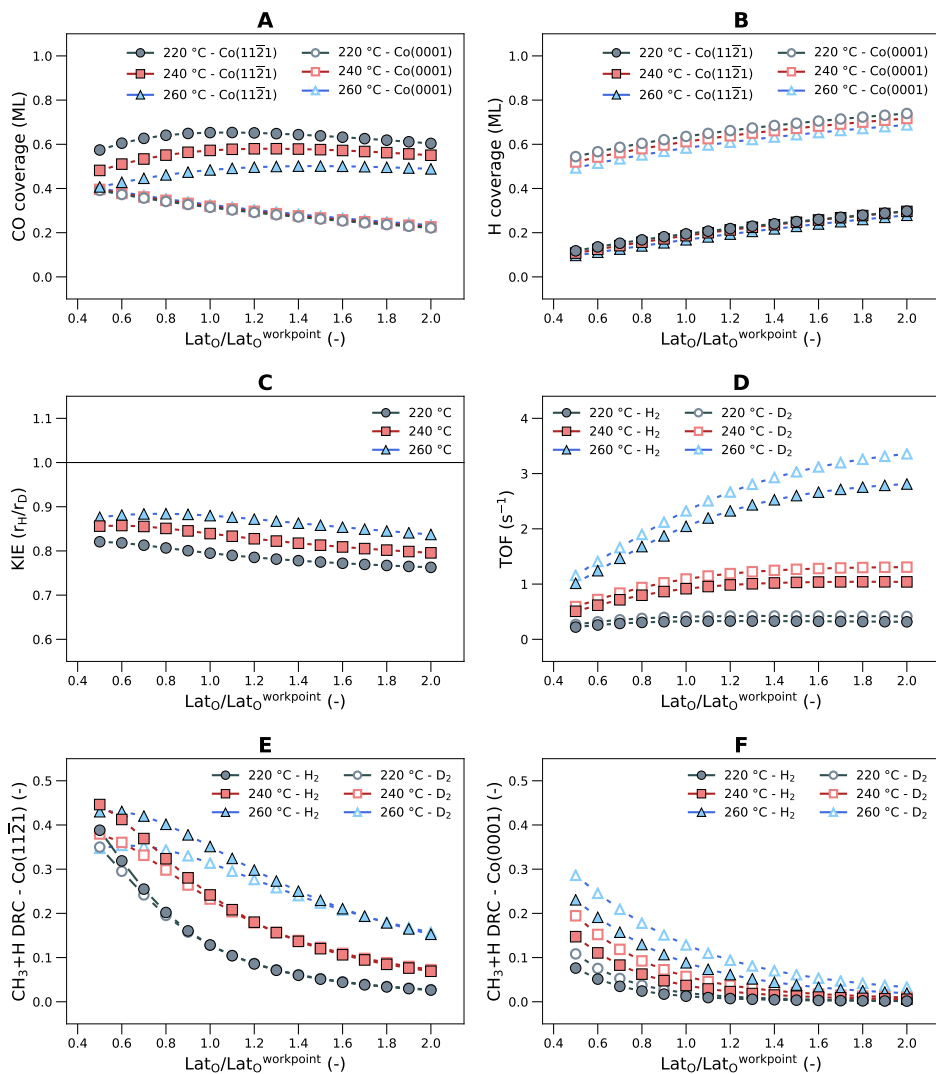


Figure B8: Sensitivity of the microkinetic modeling results at $\text{H}_2/\text{CO} = 450/45$ mbar as a function of the lateral interaction penalty per O atom. a) CO coverage on both the stepped Co(11 $\bar{1}$ 21) surface and the terrace Co(0001) surface; b) H coverage; c) Kinetic isotope effect for CO conversion; d) TOF of CO conversion for both a hydrogen and a deuterium feed; e) Degree of rate control for the final hydrogenation step on the stepped Co(11 $\bar{1}$ 21) surface; f) Degree of rate control for the final hydrogenation step on the terrace Co(0001) surface.

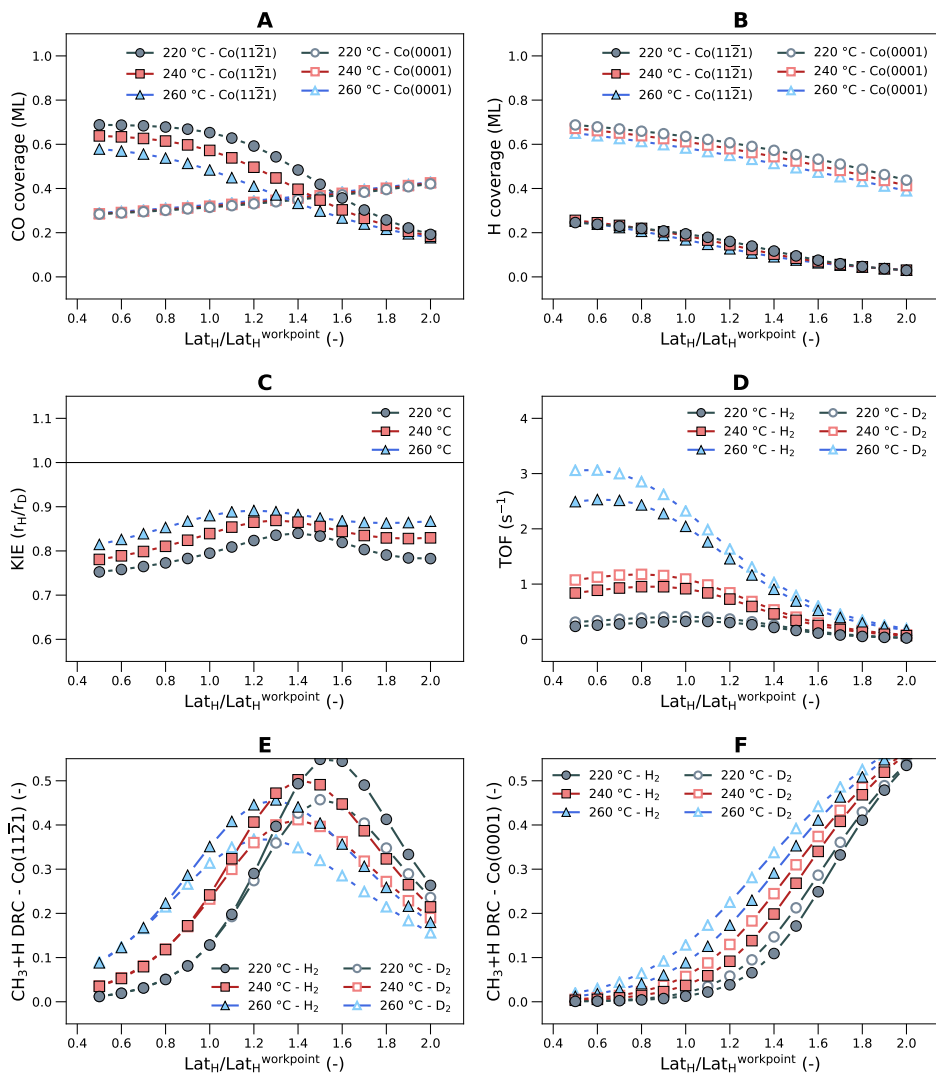


Figure B9: Sensitivity of the microkinetic modeling results at $\text{H}_2/\text{CO} = 450/45$ mbar as a function of the lateral interaction penalty per H atom. a) CO coverage on both the stepped $\text{Co}(11\bar{1}\bar{1})$ surface and the terrace $\text{Co}(0001)$ surface; b) H coverage; c) Kinetic isotope effect for CO conversion; d) TOF of CO conversion for both a hydrogen and a deuterium feed; e) Degree of rate control for the final hydrogenation step on the stepped $\text{Co}(11\bar{1}\bar{1})$ surface; f) Degree of rate control for the final hydrogenation step on the terrace $\text{Co}(0001)$ surface.

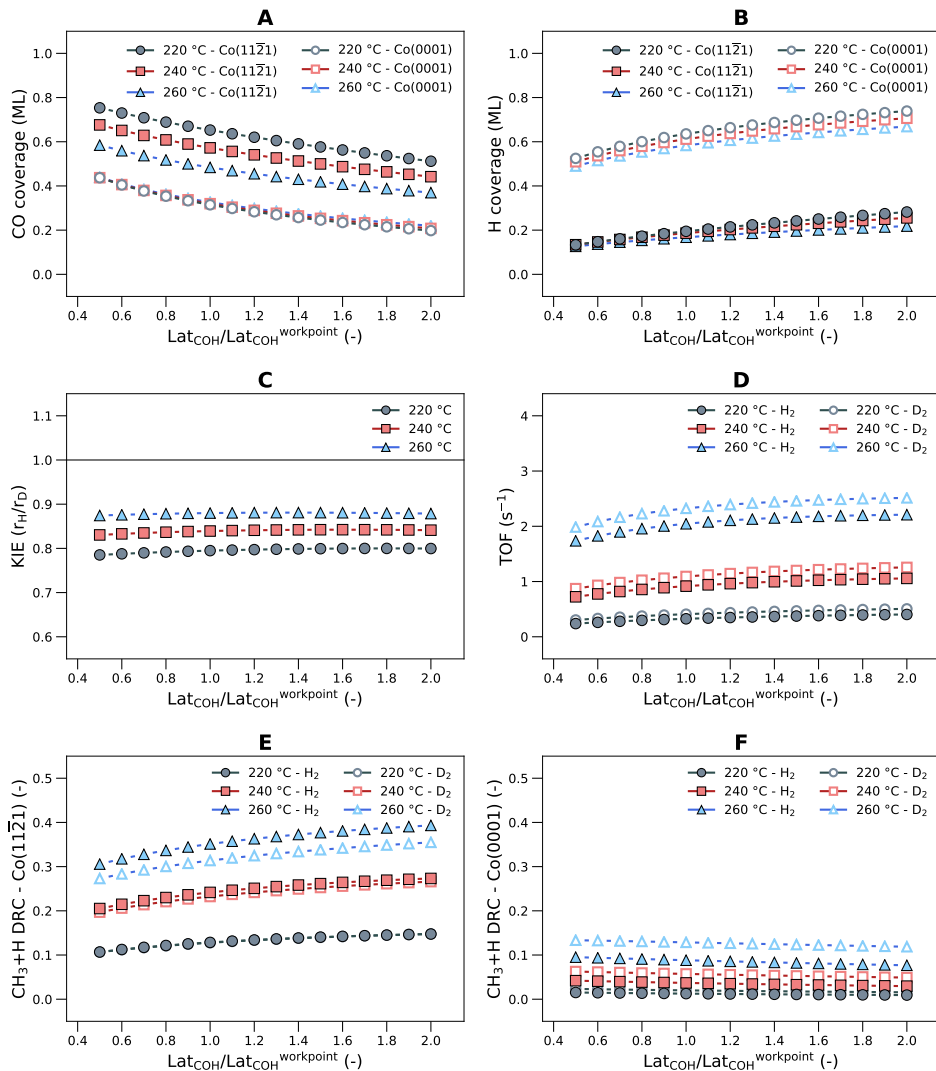


Figure B10: Sensitivity of the microkinetic modeling results at H₂/CO = 450/45 mbar to changing at the same time the lateral interaction penalties per atom of C, O, and H. a) CO coverage on both the stepped Co(11 $\bar{1}$ 21) surface and the terrace Co(0001) surface; b) H coverage; c) Kinetic isotope effect for CO conversion; d) TOF of CO conversion for both a hydrogen and a deuterium case; e) Degree of rate control for the final hydrogenation step on the stepped Co(11 $\bar{1}$ 21) surface; f) Degree of rate control for the final hydrogenation step on the terrace Co(0001) surface.

Table B9: Migration barriers and vibrational partition functions for the migration reactions in the microkinetic model between the Co(0001) and Co(11 $\bar{2}$ 1) surfaces. The migration barriers are based on the reaction enthalpy of migration with an additional 20 kJ/mol barrier.

Migrating intermediate	Migration barrier		$Q_{\text{step}}/Q_{\text{terrace}}$		
	Terrace to step (kJ/mol)	Step to Terrace (kJ/mol)	493.15 K	513.15 K	523.15 K
	C*	20.00	74.71	1.12	1.13
CH*	20.00	29.09	1.10	1.10	1.10
CH ₂ *	20.00	38.87	1.38	1.39	1.40
CH ₃ *	20.00	28.12	2.10	2.11	2.12
O*	20.00	40.13	1.14	1.14	1.15
OH*	20.00	57.27	1.48	1.48	1.47
CD*	20.00	29.06	1.08	1.08	1.08
CD ₂ *	20.00	39.02	1.37	1.38	1.39
CD ₃ *	20.00	28.39	2.19	2.20	2.21
OD*	20.00	57.60	1.40	1.40	1.40

CHAPTER 6

FIRST-PRINCIPLES BASED MICROKINETIC MODELING OF FISCHER-TROPSCH SYNTHESIS ON COBALT

Contents

6.1	Introduction	126
6.2	Computational methods	128
6.3	Results and discussion	129
6.3.1	Elementary steps for C ₂ formation	130
6.3.2	Elementary steps for C ₃ formation	131
6.3.3	Extrapolation barriers for C ₄₊ formation	134
6.3.4	Adsorption and desorption steps	135
6.3.5	Microkinetics simulations of FT synthesis: Co(11 $\bar{2}$ 1)	135
6.3.6	Microkinetics simulations of FT synthesis: Co(11 $\bar{2}$ 1) + Co(0001)	143
6.3.7	Microkinetics simulations of CO ₂ hydrogenation	152
6.4	Conclusions	160
6.5	References	161
	Appendix C	165
	Appendix D	182

Abstract

A microkinetic model is developed describing all relevant elementary reaction steps underlying the Fischer-Tropsch (FT) reaction at Co(11 $\bar{2}$ 1) step-edge and Co(0001) terrace sites. Important aspects such as lateral interactions, different chain-growth mechanisms, and the migration of adsorbed species between the two considered surfaces in dual-site model are considered. Overall, CH_x-CH_y coupling pathways relevant to the carbide mechanism have

favorable barriers compared to CO dissociation, while the overall barrier for chain growth via CO insertion is much higher. Microkinetics simulations of the Co(11 $\bar{2}$ 1) surface predict kinetic parameters that correspond well with experimental kinetic data obtained for cobalt catalysts. The chain-growth probability decreases with increasing temperature and H₂/CO ratio, which is caused by lower CH_x and H coverage. The CH₄ selectivity is much lower than experimentally observed, showing that step-edge sites mainly catalyze formation of olefins. O removal and CO dissociation are steps that significantly control the overall CO consumption rate. The simulations show that the Co(11 $\bar{2}$ 1) model surface is highly active and selective for the FT reaction with a proper chain-growth probability. Adding terrace Co(0001) sites in a dual-site model leads to a substantially higher CH₄ selectivity at the expense of the C₂₊-hydrocarbons selectivity. At typical FT conditions, chain growth occurs exclusively at step-edge sites, while additional CH₄ stems from CH and CH₃ migration from step-edge to terrace sites followed by their hydrogenation. Under conditions of low CO coverage, a very small contribution of chain growth on terrace sites is noted. Replacing CO by CO₂ as the reactant shifts the product distribution nearly completely to CH₄ with CO as a minor by-product. The much higher H/CO coverage ratio during CO₂ hydrogenation in comparison to CO hydrogenation causes the high CH₄ selectivity. The current results provide novel insight into the importance of a proper balance of CO and H species at the surface and the role of low-reactive terrace sites close to step-edge sites in the formation of CH₄ during the FT reaction.

6.1 Introduction

Fischer-Tropsch (FT) synthesis is an important process for the conversion of synthesis gas into liquid transportation fuels. Supported cobalt and iron carbide catalysts are predominantly used as heterogeneous catalysts in commercial FT technology [1]. Understanding the mechanism of the complex sequence of elementary reaction steps that underlie the conversion of CO and H₂ into long-chain hydrocarbons is interesting from the fundamental as well as the practical perspective [2]. Computational chemistry can be of great utility in understanding the relation between the composition of the adsorbed layer and the balanced rates of reactions such as the generation growth species by CO dissociation, C–C coupling, product desorption and O removal that give rise to high activity and selectivity on the basis of particular surface topologies reflecting facets and sites at the surface of nanoparticles. While density functional theory (DFT) is the state-of-the-art technique used in computational heterogeneous catalysis to determine the energetics (stable states, transition states) of the individual elementary reaction steps underlying the mechanism at (periodic) surface, microkinetics can predict the composition of the adsorbed layer and elementary reaction rates under steady-state and transient conditions. A large number of such computational studies have already been devoted to the FT reaction [3–23]. Many of these use calculations to determine activation barriers of important elementary reaction steps with a common focus on CO bond dissociation [5–10, 13, 15, 19, 21]. Relatively few studies have addressed the complete reaction network of the FT reaction by microkinetics simulations, which can

help to resolve aspects such as rate- and selectivity-controlling steps [24–29]. There remains a need to better understand structure sensitivity, i.e. the importance of step-edge sites and the involvement, if at all, of terrace sites, and the role of lateral interactions. These important aspects have been largely neglected so far in first-principles-based microkinetics simulations.

CO dissociation is a crucial step in the overall FT reaction as it provides the CH_x growth monomer in the carbide mechanism or initiates chain growth in the CO-insertion mechanism. In the carbide mechanism, the activation barrier of this step has to be sufficiently low to maintain a high formation rate of monomeric species that can be inserted into the growing hydrocarbon chains [3, 4, 9, 30]. Two main reaction channels for CO bond dissociation at the catalytic surface are usually considered. In the first mechanism, the C–O bond is directly cleaved into atomic carbon and oxygen. The alternative is the hydrogenation of adsorbed CO to $\text{CH}_x\text{O}(\text{H})$ species in which the C–O bond is weakened leading to a lower barrier than the direct pathway. However, the overall barrier will also depend on the activation barrier for the hydrogenation of adsorbed CO. The previous chapters have shown that these direct and H-assisted pathways have different overall activation barriers on both the terrace and stepped surfaces exposed on a cobalt nanoparticle. While the H-assisted HCO-pathway is preferred on the terrace Co(0001) surface, the corresponding overall barrier of 182 kJ/mol is too high to produce FT monomers at rates comparable to experimental turnovers that are of the order 10^{-2} - 10^{-1} s^{-1} [31, 32]. The direct CO dissociation step on the stepped Co(11 $\bar{2}$ 1) surface has a much lower barrier (100 kJ/mol), supporting the hypothesis that step-edge sites are the active sites of CO dissociation in the FT reaction.

The monomeric CH_x species can polymerize into hydrocarbon chains through carbon-carbon coupling steps and subsequent (de-)hydrogenation steps. A key question is whether this chain growth occurs near the CO dissociation site on the step-edge, or whether the chain growth occurs on the exposed terrace facets of the cobalt nanoparticle [33]. Other questions relate to the nature of the coupling CH_x species, the reversibility of the coupling steps, and the relation between chain growth and methane formation.

Microkinetic modeling can provide detailed insight into these mechanistic fundamentals, because it can predict intrinsic rates for elementary reaction steps underlying a complex mechanism such as that of the FT reaction. In this chapter we will focus on the reaction energetics of the FT reaction using DFT. In earlier chapters, we already discussed in detail relevant pathways for CO dissociation, C hydrogenation to CH_4 and O hydrogenation to H_2O on model step-edge and terrace sites. Here, we will focus on the elementary reaction steps related to chain growth and product formation. Using the corresponding energetics, microkinetics simulations were performed to predict rates, product distribution and other relevant kinetic information for step-edge and terrace model surfaces. Following simulations of these two extreme cases, we also investigated the influence of migration of relevant surface reaction intermediates in dual-site surface models that contained different ratios of step-edge and terrace sites, as can be expected to occur on nanoparticles. A thorough sensitivity analysis applied to such simulations unveils the dominant mechanistic pathways underlying the FT process.

6.2 Computational methods

All quantum-chemical calculations were performed using a plane-wave density functional theory approach with the projector-augmented wave (PAW) method [34], as implemented in the Vienna ab initio simulation package (VASP) [35–38]. For exchange-correlation, the Perdew-Burke-Ernzerhof (PBE) functional was used [39]. The plane-wave basis set was limited to a 400 eV kinetic energy cut-off base. A gamma-centered Monkhorst-Pack $21 \times 21 \times 21$ k-point mesh [40] was used for bulk HCP Co, and a $5 \times 5 \times 1$ k-point mesh for Co surface slabs. Calculations for molecular references in the gas phase only employed the gamma point in a $10 \times 10 \times 10 \text{ \AA}^3$ cell. We used Co(0001) and Co(11 $\bar{2}$ 1) as model surfaces for the terrace sites and step-edges on cobalt nanoparticles. These surfaces were chosen as Co(0001) is often used in experimental surface science studies [41, 42] and the Co(11 $\bar{2}$ 1) surface exposes step-edge sites that are highly active for CO dissociation [13]. The particular configuration of atoms in the Co(11 $\bar{2}$ 1) step-edge site is a perturbed arrangement of the classical B₅-site as referred to by Van Hardeveld and Hartog [43]. With a barrier of 100 kJ/mol for direct CO dissociation this site is more active than e.g. the FCC Co(311) facet at ~ 150 kJ/mol [13]. The Co lattice parameters for our calculations correspond to 2.49 Å, 2.49 Å and 4.03 Å for the *a*, *b* and *c* directions respectively. The Co(0001) surface was constructed from a (3 × 3) unit cell with 5 atomic layers, which corresponds to 45 Co atoms per unit cell. The Co(11 $\bar{2}$ 1) surface was constructed from a (2 × 2) unit cell with 3 atomic layers (48 Co atoms per unit cell). All reactions were performed in the low coverage limit. Adsorbates on the Co(0001) surface slab were placed with mirror symmetry in the *ab*-plane to avoid spurious dipole-dipole interactions between neighboring unit cells. For the Co(11 $\bar{2}$ 1) surface slab the adsorbates were placed using inversion symmetry. All atomic positions were optimized using the conjugate-gradient technique. We explored reaction paths with the climbing image nudged elastic band (cNEB) implementation [44–46]. The transition states (TS) were optimized using a quasi-Newton algorithm. The true nature of each TS was confirmed by the occurrence of a single imaginary frequency in the direction of the reaction coordinate. The Hessian matrices for the frequency calculations were determined using the finite displacement technique. The corresponding vibrations were also used to compute the zero-point energy (ZPE) corrections and vibrational partition functions for all adsorbed species and transition states.

The microkinetics simulations were carried out using the in-house developed MKMCXX code [24, 47]. An isobaric and isothermal continuous stirred tank reactor (CSTR) model was used as earlier described in Chapter 5. The flow rates at the reactor inlet were chosen to obtain a residence time of 1 s. The surface area of the active sites was set to 5.38 \AA^2 , which corresponds to the area of a (1 × 1) unit cell of Co(0001). All reaction steps were corrected for entropy, as described in Chapter 5. Lateral interactions were implemented by defining a lateral penalty for each species. The penalty for a species *x* corresponded to Eq. (6.1) and Eq. (6.2).

$$E_x^{\text{lat}} = E_x^{\theta=1} \times \frac{(101^{\theta_{\text{lat}}} - 1)}{100} \quad (6.1)$$

$$\theta_{\text{lat}} = \theta_{\text{total}} - \theta_* - 0.5 \cdot \theta_{\text{H}} \quad (6.2)$$

We used lateral interaction parameters of $E_{\text{CO}}^{\theta=1} = 450$ kJ/mol, $E_{\text{C}}^{\theta=1} = E_{\text{O}}^{\theta=1} = 300$ kJ/mol, and $E_{\text{H}}^{\theta=1} = 100$ kJ/mol, representing the decreased stability of these species at higher coverages as described in Chapter 3. In the current implementation, we left out the terms θ_{LB} and θ_{UB} in Eq. (2), which resulted in a better description of the DFT-lateral interactions as a function of coverage as compared with the model in Chapter 3. We assumed that all surface species contribute equally to the lateral interaction potential with the exception of hydrogen. Similar corrections were applied to the adsorption energies of CO and CO₂ to account for the over-binding and, at the same time, maintaining thermodynamic consistency of the reaction heats with tabulated data for methanation and the water-gas shift reaction [48].

The CO conversion (X_{CO}) and CH₄ selectivity (S_{CH_4}) within the CSTR implementation were calculated from the molar flow rates (F_i) as shown in Eq. (6.3) and Eq. (6.4):

$$X_{\text{CO}} = \frac{(F_{\text{CO}}^{\text{in}} - F_{\text{CO}}^{\text{out}})}{F_{\text{CO}}^{\text{in}}} \quad (6.3)$$

$$S_{\text{CH}_4} = \frac{F_{\text{CH}_4}^{\text{out}}}{(F_{\text{CO}}^{\text{in}} - F_{\text{CO}}^{\text{out}})} \quad (6.4)$$

The chain-growth probability (α) is defined as the rate of propagation (r_p) over the sum of the rates of propagation and termination (r_t). We determined the chain-growth probability from the slope of the Anderson-Schulz-Flory (ASF) distribution for carbon numbers (n) 5 to 8.

$$\alpha = \frac{r_p}{r_p + r_t} \cong \exp\left(\frac{d \ln F_{\text{C}_n}^{\text{out}}}{dn}\right) \quad (6.5)$$

We performed a sensitivity analysis for every elementary reaction step in order to determine the degree of rate control (DRC), the degree of selectivity control (DSC) and degree of chain-growth control (DCGC).

$$\text{DRC}_{\text{CO}}^i = \left(\frac{\partial \ln r_{\text{CO}}}{\partial \ln k_i}\right)_{k_{j \neq i}, K_i} \quad (6.6)$$

$$\text{DSC}_{\text{CH}_4}^i = S_{\text{CH}_4} \cdot (\text{DRC}_{\text{CH}_4}^i - \text{DRC}_{\text{CO}}^i) \quad (6.7)$$

$$\text{DCGC}^i = \left(\frac{\partial \alpha}{\partial \ln k_i}\right)_{k_{j \neq i}, K_i} \quad (6.8)$$

6.3 Results and discussion

In the following sections, a microkinetic model for CO hydrogenation to long-chain hydrocarbons will be presented together with simulations based on this model that predict important aspects of the FT reaction such as CO conversion rate, product distribution, chain-growth probability, surface coverages and degrees of rate and selectivity control. We will discuss the

Table 6.1: Elementary reaction step barriers for carbon-carbon coupling reactions on Co(0001) and Co(11 $\bar{2}$ 1). All barriers are corrected for the zero-point energy and are referenced to the most stable surface intermediates.

Elementary reaction	Co(0001)		Co(11 $\bar{2}$ 1)	
	E_{act} forward (kJ/mol)	E_{act} backward (kJ/mol)	E_{act} forward (kJ/mol)	E_{act} backward (kJ/mol)
$\text{C}^* + \text{C}^* \rightleftharpoons \text{CC}^*$	106	142	86	112
$\text{C}^* + \text{CH}^* \rightleftharpoons \text{CCH}^*$	87	142	65	95
$\text{C}^* + \text{CH}_2^* \rightleftharpoons \text{CCH}_2^*$	75	133	81	98
$\text{C}^* + \text{CH}_3^* \rightleftharpoons \text{CCH}_3^*$	99	164	97	92
$\text{CH}^* + \text{CH}^* \rightleftharpoons \text{CHCH}^*$	65	117	70	62
$\text{CH}^* + \text{CH}_2^* \rightleftharpoons \text{CHCH}_2^*$	63	67	69	69
$\text{CH}^* + \text{CH}_3^* \rightleftharpoons \text{CHCH}_3^*$	108	94	93	73
$\text{CH}_2^* + \text{CH}_2^* \rightleftharpoons \text{CH}_2\text{CH}_2^*$	40	76	112	141
$\text{CH}_2^* + \text{CH}_3^* \rightleftharpoons \text{CH}_2\text{CH}_3^*$	98	95	102	97

formation barriers of C_2 and C_3 olefins and paraffins and adsorption and desorption rate constants of reactants and products. Corrections will be made to the desorption energies of the product molecules and the extrapolated C_{4+} formation barriers in order to be consistent with the overall thermodynamics of the FT reaction. Although mostly within the accuracy of the DFT energetics, these corrections are important for a thermodynamically consistent microkinetic model.

6.3.1 Elementary steps for C_2 formation

We computed the barriers for the $\text{CH}_x + \text{CH}_y$ coupling reactions on both surfaces and found that most barriers are lower than the activation barrier for direct CO scission on the step-edge (<100 kJ/mol). Table 6.1 shows that the lowest coupling barrier on the Co(0001) surface is the reaction between 2 CH_2 fragments with a forward barrier of only 40 kJ/mol. On the Co(11 $\bar{2}$ 1) surface, the C+CH coupling has the lowest barrier with a value of 65 kJ/mol among the investigated reaction pathways. We also calculated the overall barriers for these steps by taking into account the reaction heats for the formation of the $\text{CH}_{x/y}$ species from atomic C as presented in Chapter 5. In this way, the barriers increase to 78 kJ/mol and 85 kJ/mol for $\text{CH}_2 + \text{CH}_2$ coupling on Co(0001) and C+CH coupling on Co(11 $\bar{2}$ 1) respectively. Due to the exothermic nature of CH formation on the terrace Co(0001) surface the lowest overall barriers are the CH+CH and CH+ CH_2 coupling steps. Both steps are limited by a barrier of 71 kJ/mol for hydrogenation of C to CH.

We expect that the rate of C_2 formation is controlled by the CO dissociation barrier, as the lowest overall barriers for C-C coupling are lower than the lowest CO dissociation pathway. An alternative chain growth pathway is via the CO insertion mechanism. In this mechanism CO adsorbates are inserted into the growing hydrocarbon chain and C-O bond scission occurs after formation of the C-C bond. The CO insertion mechanism is expected to prevail only if the overall barriers for coupling and subsequent C-O bond scission are

Table 6.2: Elementary reaction step barriers for the CO-insertion mechanism on Co(0001) and Co(11 $\bar{2}$ 1). All barriers are corrected for the zero-point energy and are referenced to the most stable surface intermediates.

Elementary reaction	Co(0001)		Co(11 $\bar{2}$ 1)	
	E_{act} forward (kJ/mol)	E_{act} backward (kJ/mol)	E_{act} forward (kJ/mol)	E_{act} backward (kJ/mol)
$\text{C}^* + \text{CO}^* \rightleftharpoons \text{CCO}^*$	85	67	94	55
$\text{CH}^* + \text{CO}^* \rightleftharpoons \text{CHCO}^*$	86	46	103	65
$\text{CH}_2^* + \text{CO}^* \rightleftharpoons \text{CH}_2\text{CO}^*$	94	27	131	82
$\text{CH}_3^* + \text{CO}^* \rightleftharpoons \text{CH}_3\text{CO}^*$	186	118	129	60
$\text{CCO}^* \rightleftharpoons \text{CC}^* + \text{O}^*$	192	180	122	188
$\text{CHCO}^* \rightleftharpoons \text{CCH}^* + \text{O}^*$	144	173	80	151
$\text{CH}_2\text{CO}^* \rightleftharpoons \text{CCH}_2^* + \text{O}^*$	88	147	74	143
$\text{CH}_3\text{CO}^* \rightleftharpoons \text{CCH}_3^* + \text{O}^*$	64	131	69	134

lower than the 100 kJ/mol barrier for direct CO scission, which is the highest barrier for the carbide mechanism. Table 6.2 shows this is not the case for the considered Co surfaces. The lowest CO coupling barrier is 85 kJ/mol for C+CO on the Co(0001) surface. However, the corresponding C–O bond scission in CCO has a high barrier of 192 kJ/mol. Relative to C, H, and CO, the lowest overall barriers for CH_xC –O scission are 165 kJ/mol for CHCO on Co(0001) and 139 kJ/mol for CHCO on Co(11 $\bar{2}$ 1).

Table 6.3 lists the barriers for hydrogenation of C_2 species. All barriers are below 100 kJ/mol, except for CCH dehydrogenation and CHCH hydrogenation on Co(0001). The majority of the hydrogenation reactions are endothermic, indicating that many of these steps will be pseudo-equilibrated during the FT process. Figure 6.1 shows the reaction energy diagrams for hydrogenation of adsorbed CC species on the Co(0001) and Co(11 $\bar{2}$ 1) surfaces. The overall barrier for CH_2CH_2 formation from CC is 80 kJ/mol on the Co(0001) surface and 128 kJ/mol on the Co(11 $\bar{2}$ 1) surface. However, on the Co(0001) surface the CHCH state is lowest in energy relative to the states of adsorbed CC and H. Referencing the overall barrier to the CHCH state gives a barrier of 133 kJ/mol, which is similar to that of the stepped surface. Formation of CH_3CH_3 from CC corresponds to an overall barrier of 183 kJ/mol on Co(11 $\bar{2}$ 1). On Co(0001), this barrier is 160 kJ/mol referenced to CC and 213 kJ/mol referenced to CHCH. Regardless of the surface and the reference state, the overall barrier for CH_3CH_3 formation is clearly higher than the one for CH_2CH_2 formation with a difference of 55–80 kJ/mol. Although the desorption barrier for CH_2CH_2 is 77–101 kJ/mol higher than for CH_3CH_3 (Section 6.3.4), the desorption rate will be strongly increased by the gain in entropy. Therefore, we expect that ethylene is the preferred product over ethane.

6.3.2 Elementary steps for C_3 formation

In the microkinetics simulations, we aimed at including chain-growth step for hydrocarbons with a length of 20 C atoms in order to exclude significant cut-off effects on the FT kinetics [26]. As explicit computation of all barriers of these elementary reaction steps is unreasonably

Table 6.3: Elementary reaction step barriers for C_2 -hydrogenation reactions on Co(0001) and Co(11 $\bar{2}$ 1). All barriers are corrected for the zero-point energy and are referenced to the most stable surface intermediates.

Elementary reaction	Co(0001)		Co(11 $\bar{2}$ 1)	
	E_{act} forward (kJ/mol)	E_{act} backward (kJ/mol)	E_{act} forward (kJ/mol)	E_{act} backward (kJ/mol)
$CC^* + H^* \rightleftharpoons CCH^*$	70	108	54	39
$CCH^* + H^* \rightleftharpoons CCH_2^*$	78	44	61	27
$CCH_2^* + H^* \rightleftharpoons CCH_3^*$	46	54	61	36
$CHCH^* + H^* \rightleftharpoons CHCH_2^*$	102	16	36	24
$CHCH_2^* + H^* \rightleftharpoons CHCH_3^*$	48	31	38	15
$CH_2CH_2^* + H^* \rightleftharpoons CH_2CH_3^*$	47	9	44	6
$CCH^* + H^* \rightleftharpoons CHCH^*$	73	88	69	10
$CCH_2^* + H^* \rightleftharpoons CHCH_2^*$	50	15	43	7
$CCH_3^* + H^* \rightleftharpoons CHCH_3^*$	62	2	51	17
$CHCH_2^* + H^* \rightleftharpoons CH_2CH_2^*$	48	41	42	50
$CHCH_3^* + H^* \rightleftharpoons CH_2CH_3^*$	64	37	34	27
$CH_2CH_3^* + H^* \rightleftharpoons CH_3CH_3^*$	84	85	67	57

expensive, we extrapolated DFT-based C_2 formation data. For this purpose, we replaced one of the H atoms of C_1 and C_2 surface fragments with a group representing a dangling chain of $(CH_2)_nCH_3$. To assess the validity of this approach, we explicitly computed the formation barriers of C_3 fragments starting from C_2 intermediates. An advantage of this approach is that we can extrapolate from C_2 - C_3 data rather than from C_1 - C_2 data [17].

Table 6.4 shows the computed energy barriers for the C_1 - C_2 coupling reactions leading to C_3 species. We only considered the coupling of C_1 species with C_2 species of the form CH_xCH_3 . The results are mostly very similar to the C_2 formation steps in Table 6.2. The largest differences in forward coupling barriers are 23 kJ/mol and 14 kJ/mol for the Co(0001) and Co(11 $\bar{2}$ 1) surfaces, respectively. The largest differences in the decoupling barriers are 39

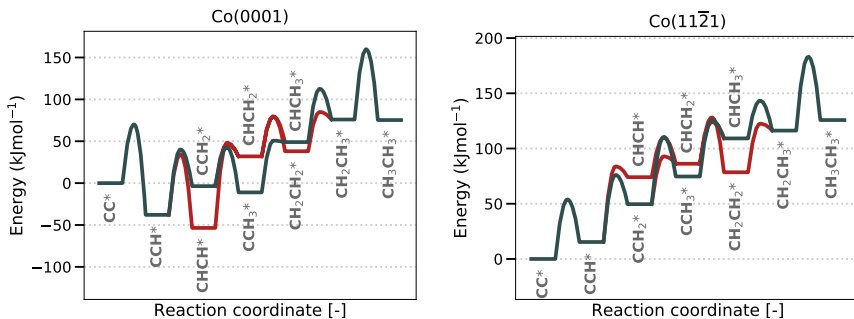


Figure 6.1: Reaction energy diagrams for the C_2 hydrogenation reactions on the terrace Co(0001) and stepped Co(11 $\bar{2}$ 1) surfaces. The energies are referenced to the states of adsorbed CC and H.

Table 6.4: Elementary reaction step barriers for C₃-formation reactions on Co(0001) and Co(11 $\bar{2}$ 1). All barriers are corrected for the zero-point energy and are referenced to the most stable surface intermediates.

Elementary reaction	Co(0001)		Co(11 $\bar{2}$ 1)	
	E _{act} forward (kJ/mol)	E _{act} backward (kJ/mol)	E _{act} forward (kJ/mol)	E _{act} backward (kJ/mol)
C* + CCH ₃ * ⇌ CCCH ₃ *	85	128	79	112
C* + CHCH ₃ * ⇌ CCHCH ₃ *	83	151	81	112
C* + CH ₂ CH ₃ * ⇌ CCH ₂ CH ₃ *	76	169	93	99
CH* + CCH ₃ * ⇌ CHCCH ₃ *	83	118	73	67
CH* + CHCH ₃ * ⇌ CHCHCH ₃ *	69	80	78	94
CH* + CH ₂ CH ₃ * ⇌ CHCH ₂ CH ₃ *	120	134	80	75
CH ₂ * + CCH ₃ * ⇌ CH ₂ CCH ₃ *	81	63	72	55
CH ₂ * + CHCH ₃ * ⇌ CH ₂ CHCH ₃ *	50	88	106	140
CH ₂ * + CH ₂ CH ₃ * ⇌ CH ₂ CH ₂ CH ₃ *	91	119	96	104
CH ₃ * + CCH ₃ * ⇌ CH ₃ CCH ₃ *	154	80	111	54
CH ₃ * + CHCH ₃ * ⇌ CH ₃ CHCH ₃ *	144	113	102	97

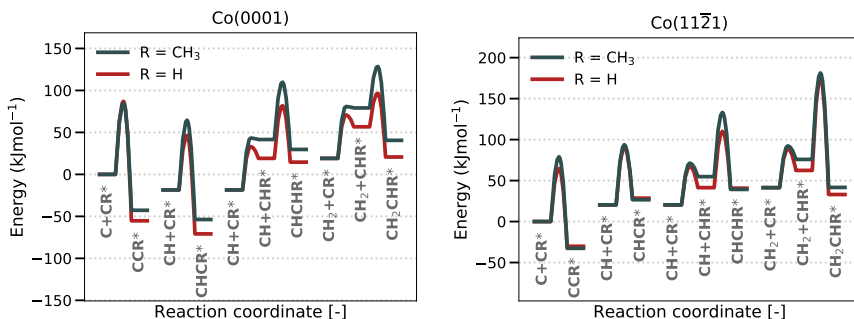


Figure 6.2: Reaction energy diagrams for the C+CR, CH+CR, CH+CHR, and CH₂+CHR coupling reactions on the terrace Co(0001) and stepped Co(11 $\bar{2}$ 1) surfaces. The energies are referenced to the states of adsorbed C, CR, and H.

kJ/mol for the Co(0001) surface and 25 kJ/mol for the Co(11 $\bar{2}$ 1) surface. We constructed reaction energy diagrams for the C+CR, CH+CR, CH+CHR, and CH₂+CHR coupling reactions, where R is either H or CH₃. Figure 6.2 shows that, on the Co(0001) surface, the C₃ coupling products are slightly less stable than the C₂ products. Nevertheless, the C+CR and CH+CR pathways remain below 100 kJ/mol. The differences are smaller on the stepped Co(11 $\bar{2}$ 1) surface. Again, the C₃ coupling steps C+CR and CH+CR are lower than 100 kJ/mol. Therefore, we expect one of these two pathways to be the dominant chain-growth pathway.

Table 6.5 lists the barriers for hydrogenation of C₃ species. Nearly all barriers are below 100 kJ/mol, similar to those of the C₂ hydrogenation steps. The corresponding reaction energy diagrams can be found in Figure 6.3. The overall barrier from adsorbed CCCH₃ to adsorbed CH₂CHCH₃ is 128 kJ/mol on the Co(0001) surface and 114 kJ/mol on the

Table 6.5: Elementary reaction step barriers for C₃-hydrogenation reactions on Co(0001) and Co(11 $\bar{2}$ 1). All barriers are corrected for the zero-point energy and are referenced to the most stable surface intermediates.

Elementary reaction	Co(0001)		Co(11 $\bar{2}$ 1)	
	E _{act} forward (kJ/mol)	E _{act} backward (kJ/mol)	E _{act} forward (kJ/mol)	E _{act} backward (kJ/mol)
CCCH ₃ * + H* ⇌ CCHCH ₃ *	99	65	62	26
CCHCH ₃ * + H* ⇌ CCH ₂ CH ₃ *	53	49	65	33
CHCCH ₃ * + H* ⇌ CHCHCH ₃ *	98	15	69	57
CHCHCH ₃ * + H* ⇌ CHCH ₂ CH ₃ *	45	20	70	43
CH ₂ CCH ₃ * + H* ⇌ CH ₂ CHCH ₃ *	94	90	92	109
CH ₂ CHCH ₃ * + H* ⇌ CH ₂ CH ₂ CH ₃ *	45	8	38	4
CH ₃ CCH ₃ * + H* ⇌ CH ₃ CHCH ₃ *	47	30	10	29
CH ₃ CHCH ₃ * + H* ⇌ CH ₃ CH ₂ CH ₃ *	57	85	61	53
CCCH ₃ * + H ⇌ CHCCH ₃ *	72	82	68	9
CHCCH ₃ * + H* ⇌ CH ₂ CCH ₃ *	105	15	57	25
CH ₂ CCH ₃ * + H* ⇌ CH ₃ CCH ₃ *	98	42	53	10
CCHCH ₃ * + H* ⇌ CHCHCH ₃ *	52	14	48	12
CHCHCH ₃ * + H* ⇌ CH ₂ CHCH ₃ *	55	44	42	39
CH ₂ CHCH ₃ * + H* ⇌ CH ₃ CHCH ₃ *	82	14	45	4
CCH ₂ CH ₃ * + H* ⇌ CHCH ₂ CH ₃ *	61	1	50	19
CHCH ₂ CH ₃ * + H* ⇌ CH ₂ CH ₂ CH ₃ *	62	38	37	29
CH ₂ CH ₂ CH ₃ * + H* ⇌ CH ₃ CH ₂ CH ₃ *	84	81	67	51

Co(11 $\bar{2}$ 1) surface. The overall barriers for CH₃CH₂CH₃ formation are 205 kJ/mol and 174 kJ/mol, respectively. Similar to C₂ hydrogenations, these overall barriers are higher than the barrier for CO dissociation. The formation of the paraffin is more difficult than that of the olefin. The species with the lowest energy that can participate in chain growth (CCH₂CH₃) has an overall formation barrier comparable to that of CO dissociation. This is an indication why cobalt can be a successful Fischer-Tropsch catalyst: CO bond scission and chain growth compete, while termination to olefins has a slightly higher barrier than these steps.

6.3.3 Extrapolation barriers for C₄₊ formation

Explicit DFT calculations showed that the reaction energetics for C₂ and C₃ olefin and paraffin formation are comparable in terms of overall reaction barriers. The largest differences occur for the Co(0001) surface. Substitution of CH₃ by a larger CH₂CH₃ group should have a smaller influence relatively speaking. Accordingly, we expect that the stability differences between C₃ and C₄ (and between C₄ and C₅, etc.) are smaller than those between C₂ and C₃. Thus, we assumed that the barriers for the formation of hydrocarbon chains with 4 or more C atoms are the same as the barriers computed for C₃ species. We further corrected these data to obey thermodynamic consistency according to the approach outlined in Appendix C.2.

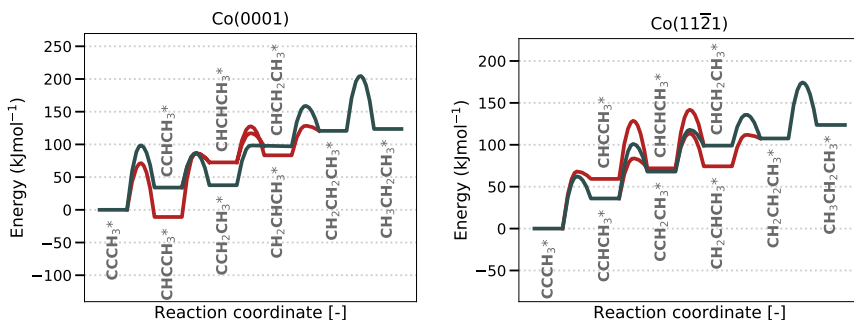


Figure 6.3: Reaction energy diagram for the C_3 hydrogenation reactions on the terrace $Co(0001)$ and stepped $Co(11\bar{2}1)$ surfaces. The energies are referenced to the states of adsorbed $CCCH_3$ and H.

Table 6.6: Enthalpic desorption barriers for hydrocarbon species on $Co(0001)$ and $Co(11\bar{2}1)$. All barriers are corrected for the zero-point energy.

Elementary reaction	$Co(0001)$ Desorption barrier (kJ/mol)	$Co(11\bar{2}1)$ Desorption barrier (kJ/mol)
$CH_2CH_2 + * \rightleftharpoons CH_2CH_2^*$	81	112
$CH_3CH_3 + * \rightleftharpoons CH_3CH_3^*$	4	11
$CH_2CHCH_3 + * \rightleftharpoons CH_2CHCH_3^*$	69	95
$CH_3CH_2CH_3 + * \rightleftharpoons CH_3CH_2CH_3^*$	3	6
$CH_2CH-R + * \rightleftharpoons CH_2CH-R^*$	69	95
$CH_3CH_2-R + * \rightleftharpoons CH_3CH_2-R^*$	2	5

6.3.4 Adsorption and desorption steps

The enthalpy barriers for desorption of hydrocarbon species with two or more C atoms are given in Table 6.6. The desorption barriers for C_2 and C_3 were determined with DFT calculations and include small corrections to achieve thermodynamic consistency as described in Appendix C.1. The C_{4+} barriers were taken to be the same as the C_3 barriers with similar additional corrections corresponding to the tabulated data. The resulting energies show that the olefins have a desorption barrier in the 69–112 kJ/mol range, while the paraffins only have a small desorption barrier of 2–11 kJ/mol. Adsorption is relatively speaking stronger for C_2 species and systematically 3–31 kJ/mol stronger on the stepped $Co(11\bar{2}1)$ surface than on the terrace $Co(0001)$ surface.

6.3.5 Microkinetics simulations of FT synthesis: $Co(11\bar{2}1)$

The microkinetics simulations were carried out using the energetics for relevant elementary reaction steps including CO dissociation, C hydrogenation to CH_4 , O hydrogenation to H_2O , CO_2 formation and C–C coupling reactions and hydrogenations to olefins and paraffins. We compare our results to experimental kinetic data published by Chen et al. for a Co/SiO_2 catalyst [30, 33, 49–51], because they were obtained under conditions free from heat and

mass transfer limitations. Moreover, experimental steady-state isotopic transient kinetic analysis (SSITKA) data reported in this work allowed determining the CO surface coverage under working conditions. A kinetic analysis of the various steady-state and transient kinetic data demonstrated different regimes of rate-controlling steps as a function of temperature and H₂/CO ratio. For this purpose, we have chosen as reaction conditions temperatures of 220 °C, 240 °C and 260 °C, a CO pressure in the 90-534 mbar range and a H₂ pressure in the 225-1500 mbar range. Typically, partial pressures were varied at each temperature to establish the influence on CO conversion and product distribution. In these simulations, the total pressure was kept constant at 5000 mbar by using an inert flow. Reaction orders in CO and H₂ and apparent activation energies were also determined at each set of conditions. A continuously stirred tank reactor (CSTR) model was used for these microkinetics simulations. We adjusted the space velocity to such value that relatively low CO conversion was obtained. The influence of higher CO conversion on the microkinetics is discussed in Appendix C.4. Kinetic parameters were extracted from these microkinetics simulations. We will discuss these below, first for Co(11 $\bar{2}$ 1) surface model, then for the case that terrace sites are added to such a model.

Figure 6.4 shows kinetic data for the Co(11 $\bar{2}$ 1) surface obtained by varying the CO partial pressure under constant H₂ pressure. As expected, the CO conversion decreases with increasing CO partial pressure. The corresponding TOF (turnover frequency) values slightly decrease with increasing CO partial pressure, which is also evident from the slight negative reaction orders with respect to CO (-0.1 to -0.2 range), consistent with many experimentally reported reaction orders. The TOF is in the 1-10 s⁻¹ range, which is higher than experimentally reported. Obviously, this can be explained by the fact that the experimental TOFs are usually based on the total available cobalt surface area [30], which also includes low- or non-reactive sites in addition to step-edge sites. The simulations predict that, in the explored H₂/CO ratio range, the CH₄ selectivity is between 1-6%, which is substantially lower than observed in the experimental data [30–32]. For instance, in the work of Bezemer et al. [31] the CH₄ selectivity was 22-53% at a H₂/CO ratio of 2 at a comparable total pressure. The CH₄ selectivity reported by Chen et al. was in the 10-90% range under similar conditions. The predicted CO₂ selectivity is below 1%, which is in line with experimental data [50]. The low CO₂ selectivity relates to a higher overall barrier for CO₂ formation (127 kJ/mol) in comparison with the overall barrier of H₂O formation (101 kJ/mol). With respect to C₂₊ products, mostly olefins with a negligible amount of paraffins are formed under these conditions. This indicates that olefins are the primary products of the FT reaction.

With increasing CO partial pressure, the CH₄ selectivity decreases (increasing C₂₊ selectivity). A higher CO coverage associated with the higher CO partial pressure leads to a lower H coverage, which explains the lower CH₄ selectivity and a slightly higher CO₂ selectivity (lower H₂O selectivity). This is commonly reported in experimental studies. The chain-growth probability also strongly increases with CO partial pressure. Earlier, Kruse and co-workers used this trend to claim that CO is the growth monomer for obtaining longer hydrocarbon chains [52]. The main reaction pathway followed for obtaining long

hydrocarbon chains in these simulations is, however, growth by CH_x monomers. The main reasons for a higher chain-growth probability with increasing CO partial pressure are a higher CH_x monomer concentration and a lower H coverage. The higher CH_x concentration increases the rate of chain-growth reactions, while the lower H coverage decreases the rate of termination reactions. The CO reaction orders become slightly more negative with increasing CO partial pressure, likely because the higher CO coverage suppresses the free site coverage and thus CO dissociation. The dependence of CO reaction order on temperature is weak. The H_2 reaction order increases with CO partial pressure and is more strongly affected by temperature. We observed that a higher temperature led to an increase of the H_2 reaction order. We attribute this to a significant increase of the coverage with atomic C (from 7% at 220°C to 12% at 260°C at a H_2/CO ratio of 10). Thus, we speculate that the increased H_2 reaction order is due to C hydrogenation to products becoming more rate-controlling.

Figure 6.5 shows the influence of varying the H_2 partial pressure on the microkinetics. The positive reaction order with respect to H_2 is evident from the increasing CO conversion with higher H_2 partial pressure, which is consistent with many experimental observations. The product distribution changed in the following way with increasing H_2 partial pressure: the CH_4 selectivity increased, the CO_2 selectivity slightly decreased and the chain-growth probability strongly decreased. At the highest H_2/CO ratio of 10, the H_2 reaction order decreased to 0.3-0.6 (from 0.7-0.9 at a H_2/CO ratio of 2). The corresponding atomic C coverage decreases from a range of 10-16% to 5-10%, which may indicate that C hydrogenation becomes less rate-controlling. Although CH_4 selectivity increases with H_2 partial pressure, the CH_4 selectivity remains below 10%, even at a H_2/CO ratio of 10.

Figure 6.6 shows the dependence of DRC, DSC for CH_4 and DCGC as a function of the temperature at a H_2/CO ratio of 2. The rate of CO consumption is significantly controlled by O removal for which the first hydrogenation step is the slowest. Other steps contributing to the DRC are CO dissociation, chain-growth steps and hydrogenation steps. The finding that O removal is a rate-controlling step is consistent with the predictions of periodic FT activity trends presented in the work of Filot et al. [24]. In the work of Chen et al., CO dissociation, CH_x hydrogenation to CH_4 and O removal steps were also identified as rate-controlling steps under conditions where CH_4 is a dominant product [49]. In agreement with this, we find that at higher temperature the DSC for CH_3 hydrogenation to CH_4 is high. Moreover, we observe in line with the Chen data that the contribution of CO dissociation to the rate control becomes more substantial at lower temperature. The data also show that the chain-growth probability is mainly controlled by the rate of the dominant coupling step, which is $\text{C}+\text{C}-(\text{CH}_2)_n\text{CH}_3$. Chain growth is inhibited by hydrogenation of $\text{CHCH}-(\text{CH}_2)_n\text{CH}_3$ intermediates, because the product can desorb as an olefin.

Figure 6.7 depicts the reaction network (relative rates and surface coverages) at a temperature of 220 °C and a H_2/CO ratio of 2. The rates are given carbon-based and relative to CO. Also indicated for each step are (in dark-red italic font) the ratios of the backward rates over the forward rates (equilibration ratios). Ratios close to unity represent a quasi-equilibrium for the indicated elementary reaction step, ratios close to

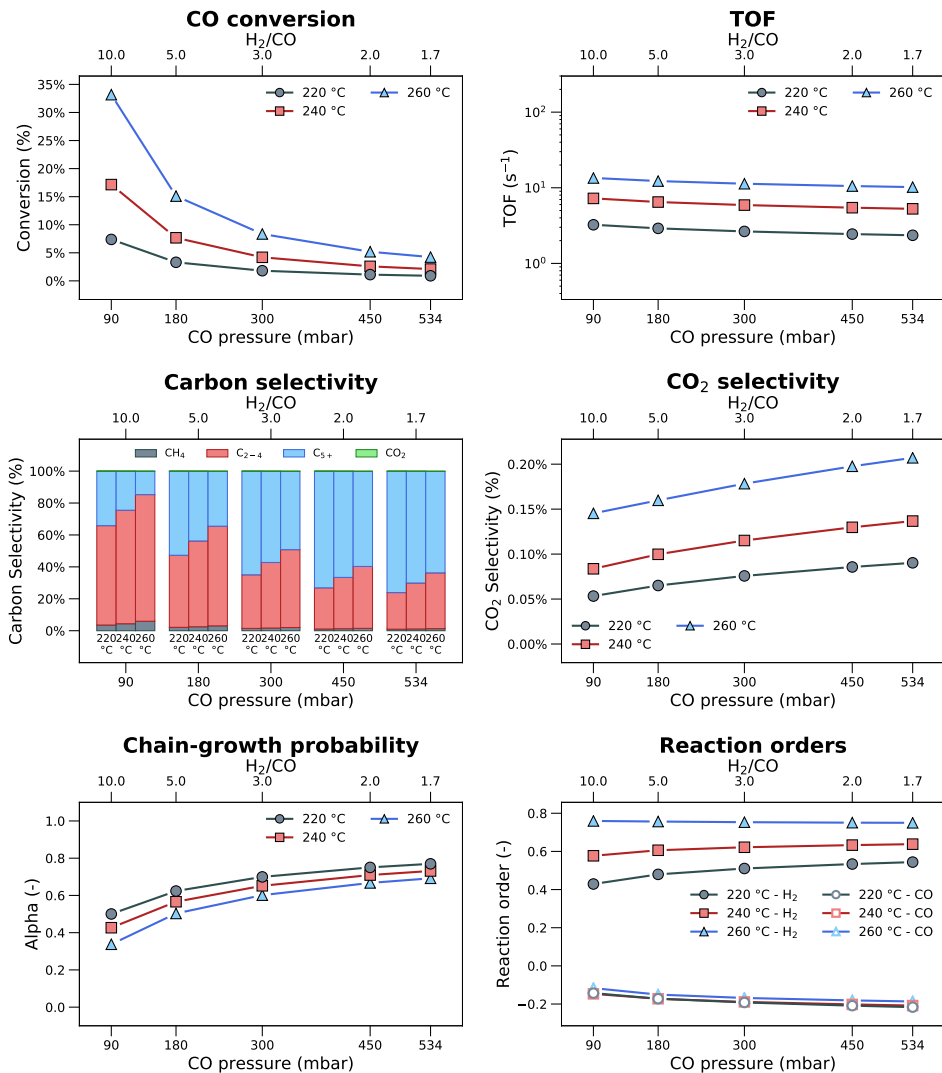


Figure 6.4: Microkinetics simulations of the FT synthesis reaction on the Co(11 $\bar{1}$) surface with varying CO pressure (conditions: T = 220/240/260 °C, p_{H₂} = 900 mbar, p_{CO} = 90-534 mbar, p_T = 5000 mbar). Note that all conversion and TOF data are based on CO consumption, all product selectivities are carbon-based and the chain-growth probability is based on the slope of ASF plot for carbon numbers 5-8.

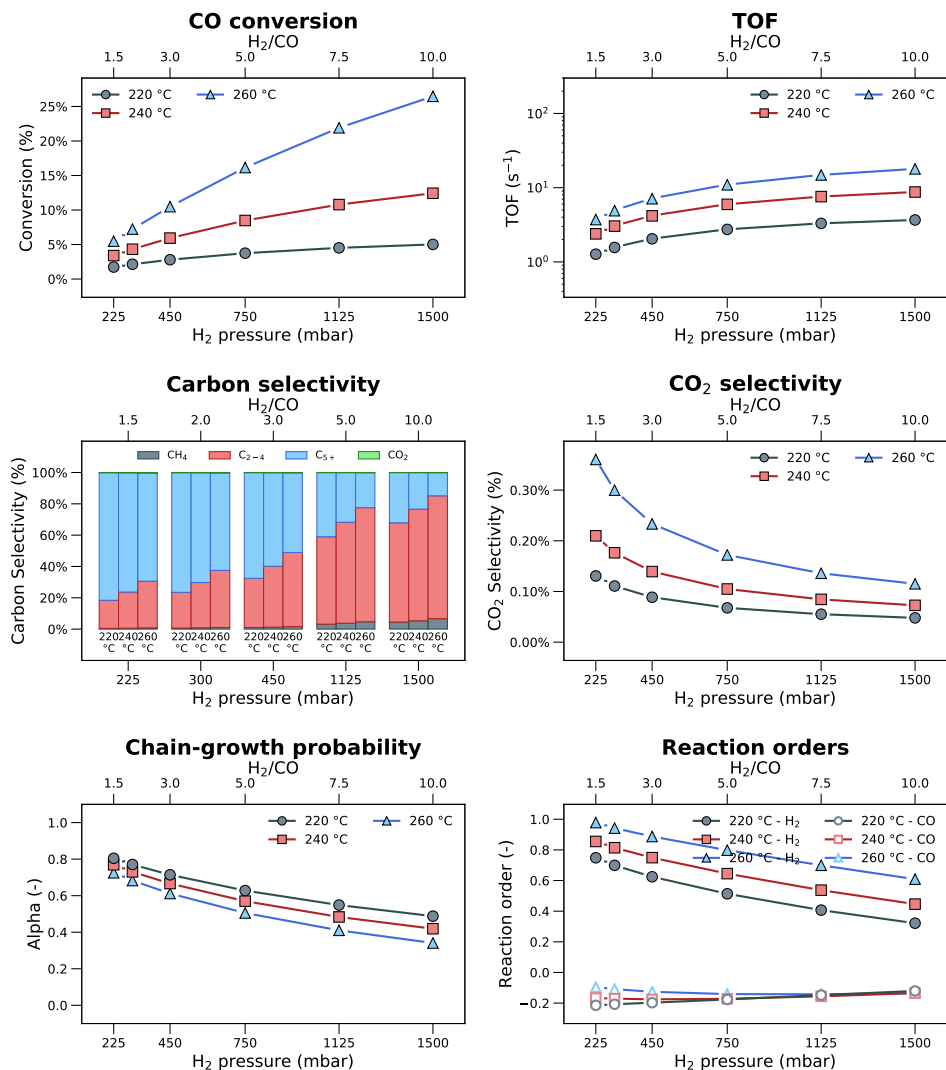


Figure 6.5: Microkinetics simulations of the FT synthesis reaction on the Co(11 $\bar{1}$ 1) surface with varying H₂ pressure (conditions: T = 220/240/260 °C, p_{H₂} = 225-1500 mbar, p_{CO} = 150 mbar, p_T = 5000 mbar). Note that all conversion and TOF data are based on CO consumption, all product selectivities are carbon-based and the chain-growth probability is based on the slope of ASF plot for carbon numbers 5-8.

zero a negligible contribution of the reverse reaction. Nearly all carbon from CO leads to atomic carbon, as the CO₂ selectivity is only 0.09% under these conditions. The CO dissociation reaction is partially equilibrated, as indicated by the equilibration ratio of 0.76 for this step. Oxygen is mainly removed via O hydrogenation followed by OH+OH proton shuffling as H₂O. This pathway is less equilibrated than CO dissociation and has equilibration ratios of 0.33 and 0.11 for OH formation and proton shuffling, respectively. The CH₄ selectivity is below 1%, which means that nearly all C atoms obtained from CO dissociation (~99%) are coupled to C₂₊ hydrocarbons. It is important to note that chain growth via CO insertion has a negligible contribution (0.001%) to the formation of C₂₊-hydrocarbons. Most of the CH_x coupling reactions involve atomic C adsorbates (88.7%), with the remaining 10.2% of C species being inserted as CH. While the coupling reactions to form C₂ species are fully equilibrated, the C₃₊ formation steps have no appreciable backward rate. CH₂CH₂ formation follows the pathway CC → CCH → CHCH → CHCH₂ → CH₂CH₂. The species that undergo hydrogenation are both CC (from C+C) or CCH (from C+CH). Most hydrogenation steps are fully or partially equilibrated, except for the hydrogenation steps that lead to either CH₂CH₂ or CH₂CH₃. The contribution of ethane formation is very low. Of all the C₂ surface adsorbates, only CCH₃ (obtained via CC → CCH → CCH₂ → CCH₃) is involved in chain growth. The main C₃₊ pathway resulting in olefins starts at CC-(CH₂)_nCH₃. The carbon-based rate of 391.7% (relative to CO dissociation) of this species to CCH-(CH₂)_nCH₃ is higher than 100%, because we combined the nodes of all C₃₊ chain lengths. This means that, on average, a C atom is involved in the hydrogenation step of type CC-(CH₂)_nCH₃ → CCH-(CH₂)_nCH₃ for about three additional increments of the carbon number *n*. Hydrogenation of CCH-(CH₂)_nCH₃ to CHCH-(CH₂)_nCH₃ amounts to a relative rate of 97.3%, which leads to termination as olefin via the chain-growth inhibiting hydrogenation to CH₂CH-(CH₂)_nCH₃. Hydrogenation to CCH₂-(CH₂)_nCH₃ represents a relative rate of 294.5%, and will lead to further propagation via the dominant C+C-(CH₂)_nCH₃ coupling step. The ratio between these rates relates to the chain-growth probability, i.e. $\alpha = \frac{r_p}{r_p+r_t} = \frac{2.945}{2.945+0.973} = 0.75$. Again, most hydrogenation steps are equilibrated, except for those leading to termination of the olefin.

Summarizing, microkinetics simulations show that the Co(11 $\bar{2}$ 1) model surface is highly active and selective for the FT reaction with a proper chain-growth probability, a relatively low CH₄ selectivity and very low CO₂ selectivity. The main reaction channel is direct CO dissociation to atomic C and O, which are respectively removed as CH₄ and C₂₊-hydrocarbons and H₂O. Dominant chain-growth pathways are of the C+C-(CH₂)_nCH₃ type. Kinetic parameters such as CO and H₂ reaction orders are in reasonable agreement with experimental data. Other trends such as the decreasing chain-growth probability with increasing temperature and H₂/CO ratio are also consistent with many observations in the literature.

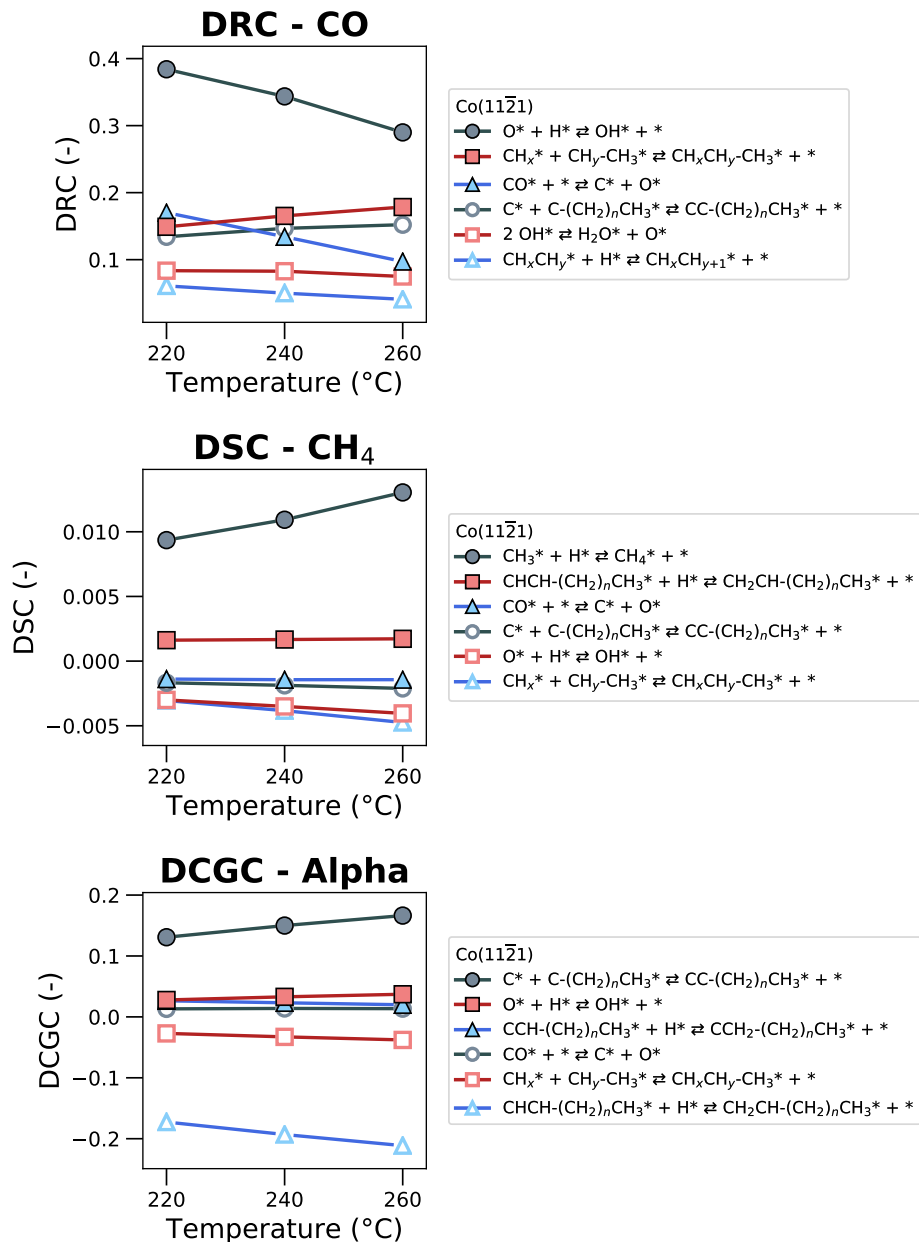


Figure 6.6: Sensitivity analysis of the FT reaction network on Co(11 $\bar{2}$ 1) (conditions: T = 220/240/260 °C, p_{H_2} = 667 mbar, p_{CO} = 333 mbar, p_T = 5000 mbar).

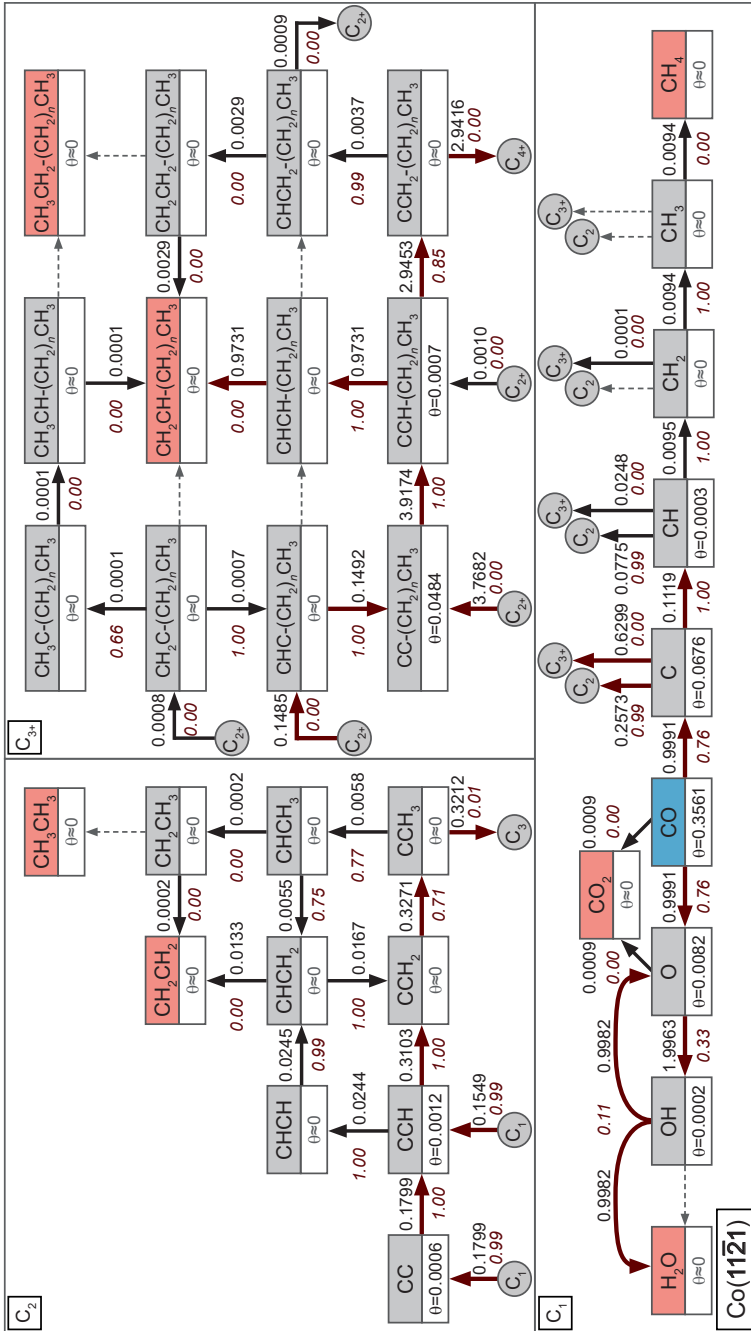


Figure 6.7: Reaction network analysis of the FT reaction on Co(111̄21) (conditions: $T = 220$ °C, $p_{\text{H}_2} = 667$ mbar, $p_{\text{CO}} = 333$ mbar, $p_{\text{T}} = 5000$ mbar). The values indicated next to the arrows are: (regular font – black) the net relative carbon-based rates between species, normalized to the consumption of CO; (italics – dark red) the ratio of the backward rate over the forward rate. The arrows to and from the circles indicate coupling reactions. Dashed arrows indicate rates lower than 0.0001. Coverages below 0.0001 ML are indicated by $\theta \approx 0$.

6.3.6 Microkinetics simulations of FT synthesis: Co(11 $\bar{2}$ 1) + Co(0001)

In Chapter 5, we showed that the Co(0001) terrace model has a very low activity towards CO dissociation and, therefore, mainly produces CH₄ at a very low rate. It was also demonstrated that coupling a Co(11 $\bar{2}$ 1) surface to a Co(0001) surface can lead to CH₄ formation on terrace sites, because CH_x species generated at the step-edge can migrate to the terrace. Simulation of the Co(11 $\bar{2}$ 1) surface in the previous section predicted a low CH₄ selectivity. We considered herein that the presence of terrace sites in a real cobalt nanoparticle catalyst might explain the higher CH₄ selectivity observed in experimental studies. Accordingly, we performed microkinetics simulations of a mean-field dual-site model comprising both Co(11 $\bar{2}$ 1) and Co(0001) surfaces in different proportions.

Figure 6.8 and Figure 6.9 show the main results for such a model at a H₂/CO ratio of 2 under a total pressure of 1 bar as a function of the step-to-terrace ratio. For example, at a ratio of 0.1 the surface model is made up by 9% Co(11 $\bar{2}$ 1) and 91% Co(0001) sites. Figure 6.8 shows that the activity increases when the step-to-terrace ratio increases. This result is expected as only the step-edge sites can dissociate CO at a relevant rate. The resulting TOF values normalized to the total surface are much lower (TOF = 0.26 s⁻¹, T = 220 °C) at a step-to-terrace ratio of 0.1. This TOF is still an order of magnitude higher than the value of 0.01 s⁻¹ reported by Chen et al. [30]. The chain-growth probability at 220 °C increases from 0.72 to 0.75 with an increase of the step-to-terrace ratio from 0.1 to 0.9. These values are in reasonable agreement with an experimental study where the terrace surfaces were passivated with graphitic carbon [50]. Analysis of chain-growth pathways shows that coupling reactions predominantly take place at the step-edge surface. Below we will show that chain growth on terrace sites can also contribute under particular conditions of very low CO partial pressure (low CO coverage). Another important insight from these simulations is that the CH₄ selectivity is increased with respect to the step-edge-only model discussed above. For instance, at a low step-to-terrace ratio of 0.1 the CH₄ selectivity is in the 49-63% range, which is closer to experimental literature data. We found that the underlying mechanism for additional CH₄ formation is the migration of CH_x species from Co(11 $\bar{2}$ 1) to Co(0001) terrace followed by hydrogenation to CH₄. The dominant migrating species is CH₃, which is in line with the findings in Chapter 5. The CO₂ selectivity is less affected by the presence of terrace sites at low temperature because of the relatively higher rate of O hydrogenation to H₂O on Co(11 $\bar{2}$ 1). Nevertheless, at a higher temperature, the CO₂ selectivity slightly increases with the presence of more step sites. The additional amount of CO₂ is formed due to the increased atomic O coverage at higher conversion. This has also been experimentally observed [50]. The data show that the CO coverage is around 0.3 ML for both surfaces, nearly independent from the step-to-terrace ratio. The H coverage on both surfaces is also similar, although the H coverage is about two times higher on the terrace surface. We can explain this difference by the higher adsorption strength of hydrogen on the Co(0001) terrace and the presence of atomic C on the stepped surface.

Figure 6.9 shows the apparent activation energy, reaction orders, and hydrocarbon product distribution. The apparent activation energy is a function of the step-to-terrace ratio with values in the 88-96 kJ/mol range at the lowest ratio (0.1) and in the 59-85

kJ/mol range at the highest ratio (0.9). These changes go together with a shift in the product distribution from CH_4 to C_{2+} products. The apparent activation energy decreases at higher temperature, which is also due to a higher CO conversion (Appendix C.5). While the chain-growth probability only slightly increases at high step-to-edge ratios, the C_{2+} selectivity strongly increases because less CH_x growth monomers migrate to the terrace surface, where they form CH_4 . It is important to note that for all of the explored step-to-surface ratios the CH_4 selectivity remains above the value predicted on the basis of the chain-growth probability, while the ethylene selectivity remains always below the predicted value. As shown in Figure 6.9, however, the CH_4 selectivity for a simulation of only the $\text{Co}(11\bar{2}1)$ is lower than the predicted ASF value. Thus, a major conclusion is that a stepped surface can efficiently convert CO in C_{2+} hydrocarbons with a low CH_4 and C_2 selectivity, which relates to the overall formation barriers of CH_4 , C_2 and C_{3+} species with respect to CO. The higher CH_4 selectivity observed in experiment is most likely due to the migration of CH_x species from the stepped surface to terraces where termination towards CH_4 is predominant.

We then investigated a combined surface model consisting of 10% $\text{Co}(11\bar{2}1)$ and 90% $\text{Co}(0001)$. This step-to-terrace ratio reflects a conservative estimate of the abundance of step-edge sites on optimum cobalt nanoparticles ~ 6 nm [20]. We varied the CO pressure while keeping the H_2 pressure constant. The changes in CO conversion and TOF are similar to the microkinetics simulations discussed above for the $\text{Co}(11\bar{2}1)$ surface and can be found in Appendix C.5. Despite that there are 10 times less sites for CO dissociation, the TOF decreases only by a factor in the 5-8 range. This difference is caused by the removal of CH_x species from the step-edge site to terrace sites. Kinetically, the rate of $\text{C}+\text{O}$ recombination is suppressed by this. The effect on the product distribution is a higher CH_4 selectivity, which is in the 77-88% range at the high H_2/CO ratio of 10 and decreases to 48-62% at a H_2/CO ratio of 2. The CO_2 selectivity is nearly same as for the $\text{Co}(11\bar{2}1)$ simulations. These values for the CH_4 and CO_2 selectivity correspond very well to the data reported by Chen et al. [30]. Figure 6.10 shows the apparent activation energy, reaction orders, and hydrocarbon product distribution as a function of CO partial pressure. The apparent activation energy is of the order 90-100 kJ/mol, which is in good agreement with a wide range of experimentally reported activation energies for FT catalysts [2, 53–58]. The apparent activity decreases at higher CO partial pressure when more C_{2+} products are obtained. Also, the positive H_2 reaction order close to unity and the slightly negative CO reaction order correspond to earlier experimental data [2, 53, 59]. The trends in CO and H_2 reaction orders can be explained by competitive adsorption between CO and H_2 . The slightly increased CO coverage at higher CO partial pressure (Appendix C.6) causes a similar decrease in the H coverage. This also leads to hydrogenation termination reactions involving H becoming slightly more rate controlling. From the ASF distributions, we can infer that the chain-growth probability increases with increasing CO partial pressure and is higher at lower temperature. An unexpected phenomenon is observed at low CO partial pressure and higher temperature. The ASF distribution is a convolution of two chain-growth processes. The reason for the anomalous behavior is the growing contribution of chain

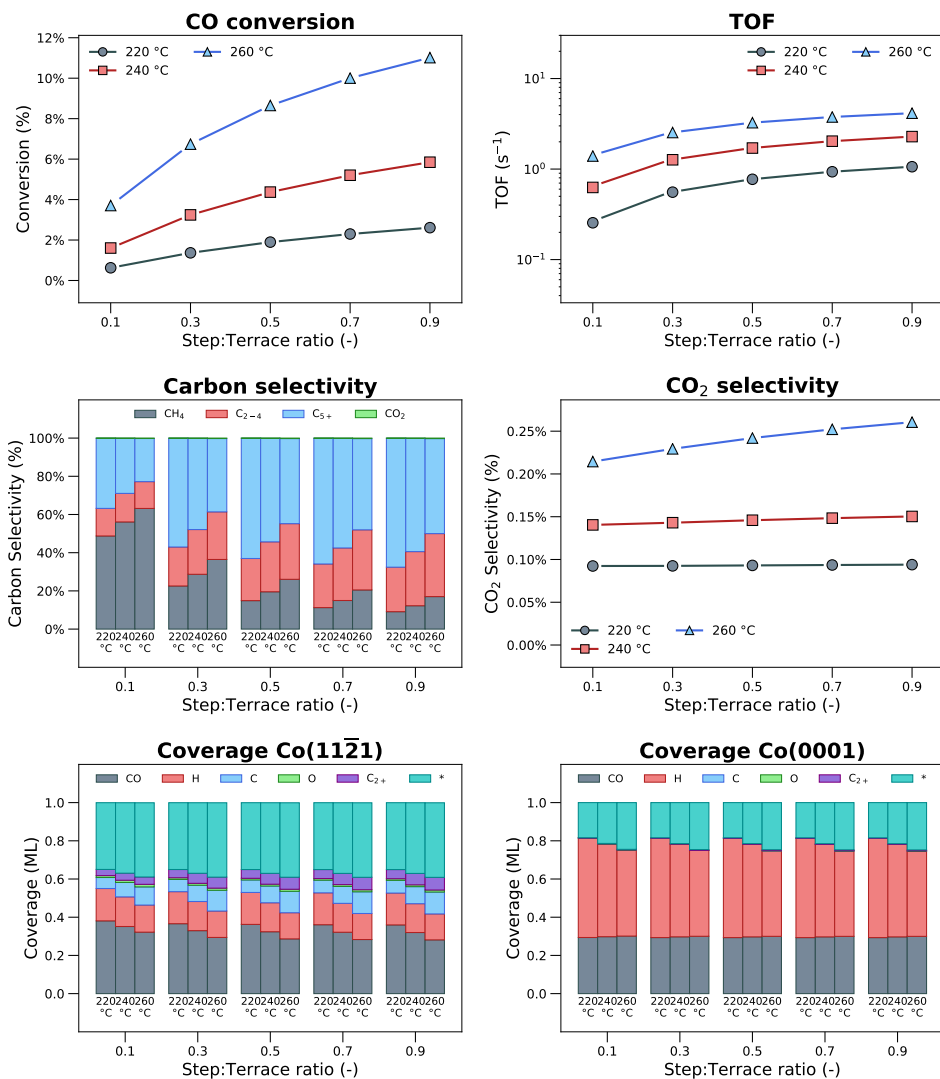


Figure 6.8: Microkinetics simulations of the FT synthesis reaction on a combined surface consisting of Co(1121) and Co(0001) with varying Co(1121):Co(0001) ratio (conditions: $T = 220/240/260$ °C, $p_{H_2} = 667$ mbar, $p_{CO} = 333$ mbar, $p_T = 5000$ mbar). Note that all conversion and TOF data are based on CO consumption and all product selectivities are carbon-based.

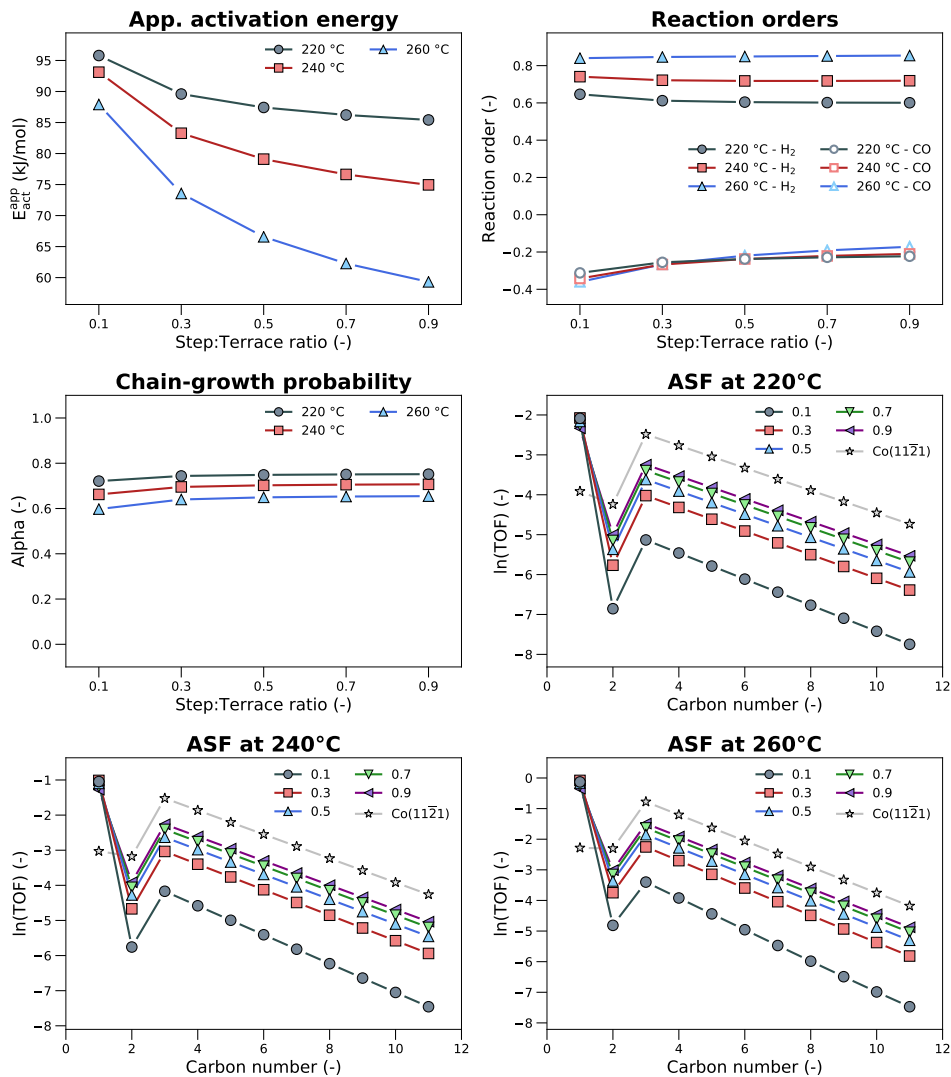


Figure 6.9: Microkinetics simulations of the FT synthesis reaction on a combined surface consisting of $\text{Co}(11\bar{1})$ and $\text{Co}(0001)$ with varying $\text{Co}(11\bar{1})$: $\text{Co}(0001)$ ratio (conditions: $T = 220/240/260$ °C, $p_{\text{H}_2} = 667$ mbar, $p_{\text{CO}} = 333$ mbar, $p_{\text{T}} = 5000$ mbar). Note that the chain-growth probability is based on the slope of ASF plot for carbon numbers 5-8.

growth at the terrace surface when the CO coverage is decreased (lower CO partial pressure, higher temperature). In an absolute sense, this contribution is very low and only noticeable when the total formation rate of C₂₊-hydrocarbons at the step-edge surface becomes very low. The key factor determining the contribution of chain growth at the terrace surface is the CH_x coverage. For the Co(11 $\bar{2}$ 1)-only simulations, the dominant coupling reaction are of the type C+C-(CH₂)_nCH₃. The rate of this reaction depends strongly on the coverage of atomic C. The rate of this C-coupling pathway is very low on Co(0001), because C is much less stable (by 55 kJ/mol) on terrace sites (Appendix B) than on step-edge sites. However, CH is only 9 kJ/mol less stable on the Co(0001) surface than on the Co(11 $\bar{2}$ 1) surface. The chain-growth probability at the terrace surface is higher, however, because the CH-coupling pathway on Co(0001) has a lower barrier than the C-coupling pathway on Co(11 $\bar{2}$ 1). A requirement for such an alkylidyne chain-growth mechanism, which has been postulated recently by Weststrate et al. [60, 61], is a high enough CH coverage. In our dual-site model, this implies a high enough rate of migration of CH species from step-edge to terrace sites. This condition is only met at relatively high H₂/CO ratios and high temperatures. This implies that chain growth on terrace sites is only relevant under conditions where CH₄ is the dominant product. Chain growth on terrace sites is thus not relevant for practical FT synthesis at higher CO coverage. We also investigated the effect of varying H₂ partial pressure at a constant CO partial pressure for the same step-to-terrace ratio. The corresponding data are shown in Appendix C.7. The changes in kinetic parameters are quite similar to those with varying CO partial pressure, when the changes are considered in terms of the H₂/CO ratio. The chain-growth probability decreases and the CH₄ selectivity increases at higher H₂ pressure (Appendix C.7). Similar effects on the anomalous chain-growth behavior are observed at the highest H₂ pressure, especially at higher temperature.

We also investigated the rate- and selectivity-controlling steps for the dual-site model at a H₂/CO ratio of 2. The results of this analysis are shown in Figure 6.11. We can compare these results to those for the Co(11 $\bar{2}$ 1)-only surface shown in Figure 6.6. The most significant difference is that CH₃ hydrogenation to CH₄ is contributing more significantly to the overall degree of rate control. This difference is due to the higher rate of CH₄ formation related to the migration of CH₃ from step-edge to terrace sites, where hydrogenation to CH₄ takes place. Indeed, the DRC of CH₃ hydrogenation on terrace sites increases strongly with temperature at the expense of the DRC of O hydrogenation to OH and CO dissociation on step-edge sites. Thus, we can state that the inclusion of terrace sites in the microkinetic model results in a much better correspondence of the modelled kinetics with experimental data of Chen et al. [30, 49]. Consistently, the DSC of CH₄ is most significantly determined by CH₃ hydrogenation on terrace sites. With respect to the DCGC, we find similar controlling steps for chain growth: chain growth is limited and inhibited by respectively C+C-(CH₂)_nCH₃ and CHCH-(CH₂)_nCH₃ hydrogenation steps on step-edge sites.

Figure 6.12 depicts the reaction network including relative carbon-based rates, coverage, and equilibration ratios for the two surfaces at a temperature of 220 °C and a H₂/CO ratio

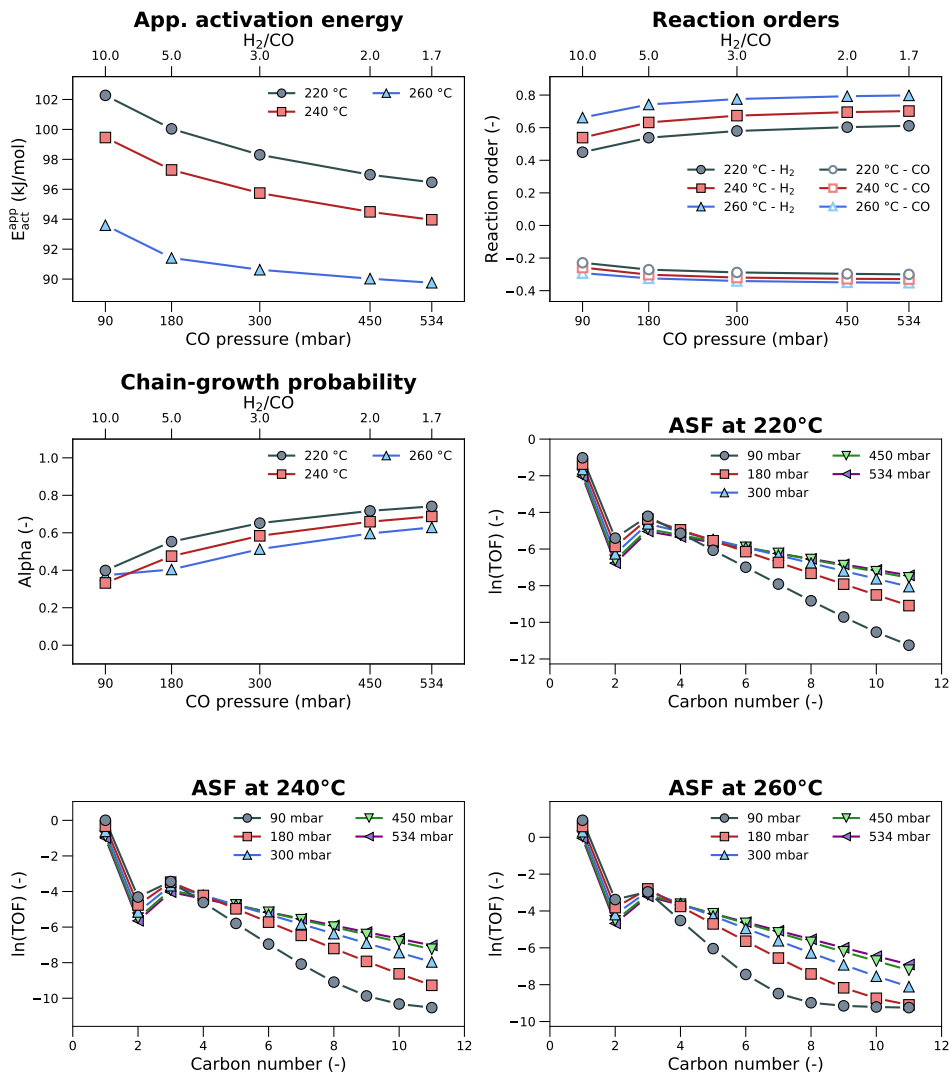


Figure 6.10: Microkinetics simulations of the FT synthesis reaction on a combined surface consisting of 10% $\text{Co}(11\bar{2}1)$ and 90% $\text{Co}(0001)$ with varying CO pressure (conditions: $T = 220/240/260$ °C, $p_{\text{H}_2} = 900$ mbar, $p_{\text{CO}} = 90\text{-}534$ mbar, $p_{\text{T}} = 5000$ mbar). Note that the chain-growth probability is based on the slope of ASF plot for carbon numbers 5-8.

of 2. The reaction pathways for this case are similar to those shown in Figure 6.7, with migration of CH_x species to the terrace $\text{Co}(0001)$ surface as the most significant difference. To this migration CH_3 contributes the most as it is weakest bound among the CH_x surface adsorbates. CH migration is also relevant because this is a relatively stable species at the surface. Most of these migration steps lead to CH_4 production on the terrace surface, constituting 45.1% of the total rate. Both the hydrogenation steps from C to CH_3 and the migration steps of these species are equilibrated. We observed no appreciable rate from CH_4 back to CH_3 . From CH , 4.0% of the carbon-based rate leads to chain growth at the terrace surface. Incorporation of CH_x on the stepped surface is lower than on the $\text{Co}(11\bar{2}1)$ -only surface model, because more CH_x species are involved in CH_4 formation on the terrace surface. Relative carbon-based rates of 44.7% and 5.5% were found for coupling reactions on the stepped surface with C and CH , respectively. The dominant C_2 - and C_3 -hydrocarbon formation pathways remain the same, with lower absolute values as compared to the $\text{Co}(11\bar{2}1)$ -only surface. Again, the chain growth via CO insertion has a negligible contribution (0.001%) to the formation of C_{2+} -hydrocarbons. From the $\text{CCH}-(\text{CH}_2)_n\text{CH}_3$ state, the propagation path to $\text{CCH}_2-(\text{CH}_2)_n\text{CH}_3$ has a relative rate of 127.7%, while the relative termination rate to $\text{CHCH}-(\text{CH}_2)_n\text{CH}_3$ is 49.2%. The corresponding ratio gives the chain-growth probability $\alpha = \frac{r_p}{r_p+r_t} = \frac{1.277}{1.277+0.492} = 0.72$, which is slightly lower than found for the $\text{Co}(11\bar{2}1)$ -only surface model.

To sum up, the microkinetics simulations of the dual-site model show that the presence of $\text{Co}(0001)$ mainly leads to higher CH_4 selectivity at the expense of the formation of C_{2+} -hydrocarbons. The CH_4 selectivity for the model consisting of 10% $\text{Co}(11\bar{2}1)$ and 90% $\text{Co}(0001)$ is in line with experimental observations. The effects of CO and H_2 partial pressure are similar to the $\text{Co}(11\bar{2}1)$ -only surface, and the apparent activation energy and reaction orders are in good agreement with experimental data. A kinetic analysis of the reaction network shows that CH_4 is mainly formed from CH and CH_3 species that migrate from the stepped surface to the $\text{Co}(0001)$ terrace.

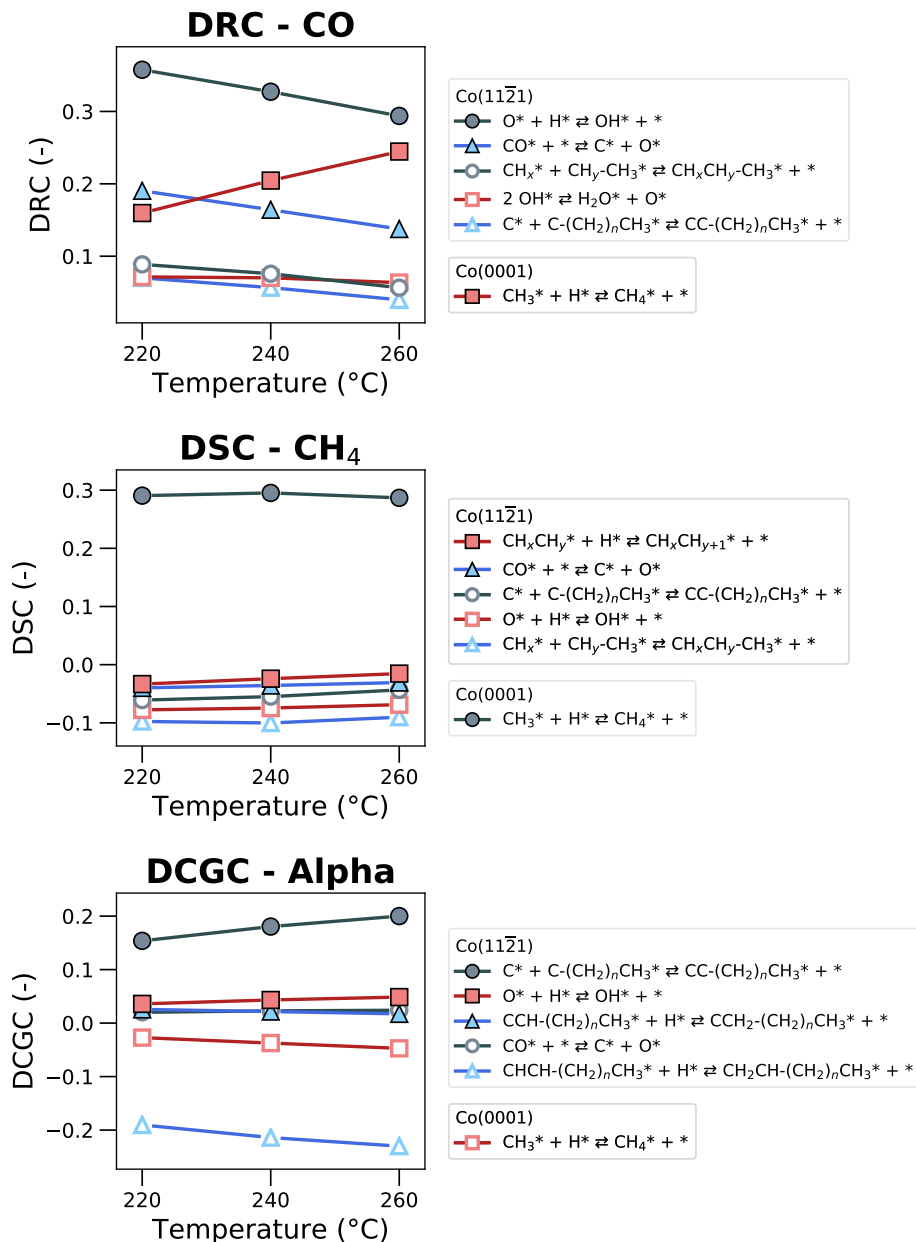


Figure 6.11: Sensitivity analysis of the FT reaction network on a combined surface consisting of 10% Co(1121) and 90% Co(0001) (conditions: $T = 220/240/260$ °C, $p_{\text{H}_2} = 667$ mbar, $p_{\text{CO}} = 333$ mbar, $p_{\text{T}} = 5000$ mbar).

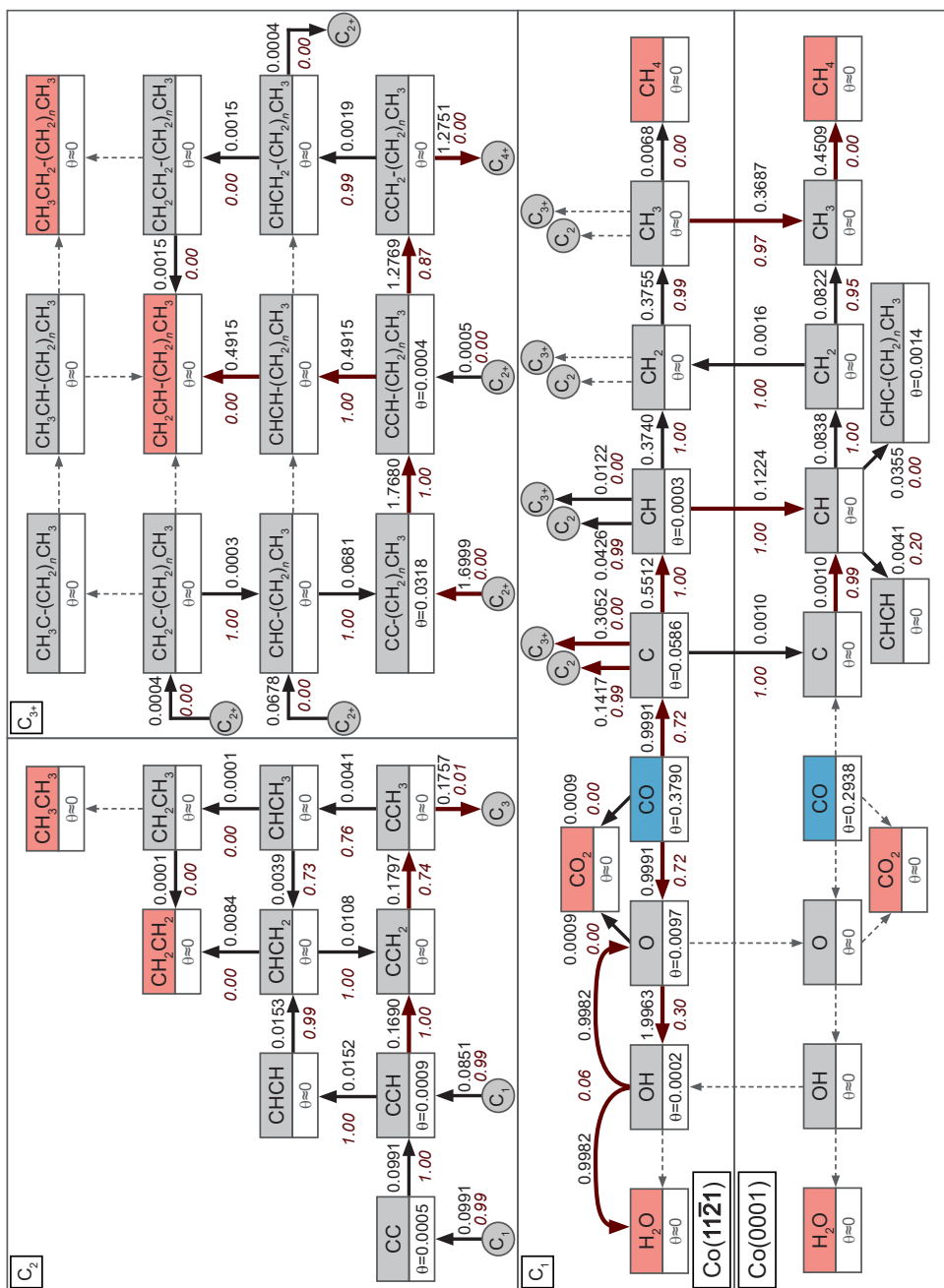


Figure 6.12: Reaction network analysis of the FT reaction on a combined surface consisting of 10% Co(11 $\bar{2}$ 1) and 90% Co(0001) (conditions: $T = 220$ °C, $p_{H_2} = 667$ mbar, $p_{CO} = 333$ mbar, $p_T = 5000$ mbar). The values indicated next to the arrows are: (regular font – black) the net relative carbon-based rates between species, normalized to the consumption of CO; (italics – dark red) the ratio of the backward rate over the forward rate. The arrows to and from the circles indicate coupling reactions. Dashed arrows indicate rates lower than 0.0001. Coverages below 0.0001 ML are indicated by $\theta \approx 0$.

6.3.7 Microkinetics simulations of CO₂ hydrogenation

In future energy scenarios, great emphasis is placed on an increased share of renewable energy in order to decrease CO₂ emissions from fossil energy combustion, which negatively affect the climate. Among renewable forms of energy, especially electricity from sunlight and wind is projected to play an important role in driving the energy transition. Currently, about one third of the energy demand covers our everyday mobility needs, largely by liquid transportation fuels obtained from crude oil refining. Given the growth in gross domestic product (GDP) in the developing countries, it is clear that the demand for liquid transportation fuels will also keep on increasing. Recently, the global refining capacity exceeded 100 million barrels of oil per day. An ever-growing scenario for the oil refining industry is however unsustainable in view of the Paris agreement.

Although a substantial part of the energy demand for mobility can be covered by electricity in the coming decades, electrification of heavy-duty transport and aviation is less realistic. This implies that there will remain a substantial need for liquid transportation fuels. As biomass can probably cover only a relatively small fraction of this demand, it is increasingly realized that liquid transportation fuels should be produced from renewable energy forms. The most often considered scenario is to reduce CO₂ with renewable energy (and H₂O) to liquid hydrocarbons that are compatible with current transportation fuels. Among the various approaches, reduction with H₂ obtained by for instance water electrolysis using renewable electricity is the most explored one. The conversion of CO₂ with H₂ in liquid hydrocarbons can be achieved by FT chemistry.

Most often, FT synthesis of hydrocarbons from a mixture of CO₂ and H₂ involves two consecutive steps [62]. First, CO₂ is converted into CO via the reverse water-gas shift (R-WGS) reaction [63, 64], followed by FT synthesis using the resulting synthesis gas mixture and conventional FT catalysts. By also integrating hydrocracking, the Power-to-X (P2X) Kopernikus project demonstrated that the total system of CO₂ capture and conversion can fit in a modular container [65, 66]. Hydrocracking can be achieved via a bifunctional catalyst consisting of Pt on H-ZSM-5 [67]. Another approach has been recently described using a combination of an iron-based catalyst and zeolite, i.e. Na-Fe₃O₄/HZSM-5 [68]. In this case, the promoted iron component is involved in chain growth, while the zeolite results in lowering of the hydrocarbon number by cracking in order to yield gasoline. Indeed, iron-based catalysts have been used for CO₂-based FT synthesis before in which carburization and alkali promotion can suppress the formation of CH₄ in favor of higher hydrocarbons [69]. On the other hand, it has also been found that cobalt-based catalysts mostly produce CH₄ [70, 71]. Considering the need to remove an extra O atom in CO₂ compared to CO, more H₂ is needed. The higher H₂ partial pressure will probably lead to a higher H coverage, resulting in a lower chain-growth probability. The surface H/C ratio will therefore further increase because the conversion of CO₂ to C is likely slower than that of CO to C. The work of Dorner et al [72]. showed that the product distribution of CO₂ hydrogenation over Co-Pt/Al₂O₃ can be shifted from methane to longer hydrocarbons by changing the feed gas ratio to low H₂/CO₂ ratios (3:1→1:1). An intriguing result from these experiments is that the ASF distributions have a relatively high chain-growth probability, although the

underlying C_{2+} -hydrocarbons formation rate is low. This chain-growth probability ranges from 0.41 to 0.54 with the H_2/CO_2 ratio decreasing from 3 to 1. In previous sections, we found similar chain-growth probabilities at low C_{2+} selectivity for high H_2/CO ratios on a cobalt model catalyst consisting of 10% Co(11 $\bar{2}$ 1) and 90% Co(0001) surfaces. Because our kinetic mechanism for CO hydrogenation includes CO_2 formation and CO can be reversibly formed from CO_2 , we can also investigate and compare the product distribution using the same dual site model by replacing CO with CO_2 in a CO/H_2 reaction mixture.

Figure 6.13 and Figure 6.14 show kinetic data for the combined surface obtained by varying the CO_2 partial pressure under constant H_2 pressure. The TOF is 0.1-0.2 s^{-1} at 220 °C, which is an order of magnitude lower than the rate of CO hydrogenation at the same temperature. The product distribution is completely shifted to CH_4 with a significant contribution of CO formation (CO selectivity in the range 1-8%). Contrary to CO hydrogenation, the TOF for CO_2 hydrogenation increases as a function of CO_2 pressure. This is because CO_2 binds much weaker than CO, so that an increasing CO_2 pressure leads to a higher CO_2 coverage. We note the adsorption energy of CO_2 on the Co(11 $\bar{2}$ 1) surface of 112 kJ/mol (Chapter 5) is nearly equal to the entropy loss upon adsorption from the gas phase at relevant temperatures. An analysis of the composition of the adsorbed layer shows that the CO and H coverages at low H_2/CO_2 ratios are similar to the coverages observed for CO hydrogenation at very high H_2/CO ratio. Thus, this composition of the adsorbed layer is consistent with the dominant formation of CH_4 . Figure 6.14 shows that the apparent activation energy depends strongly on the temperature and has a high value of ~ 130 kJ/mol at 220 °C. The high apparent activation energy and the strong influence of temperature on the apparent activation energy is due to the high H coverage, which also causes a negative reaction order in H_2 , while the CO_2 order is positive. Experimental work on CO_2 methanation shows an apparent activation energy of 80-100 kJ/mol ($T = 200-300$ °C, $p_{H_2} = 750$ mbar, $p_{CO_2} = 250$ mbar) [73]. Another work reports a value of ~ 70 kJ/mol at a very low pressure of 2-3 mbar and a very high H_2/CO_2 ratio of 40 [74]. Likely, the low barrier for these conditions follows from a low H coverage. Experimental work at a high hydrogen coverage ($T = 180-222$ °C, $p_{H_2} = 8917$ mbar, $p_{CO_2} = 2229$ mbar, 11 atm) shows a higher apparent activation energy of 171 kJ/mol, while a much lower value of 93 kJ/mol was observed at a total pressure of 1 atm [75].

The ASF distributions show a steep decline up to a chain length of 4. For C_{4+} , the chain-growth probability increases despite remaining low at $\sim 0.17-0.24$ at a H_2/CO_2 ratio of 1.7. We performed a similar investigation by varying the H_2 pressure at a constant CO_2 pressure. The results follow the same trends as a function of H_2/CO_2 ratio and can be found in Appendix D.1. In most cases the C_{2+} selectivity was highest at low H_2/CO_2 ratios. For these conditions, the CH_4 selectivity is lowered, but the limited availability hydrogen at the surface results in a relatively stronger increase of the CO selectivity.

We applied our DRC, DSC, and DCGC analysis to CO_2 hydrogenation on the dual-site model at H_2/CO_2 ratio of 3. The results are shown in Figure 6.15. The elementary reaction steps that most significantly control the CO_2 conversion rate are CO_2 and CO dissociation. Both reactions proceed in appreciable rates only on the Co(11 $\bar{2}$ 1) surface. At 220 °C, CO

dissociation is more rate-controlling than CO_2 dissociation, because the barrier for CO dissociation is 16 kJ/mol higher than that of CO_2 dissociation at the stepped surface. At 260 °C, CO_2 dissociation becomes more rate-controlling, because it is limited by the unfavorable adsorption equilibrium at higher temperature. Because the H coverage decreases with temperature, the hydrogenation of CH_3 to CH_4 on the terrace surface contributes slightly to the rate control. To understand how CH_4 selectivity could be suppressed, we determined the degree of selectivity control to CH_4 . As expected, the final hydrogenation step to CH_4 strongly controls the selectivity to CH_4 . This control is shared between the step and terrace surfaces, with a higher contribution of the terrace hydrogenation step. Enhancing CO dissociation leads to lower CO selectivity and thus more CH_4 . CO_2 dissociation and CHCH_2 hydrogenation are both inhibiting steps for the formation of CH_4 . The hydrogenation step of CHCH_2 will lead to desorption of CH_2CH_2 and thus higher C_2 selectivity. Enhanced CO_2 dissociation will however not only lead to more C_{2+} -hydrocarbons, but also to a higher CO selectivity. Finally, the degree of chain-growth control shows that coupling reactions of the type $\text{CH}+\text{C}-(\text{CH}_2)_n\text{CH}_3$ control the chain-growth probability. Chain growth occurs on the terrace sites and is inhibited by hydrogenation of $\text{CHCH}-(\text{CH}_2)_n\text{CH}_3$ to the desorbing $\text{CH}_2\text{CH}-(\text{CH}_2)_n\text{CH}_3$ olefin. The dominant contribution of terrace sites to chain growth is in contrast to most of the CO-based FT results described in previous sections. For CO-based FT synthesis at a H_2/CO ratio of 2, we observed that $\text{C}+\text{C}-(\text{CH}_2)_n\text{CH}_3$ -type coupling on the stepped $\text{Co}(11\bar{2}1)$ surface controls the chain-growth rate. However, the low CO coverages in the 5-10% range for CO_2 -based FT synthesis at 220 °C corresponds to CO-based FT synthesis at a very high H_2/CO ratio. For such ratios, we also observed that CO hydrogenation to long hydrocarbons is possible via CH migration to the terrace and subsequent coupling via the same $\text{CH}+\text{C}-(\text{CH}_2)_n\text{CH}_3$ pathway at the terrace. Similar to CO-based FT synthesis, chain growth at the terrace surface results in a very low C_{2+} selectivity.

Figure 6.16 depicts the reaction network for CO_2 hydrogenation at a temperature of 220 °C and a H_2/CO_2 ratio of 3. The relative carbon-based rate of CO_2 consumption is taken as 100%. The dissociation step to CO occurs exclusively on $\text{Co}(11\bar{2}1)$ sites. Although adsorbed CO is equilibrated between step and terrace site, further dissociation of CO into atomic C proceeds exclusively on step-edge sites. CO desorption accounts for 5.4% of the rate, and chain growth via CO insertion has a negligible contribution (<0.001%), resulting in a relative rate of 94.6% towards atomic carbon. This carbon, located on the step-edge sites, can proceed to three possible destinations. The carbon can either migrate to the terrace surface, be hydrogenated to CH on the stepped surface, or be incorporated in the pool of Fischer-Tropsch products. We found that the latter pathway amounts to a relative rate of 2.0%. Because the chain-growth probability is very low, the pool of FT products is small and mostly leads to CH_2CH_2 . We did not observe migration of atomic carbon from $\text{Co}(11\bar{2}1)$ to $\text{Co}(0001)$, so the remaining 92.6% of C is hydrogenated to CH. The produced CH can again either migrate (2.0%), hydrogenate (89.2%), or be inserted into the pool of FT products (1.4%). In the degree of chain-growth control analysis (Figure 6.15) we observed that the dominant coupling reaction for the production of higher hydrocarbons is

the $\text{CH}+\text{C}-(\text{CH}_2)_n\text{CH}_3$ coupling on the $\text{Co}(0001)$ surface. However, as already evident from the ASF distributions, the relative amount of carbon atoms incorporated in hydrocarbon chains of length 5 and longer is negligible. Therefore, there is no significant rate of CH into FT products on the terrace surface. Nearly all CH on $\text{Co}(0001)$ is hydrogenated to CH_2 , of which most is further hydrogenated on the terrace surface to CH_4 . Like in the reaction network for CO hydrogenation, the majority of the CH_3 species on the stepped surface also migrate to the terrace surface to be hydrogenated to CH_4 . Thus, although chain growth is possible during CO_2 hydrogenation on cobalt, the product scope is mostly CH_4 with at best a small fraction of CH_2CH_2 .

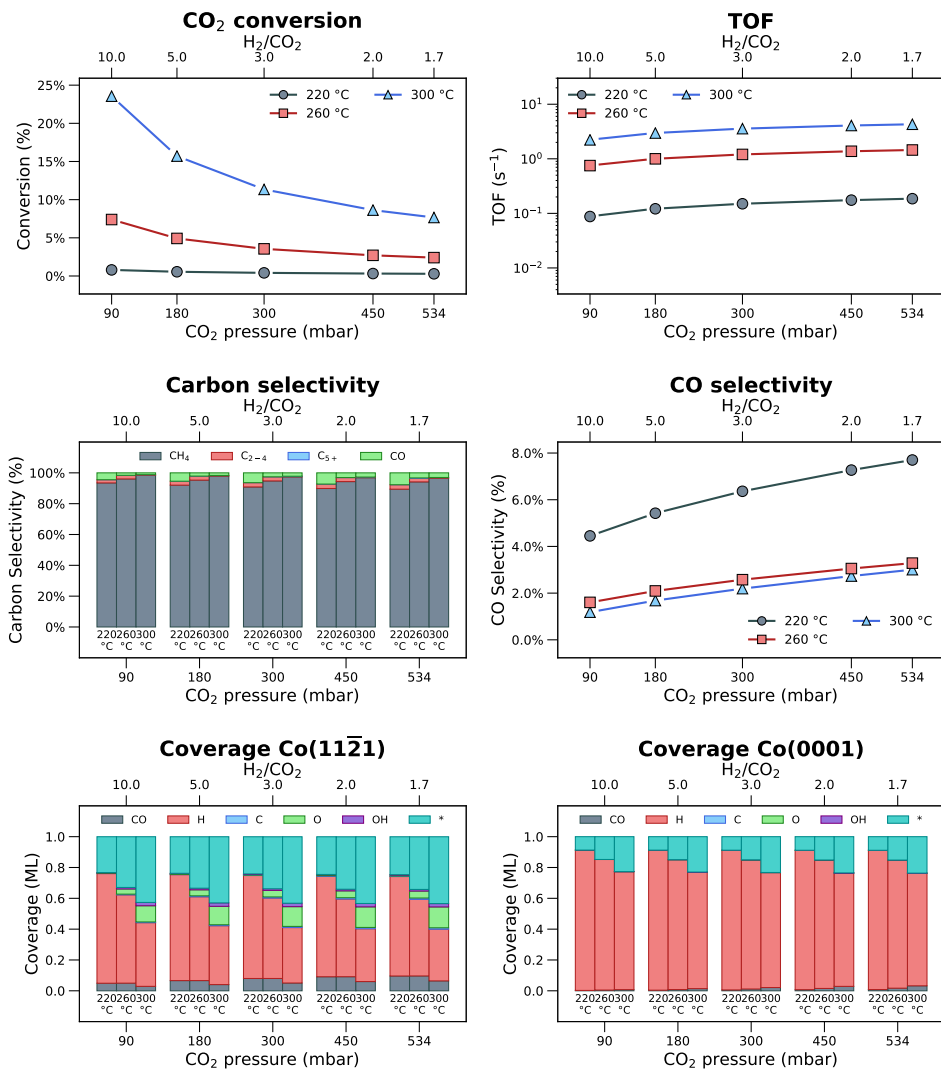


Figure 6.13: Microkinetics simulations of CO₂ hydrogenation on a combined surface consisting of 10% Co(111̄21) and 90% Co(0001) with varying CO₂ pressure (conditions: T = 220/260/300 °C, p_{H₂} = 900 mbar, p_{CO₂} = 90-534 mbar, p_T = 5000 mbar). Note that all conversion and TOF data are based on CO₂ consumption and all product selectivities are carbon-based.

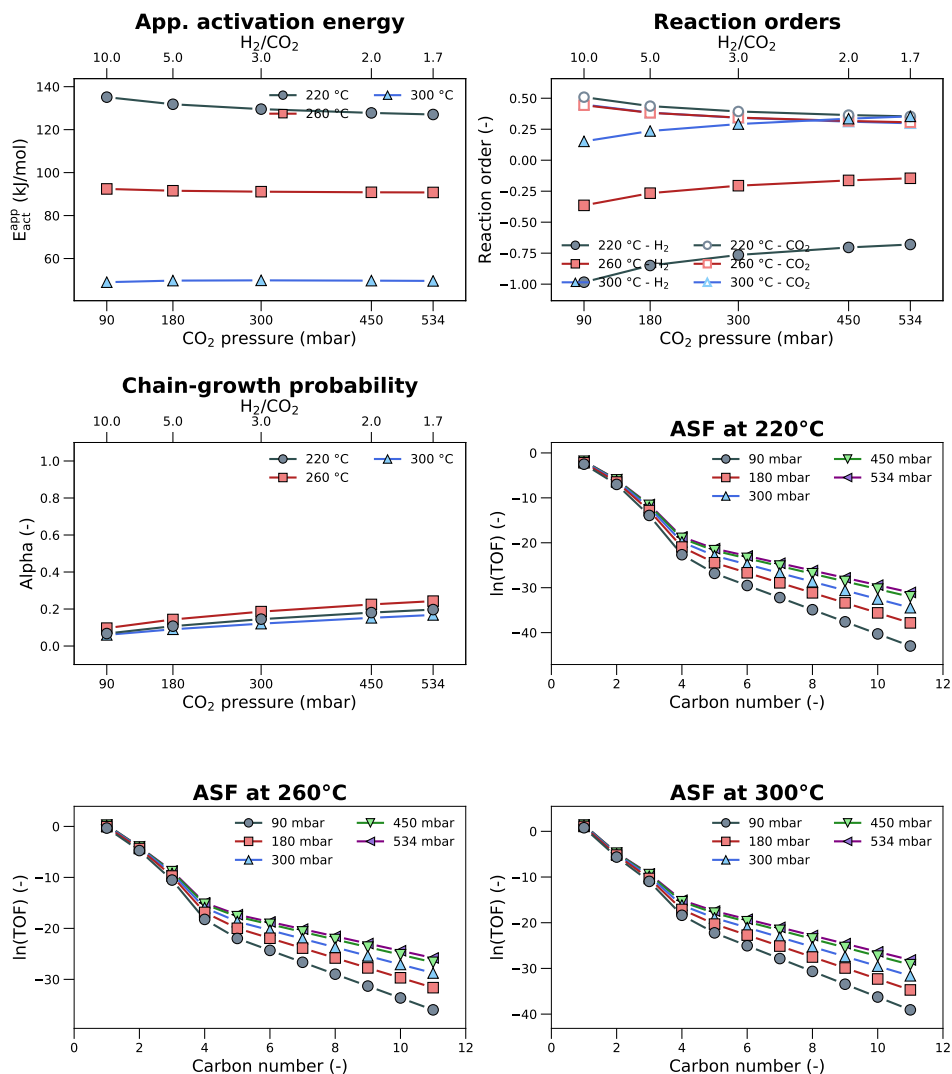


Figure 6.14: Microkinetics simulations of CO_2 hydrogenation on a combined surface consisting of 10% $\text{Co}(11\bar{2}1)$ and 90% $\text{Co}(0001)$ with varying CO_2 pressure (conditions: $T = 220/260/300^\circ\text{C}$, $p_{\text{H}_2} = 900$ mbar, $p_{\text{CO}_2} = 90\text{-}534$ mbar, $p_{\text{T}} = 5000$ mbar). Note that the chain-growth probability is based on the slope of ASF plot for carbon numbers 5-8.

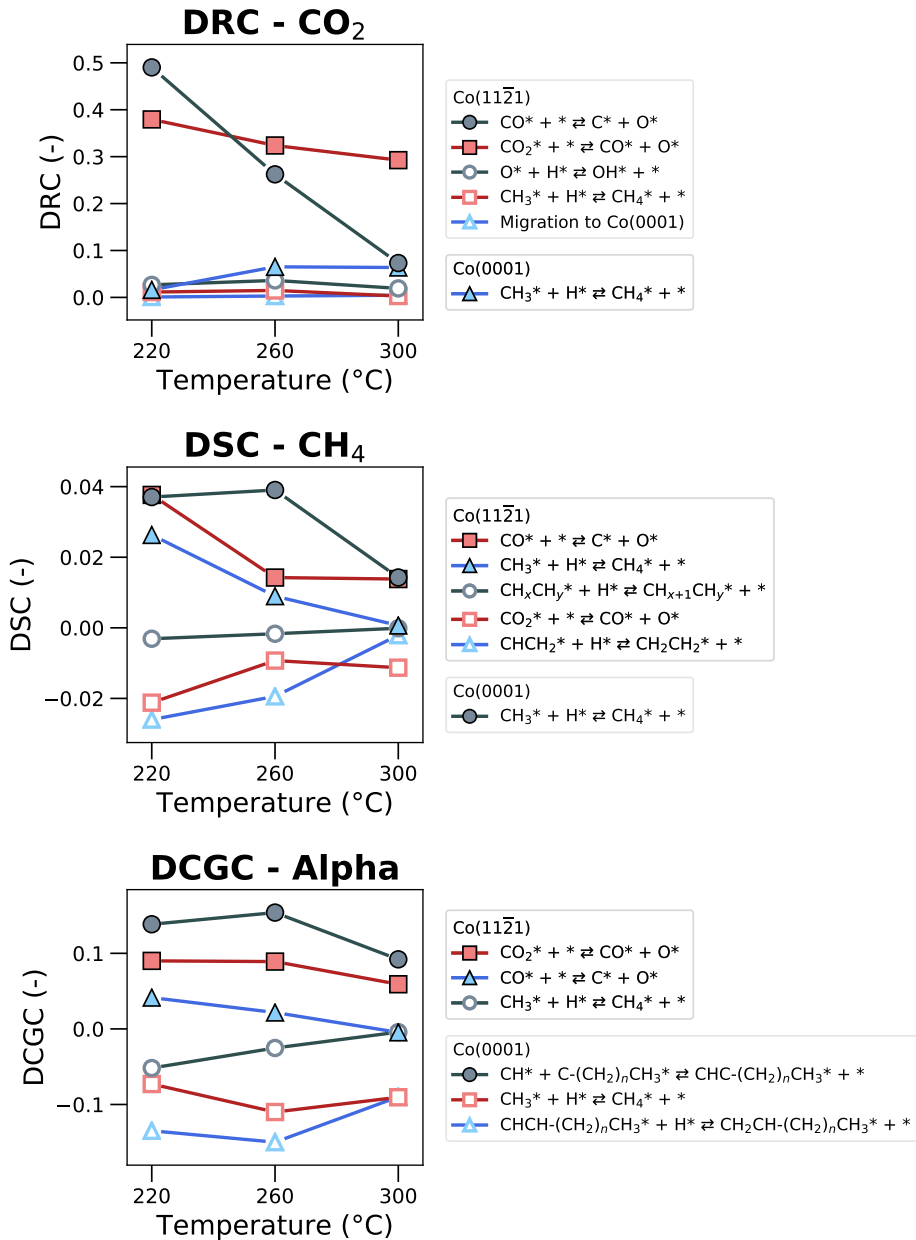


Figure 6.15: Sensitivity analysis of CO₂ hydrogenation on a combined surface consisting of 10% Co(11 $\bar{2}$ 1) and 90% Co(0001). (conditions: T = 220/260/300 °C, p_{H₂} = 750 mbar, p_{CO} = 250 mbar, p_T = 5000 mbar).

6.4 Conclusions

We carried out microkinetics simulations of the FT reaction starting from mixtures of CO and H₂ as well as from CO₂ and H₂. As surface models we used the Co(11 $\bar{2}$ 1) and Co(0001) to describe step-edges and terraces. Lateral interactions for CO and H species were involved in the calculations as well. A DFT-based dataset of energetics for CO dissociation, CH₄, CO₂ and H₂O formation was extended with energetics of elementary reaction steps of chain growth and product formation via hydrogenation. Both carbide and CO insertion mechanisms were considered for chain growth. Although CO insertion is relatively easy, the lowest overall barriers for chain growth are substantially higher than those for the carbide mechanism. Relative to C, H, and CO, the lowest overall barriers for CH_xC–O scission are 165 kJ/mol for CHCO on Co(0001) and 139 kJ/mol for CHCO on Co(11 $\bar{2}$ 1). Preferred coupling pathways that lead to C₂ hydrocarbons have barriers of 71 kJ/mol and 85 kJ/mol for CH+CH₍₂₎ coupling on Co(0001) and C+CH coupling on Co(11 $\bar{2}$ 1), respectively. These barriers are lower than the barrier for CO dissociation on Co(11 $\bar{2}$ 1). Equivalent C+CCH₃ and CH+CCH₃ coupling steps have similar activation barriers. DFT-based C₂ and C₃ hydrocarbon formation barriers were extended to longer hydrocarbon chains in order to describe chain growth. The species with the lowest energy that can participate in chain growth (CCH₂CH₃) has an overall formation barrier comparable to that of CO dissociation. CO bond scission and chain growth compete with a slightly lower barrier than that of termination to olefins.

Microkinetics simulations of the Co(11 $\bar{2}$ 1) surface predict kinetic parameters that correspond well with experimental kinetic data obtained for cobalt catalysts. TOF values are higher than experimental data, which is explained by the presence of additional less-reactive sites on real nanoparticles. The data show that the chain-growth probability decreases with increasing temperature and H₂/CO ratio. This is caused by a higher CH_x monomer concentration and a lower H coverage. The CH₄ selectivity is much lower than experimentally observed, showing that step-edge sites mainly catalyze formation of olefins. O removal and CO dissociation are steps that significantly control the overall CO consumption activity. The simulations show that the Co(11 $\bar{2}$ 1) model surface is highly active and selective for the FT reaction with a proper chain-growth probability. Adding a terrace Co(0001) surface to the step-edge model leads to small but significant changes in the outcome of the simulations. A prominent influence of the dual-site surface model is a substantially higher CH₄ selectivity at the expense of the C₂₊-hydrocarbons selectivity. A model consisting of 10% Co(11 $\bar{2}$ 1) and 90% Co(0001) surface sites leads to a product distribution with a higher CH₄ selectivity close to experimental observations. The dominant coupling pathway is C+C-(CH₂)_nCH₃. Chain growth is inhibited by hydrogenation of CHCH-(CH₂)_nCH₃ intermediates. O atoms are mainly removed via O hydrogenation followed by OH+OH proton shuffling to H₂O and O. The source of additional CH₄ is CH and CH₃ migration from step-edge to terrace sites followed by hydrogenation. Under conditions of low CO coverage, a small contribution of chain growth on terrace sites is noted in a nearly negligible amount.

Replacing CO with CO₂ may become relevant in a scenario in which fossil energy is replaced by renewable hydrogen and would be an interesting manner to obtain renewable

liquid transportation fuels with FT chemistry. The investigation of CO₂ hydrogenation on the same dual-site model as explored for CO hydrogenation shifts the product distribution nearly completely to CH₄ with CO as a minor by-product. The reason for this is the low CO coverage under steady-state conditions, resulting in a very low rate of formation of the chain growth monomer. This together with the high H coverage results in hydrogenation being dominant. The product distribution corresponds to the product distribution obtained for conventional FT synthesis at a high H₂/CO ratio.

6.5 References

- [1] M. E. Dry, *Catalysis Today* **2002**, *71*, 227–241.
- [2] G. P. Van Der Laan, A. A. C. M. Beenackers, *Catalysis Reviews* **1999**, *41*, 255–318.
- [3] Q. Ge, M. Neurock, H. A. Wright, N. Srinivasan, *The Journal of Physical Chemistry B* **2002**, *106*, 2826–2829.
- [4] Z.-P. Liu, P. Hu, *Journal of the American Chemical Society* **2002**, *124*, 11568–11569.
- [5] S. Shetty, A. P. Jansen, R. A. van Santen, *J Am Chem Soc* **2009**, *131*, 12874–5.
- [6] M. Ojeda, R. Nabar, A. U. Nilekar, A. Ishikawa, M. Mavrikakis, E. Iglesia, *Journal of Catalysis* **2010**, *272*, 287–297.
- [7] S. Shetty, R. A. van Santen, *Phys Chem Chem Phys* **2010**, *12*, 6330–2.
- [8] S. B. Vendelbo, M. Johansson, D. J. Mowbray, M. P. Andersson, F. Abild-Pedersen, J. H. Nielsen, J. K. Nørskov, I. Chorkendorff, *Topics in Catalysis* **2010**, *53*, 357–364.
- [9] S. G. Shetty, I. M. Ciobica, E. J. Hensen, R. A. van Santen, *Chem Commun (Camb)* **2011**, *47*, 9822–4.
- [10] P. van Helden, J.-A. van den Berg, I. M. Ciobîcă, *Catalysis Science & Technology* **2012**, *2*, 491–494.
- [11] P. van Helden, J.-A. van den Berg, C. J. Weststrate, *ACS Catalysis* **2012**, *2*, 1097–1107.
- [12] D. D. Hibbitts, B. T. Loveless, M. Neurock, E. Iglesia, *Angew Chem Int Ed Engl* **2013**, *52*, 12273–8.
- [13] J. X. Liu, H. Y. Su, D. P. Sun, B. Y. Zhang, W. X. Li, *J Am Chem Soc* **2013**, *135*, 16284–7.
- [14] J.-X. Liu, H.-Y. Su, W.-X. Li, *Catalysis Today* **2013**, *215*, 36–42.
- [15] B. T. Loveless, C. Buda, M. Neurock, E. Iglesia, *J Am Chem Soc* **2013**, *135*, 6107–21.
- [16] M. Zhuo, A. Borgna, M. Saeys, *Journal of Catalysis* **2013**, *297*, 217–226.
- [17] I. A. W. Filot, R. A. van Santen, E. J. M. Hensen, *Catal. Sci. Technol.* **2014**, *4*, 3129–3140.
- [18] G. T. K. K. Gunasooriya, A. P. van Bavel, H. P. C. E. Kuipers, M. Saeys, *Surface Science* **2015**, *642*, L6–L10.

- [19] D. Hibbitts, E. Dybeck, T. Lawlor, M. Neurock, E. Iglesia, *Journal of Catalysis* **2016**, *337*, 91–101.
- [20] P. van Helden, I. M. Ciobică, R. L. J. Coetzer, *Catalysis Today* **2016**, *261*, 48–59.
- [21] M. A. Petersen, J. A. van den Berg, I. M. Ciobica, P. van Helden, *ACS Catalysis* **2017**, *7*, 1984–1992.
- [22] H.-Y. Su, Y. Zhao, J.-X. Liu, K. Sun, W.-X. Li, *Catalysis Science & Technology* **2017**, *7*, 2967–2977.
- [23] N. Yang, A. J. Medford, X. Liu, F. Studt, T. Bligaard, S. F. Bent, J. K. Nørskov, *Journal of the American Chemical Society* **2016**, *138*, 3705–3714.
- [24] I. A. Filot, R. A. van Santen, E. J. Hensen, *Angew Chem Int Ed Engl* **2014**, *53*, 12746–12750.
- [25] I. A. W. Filot, R. J. P. Broos, J. P. M. van Rijn, G. J. H. A. van Heugten, R. A. van Santen, E. J. M. Hensen, *ACS Catalysis* **2015**, *5*, 5453–5467.
- [26] R. A. van Santen, A. J. Markvoort, I. A. W. Filot, M. M. Ghouri, E. J. M. Hensen, *Physical Chemistry Chemical Physics* **2013**, *15*, 17038–17063.
- [27] I. A. W. Filot, B. Zijlstra, R. J. P. Broos, W. Chen, R. Pestman, E. J. M. Hensen, *Faraday Discussions* **2017**, *197*, 153–164.
- [28] P. van Helden, J.-A. v. d. Berg, M. A. Petersen, W. Janse van Rensburg, I. M. Ciobică, J. van de Loosdrecht, *Faraday Discussions* **2017**, *197*, 117–151.
- [29] R. Zhang, L. Kang, H. Liu, L. He, B. Wang, *Computational Materials Science* **2018**, *145*, 263–279.
- [30] W. Chen, I. A. W. Filot, R. Pestman, E. J. M. Hensen, *ACS Catalysis* **2017**, *7*, 8061–8071.
- [31] G. L. Bezemer, J. H. Bitter, H. P. Kuipers, H. Oosterbeek, J. E. Holewijn, X. Xu, F. Kapteijn, A. J. van Dillen, K. P. de Jong, *J Am Chem Soc* **2006**, *128*, 3956–64.
- [32] J. P. den Breejen, P. B. Radstake, G. L. Bezemer, J. H. Bitter, V. Froseth, A. Holmen, K. P. de Jong, *J Am Chem Soc* **2009**, *131*, 7197–203.
- [33] W. Chen, R. Pestman, F.-K. Chiang, E. J. M. Hensen, *Journal of Catalysis* **2018**, *366*, 107–114.
- [34] P. E. Blochl, *Phys Rev B Condens Matter* **1994**, *50*, 17953–17979.
- [35] G. Kresse, J. Hafner, *Physical Review B* **1993**, *47*, 558–561.
- [36] G. Kresse, J. Hafner, *Physical Review B* **1994**, *49*, 14251–14269.
- [37] G. Kresse, J. Furthmüller, *Computational Materials Science* **1996**, *6*, 15–50.
- [38] G. Kresse, J. Furthmüller, *Physical Review B* **1996**, *54*, 11169–11186.
- [39] J. P. Perdew, K. Burke, M. Ernzerhof, *Physical Review Letters* **1996**, *77*, 3865–3868.
- [40] H. J. Monkhorst, J. D. Pack, *Physical Review B* **1976**, *13*, 5188–5192.

- [41] J. Lahtinen, J. Vaari, K. Kauraala, *Surface Science* **1998**, *418*, 502–510.
- [42] C. J. Weststrate, J. van de Loosdrecht, J. W. Niemantsverdriet, *Journal of Catalysis* **2016**, *342*, 1–16.
- [43] R. Van Hardeveld, F. Hartog, *Surface Science* **1969**, *15*, 189–230.
- [44] G. Mills, H. Jónsson, G. K. Schenter, *Surface Science* **1995**, *324*, 305–337.
- [45] G. Henkelman, B. P. Uberuaga, H. Jonsson, *Journal of Chemical Physics* **2000**, *113*, 9901–9904.
- [46] G. Henkelman, H. Jónsson, *The Journal of Chemical Physics* **2000**, *113*, 9978–9985.
- [47] I. A. W. Filot, B. Zijlstra, E. J. M. Hensen, MKMCXX, a C++ program for constructing microkinetic models, <http://www.mkmcxx.nl/>.
- [48] J. Xu, G. F. Froment, *AIChE Journal* **1989**, *35*, 88–96.
- [49] W. Chen, R. Pestman, B. Zijlstra, I. A. W. Filot, E. J. M. Hensen, *ACS Catalysis* **2017**, *7*, 8050–8060.
- [50] W. Chen, T. F. Kimpel, Y. Song, F. K. Chiang, B. Zijlstra, R. Pestman, P. Wang, E. J. M. Hensen, *ACS Catalysis* **2018**, *8*, 1580–1590.
- [51] W. Chen, B. Zijlstra, I. A. W. Filot, R. Pestman, E. J. M. Hensen, *ChemCatChem* **2018**, *10*, 136–140.
- [52] J. Schweicher, A. Bundhoo, N. Kruse, *Journal of the American Chemical Society* **2012**, *134*, 16135–16138.
- [53] I. C. Yates, C. N. Satterfield, *Energy & Fuels* **1991**, *5*, 168–173.
- [54] T. Herranz, X. Deng, A. Cabot, J. Guo, M. Salmeron, *The Journal of Physical Chemistry B* **2009**, *113*, 10721–10727.
- [55] J. Yang, E. Z. Tveten, D. Chen, A. Holmen, *Langmuir* **2010**, *26*, 16558–16567.
- [56] E. Rebmann, P. Fongarland, V. Lecocq, F. Diehl, Y. Schuurman, *ChemCatChem* **2017**, *9*, 2344–2351.
- [57] F. Kapteijn, R. M. de Deugd, J. A. Moulijn, *Catalysis Today* **2005**, *105*, 350–356.
- [58] Z. Yan, Z. Wang, D. B. Bukur, D. W. Goodman, *Journal of Catalysis* **2009**, *268*, 196–200.
- [59] R. Zennaro, M. Tagliabue, C. H. Bartholomew, *Catalysis Today* **2000**, *58*, 309–319.
- [60] C. J. Weststrate, I. M. Ciobică, A. M. Saib, D. J. Moodley, J. W. Niemantsverdriet, *Catalysis Today* **2014**, *228*, 106–112.
- [61] C. J. Weststrate, P. van Helden, J. W. Niemantsverdriet, *Catalysis Today* **2016**, *275*, 100–110.
- [62] E. Billig, M. Decker, W. Benzinger, F. Ketelsen, P. Pfeifer, R. Peters, D. Stolten, D. Thrän, *Journal of CO₂ Utilization* **2019**, *30*, 130–141.
- [63] Y. A. Daza, J. N. Kuhn, *RSC Advances* **2016**, *6*, 49675–49691.

- [64] Y. A. Daza, R. A. Kent, M. M. Yung, J. N. Kuhn, *Industrial & Engineering Chemistry Research* **2014**, *53*, 5828–5837.
- [65] Federal Ministry of Education and Research, The P2X Kopernikus project, <https://www.kopernikus-projekte.de/en/projects/power2x>.
- [66] R. Dittmeyer, M. Klumpp, P. Kant, G. Ozin, *Nature Communications* **2019**, *10*, 1818.
- [67] C. Sun, T. Zhan, P. Pfeifer, R. Dittmeyer, *Chemical Engineering Journal* **2017**, *310*, 272–281.
- [68] J. Wei, Q. Ge, R. Yao, Z. Wen, C. Fang, L. Guo, H. Xu, J. Sun, *Nature Communications* **2017**, *8*, 15174.
- [69] T. Riedel, M. Claeys, H. Schulz, G. Schaub, S.-S. Nam, K.-W. Jun, M.-J. Choi, G. Kishan, K.-W. Lee, *Applied Catalysis A: General* **1999**, *186*, 201–213.
- [70] Y. Zhang, G. Jacobs, D. E. Sparks, M. E. Dry, B. H. Davis, *Catalysis Today* **2002**, *71*, 411–418.
- [71] A. N. Akin, M. Ataman, A. E. Aksoylu, Z. I. Önsan, *Reaction Kinetics and Catalysis Letters* **2002**, *76*, 265–270.
- [72] R. W. Dorner, D. R. Hardy, F. W. Williams, B. H. Davis, H. D. Willauer, *Energy & Fuels* **2009**, *23*, 4190–4195.
- [73] S. K. Beaumont, S. Alayoglu, C. Specht, N. Kruse, G. A. Somorjai, *Nano Letters* **2014**, *14*, 4792–4796.
- [74] R. L. Palmer, D. A. Vroom, *Journal of Catalysis* **1977**, *50*, 244–251.
- [75] G. D. Weatherbee, C. H. Bartholomew, *Journal of Catalysis* **1984**, *87*, 352–362.

Appendix C

C.1. Overall thermodynamics

Figure C1 shows enthalpic and entropic contributions to the gas-phase energies of CO, CO₂, H₂, H₂O, CH₄, and C₂H₄ as a function of temperature. These values were obtained from thermodynamic tables [1] using the Shomate equation [2]. For longer hydrocarbons, we assumed a similar temperature dependence of paraffins and olefins with temperature as determined for CH₄ and C₂H₄, respectively.

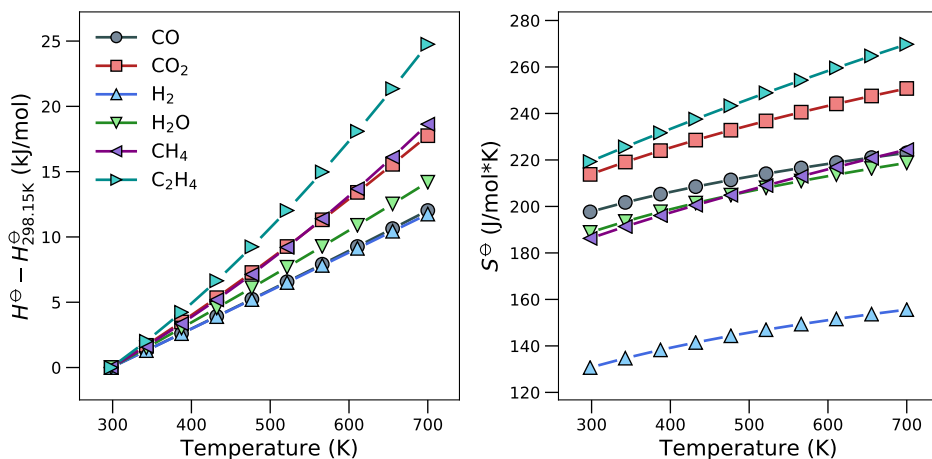


Figure C1: Enthalpic (left panel) and entropic (right panel) contributions to the gas-phase energies of CO, CO₂, H₂, H₂O, CH₄, and C₂H₄ as a function of temperature.

Figure C2 displays the enthalpic and entropic contributions to the reaction energy of the reaction of CO and H₂ into paraffins and olefins under standard conditions. We calculated that the enthalpic reaction energy changes by -152 kJ/mol upon extending the hydrocarbon chain with one CH₂ unit. The change in the entropic reaction energy was -231 J/mol·K. We found that the standard state entropy of hydrocarbon chains increases by 39.2 J/mol·K per CH₂ group.

Together, these reaction energies and temperature corrections allow obtaining the Gibbs free energy change for CO hydrogenation into paraffins and olefins of any length. Figure C3 shows that, at 493.15 K, the enthalpic reaction energy is larger than the entropic difference. Correspondingly, the Gibbs free energy change is negative for all chain lengths. Furthermore, the formation of paraffins is favored and the thermodynamic driving force for paraffins formation with respect to olefins formation increases with chain length. The right panel of Figure 3 shows that the Gibbs free energy difference becomes positive at high temperatures (>600 K). Under such conditions, the production of shorter chain lengths is favored.

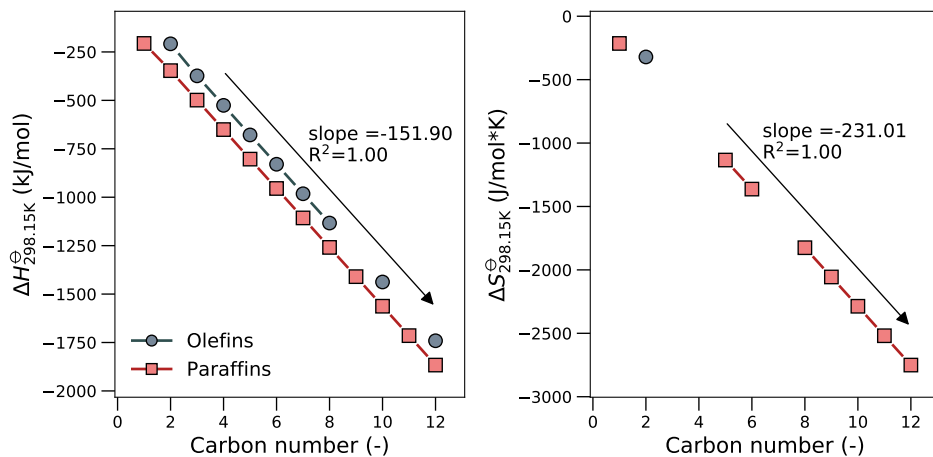


Figure C2: Enthalpic (left panel) and entropic (right panel) contributions to the reaction energy of CO hydrogenation into paraffins and olefins.

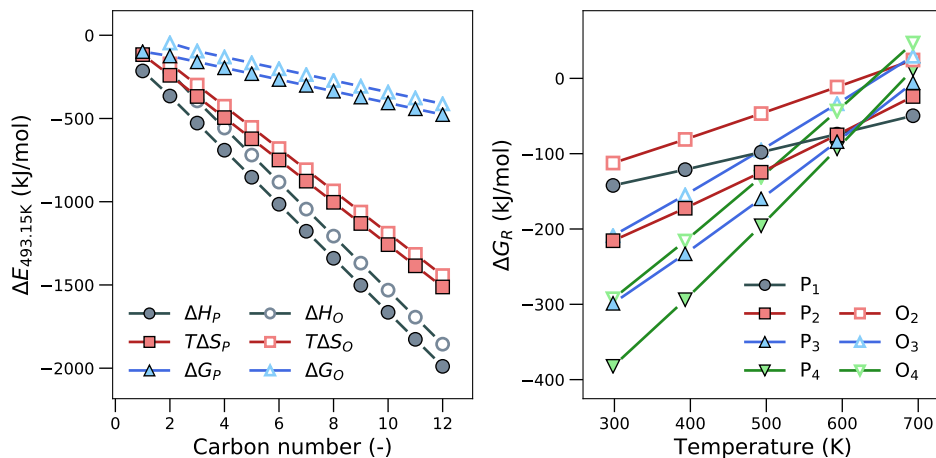


Figure C3: Reaction energy for the formation of hydrocarbon chains. (left panel) enthalpic, entropic and Gibbs free reaction energy at 493.15 K. (right panel) Gibbs free reaction energy of C_1 - C_4 production as a function of temperature.

C.2. Extrapolation corrections

The extension of a hydrocarbon chain by one CH_2 -group will increase the reaction energy. This increase is in part due to the enthalpy difference between one produced H_2O molecule and consumed CO and H_2 molecules. Removing this term results in $E_{\text{CH}_2}^{\text{thermo}}$, which reflects the enthalpic difference between gaseous hydrocarbons of length $n + 1$ and n .

$$E_{\text{CH}_2}^{\text{thermo}} = \left(E_{\text{HC},n+1}^{\text{thermo}} - E_{\text{HC},n}^{\text{thermo}} \right) - \left(E_{\text{H}_2\text{O}}^{\text{thermo}} - E_{\text{CO}}^{\text{thermo}} - 2E_{\text{H}_2}^{\text{thermo}} \right) \quad (6.9)$$

A difference between this value and the DFT-extrapolated values originates from inaccuracies in the energetics of the elementary reaction steps. To obtain thermodynamic consistency, we modify the energetics of the coupling reactions by δH_i^{corr} according to:

$$\delta H_{\text{CR}}^{\text{corr}} = E_{\text{CH}_2}^{\text{thermo}} - \left(E_{\text{CCH}_2\text{CH}_3}^{\text{DFT}} - E_{\text{CCH}_3}^{\text{DFT}} \right) \quad (6.10)$$

$$\delta H_{\text{CHR}}^{\text{corr}} = E_{\text{CH}_2}^{\text{thermo}} - \left(E_{\text{CHCH}_2\text{CH}_3}^{\text{DFT}} - E_{\text{CHCH}_3}^{\text{DFT}} \right) \quad (6.11)$$

$$\delta H_{\text{CH}_2\text{R}}^{\text{corr}} = E_{\text{CH}_2}^{\text{thermo}} - \left(E_{\text{CH}_2\text{CH}_2\text{CH}_3}^{\text{DFT}} - E_{\text{CH}_2\text{CH}_3}^{\text{DFT}} \right) \quad (6.12)$$

Analogous to such an enthalpy correction, the entropy correction Q_i^{corr} is defined as:

$$Q_{\text{CR}}^{\text{corr}} = \frac{Q_{\text{CH}_2}^{\text{thermo}}}{\left(Q_{\text{CCH}_2\text{CH}_3}^{\text{DFT}} / Q_{\text{CCH}_3}^{\text{DFT}} \right)} \quad (6.13)$$

$$Q_{\text{CHR}}^{\text{corr}} = \frac{Q_{\text{CH}_2}^{\text{thermo}}}{\left(Q_{\text{CHCH}_2\text{CH}_3}^{\text{DFT}} / Q_{\text{CHCH}_3}^{\text{DFT}} \right)} \quad (6.14)$$

$$Q_{\text{CH}_2\text{R}}^{\text{corr}} = \frac{Q_{\text{CH}_2}^{\text{thermo}}}{\left(Q_{\text{CH}_2\text{CH}_2\text{CH}_3}^{\text{DFT}} / Q_{\text{CH}_2\text{CH}_3}^{\text{DFT}} \right)} \quad (6.15)$$

Q_i^{DFT} is the vibrational partition function of adsorbed component i . For the entropy factor $Q_{\text{CH}_2}^{\text{thermo}}$ we computed the ratio of the vibrational partition functions of adsorbed C_2 and C_3 olefins after removing the vibrational contributions of one produced H_2O molecules and consumed CO and H_2 molecules according to

$$Q_{\text{CH}_2}^{\text{thermo}} = \frac{Q_{\text{CH}_2\text{CHCH}_3}^{\text{DFT}} / Q_{\text{CH}_2\text{CH}_2}^{\text{DFT}}}{Q_{\text{H}_2\text{O}}^{\text{DFT}} / \left(Q_{\text{CO}}^{\text{DFT}} (Q_{\text{H}}^{\text{DFT}})^4 \right)} \quad (6.16)$$

Likewise, the vibrational partition functions of the desorbing hydrocarbons are increased by a factor of $Q_{\text{CH}_2\text{CHCH}_3}^{\text{DFT}} / Q_{\text{CH}_2\text{CH}_2}^{\text{DFT}}$ for each extension of the hydrocarbon chain.

Table C1 contains the resulting thermodynamic correction factors for the C_{4+} formation reactions. The enthalpy corrections are below 3 kJ/mol, showing that the DFT data is more than accurate enough for this method of extrapolation. The entropy corrections at 493.15 K to barriers are of the order of 7-15 kJ/mol on the $\text{Co}(0001)$ surface and 2-4 kJ/mol on the $\text{Co}(11\bar{2}1)$ surface. We expect that the slightly larger corrections for the $\text{Co}(0001)$ surface follow from the more pronounced differences in stability between the C_2 and C_3

species on that surface.

Table C1: Thermodynamic correction factors for C_{4+} formation reactions on Co(0001) and Co(11 $\bar{2}$ 1).

Correction factor -R = $(CH_2)_nCH_3$	Co(0001)	Co(11 $\bar{2}$ 1)
$+\Delta H$	<u>kJ/mol</u>	<u>kJ/mol</u>
$CH_x^* + C-R^* \rightleftharpoons CH_xC-R^*$	-1.27	-0.65
$CH_x^* + CH-R^* \rightleftharpoons CH_xCH-R^*$	-0.66	2.82
$CH_x^* + CH_2-R^* \rightleftharpoons CH_xCH_2-R^*$	2.69	1.37
$-T\Delta S$ (493.15 K)	<u>Q_{FS}/Q_{IS}</u>	<u>Q_{FS}/Q_{IS}</u>
$CH_x^* + C-R^* \rightleftharpoons CH_xC-R^*$	0.0229	0.623
$CH_x^* + CH-R^* \rightleftharpoons CH_xCH-R^*$	0.1071	0.491
$CH_x^* + CH_2-R^* \rightleftharpoons CH_xCH_2-R^*$	0.1706	0.366
$-T\Delta S$ (493.15 K) per n	<u>Q_{vib}</u>	<u>Q_{vib}</u>
Desorbing hydrocarbon	12.371	27.479

C.3. Vibrational partition functions

Table C2: Ratios of vibrational partition functions at 493.15 K for carbon-carbon coupling reactions on Co(0001) and Co(11 $\bar{2}$ 1).

Elementary reaction	Co(0001) at 493.15 K		Co(11 $\bar{2}$ 1) at 493.15 K	
	Q_{TS}/Q_{IS}	Q_{TS}/Q_{FS}	Q_{TS}/Q_{IS}	Q_{TS}/Q_{FS}
$C^* + C^* \rightleftharpoons CC^*$	1.09	6.91×10^{-1}	7.20×10^{-1}	4.16×10^{-1}
$C^* + CH^* \rightleftharpoons CCH^*$	9.74×10^{-1}	6.61×10^{-1}	7.01×10^{-1}	4.01×10^{-1}
$C^* + CH_2^* \rightleftharpoons CCH_2^*$	7.67×10^{-1}	4.55×10^{-1}	3.78×10^{-1}	3.57×10^{-1}
$C^* + CH_3^* \rightleftharpoons CCH_3^*$	1.55	1.80	5.65×10^{-1}	3.54×10^{-1}
$CH^* + CH^* \rightleftharpoons CHCH^*$	9.38×10^{-1}	7.85×10^{-1}	6.28×10^{-1}	4.12×10^{-1}
$CH^* + CH_2^* \rightleftharpoons CHCH_2^*$	6.65×10^{-1}	3.63×10^{-1}	3.82×10^{-1}	4.52×10^{-1}
$CH^* + CH_3^* \rightleftharpoons CHCH_3^*$	1.16	3.46×10^{-1}	7.54×10^{-1}	1.19
$CH_2^* + CH_2^* \rightleftharpoons CH_2CH_2^*$	4.77×10^{-1}	2.40×10^{-1}	7.27×10^{-1}	3.57×10^{-1}
$CH_2^* + CH_3^* \rightleftharpoons CH_2CH_3^*$	2.25	7.41×10^{-1}	1.75	1.11

Table C3: Ratios of vibrational partition functions at 493.15 K for the CO-insertion mechanism on Co(0001) and Co(11 $\bar{2}$ 1).

Elementary reaction	Co(0001) at 493.15 K		Co(11 $\bar{2}$ 1) at 493.15 K	
	$Q_{\text{TS}}/Q_{\text{IS}}$	$Q_{\text{TS}}/Q_{\text{FS}}$	$Q_{\text{TS}}/Q_{\text{IS}}$	$Q_{\text{TS}}/Q_{\text{FS}}$
$\text{C}^* + \text{CO}^* \rightleftharpoons \text{CCO}^*$	4.08×10^{-1}	1.61×10^{-1}	1.85	1.02
$\text{CH}^* + \text{CO}^* \rightleftharpoons \text{CHCO}^*$	9.52×10^{-2}	2.86×10^{-1}	4.97×10^{-1}	9.83×10^{-1}
$\text{CH}_2^* + \text{CO}^* \rightleftharpoons \text{CH}_2\text{CO}^*$	1.68×10^{-1}	5.86×10^{-1}	2.36×10^{-1}	4.70×10^{-1}
$\text{CH}_3^* + \text{CO}^* \rightleftharpoons \text{CH}_3\text{CO}^*$	2.85×10^{-1}	4.90×10^{-1}	5.26×10^{-1}	9.54×10^{-1}
$\text{CCO}^* \rightleftharpoons \text{CC}^* + \text{O}^*$	7.21×10^{-2}	1.41	2.60×10^{-1}	5.58×10^{-1}
$\text{CHCO}^* \rightleftharpoons \text{CCH}^* + \text{O}^*$	7.53×10^{-1}	2.08	7.40×10^{-1}	5.99×10^{-1}
$\text{CH}_2\text{CO}^* \rightleftharpoons \text{CCH}_2^* + \text{O}^*$	6.11×10^{-1}	1.27	5.16×10^{-1}	6.87×10^{-1}
$\text{CH}_3\text{CO}^* \rightleftharpoons \text{CCH}_3^* + \text{O}^*$	3.58×10^{-1}	2.94	4.80×10^{-1}	4.65×10^{-1}

Table C4: Ratios of vibrational partition functions at 493.15 K for C₂-hydrogenation reactions on Co(0001) and Co(11 $\bar{2}$ 1).

Elementary reaction	Co(0001) at 493.15 K		Co(11 $\bar{2}$ 1) at 493.15 K	
	$Q_{\text{TS}}/Q_{\text{IS}}$	$Q_{\text{TS}}/Q_{\text{FS}}$	$Q_{\text{TS}}/Q_{\text{IS}}$	$Q_{\text{TS}}/Q_{\text{FS}}$
$\text{CC}^* + \text{H}^* \rightleftharpoons \text{CCH}^*$	7.44×10^{-1}	5.72×10^{-1}	7.71×10^{-1}	5.84×10^{-1}
$\text{CCH}^* + \text{H}^* \rightleftharpoons \text{CCH}_2^*$	8.46×10^{-1}	3.79×10^{-1}	6.11×10^{-1}	4.32×10^{-1}
$\text{CCH}_2^* + \text{H}^* \rightleftharpoons \text{CCH}_3^*$	6.67×10^{-1}	7.35×10^{-1}	9.72×10^{-1}	2.50×10^{-1}
$\text{CHCH}^* + \text{H}^* \rightleftharpoons \text{CHCH}_2^*$	5.65×10^{-1}	1.89×10^{-1}	1.92	1.47
$\text{CHCH}_2^* + \text{H}^* \rightleftharpoons \text{CHCH}_3^*$	8.27×10^{-1}	2.56×10^{-1}	7.42×10^{-1}	3.86×10^{-1}
$\text{CH}_2\text{CH}_2^* + \text{H}^* \rightleftharpoons \text{CH}_2\text{CH}_3^*$	5.21×10^{-1}	1.93×10^{-1}	9.97×10^{-1}	5.02×10^{-1}
$\text{CCH}^* + \text{H}^* \rightleftharpoons \text{CHCH}^*$	3.56	3.14	1.18	1.03
$\text{CCH}_2^* + \text{H}^* \rightleftharpoons \text{CHCH}_2^*$	1.06	7.00×10^{-1}	8.73×10^{-1}	8.35×10^{-1}
$\text{CCH}_3^* + \text{H}^* \rightleftharpoons \text{CHCH}_3^*$	4.07	7.55×10^{-1}	6.49×10^{-1}	1.25
$\text{CHCH}_2^* + \text{H}^* \rightleftharpoons \text{CH}_2\text{CH}_2^*$	1.06	4.99×10^{-1}	1.70	3.02×10^{-1}
$\text{CHCH}_3^* + \text{H}^* \rightleftharpoons \text{CH}_2\text{CH}_3^*$	1.27	7.15×10^{-1}	2.18	3.75×10^{-1}
$\text{CH}_2\text{CH}_3^* + \text{H}^* \rightleftharpoons \text{CH}_3\text{CH}_3^*$	2.69	2.56×10^{-2}	4.30×10^{-1}	1.98×10^{-2}

Table C5: Ratios of vibrational partition functions at 493.15 K for C₃-formation reactions on Co(0001) and Co(11 $\bar{2}$ 1).

Elementary reaction	Co(0001) at 493.15 K		Co(11 $\bar{2}$ 1) at 493.15 K	
	$Q_{\text{TS}}/Q_{\text{IS}}$	$Q_{\text{TS}}/Q_{\text{FS}}$	$Q_{\text{TS}}/Q_{\text{IS}}$	$Q_{\text{TS}}/Q_{\text{FS}}$
$\text{C}^* + \text{CCH}_3^* \rightleftharpoons \text{CCCH}_3^*$	3.60	7.39×10^{-1}	1.49×10^{-1}	1.04×10^{-1}
$\text{C}^* + \text{CHCH}_3^* \rightleftharpoons \text{CCHCH}_3^*$	8.81×10^{-1}	5.99×10^{-1}	4.56×10^{-1}	1.19×10^{-1}
$\text{C}^* + \text{CH}_2\text{CH}_3^* \rightleftharpoons \text{CCH}_2\text{CH}_3^*$	7.20×10^{-1}	3.29×10^{-1}	1.10	7.86×10^{-1}
$\text{CH}^* + \text{CCH}_3^* \rightleftharpoons \text{CHCCH}_3^*$	6.18	1.40	3.44×10^{-1}	1.93×10^{-1}
$\text{CH}^* + \text{CHCH}_3^* \rightleftharpoons \text{CHCHCH}_3^*$	6.25×10^{-1}	3.82×10^{-1}	8.43×10^{-1}	2.26×10^{-1}
$\text{CH}^* + \text{CH}_2\text{CH}_3^* \rightleftharpoons \text{CHCH}_2\text{CH}_3^*$	6.42×10^{-1}	3.56×10^{-1}	8.42×10^{-1}	1.20
$\text{CH}_2^* + \text{CCH}_3^* \rightleftharpoons \text{CH}_2\text{CCH}_3^*$	1.88	7.46×10^{-1}	1.81×10^{-1}	4.70×10^{-1}
$\text{CH}_2^* + \text{CHCH}_3^* \rightleftharpoons \text{CH}_2\text{CHCH}_3^*$	4.49×10^{-1}	4.70×10^{-1}	1.38	2.01×10^{-1}
$\text{CH}_2^* + \text{CH}_2\text{CH}_3^* \rightleftharpoons \text{CH}_2\text{CH}_2\text{CH}_3^*$	2.03×10^{-1}	1.97×10^{-1}	1.11	4.74×10^{-1}
$\text{CH}_3^* + \text{CCH}_3^* \rightleftharpoons \text{CH}_3\text{CCH}_3^*$	2.90	4.63×10^{-1}	3.09×10^{-1}	6.28×10^{-1}
$\text{CH}_3^* + \text{CHCH}_3^* \rightleftharpoons \text{CH}_3\text{CHCH}_3^*$	7.74×10^{-1}	4.43×10^{-1}	5.43×10^{-1}	3.26×10^{-1}

Table C6: Ratios of vibrational partition functions at 493.15 K for C₃-hydrogenation reactions on Co(0001) and Co(11 $\bar{2}$ 1).

Elementary reaction	Co(0001) at 493.15 K		Co(11 $\bar{2}$ 1) at 493.15 K	
	Q_{TS}/Q_{IS}	Q_{TS}/Q_{FS}	Q_{TS}/Q_{IS}	Q_{TS}/Q_{FS}
CCCH ₃ * + H* \rightleftharpoons CCHCH ₃ *	8.31×10^{-1}	5.12×10^{-1}	5.98×10^{-1}	4.32×10^{-1}
CCHCH ₃ * + H* \rightleftharpoons CCH ₂ CH ₃ *	6.43×10^{-1}	2.43×10^{-1}	5.57×10^{-1}	2.63×10^{-1}
CHCCH ₃ * + H* \rightleftharpoons CHCHCH ₃ *	2.91×10^{-1}	1.46×10^{-1}	3.58×10^{-1}	3.32×10^{-1}
CHCHCH ₃ * + H* \rightleftharpoons CHCH ₂ CH ₃ *	5.35×10^{-1}	2.74×10^{-1}	3.00×10^{-1}	2.74×10^{-1}
CH ₂ CCH ₃ * + H* \rightleftharpoons CH ₂ CHCH ₃ *	6.22×10^{-1}	3.06×10^{-1}	6.77	7.33×10^{-1}
CH ₂ CHCH ₃ * + H* \rightleftharpoons CH ₂ CH ₂ CH ₃ *	6.05×10^{-1}	3.16×10^{-1}	4.07×10^{-1}	2.05×10^{-1}
CH ₃ CCH ₃ * + H* \rightleftharpoons CH ₃ CHCH ₃ *	7.91×10^{-1}	5.26×10^{-1}	4.33×10^{-1}	2.48×10^{-1}
CH ₃ CHCH ₃ * + H* \rightleftharpoons CH ₃ CH ₂ CH ₃ *	2.62	5.74×10^{-2}	8.63	2.44×10^{-1}
CCCH ₃ * + H \rightleftharpoons CHCCH ₃ *	3.11	2.46	1.21	7.42×10^{-1}
CHCCH ₃ * + H* \rightleftharpoons CH ₂ CCH ₃ *	3.30×10^{-1}	2.96×10^{-1}	6.11×10^{-1}	1.21
CH ₂ CCH ₃ * + H* \rightleftharpoons CH ₃ CCH ₃ *	6.19	1.41	1.29	3.92×10^{-1}
CCHCH ₃ * + H* \rightleftharpoons CHCHCH ₃ *	1.04	6.69×10^{-1}	5.92×10^{-1}	4.66×10^{-1}
CHCHCH ₃ * + H* \rightleftharpoons CH ₂ CHCH ₃ *	6.07×10^{-1}	5.34×10^{-1}	9.99×10^{-1}	2.31×10^{-1}
CH ₂ CHCH ₃ * + H* \rightleftharpoons CH ₃ CHCH ₃ *	2.61	8.04×10^{-1}	3.43×10^{-1}	5.50×10^{-1}
CCH ₂ CH ₃ * + H* \rightleftharpoons CHCH ₂ CH ₃ *	7.58×10^{-1}	6.59×10^{-1}	7.40×10^{-1}	1.13
CHCH ₂ CH ₃ * + H* \rightleftharpoons CH ₂ CH ₂ CH ₃ *	1.76	1.58	1.63	2.08×10^{-1}
CH ₂ CH ₂ CH ₃ * + H* \rightleftharpoons CH ₃ CH ₂ CH ₃ *	3.16	4.09×10^{-2}	8.51×10^{-1}	7.65×10^{-2}

Table C7: Ratios of vibrational partition functions at 493.15 K for adsorption of hydrocarbon species on Co(0001) and Co(11 $\bar{2}$ 1). For thermodynamic consistency we have set Q_{TS} and Q_{IS} to equal unity.

Elementary reaction	Co(0001) at 493.15 K		Co(11 $\bar{2}$ 1) at 493.15 K	
	Q_{TS}/Q_{IS}	Q_{TS}/Q_{FS}	Q_{TS}/Q_{IS}	Q_{TS}/Q_{FS}
CH ₂ CH ₂ + * \rightleftharpoons CH ₂ CH ₂ *	-	6.93×10^{-3}	-	3.55×10^{-3}
CH ₃ CH ₃ + * \rightleftharpoons CH ₃ CH ₃ *	-	1.65×10^{-5}	-	5.12×10^{-5}
CH ₂ CHCH ₃ + * \rightleftharpoons CH ₂ CHCH ₃ *	-	5.60×10^{-4}	-	1.29×10^{-4}
CH ₃ CH ₂ CH ₃ + * \rightleftharpoons CH ₃ CH ₂ CH ₃ *	-	2.57×10^{-6}	-	3.64×10^{-6}

C.4. Fischer-Tropsch synthesis on the Co(11 $\bar{2}$ 1) surface as function of catalyst loading

Figure C4 shows the effects of varying the catalyst loading in the CSTR model. As expected, the CO conversion increases upon increasing the catalyst loading. Likewise, both CO conversion and TOF increase at higher temperature. At differential conditions (conversion lower than 10%) the increase in conversion scales almost linearly with catalyst loading. At higher conversion the slope decreases, which is also visible in the faster decreasing TOF. Both the CH₄ selectivity and the CO₂ increase slightly as at higher temperature and conversion. At these conditions the re-adsorption of H₂O causes a small amount (~2%) of atomic oxygen to be adsorbed on the cobalt surface. This oxygen not only reacts with CO to form CO₂, but it also recombines with atomic carbon to CO. Correspondingly, the chain growth probability decreases together with the TOF. The reaction orders plot shows that the reaction order in hydrogen is always positive and increases by higher temperature and conversion in the range of 0.6-0.9. The reaction order in CO is negative below 30% conversion and increases from -0.2 to 0.2 at 50% conversion. These changes in the reaction orders in CO and H₂ can be directly related to the increased oxygen coverage on the surface. Higher CO pressures will increase the generation of oxygen, while higher H₂ pressures will aid the removal of oxygen.

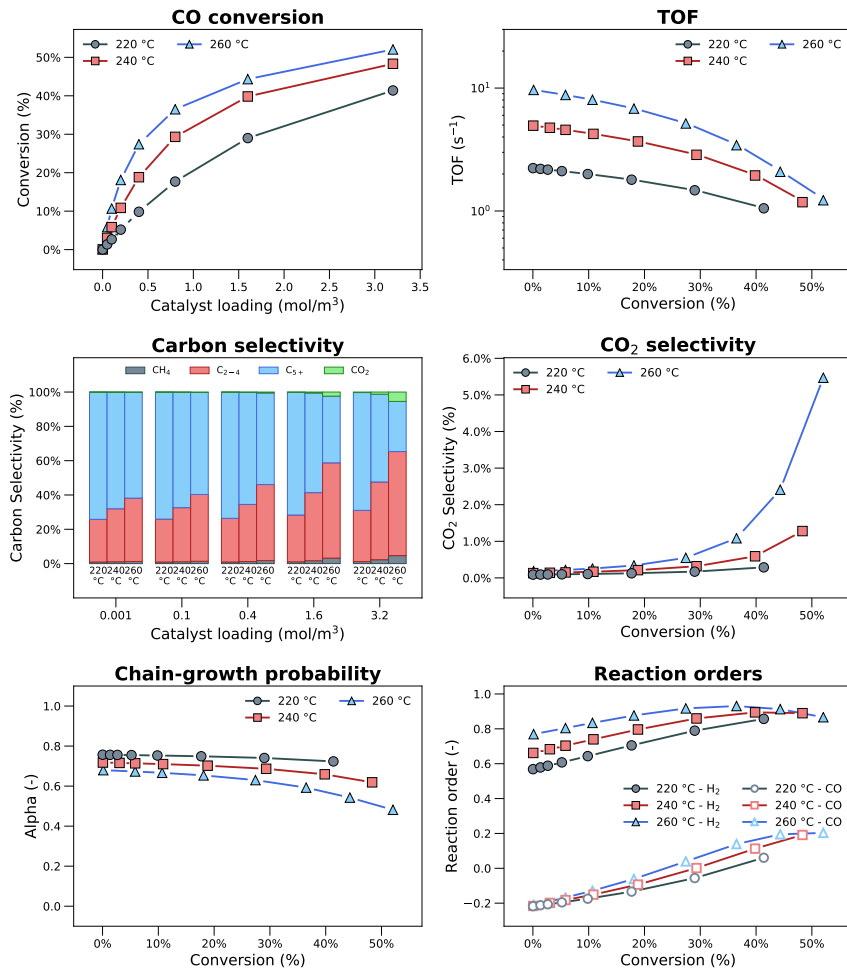


Figure C4: Microkinetics simulations of the FT synthesis reaction on the Co(11 $\bar{1}$) surface with varying catalyst loading. The simulation conditions are: T=220/240/260°C, p_{H₂}=667mbar, p_{CO}=333mbar. The conversion and TOF are based on CO consumption. All selectivities are carbon based. The chain growth probability is based on the slope of carbon numbers 5-8.

C.5. Fischer-Tropsch synthesis on the dual surface as function of catalyst loading

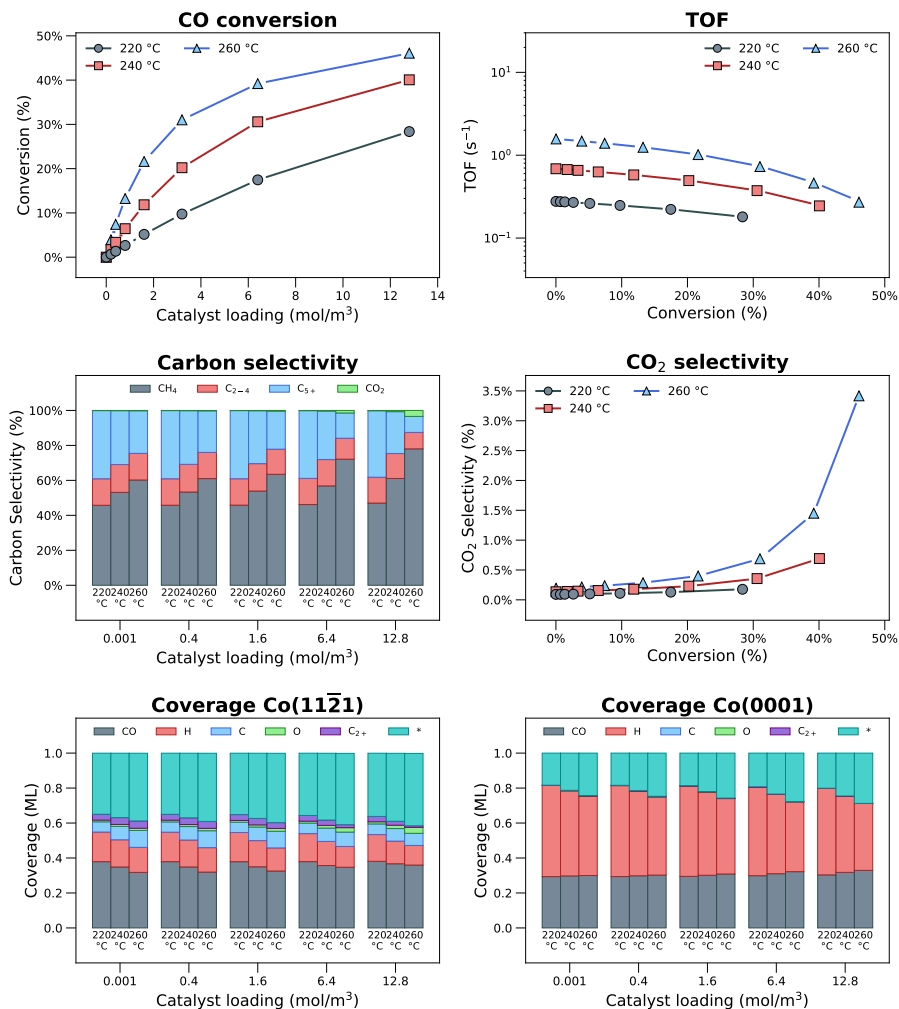


Figure C5: Microkinetics simulations of the FT synthesis reaction on a combined surface consisting of 10% Co(11 $\bar{2}$ 1) and 90% Co(0001) with varying catalyst loading (conditions: T = 220/240/260 °C, p_{H₂} = 667 mbar, p_{CO} = 333 mbar, p_T = 5000 mbar). Note that all conversion and TOF data are based on CO consumption and all product selectivities are carbon-based.

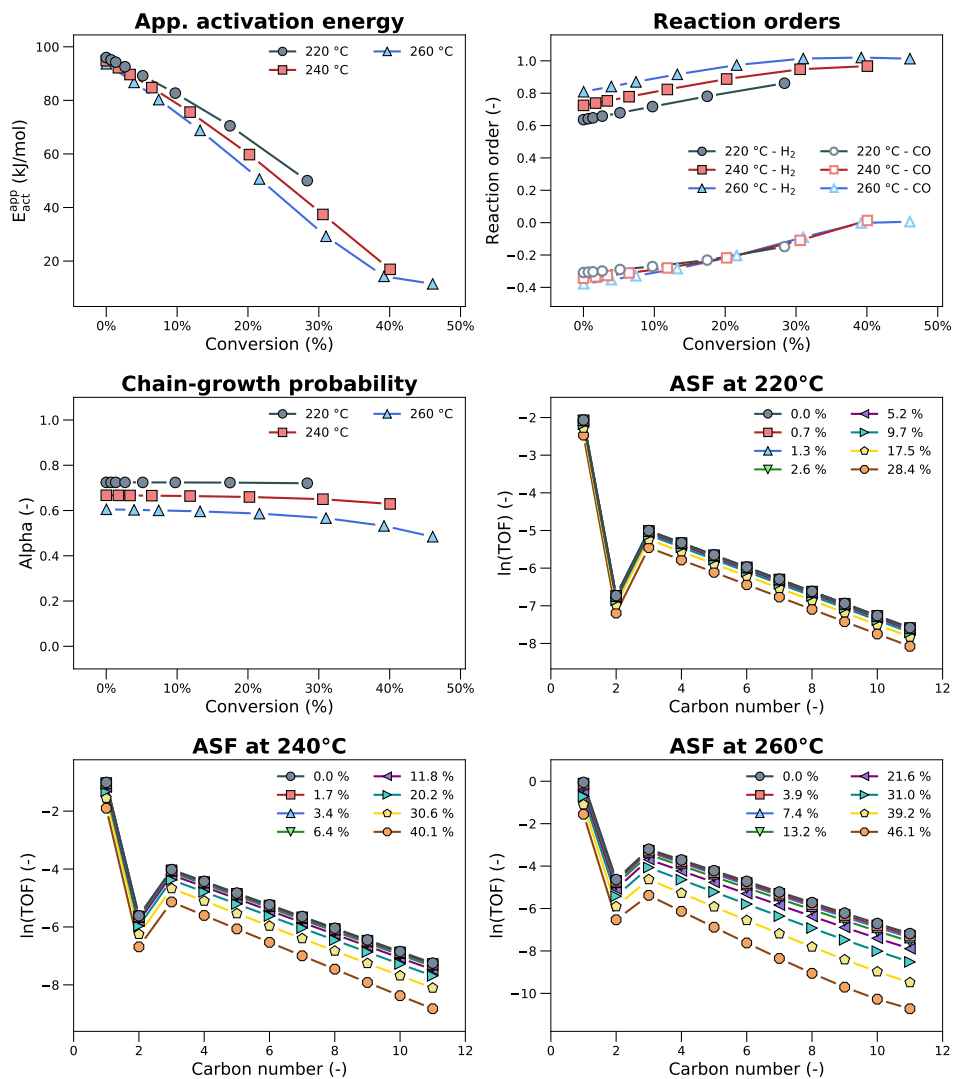


Figure C6: Microkinetics simulations of the FT synthesis reaction on a combined surface consisting of 10% $\text{Co}(11\bar{2}1)$ and 90% $\text{Co}(0001)$ with varying catalyst loading (conditions: $T = 220/240/260$ °C, $p_{\text{H}_2} = 667$ mbar, $p_{\text{CO}} = 333$ mbar, $p_{\text{T}} = 5000$ mbar). Note that the chain-growth probability is based on the slope of ASF plot for carbon numbers 5-8.

C.6. Fischer-Tropsch synthesis on the dual surface as function of CO pressure

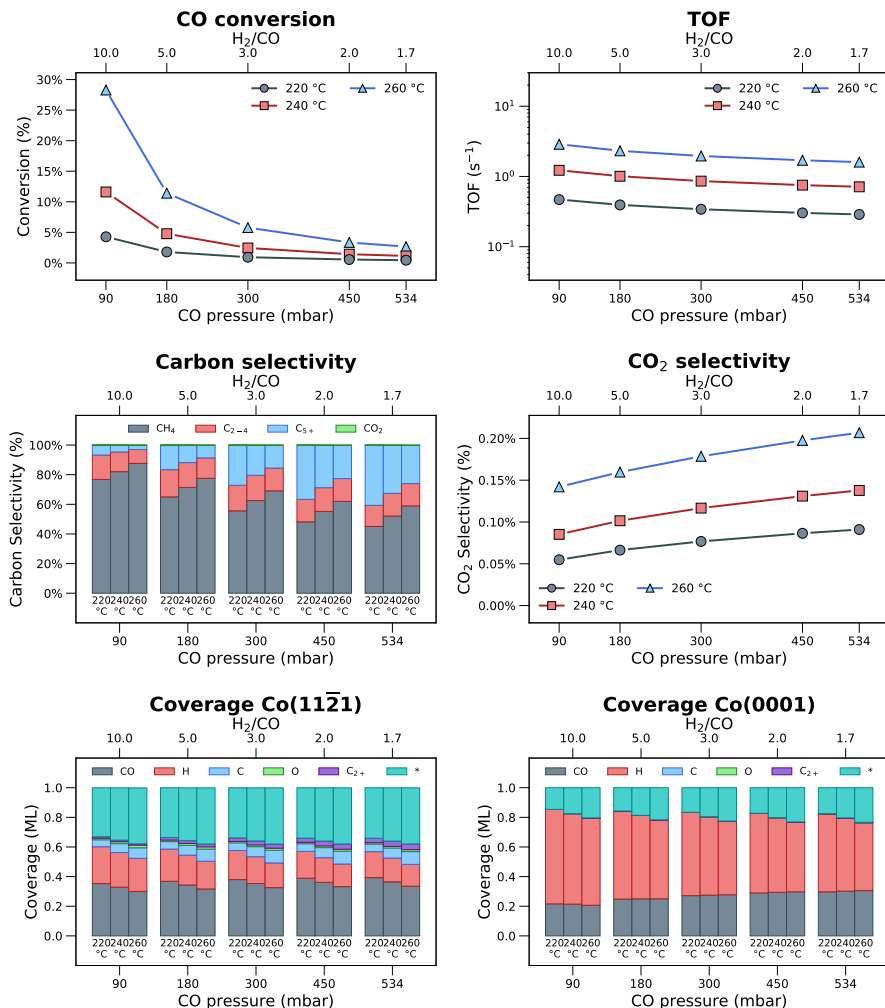


Figure C7: Microkinetics simulations of the FT synthesis reaction on a combined surface consisting of 10% Co(111̄1) and 90% Co(0001) with varying CO pressure (conditions: $T = 220/240/260$ °C, $p_{\text{H}_2} = 900$ mbar, $p_{\text{CO}} = 90\text{-}534$ mbar, $p_{\text{T}} = 5000$ mbar). Note that all conversion and TOF data are based on CO consumption, all product selectivities are carbon-based.

C.7. Fischer-Tropsch synthesis on the dual surface as function of H_2 pressure

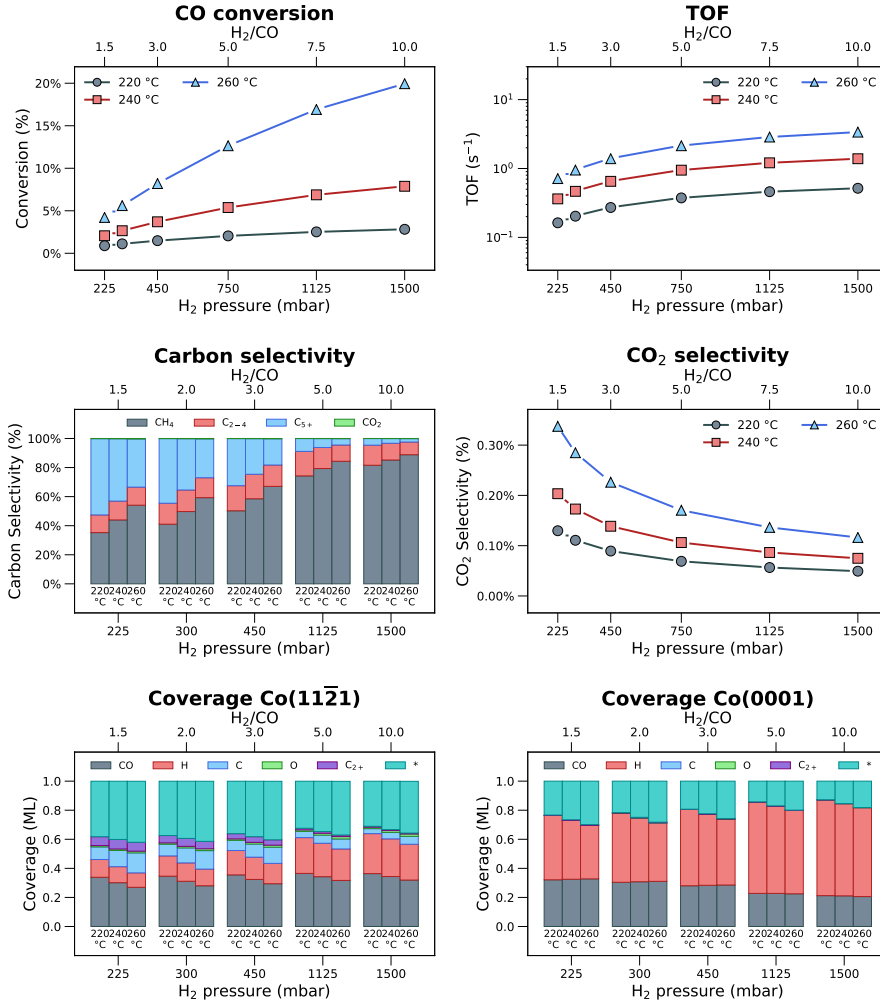


Figure C8: Microkinetics simulations of the FT synthesis reaction on a combined surface consisting of 10% Co(11 $\bar{2}$ 1) and 90% Co(0001) with varying H_2 pressure (conditions: $T = 220/240/260$ °C, $p_{H_2} = 225-1500$ mbar, $p_{CO} = 150$ mbar, $p_T = 5000$ mbar). Note that all conversion and TOF data are based on CO consumption, all product selectivities are carbon-based.

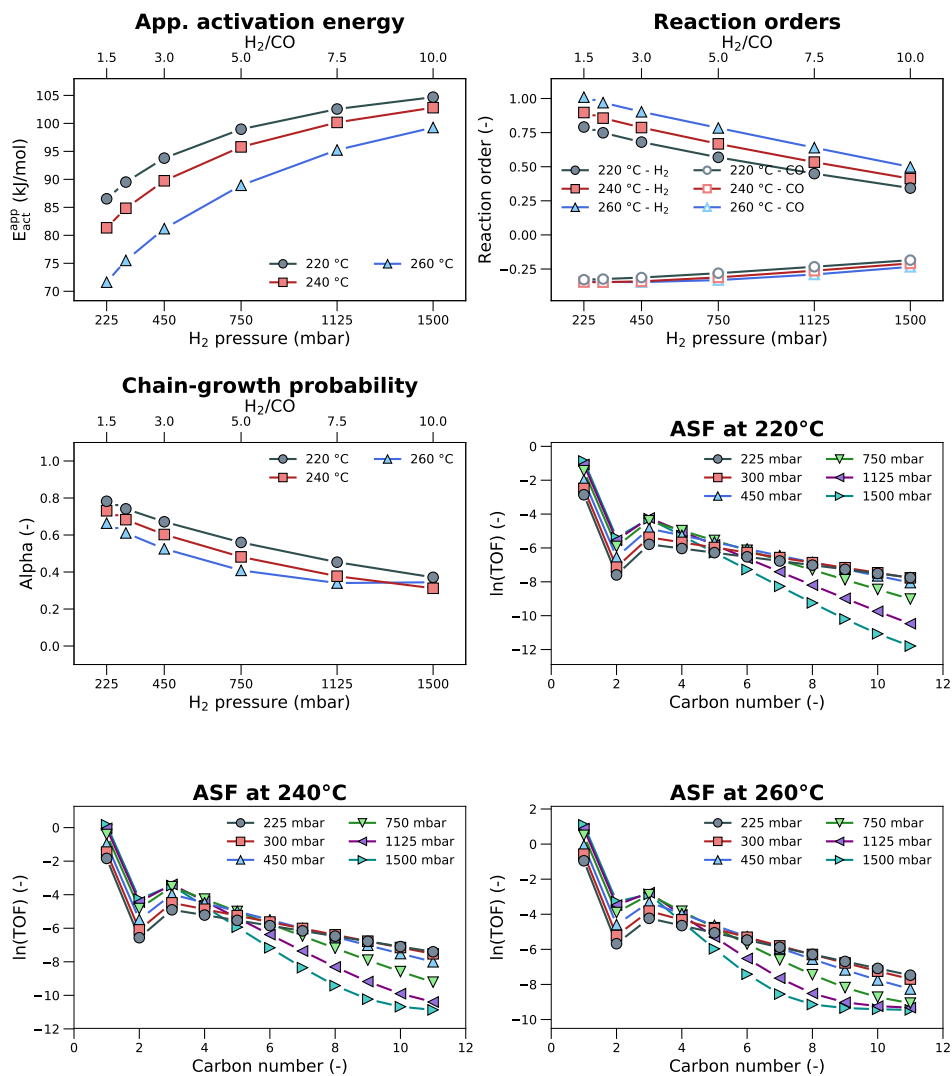


Figure C9: Microkinetics simulations of the FT synthesis reaction on a combined surface consisting of 10% $\text{Co}(11\bar{1})$ and 90% $\text{Co}(0001)$ with varying H_2 pressure (conditions: $T = 220/240/260^\circ\text{C}$, $p_{\text{H}_2} = 225\text{-}1500$ mbar, $p_{\text{CO}} = 150$ mbar, $p_{\text{T}} = 5000$ mbar). Note that the chain-growth probability is based on the slope of ASF plot for carbon numbers 5-8.

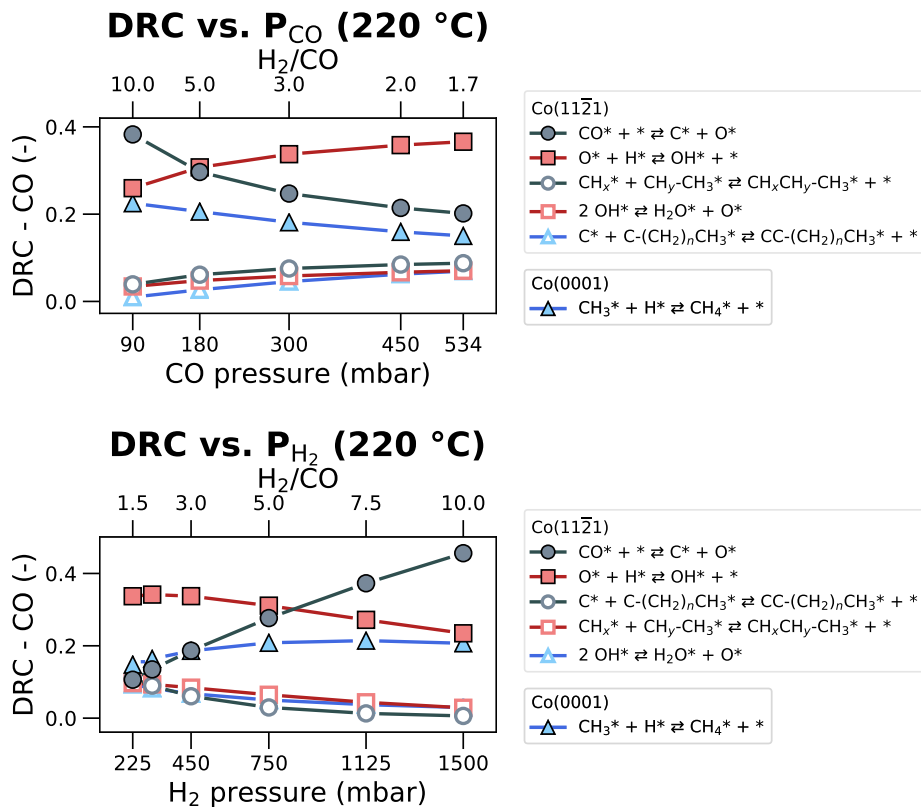
C.8. DRC, DSC, and DCGC as function of CO and H₂ pressure

Figure C10: DRC analysis of the FT reaction network on a combined surface consisting of 10% Co(11 $\bar{2}$ 1) and 90% Co(0001) with varying CO pressure (conditions: T = 220/240/260 °C, p_{H2} = 900 mbar, p_{CO} = 90-534 mbar, p_T = 5000 mbar) and with varying H₂ pressure (conditions: T = 220 °C, p_{H2} = 225-1500 mbar, p_{CO} = 150 mbar, p_T = 5000 mbar).

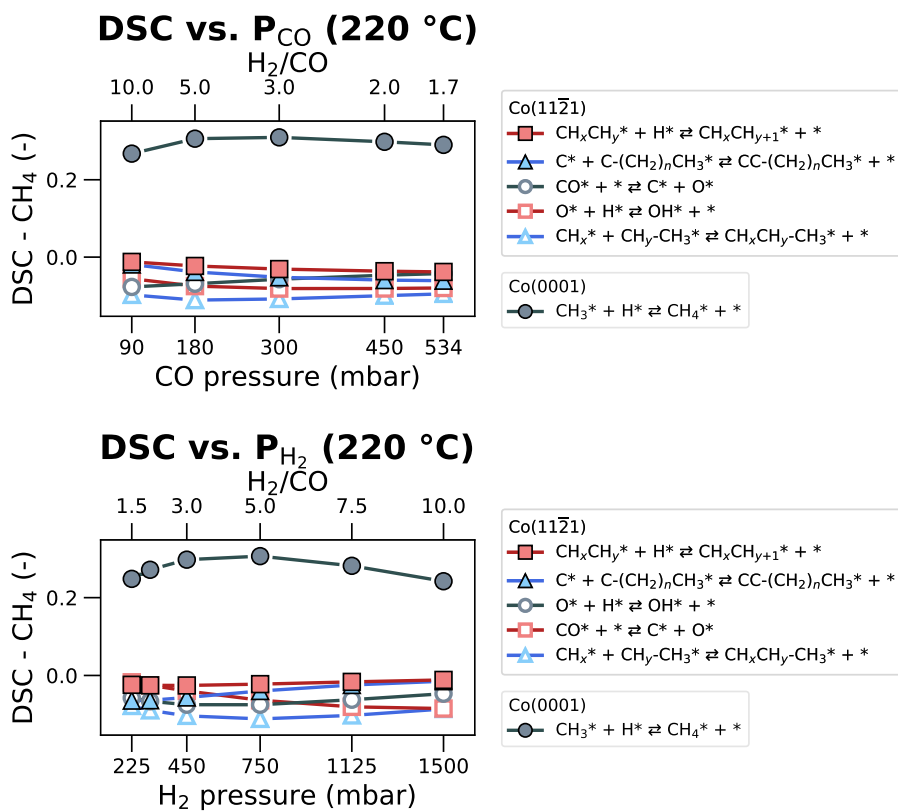


Figure C11: DSC analysis of the FT reaction network on a combined surface consisting of 10% Co(11 $\bar{2}$ 1) and 90% Co(0001) with varying CO pressure (conditions: T = 220 °C, p_{H_2} = 900 mbar, p_{CO} = 90-534 mbar, p_T = 5000 mbar) and with varying H₂ pressure (conditions: T = 220/240/260 °C, p_{H_2} = 225-1500 mbar, p_{CO} = 150 mbar, p_T = 5000 mbar).

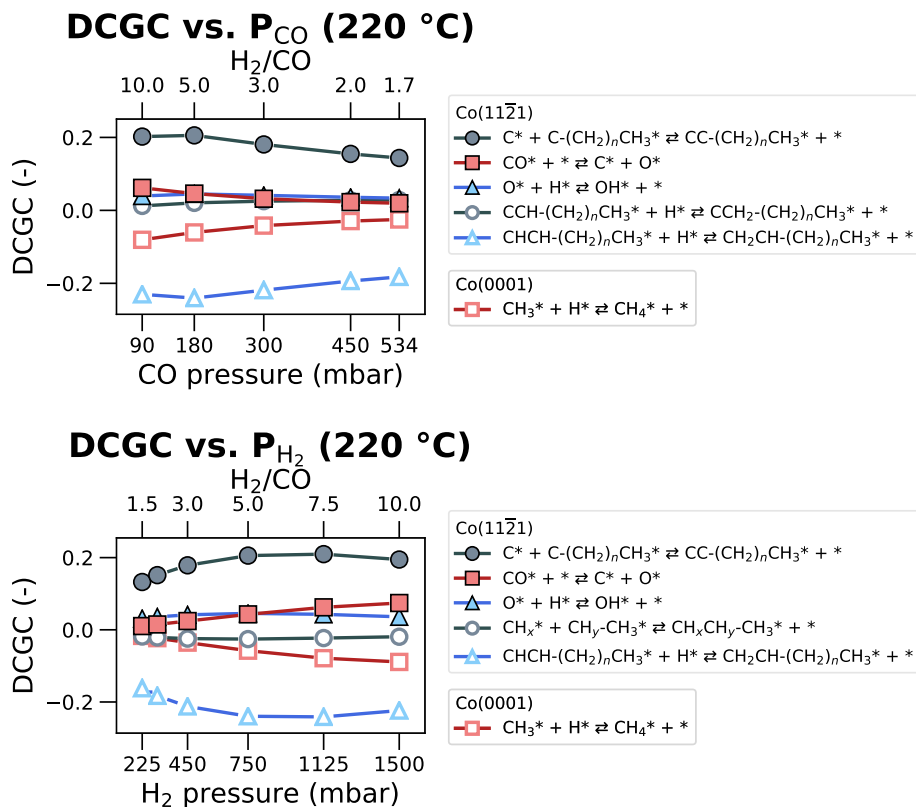


Figure C12: DCGC analysis of the FT reaction network on a combined surface consisting of 10% Co(11 $\bar{2}$ 1) and 90% Co(0001) with varying CO pressure (conditions: T = 220/240/260 °C, p_{H_2} = 900 mbar, p_{CO} = 90-534 mbar, p_T = 5000 mbar) and with varying H₂ pressure (conditions: T = 220 °C, p_{H_2} = 225-1500 mbar, p_{CO} = 150 mbar, p_T = 5000 mbar).

C.9. Reaction equilibrium of CO dissociation and oxygen hydrogenation

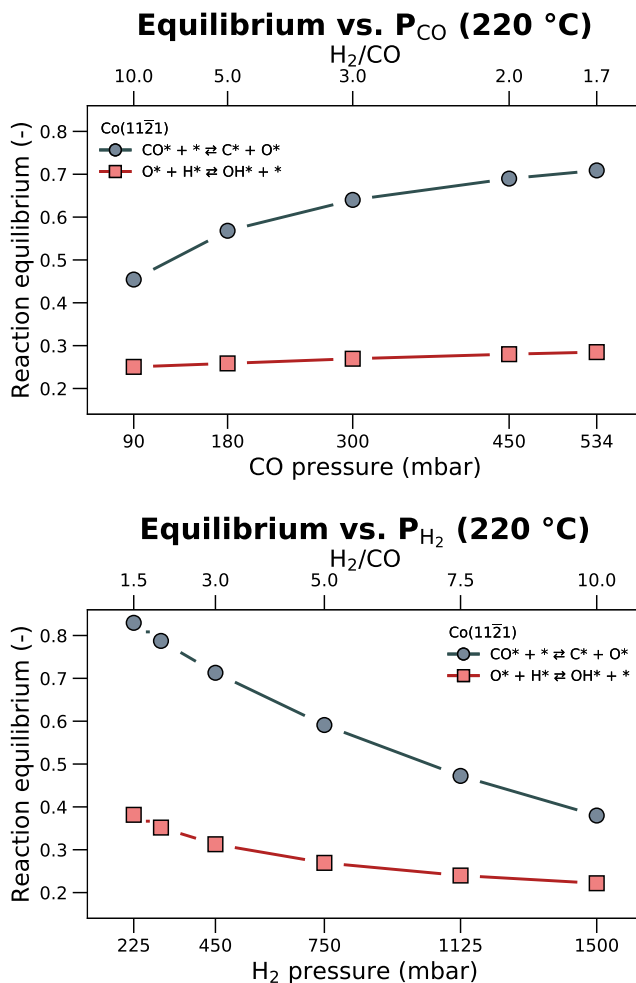


Figure C13: Reaction equilibrium (backward / forward rate) for CO dissociation and oxygen hydrogenation on a combined surface consisting of 10% Co(11 $\bar{2}$ 1) and 90% Co(0001) with varying CO pressure (conditions: T = 220/240/260 °C, p_{H_2} = 900 mbar, p_{CO} = 90-534 mbar, p_T = 5000 mbar) and with varying H₂ pressure (conditions: T = 220 °C, p_{H_2} = 225-1500 mbar, p_{CO} = 150 mbar, p_T = 5000 mbar).

C.10. References

- [1] *Journal of Physical and Chemical Reference Data* **1982**, 11, 695–940.
- [2] C. H. Shomate, *The Journal of Physical Chemistry* **1954**, 58, 368–372.

Appendix D

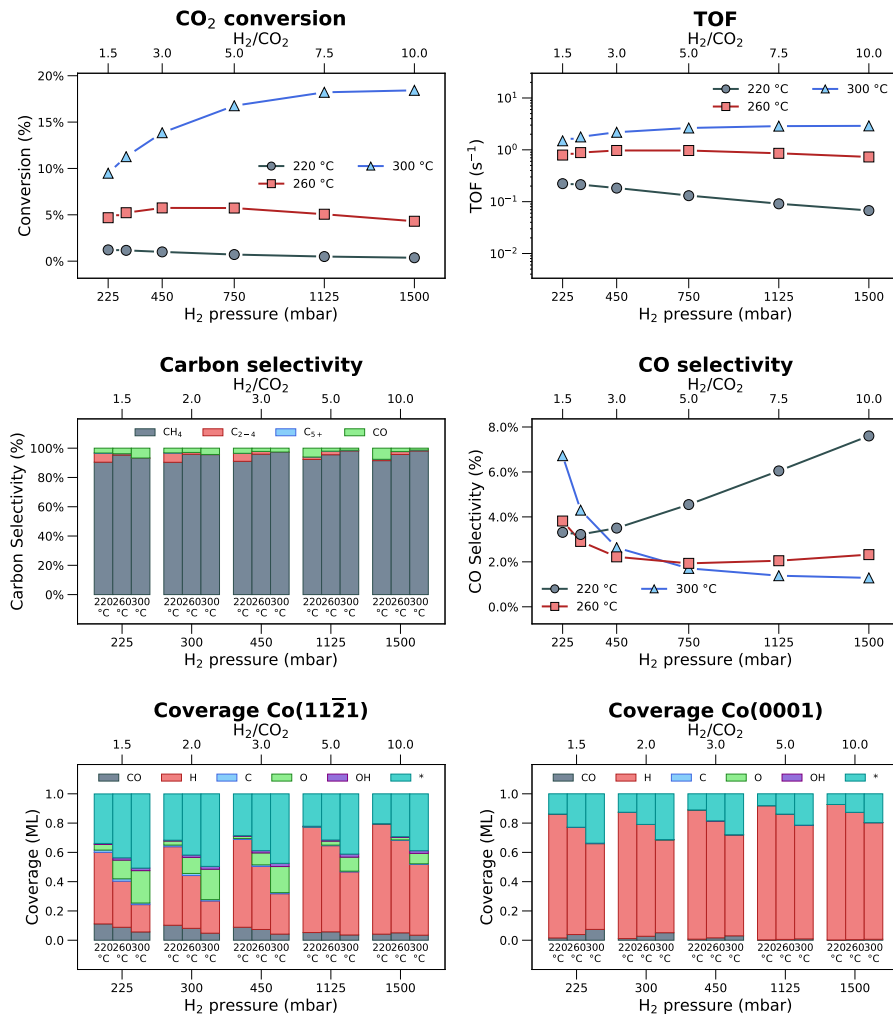
D.1. CO₂ hydrogenation on the dual surface as a function of H₂ pressure

Figure D1: CO₂ hydrogenation on 10% Co(1121) and 90% Co(0001) with varying H₂ pressure (conditions: T=220/260/300 °C, p_{H2} = 225-1500 mbar, p_{CO2} = 150 mbar, p_T = 5000 mbar).

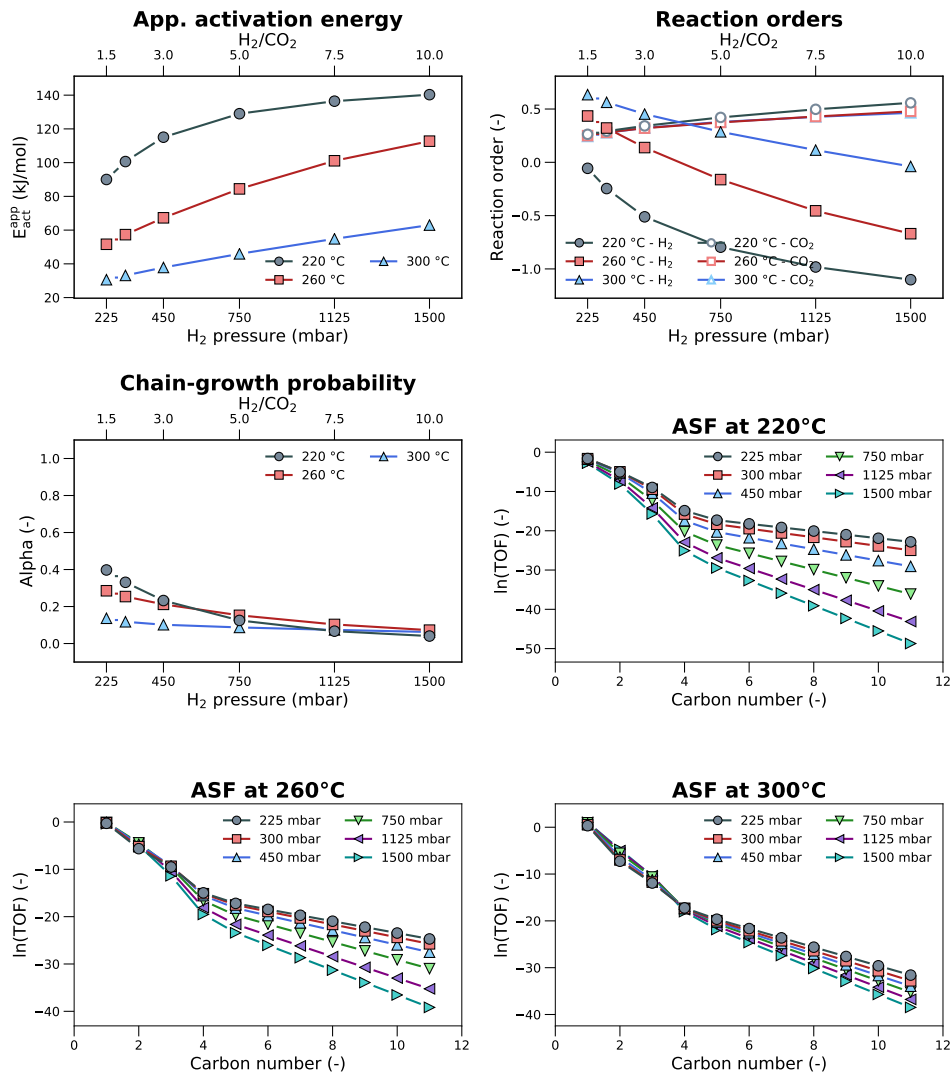


Figure D2: CO₂ hydrogenation on 10% Co(11 $\bar{2}$ 1) and 90% Co(0001) with varying H₂ pressure (conditions: T=220/260/300 °C, p_{H2} = 225-1500 mbar, p_{CO2} = 150 mbar, p_T = 5000 mbar).

CHAPTER 7

FIRST-PRINCIPLES MICROKINETICS SIMULATIONS OF ELECTROCHEMICAL REDUCTION OF CO₂ OVER CU CATALYSTS

Contents

7.1	Introduction	186
7.2	Computational methods	188
7.2.1	Density functional theory calculations	188
7.2.2	Potential-dependent reaction barriers	189
7.2.3	Microkinetic simulations	191
7.3	Results and discussion	192
7.4	Conclusions	208
7.5	References	208
	Appendix E	213

Abstract

Electrochemical reduction of CO₂ can contribute to the storage of excess renewable electricity in chemical bonds. Here we incorporate reaction energetics for CO₂ reduction on Cu(111) and Cu(211) determined by DFT calculations in microkinetics simulations to predict the influence of surface topology, the presence of water and possible diffusion limitations on current density-potential curves and Faradaic efficiencies. A reaction-diffusion model was used that takes into account the effect of electrochemical potential on the stability of intermediates and associated activation barriers in proton-coupled electron transfer steps as well as diffusion of protons and CO₂ from the bulk electrolyte to the electrode surface. The basic model can well reproduce hydrogen evolution including the effect of proton

diffusion limitations and a shift of proton reduction (low potential) to water reduction (high potential). Considering CO₂ electro-reduction, the stepped Cu(211) surface is more active than the Cu(111) terrace towards HCOO(H), CO and CH₄. The presence of a catalytic H₂O molecule increases the overall rate and selectivity to products (CO and CH₄) derived from dissociated CO₂. A catalytic H₂O molecule facilitates the difficult electrochemical CO₂ activation step to COOH and suppresses the competing activation step towards HCOO, which mainly yields HCOO(H). In general, the current densities increase at higher negative potential and the products follow the sequence CO₂ → CO → CH₄. That is to say, CO₂ is converted to CO via COOH dissociation, followed by CO hydrogenation. Trend-wise, the simulated product distribution follows the potential-dependent distribution observed in experiment. The low selectivity to CH₃OH can be understood from the fast electrochemical steps that lead to CH_x-OH dissociation. At high overpotentials the hydrogenation step from CO₂ to COOH controls both activity and selectivity towards CH₄. At high potential CO₂ reduction becomes increasingly diffusion-limited, thus limiting the selectivity of CO₂ reduction *vs.* hydrogen evolution. This aspect supports the need for better design of mass transfer in electrochemical reactors, which operate at high current density.

7.1 Introduction

Our modern highly industrialized economy is largely dependent on the availability of cheap non-renewable fossil resources. Oil, gas and coal remain the major source of energy and chemicals, resulting not only in air pollution but also in the release of large amounts of carbon dioxide (CO₂), one of the primary causes of global warming. It is therefore pivotal to replace these unsustainable sources of energy and chemical by renewable ones. The most likely scenario for such a transition is that a mix of renewable energy sources will increasingly contribute to the global energy demand. A major contribution will come from green electricity generated by solar panels and wind turbines. The intermittency of such electricity requires the development of scalable and affordable energy storage. Converting excess electricity to chemicals is expected to become important in the future because of the high energy density, thereby also contributing to challenges such as mobility and sustainable chemicals production. An attractive option is to convert CO₂ into fuels and chemicals that are compatible with our current energy infrastructure. This can be done indirectly by splitting water into hydrogen and oxygen followed by reducing CO₂ with hydrogen using catalytic chemistry such as the Sabatier reaction, the Fischer-Tropsch reaction or methanol synthesis into methane, liquid hydrocarbons, and methanol, respectively. Another approach would be to directly convert CO₂ electrochemically into reduced compounds, which can serve as fuels for later conversion to energy, and starting compounds for the chemical industry [1–4].

Electrochemical reduction can be used to reduce CO₂ into carbon monoxide (CO), methane (CH₄), olefins and alcohols. A large number of metals have been investigated for the electrochemical reduction of CO₂ before [5–17]. For instance, the group of Hori has extensively studied the performance in terms of current density and product distribution

achievable with common metal electrodes [12–16]. As an example, formic acid (HCOOH) and CO are the dominant products at high CO₂ pressure on Ag, Fe, Co, Rh, Ni, Pd and Pt [18], while CH₄ is the main product on Cu [12]. There have also been attempts to clarify the structure sensitivity of CO₂ electro-reduction for different transition metal electrodes [11]. Currently, there is a large research effort focused on increasing the efficiency, selectivity and stability of the catalytic materials for CO₂ electro-reduction [10, 19].

Cu stands out as it is the only metal that can convert CO₂ with a reasonable selectivity to valuable CH₄ and ethylene (C₂H₄) hydrocarbon products in aqueous electrolyte at ambient temperature [14, 20–25]. Several works already showed that CO₂ reduction is sensitive to the surface topology of Cu [26–34]. For instance, Cu nanoparticles supported on glassy carbon display a current density to CH₄ that is up to four times higher than a Cu foil [29]. In a computational study of CO₂ hydrogenation on Cu clusters and nanoparticles, we showed that a Cu₁₉ cluster displays optimum reactivity for methanol (CH₃OH) formation [34]. The facet-dependence of CO₂ hydrogenation activity and selectivity has also been emphasized in experimental studies [9, 35–38]. For instance, the electrochemical reduction of CO₂ on Cu foams with a high surface roughness and porosity yields predominantly HCOOH with lower concentrations of CO, methane, and ethylene as compared with a smooth copper foil electrode [9].

Identification of the mechanism of electrochemical CO₂ reduction is of great significance for guiding the design of better catalysts [24, 32, 39–42]. A general trend is that CH₄ is the main product at high overpotential, while CO and HCOOH are dominant along with a large amount of hydrogen (H₂) at lower overpotential for most transition metal electrodes [12, 13, 17, 33, 43–46]. CH₃OH is a commonly reported side-product at higher overpotential [19, 47]. For example, a small amount of CH₃OH was observed by nuclear magnetic resonance (NMR) spectroscopy during electrochemical CO₂ reduction on Cu [48]. Kinetic measurements revealed that reduction of formaldehyde (CH₂O) directly yields CH₃OH with CH₄ as a side-product. These results suggest that CH₂O is not a likely reaction intermediate of the electrochemical reduction of CO₂ on Cu [47]. Similar to heterogeneous CO₂ hydrogenation, the formation of HCO or COH is thought to be the rate-determining step for electrochemical CO₂ reduction on Cu [24, 25, 49, 50]. It has for example been proposed that CH₃OH is formed through a HCO intermediate, while CH₄ formation involves a COH intermediate on Cu electrodes [43]. The slow steps for CH₃OH formation in the formate (HCOO)-like mechanism demonstrated by Gao and Au are the hydrogenation of HCO and H₂CO [51]. It has also been shown that the COH intermediate cannot be the key intermediate for CH₄ formation due to the higher barrier compared to dissociation of the HCOH intermediate [5]. Besides, CO₂ reduction to CH₃OH via a H₂COOH intermediate following hydrogenation of HCOO has been proposed for a TiO₂-Ag catalyst [52]. Despite intensive research efforts, many aspects regarding the electrochemical reduction of CO₂ on Cu surfaces remain unresolved.

At the electrode-electrolyte interface, the charge separation between the electrode metal surface and counter ions in the electrolyte creates an electrostatic potential drop, influencing the local structure and adsorption strength of reaction intermediates. Accurately

incorporating these aspects into density functional theory (DFT) calculations remains a challenge and requires an understanding of the exact molecular structure of the electrode–electrolyte interface. A few theoretical models have been developed to deal with these issues such as the reaction-center cluster model [53], the vacuum interface model based on the linear free energy method [54, 55], the external electric field model [56, 57], and the double reference model [57, 58]. The linear free energy thermochemical model developed by Nørskov and co-workers can be used to capture activity trends among different metals in a qualitative manner without taking into account explicitly the electrolyte. Peterson and co-workers used this method to show that the key step in the formation of CH₄ and C₂H₄ is the hydrogenation of CO to HCO. These authors also found that the CH₄/CH₃OH selectivity during electrochemical CO₂ reduction is determined by the rate of the hydrogenation of the methoxy (CH₃O) intermediate [59].

In the present work, we used DFT calculations together with the linear free energy model to investigate electrochemical CO₂ reduction on two periodic Cu surfaces. We also took into account the dependence of the activation barriers of elementary reaction steps involving H atoms on electrochemical potential. Microkinetics simulations were performed to compute CO₂ conversion and product formation rates as a function of the applied electrochemical potential. The rate-limiting steps for electrochemical CO₂ reduction were determined as well. Terrace Cu(111) and stepped Cu(211) surfaces were considered in our work in order to shed light on the structure sensitivity of Cu nanoparticle-catalyzed electrochemical CO₂ reduction. Although the electrolyte was not taken into account explicitly, we evaluated the impact of water molecules on the activation barriers of the elementary reaction steps of the more active stepped Cu(211) surface. We focused on the formation of HCOO, CO, CH₃OH and CH₄ and also considered the recently increasingly recognized problem of mass transfer limitations resulting in depletion of reactants like protons and CO₂ near the electrode surface. Recent work emphasizes that this aspect may render interpretation of kinetic data difficult at commercially-relevant current densities, as CO₂ electro-reduction and especially hydrogen evolution may be partially limited by slow diffusion of reactants from the bulk electrolyte [60]. The results in our work show that the current density and product distribution depend strongly on the Cu surface topology, the applied potential and the stabilization of transition states by water. Diffusion limitations significantly affect the rate and product distribution. We discuss the influence of removing such limitations on the product distribution by simulating a rotating disc electrode.

7.2 Computational methods

7.2.1 Density functional theory calculations

All DFT calculations were performed by using the Vienna ab initio simulation program (VASP), along with projected augmented wave (PAW) [61] pseudopotentials and the Perdew-Burke-Ernzerhof (PBE) functional [62]. p(3x4) and (1x4) periodic slab models were used to compute the energies of stable adsorption geometries and transition states that separate these stable states for the Cu(111) and Cu(211) surface models. Both periodic surfaces

were simulated using four equivalent (111) atomic layers. Neighboring slabs were separated by a vacuum of 20 Å to avoid spurious self-interactions. Monkhorst-Pack k-point meshes of 5x3x1 were used for these periodic models. An energy cutoff of 400 eV was employed for the plane-wave basis set. The convergence threshold for ionic steps in geometry optimization was 1×10^{-4} eV. Geometries were deemed converged when the forces on each atom were below 0.02 eV/Å. A frequency analysis was carried out on the stable states in order to confirm that these represent genuine minima. All of the electronic energies were corrected for zero-point energy (ZPE) contributions. The improved force-reversed method [63] was used to determine transition states with a force tolerance of 0.02 eV/Å. Some transition states were confirmed by using the climbing image nudged elastic band method (CI-NEB) [64]. We verified that the transition states were accompanied by a single vibrational frequency along the reaction coordinate.

7.2.2 Potential-dependent reaction barriers

The mechanism of electrochemical CO₂ reduction involves adsorption of CO₂ on the Cu surface followed by two types of reactions: (i) potential-dependent elementary reactions involving a series of proton-coupled electron transfer (PCET) steps in the associative pathway (electrochemical reactions) and (ii) potential-independent elementary reactions (non-electrochemical reactions) [65–67]. For potential-dependent electrochemical reactions of the type



the reaction free energies were calculated based on the computational hydrogen electrode (CHE) model [55]. In this model the reference potential is set to the standard hydrogen electrode (0 V *vs.* SHE). At this potential, the reaction $H^+ + e^- \rightleftharpoons \frac{1}{2}H_2$ is equilibrated at pH = 0 and 1 bar of H₂ in the gas phase at 298 K. This potential can be shifted by $-0.059 \times \text{pH}$ to reach 0 V *vs.* the reversible hydrogen electrode (RHE) at any pH. For example, at pH = 6.8 the potential of 0 V *vs.* RHE is equal to -0.40 V *vs.* SHE. Although the reaction free energy is independent of pH on the RHE scale, barrier heights still vary as a function of pH, but constant potential *vs.* RHE. Therefore, all barrier heights were defined with respect to the SHE potential. The chemical potential of the proton-electron pair can be calculated at 0 V *vs.* SHE using DFT and statistical mechanics relationships to determine the free energy of gaseous H₂. The dependence of the proton–electron pair free energy on the electrode potential can be simply determined using the linear free energy dependence of the electron energy on this potential, shifting the electron energy by $-eU$,

$$\mu(H^+) + \mu(e^-) = \frac{1}{2}\mu(H_2) - eU \quad (7.2)$$

where e is the elementary positive charge and U the electrode potential of interest on the SHE scale. The free energy change of a specific electrochemical reaction, ΔG , can be written

as

$$\Delta G = \Delta G^0 + eU \quad (7.3)$$

where ΔG^0 is the reaction free energy at 0 V *vs.* SHE and U is the potential measured *vs.* SHE.

In order to account for the influence of the electrode potential on the activation barrier of electrochemical reaction steps, we first determined the activation barrier for an equivalent hydrogenation reaction of the type



The activation barrier (E_a) for this reaction can be obtained by standard DFT approaches. At equilibrium $H^+ + e^- \rightleftharpoons H^*$ conditions, the activation barrier $E_a^{U^0}$ for $A + H^+ + e^- \rightleftharpoons AH^*$ equals to E_a^{DFT} . Here, U^0 is the potential relative to SHE that equals $-E_{\text{ads}}(H^*)$ for a particular surface.

The activation barriers at 0 V *vs.* SHE for $A + H^+ + e^- \rightleftharpoons AH^*$ can then be computed following the Butler–Volmer formalism [66]

$$E_{a,\text{forw}}^0 = E_{a,\text{forw}}^{\text{DFT}} + \alpha(-eU^0) \quad (7.5)$$

The reaction barriers for the backward reactions were calculated in a similar way, leading to

$$E_{a,\text{back}}^0 = E_{a,\text{back}}^{\text{DFT}} - \beta(-eU^0) \quad (7.6)$$

Here, α and $\beta(\beta = 1 - \alpha)$ are effective symmetry factors, which are approximated as Brønsted–Evans–Polanyi coefficients [68] describing the relationship between activation barriers and reaction energies. In the current work, α and β were set to 0.5 for all elementary steps as an approximation. The barrier can then be extrapolated from 0 V *vs.* SHE to other potentials by involving the electrode potential (U)

$$E_{a,\text{forw}}(U) = E_{a,\text{forw}}^0 + \alpha(eU) \quad (7.7)$$

For the backward reactions, the potential dependent activation barriers were calculated in a similar manner

$$E_{a,\text{back}}(U) = E_{a,\text{back}}^0 - \beta(eU) \quad (7.8)$$

We also took into account potential-dependent electrochemical steps of the type



Following the work of Liu and co-workers [69], we took the activation barriers for these reaction the same as for the corresponding reactions of Eq. 1, with the exception of the Volmer and Heyrovsky barriers, which we increased to satisfy the experimentally observed lower rate of hydrogen evolution via water reduction compared to proton reduction. The

effect of applied potential *vs.* SHE is the same for both types of reactions, i.e. we assume similar effective symmetry factors. The effect of pH changes will be different, as H^+ is a reactant in Eq. 1, while OH^- is a product in Eq. 2. Therefore, increasing pH will slow down proton reduction, while the forward rate for the water reduction step is unaffected. Combined, this has the consequence that increased pH, at constant potential *vs.* RHE, will lead to a decrease in proton reduction and an increase in water reduction [70].

7.2.3 Microkinetic simulations

Microkinetics simulations of electrochemical CO_2 reduction were carried out using the MKMCXX software package [71]. The basic methodology for these simulations are described elsewhere [72]. The rate constants for each electrochemical reaction step, i , is assumed to take the functional form

$$k_i = A_i \exp\left(-\frac{E_a(U)}{k_B T}\right) \quad (7.10)$$

where A_i is an effective pre-factor. As an approximation, the pre-factor was set to equal $\frac{k_B T}{h} \text{ s}^{-1}$ for all the surface elementary reactions. The non-electrochemical reaction steps are described in the same way without the potential dependency

$$k_i = A_i \exp\left(-\frac{E_{\text{act}}}{k_B T}\right) \quad (7.11)$$

We took as the active site area $5.68 \times 10^{-20} \text{ m}^2$, corresponding to two-adjacent 3-fold sites on the Cu(111) surface. We took into account literature data to simulate the hydrogen evolution reaction on Cu surfaces. The exchange current density for hydrogen evolution on Cu (at 0 V *vs.* SHE, standard hydrogen electrode) is approximately $1 \times 10^{-3} \text{ mA/cm}^2$ [73]. This was taken into account as activated hydrogen evolution with an energy barrier of 87 kJ/mol. It is known that, at high current densities obtained at high overpotentials, the availability of H^+ close to the electrochemical surface will be decreased due to diffusion limitations [60, 74]. To simulate this, we included a diffusion layer from the bulk solution to the catalyst surface. The diffusion coefficient D of H^+ in water was taken $9.31 \times 10^{-9} \text{ m}^2/\text{s}$ [73]. The diffusion layer thickness for H^+ was calculated from the Levich equation [75]

$$\delta = 1.6126 D^{\frac{1}{3}} \nu^{\frac{1}{6}} \omega^{-\frac{1}{2}} \quad (7.12)$$

where δ is the diffusion layer thickness in m, ν the kinematic viscosity of the solution in $\text{m}^2 \text{ s}^{-1}$ and ω the rotation rate of the rotating disc electrode in rad s^{-1} . The concentrations are then solved simultaneously with the surface kinetics using Fick's second law of diffusion perpendicular to the surface

$$\frac{\partial c}{\partial t} = D \frac{\partial^2 c}{\partial x^2} \quad (7.13)$$

in which c is the location- and time-dependent concentration of the diffusing compound, t the time, D the diffusion coefficient and x the distance from the surface. Discretization

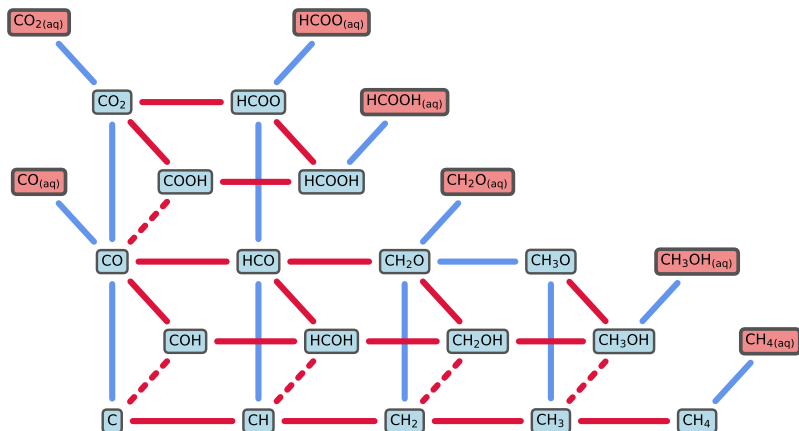
of the diffusion layer was done using 50 grid points employing a 3-point 2nd order central difference scheme. We also took diffusion of CO₂ ($D = 2 \times 10^{-9}$ m²/s) and OH⁻ ($D = 5.27 \times 10^{-9}$ m²/s) into account, for which we used as a first approximation the same diffusion layer thickness as for H⁺. As the effective surface pH will be increased at high overpotential, we may expect that the water reduction reaction will start to dominate ($A + H_2O + e^- \rightarrow AH + OH^-$) over the proton reduction mechanism. We assumed a water activity coefficient of unity and a water reduction barrier of 135 kJ/mol at 0 V *vs.* SHE (standard hydrogen electrode) based on the onset potential determined by Ooka et al. [74]. All elementary reaction steps involving hydrogen following the proton reduction mechanism as well as the water reduction mechanism were taken into account. We assumed that H₂ dissociation on Cu(111) and Cu(211) is activated with a barrier of 50 kJ/mol [76, 77]. For the non-electrochemical formation of H₂ from two adsorbed H species, we included entropy corrections. We assumed a zero free energy difference between CO₂ adsorbed on the electrode surface and CO₂ in solution. A solvated CO₂ concentration of 0.033 mol/l was used corresponding to experimental conditions of 1 bar CO₂ and water at 298 K [78]. Barriers for adsorption and desorption of CO₂ were set at 35 kJ/mol, the same as the entropy contribution of solvated CO₂ to the free energy. The CO desorption barriers were corrected with a value of 30 kJ/mol, taking into account regained entropy upon desorption and were further reduced by 23 kJ/mol to correct for overbinding considering the used DFT functional in this work [79]. For the other desorbing species, we assumed the barriers to be equal to the enthalpic differences as determined by DFT.

7.3 Results and discussion

DFT calculations were performed to determine the adsorption energies of reaction intermediates and activation barriers of candidate elementary reaction steps involved in electrochemical CO₂ reduction on terrace (111) and stepped (211) Cu surfaces. The explored reaction mechanisms for electrochemical reduction of CO₂ to HCOO(H), CO, CH₂O, CH₄ and CH₃OH are presented in Scheme 7.1. According to literature [80, 81], CO and CH_{*x*} species are involved in the formation of ethylene, although the exact mechanism has not been resolved yet. Therefore, we did not include C₂H₄ formation in the present study.

In the modeling of the CO₂ reduction pathway we include three sets of elementary reaction steps. The first set consists of potential-independent steps. This includes C–O dissociation steps of (partially hydrogenated) CO₂ and CO intermediates as well as H₂ evolution via the Volmer–Tafel mechanism [82, 83]. These reactions (Eq. 4) do not depend on the applied potential, because they do not involve either solvated protons (Eq. 7.1) or electrochemically active water molecules (Eq. 7.9). All electrochemical steps in Scheme 1 were also included in the potential-independent set, as these steps can proceed as well with surface-adsorbed atomic hydrogen. The second and third reaction sets in the microkinetic model are all electrochemical steps involving respectively solvated protons or water molecules.

Table 7.1 shows the adsorption and desorption barriers used in the microkinetic model.



Scheme 7.1: Reaction pathways for electrochemical CO₂ reduction on Cu(111) and Cu(211) surfaces. The red and blue lines represent electrochemical and non-electrochemical reactions, respectively. The dashed red lines indicate that OH can be removed either non-electrochemically as OH or electrochemically as H₂O.

These values are based on the computed enthalpies of adsorption and on entropic considerations. CO₂ adsorbs very weakly on Cu surfaces with adsorption energies of only a few kJ/mol on Cu(111) and Cu(211). The adsorption energy is slightly increased (~ 5 kJ/mol) on the latter surface in the presence of H₂O as a co-adsorbate. As the actual adsorption and desorption rate constants are difficult to predict, we assumed in the microkinetic model a similar forward and backward barrier of 35 kJ/mol for CO₂ adsorption on all surfaces. Hydrogen adsorption on Cu(211) is 22 kJ/mol more favorable as compared to the Cu(111) surface, while the presence of H₂O destabilizes hydrogen on Cu(211) by 7 kJ/mol. The computed activation barriers for the non-electrochemical surface reaction steps are presented in Table 7.2. Potential-dependent elementary reaction steps refer to electrochemical reactions in which a hydrogenation step is involved from either a proton in the solution or an electrochemically active water molecule. Examples are the formation of (partially hydrogenated) CO₂ and CO intermediates. As the stability of the H atom depends on the applied potential, it will not only affect the initial and final state of an elementary reaction step but also the activation barrier. The activation barriers were determined by DFT calculations and Eqs. (7.7) and (7.8). Equivalent reactions involving water as a proton source were also included in the microkinetic model. The activation barriers for all of the considered reactions are collected in Table 7.3.

Direct CO₂ dissociation is easier on the corrugated surface (102 kJ/mol) than on the planar terrace (140 kJ/mol). Water as a co-adsorbate lowers the barrier on the Cu(211) surface to a value of 83 kJ/mol. Alternative pathways for CO₂ activation involving hydrogenation prior to C–O bond cleavage were also considered. These hydrogenation

Table 7.1: Energetics for adsorption reactions in CO₂ reduction on Cu surfaces ($E_{\text{act}}^{\text{forw}}$ forward activation energy, $E_{\text{act}}^{\text{back}}$ backward activation energy, all energies in kJ/mol).

Elementary reaction	Cu(111)		Cu(211)		Cu(211)+H ₂ O	
	$E_{\text{act}}^{\text{forw}}$	$E_{\text{act}}^{\text{back}}$	$E_{\text{act}}^{\text{forw}}$	$E_{\text{act}}^{\text{back}}$	$E_{\text{act}}^{\text{forw}}$	$E_{\text{act}}^{\text{back}}$
CO ₂ adsorption	35	35	35	35	35	35
CO adsorption	0	23	0	35	0	40
CH ₄ adsorption	0	0	0	3	0	2
CH ₃ OH adsorption	0	6	0	34	0	48
HCOO(H) adsorption	0	27	0	44	0	34
CH ₂ O adsorption	0	0	0	35	0	40
H ₂ (g) \rightleftharpoons H + H (Tafel)	77	67	77	89	77	82

Table 7.2: Energetics for non-electrochemical reactions in CO₂ reduction on Cu surfaces ($E_{\text{act}}^{\text{forw}}$ forward activation energy, $E_{\text{act}}^{\text{back}}$ backward activation energy, all energies in kJ/mol).

Elementary reaction	Cu(111)		Cu(211)		Cu(211)+H ₂ O	
	$E_{\text{act}}^{\text{forw}}$	$E_{\text{act}}^{\text{back}}$	$E_{\text{act}}^{\text{forw}}$	$E_{\text{act}}^{\text{back}}$	$E_{\text{act}}^{\text{forw}}$	$E_{\text{act}}^{\text{back}}$
CO ₂ \rightleftharpoons CO + O	140	58	102	59	83	43
CO \rightleftharpoons C + O	373	101	291	119	307	131
HCO \rightleftharpoons CH + O	156	78	147	119	188	137
COH \rightleftharpoons C + OH	148	32	153	149	108	98
CH ₂ O \rightleftharpoons CH ₂ + O	119	75	110	89	123	99
CH ₃ O \rightleftharpoons CH ₃ + O	172	115	166	141	161	149
HCOO \rightleftharpoons HCO + O	210	25	180	44	159	29
COOH \rightleftharpoons CO + OH	39	81	30	81	14	51

steps involve electrochemical reduction of CO₂ with protons (Table 3). Then, the overall barrier for these pathways will depend on the applied electrochemical potential. This will be considered below. Here, we will focus on the gas-phase reaction energetics. Dissociation of HCOO (formate) to HCO and O is more difficult than direct CO₂ dissociation. This is in accord with an earlier report [84]. Pathways via the carboxyl intermediate are very facile on Cu(111) and Cu(211). However, formation of the COOH intermediate from CO₂ is difficult (Table C1), exhibiting barriers of 145 kJ/mol for Cu(111), 140 kJ/mol for Cu(211) and 130 kJ/mol for Cu(211) in the presence of H₂O. Thus, from an energetics point of view, direct CO₂ dissociation is favored under non-electrochemical conditions. However, under electrochemical conditions the barrier of the COOH formation step will be reduced. Furthermore, COOH is more stable by 34 kJ/mol on Cu(211) compared to Cu(111). Then, Cu(211) is the preferential surface for CO₂ dissociation via the carboxyl pathway.

Dissociation of the C–O bond in adsorbed CO was also considered. CO dissociation has the highest activation barrier among the non-electrochemical elementary reactions (Cu(111): 373 kJ/mol; Cu(211): 291 kJ/mol; Cu(211) with H₂O: 307 kJ/mol). The activation barriers for C–O bond scission of CH_{*n*}O (*n* = 1-3) intermediates were also considered and are in the 119-172 kJ/mol range for Cu(111), the 110-166 kJ/mol range for Cu(211) and the 108-188 kJ/mol range for Cu(211) in the presence of H₂O. The lowest barrier for C–O dissociation without added water is for the CH₂O surface intermediate with only small variation between

Table 7.3: Energetics for electrochemical reactions in CO₂ reduction on Cu surfaces at a potential of 0 V *vs.* SHE ($E_{\text{act}}^{\text{forw}}$ forward activation energy, $E_{\text{act}}^{\text{back}}$ backward activation energy, all energies in kJ/mol). In the microkinetic model all elementary reaction steps are possible both with H as proton source and with H₂O as proton source. For the latter, the same barriers were used.

Elementary reaction	Cu(111)		Cu(211)		Cu(211)+H ₂ O	
	$E_{\text{act}}^{\text{forw}}$	$E_{\text{act}}^{\text{back}}$	$E_{\text{act}}^{\text{forw}}$	$E_{\text{act}}^{\text{back}}$	$E_{\text{act}}^{\text{forw}}$	$E_{\text{act}}^{\text{back}}$
O + H ⇌ OH	96	151	100	171	84	148
OH + H ⇌ H ₂ O	143	209	145	113	100	90
C + H ⇌ CH	68	166	74	141	119	169
CH + H ⇌ CH ₂	48	88	64	84	66	105
CH ₂ + H ⇌ CH ₃	52	117	54	124	66	136
CH ₃ + H ⇌ CH ₄	74	146	90	126	98	134
CO + H ⇌ COH	123	23	121	23	105	5
CO + H ⇌ HCO	104	8	101	24	90	15
HCO + H ⇌ HCOH	67	21	59	26	54	4
HCO + H ⇌ CH ₂ O	65	72	48	61	71	82
COH + H ⇌ HCOH	111	69	131	119	150	125
HCOH + H ⇌ CH ₂ OH	67	109	51	102	48	98
CH ₂ O + H ⇌ CH ₂ OH	89	80	92	97	55	43
CH ₂ O + H ⇌ CH ₃ O	23	100	23	97	35	93
CH ₂ OH + H ⇌ CH ₃ OH	86	157	76	122	80	151
CH ₃ O + H ⇌ CH ₃ OH	107	90	74	50	79	80
COH + H ⇌ C + H ₂ O	80	29	63	28	35	15
HCOH + H ⇌ CH + H ₂ O	56	146	33	77	34	88
CH ₂ OH + H ⇌ CH ₂ + H ₂ O	80	167	70	83	60	103
CH ₃ OH + H ⇌ CH ₃ + H ₂ O	133	214	94	131	78	120
CO ₂ + H ⇌ COOH	147	79	137	113	129	116
CO ₂ + H ⇌ HCOO	133	141	127	143	144	159
COOH + H ⇌ HCOOH	135	175	212	222	148	133
HCOO + H ⇌ HCOOH	151	115	142	112	143	99
COOH + H ⇌ CO + H ₂ O	95	203	66	85	157	185

the two surfaces. In the presence of H₂O, the COH dissociation has the lowest barrier on Cu(211). Considering the different stability of CH_{*n*}O intermediates compared to CO, we determined overall barriers for C–O bond cleavage in HCO of 247 kJ/mol for Cu(111), 230 kJ/mol for Cu(211) and 266 kJ/mol for Cu(211) in the presence of H₂O. Over barriers for COH scission are 243 kJ/mol for Cu(111), 256 kJ/mol for Cu(211) and 211 kJ/mol for Cu(211) in the presence of H₂O. C–O bond dissociation in CH₂O is more facile with overall barriers of 199 kJ/mol for Cu(111), 185 kJ/mol for Cu(211) and 192 kJ/mol for Cu(211) in the presence of H₂O. Although C–O bond cleavage in CH₃O is substantially more difficult than in CH₂O, CH₃O is much more stable on the Cu surfaces. Thus, the overall barriers for C–O bond dissociation in CH₃O are 170 kJ/mol for Cu(111), 173 kJ/mol for Cu(211) and 175 kJ/mol for Cu(211) in the presence of H₂O. Obviously, these values reflect the overall barriers with reference to the non-electrochemical experiment.

A general observation is that the non-electrochemical elementary reaction steps are easier on the stepped Cu(211) surface than on Cu(111). The higher reactivity of the stepped surface relates to the presence of low-coordinated Cu surface atoms as well as a favorable topology for C–O dissociation reactions [85, 86]. In the presence of H₂O, the average absolute change in free-energy difference between reactant and product states is only 12 kJ/mol, similar to the results found by Goodpaster et al [87]. Furthermore, H₂O appears to lower the barriers related to X–OH intermediates.

We next took into account the effect of applying an electrochemical potential on the reaction energy diagrams. For this, we take the RHE as reference at pH = 6.8. Thus 0 V *vs.* RHE and -1 V *vs.* RHE correspond to, respectively, -0.4 V *vs.* SHE and -1.4 V *vs.* SHE. Relevant diagrams for the formation of COOH and HCOO and the dissociation of one of the C–O bonds in these intermediates as well as in adsorbed CO₂ are shown in Figure 7.1. This figure immediately shows that the PCET steps become easier when a negative potential is applied. At an applied potential of -1.0 V *vs.* RHE, the formation of COOH and HCOO is preferred over direct CO₂ dissociation for most of the considered models. While the barriers for the formation of COOH and HCOO at both potentials considered are quite similar for the different surfaces, COOH dissociation to CO + OH is always significantly easier than HCOO dissociation to HCO + O. The reaction energy diagrams suggest that at -1.0 V *vs.* RHE mechanisms involving HCOO and COOH exhibit similar overall activation barriers, because the rate is typically determined by the first hydrogenation step (Figures E16-C17).

Figure 7.2 shows the barriers for direct and H-assisted CO dissociation pathways. Direct non-electrochemical CO scission has such a high barrier that these pathways do not play a role in electrochemical CO activation. We also took into account two pathways involving direct formation of H₂O from adsorbed HCOH and adsorbed COH. Independent of the applied potential, the H-assisted pathways are always preferred. In general, we find that, while formation of partially hydrogenation CO intermediates is possible, further direct dissociation to generate CH_{*x*} species requires overcoming a high activation barrier. Only at a potential of -1.0 V *vs.* RHE, the barrier for direct COH dissociation on the Cu(211) in the presence of H₂O presents a relatively low barrier of 108 kJ/mol. Taking into account an additional PCET step in the mechanism of C–O dissociation for HCOH and COH

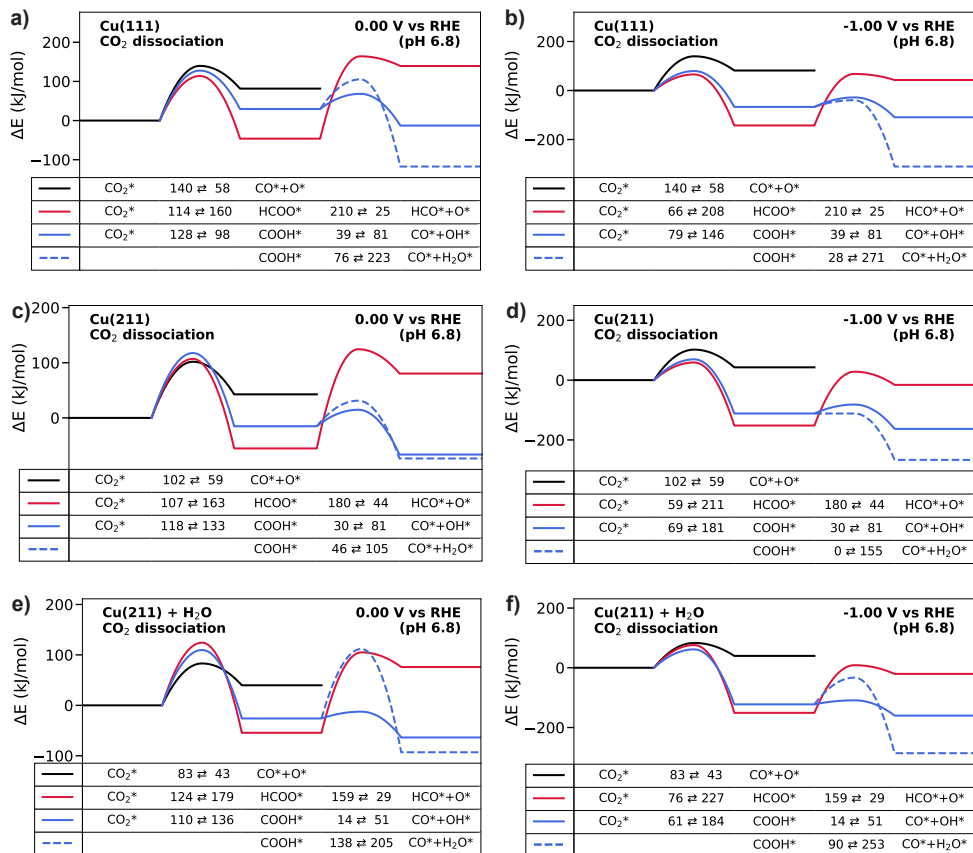


Figure 7.1: Reaction energy diagrams for the dissociation of CO₂ at 0 V and -1.0 V *vs.* RHE on Cu(111), Cu(211) and Cu(211)+H₂O at pH 6.8: (black) direct CO₂ dissociation pathway; (red) electrochemical HCOO formation followed by non-electrochemical dissociation; (blue) electrochemical COOH formation followed by non-electrochemical dissociation; (blue dash) electrochemical COOH hydrogenation to remove OH as H₂O. The numbers below the diagrams indicate the forward and backward activation barriers between the corresponding states ($E_{\text{act}}^{\text{forw}} \rightleftharpoons E_{\text{act}}^{\text{back}}$)

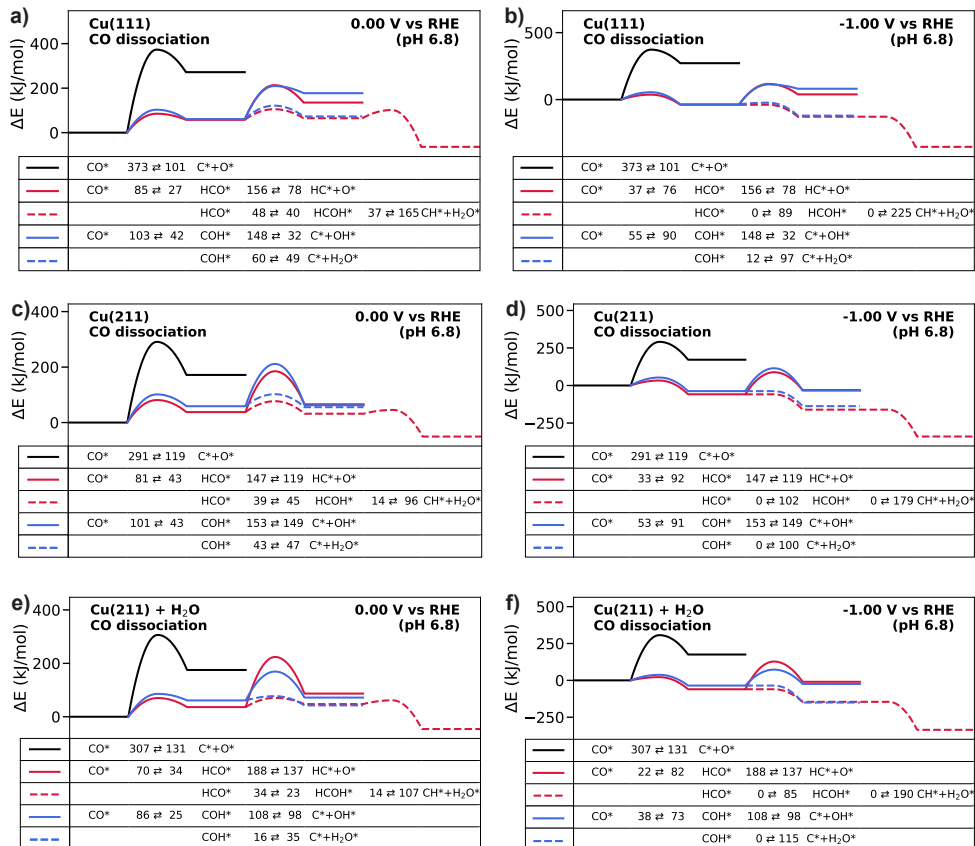


Figure 7.2: Reaction energy diagrams for the dissociation of CO at 0 V and -1.0 V *vs.* RHE on Cu(111), Cu(211) and Cu(211)+H₂O at pH 6.8: (black) direct CO dissociation pathway; (red) electrochemical HCO formation followed by non-electrochemical dissociation of HCO; (red dash) electrochemical hydrogenation to HCOH followed by hydrogenation to remove OH as H₂O; (blue) electrochemical COH formation followed by non-electrochemical dissociation of COH; (blue dash) electrochemical COH hydrogenation to remove OH as H₂O. The numbers below the diagrams indicate the forward and backward activation barriers between the corresponding states ($E_{act}^{forw} \rightleftharpoons E_{act}^{back}$)

intermediates, much more reasonable activation barriers are obtained. Even at 0 V *vs.* RHE (-0.40 V *vs.* SHE at pH 6.8), such a H₂O removal step from the HCOH state is fast. The barrier for HCO formation is slightly lower than for COH formation, suggesting that the CO → HCO → HCOH pathway is favored (Figure E18).

As we are primarily concerned to understand the selectivity towards CH₄ *vs.* CH₃OH during electrochemical CO₂ reduction, we provide in Figure 7.3 reaction energy diagrams at 0 V and -1.0 V *vs.* RHE for the formation of these two products. We start from the HCOH state as this is a likely intermediate based on the results from Figure 7.2. Both pathways from HCOH to CH₄ and CH₃OH are thermodynamically and kinetically favorable, suggesting that both products can be formed. However, at high negative potential the proton-assisted electrochemical splitting of CH₃OH into CH₃ and OH can become very fast, providing a tentative explanation for typically observed higher selectivity of CH₄ over CH₃OH [14, 33].

Using microkinetic modeling we first investigated the H₂ evolution reaction over Cu(111) in the absence of CO₂. Under acidic conditions (pH 2.5), we varied the diffusion layer thickness, which we linked to the rotation speed in a rotating disk electrode (RDE) configuration. Figure 7.4a shows an onset potential around -0.5 V for which H₂ evolution reaches current densities above 1 mA cm⁻². This is in keeping with the experimental literature [74]. Around -0.7 V *vs.* RHE, a plateau is reached as a result of diffusion limitations of protons through the diffusion layer to the electrochemical surface. This is because proton diffusion cannot keep up with the H₂ evolution rate at the electrode surface. A quadratic increase of the rotation speed roughly doubles the current density at this plateau, which is in accordance with the halved diffusion layer thickness as follows from the Levich equation. Figure 7.4b shows that the local pH at the electrode surface strongly increases when the negative potential is increased. At potentials below -1.0 V *vs.* RHE, the hydrogen evolution reaction occurs under alkaline conditions at the electrode surface. In the simulations, we see a shift from the proton reduction to the water reduction mechanism around a potential of -1.2 V *vs.* RHE (Figure E1 in the Appendix E). From these simulations, we infer that electrochemical CO₂ reduction in a solution, which is usually carried out at neutral pH and a high negative potential, is mostly governed by a surface from which hydrogen evolves via the water reduction mechanism.

Next, we performed microkinetics simulations of electrochemical CO₂ reduction on the different models at 298 K and pH 6.8. The rotation speed of the RDE configuration was set at 100 rpm. Figure 7.5a shows the total electrochemical current densities. Cu(211) is more active than Cu(111) and adding a catalytic H₂O molecule to the stepped surface further increases the current density. From the computed reaction energies, we infer that the activity increase with respect to CO₂ in the presence of a catalytic H₂O molecule is due to the lower barrier for COOH formation. Figures 7.5b-f show the Faradaic efficiencies for the different surfaces. Notably, the Cu(111) surface mainly produces H₂. On the stepped Cu(211) model, CO₂ reduction to formate competes with H₂ evolution. The lower barrier for HCOO formation on Cu(211) compared to Cu(111) results in higher Faradaic efficiency to HCOO (formate), competing with H₂ formation. Addition of a catalytic H₂O molecule

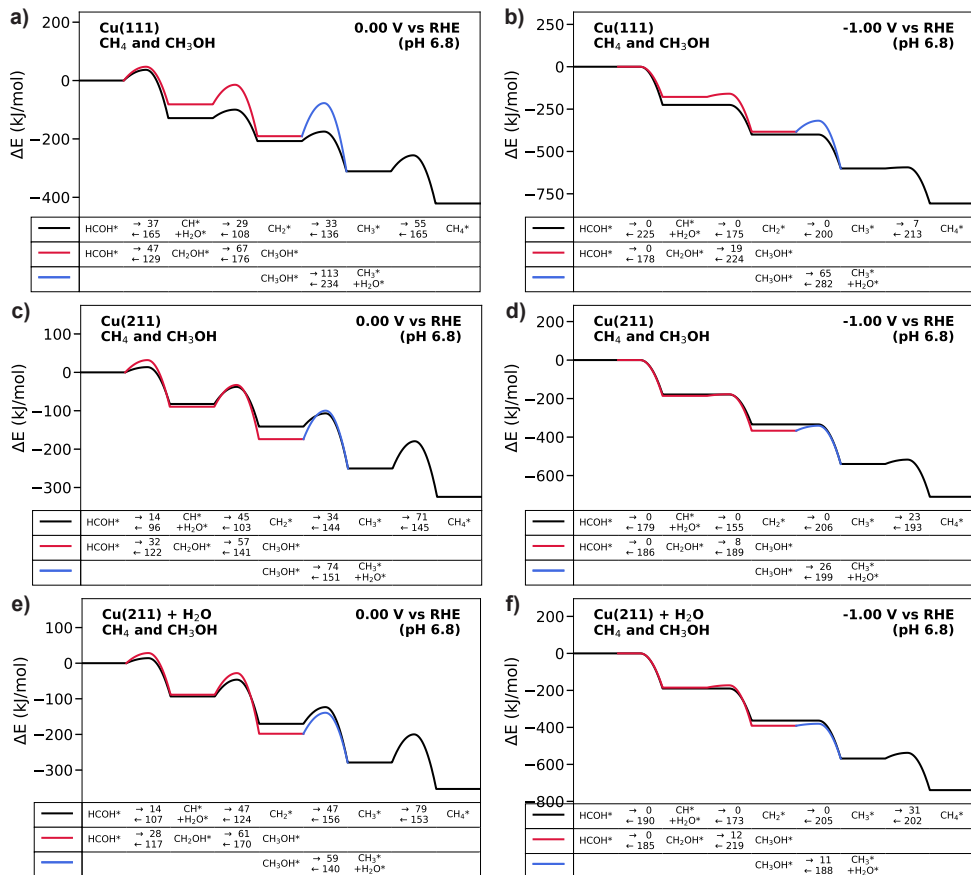


Figure 7.3: Potential energy diagrams for the formation of CH₄ and CH₃OH from HCOH at 0 V and -1.0 V vs. RHE on Cu(111), Cu(211) and Cu(211)+H₂O at pH 6.8. Three pathways are shown: (black) electrochemical HCOH hydrogenation to remove OH as H₂O, followed by CH hydrogenation to CH₄; (red) electrochemical hydrogenation of HCOH to CH₃OH; (blue) electrochemical CH₃OH hydrogenation to remove OH as H₂O. The numbers below the diagrams indicate the forward and backward activation barriers between the corresponding states ($\begin{matrix} \rightarrow E_{\text{act}}^{\text{forw}} \\ \leftarrow E_{\text{act}}^{\text{back}} \end{matrix}$)

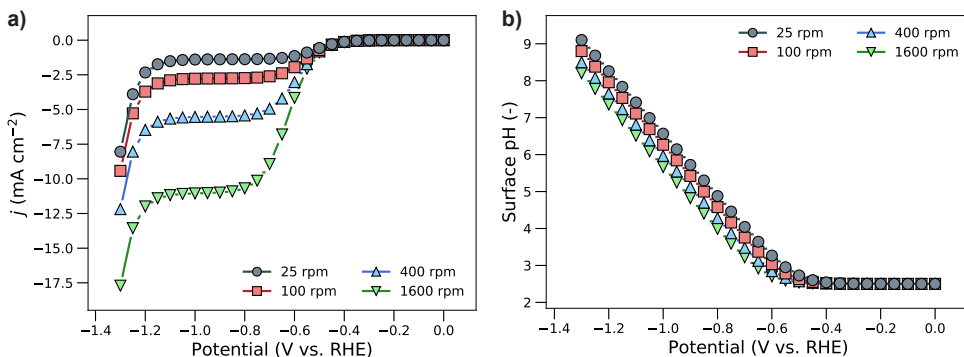


Figure 7.4: Microkinetics simulations of electrochemical hydrogen evolution for a Cu(111) surface representing a rotating disc electrode experiment in which the rotation speed was varied (298 K, pH 2.5): (a) current density; (b) local pH near the electrochemical surface.

shifts the product distribution to CO at low negative potential and CH₄ at high negative potential in competition with H₂ formation. Only a small amount of CH₃OH is formed at intermediate negative potential for this latter model. To verify the role of the COOH pathway, we carried out additional microkinetics simulations for the Cu(111) and Cu(211) models in which both forward and backward energy barriers for the hydrogenation of CO₂ to COOH were lowered by 10 kJ/mol. While this has no significant effect on Cu(111), it results in a strongly increased activity for the Cu(211) surface. Instead of predominantly HCOO, also CH₄ and CO are formed in this case. This crude sensitivity analysis shows the important role of HCOO and COOH pathways with respect to the product distribution.

Figure 7.6 shows the composition of the surface-adsorbed layer. Compared to the Cu(111) surface, the stepped Cu(211) surface already has an appreciable H coverage at low potential, which increases with more negative potential. CO₂ coverages are expectedly low, but highest for the least reactive surface. Two aspects influence the CO₂ coverage. Firstly, the presence of H at the surface limits the CO₂ coverage because of competitive adsorption. Secondly, when CO₂ reduction proceeds, the CO₂ coverage will also decrease. This decrease is mostly due to the transport limitations of CO₂ at high current densities. Figure 7.7 shows that at -1.05 V *vs.* RHE the CO₂ concentration near the surface can decrease by as much as 50%. We confirmed that this transport limitation of CO₂ is reduced for higher RDE rotation rates (Figures E2-5). Proton transport limitations are much stronger due to the already low bulk concentration at pH 6.8. This does not limit the H coverage however, as hydrogen atoms can still be deposited via the water reduction mechanism. Notably, for the standard DFT parameters we observe that the main surface intermediates are H and CO₂. Only when COOH formation barriers are decreased, we observed some OH as a surface intermediate. This effect is most pronounced for the Cu(111) surface, where easier formation of COOH results in a higher concentration of OH upon COOH dissociation.

To better understand the high selectivity to CO and CH₄ for the Cu(211)+H₂O surface, we compared the carbon-based rates at -0.5 V and -1.0 V *vs.* RHE. These results can be seen in Figure 7.8 in which the rates are expressed as relative rates. At -0.5 V about two thirds of

the carbon-based conversion rate towards CO results from direct CO₂ dissociation, while the rest goes through the COOH intermediate. The other surfaces did not present a high rate for direct CO₂ dissociation (Figures E6-9). Clearly, the barriers for this non-electrochemical step are too high without the presence of a catalytic H₂O molecule, emphasizing the role of the solvent. At -1.0 V the electrochemical steps again dominate as major pathways, and CH₄ is the main product. No contribution of HCOO dissociation was observed, also not for the HCOO-producing surfaces. All pathways leading to CH₄ go through a CH_xOH_(x=1-3) intermediate. Clearly, the fast removal of OH from these intermediates prevents the formation of CH₃OH as a final product and CH₄ formation involves hydrogenation of CO to at least HCO or HCOH (depending on the potential) before C–O bond scission takes place. This is expected as Cu is usually considered a low reactive metal among the first-row transition metals, which is not able to directly dissociate the triple C–O bond in CO.

OH removal can originate from non-electrochemical dissociation and electrochemical removal to H₂O via either free protons or water reduction. To discriminate between these steps and to understand the steps that limit the formation of particular products, we performed a degree of rate control (DRC) analysis [88]. We carried out this analysis for the different Cu(211) surfaces. Here we discuss the rate control for the Cu(211)+H₂O surface, while data for the other surfaces can be found in Appendix E. Figure 7.9 shows the 6 elementary reactions steps with the strongest control on the rate of CH₄, CH₃OH, HCOO and CO formation. As expected, COOH formation is strongly controlling the rate for all products in which one of the C–O bonds is cleaved (CH₄, CH₃OH and CO). Conversely, HCOO formation is rate-limiting for the formation of formate. We observe that all these reactions involve H₂O instead of protons, consistent with the depletion of protons across the diffusion layer in the potential range where CO₂ is reduced. Reactions that control the formation of CH₄ are HCOH formation at low potential and HCO formation at higher potential. The latter step also controls the rate of CH₃OH formation. Notably, an important step that inhibits CH₃OH formation is its dissociation into CH₃. Faster desorption of CH₃OH can counteract this inhibiting effect. The selectivity towards CO strongly depends on the adsorption strength of CO. Decreased binding of CO will lead to higher Faradaic efficiencies of CO. Removal of H adsorbates from the surface facilitates all of these reactions, as this process generates empty sites for CO₂ adsorption.

Finally, we discuss the degree of selectivity control (DSC) [89]. Although faster removal of H adsorbates can increase the total current density towards CO₂ reduction, the same applies for the current towards H₂ (Figure E12). A DSC analysis of the Cu(211)+H₂O surface is presented in Figure 7.10. Here, positive DSC values indicate that promoting a step results in enhanced Faradaic efficiency for the corresponding product, while negative DSC values indicate a lowered Faradaic efficiency by promoting a specific step. Again, the CO₂ hydrogenation steps towards COOH and HCOO are significantly controlling the selectivity to either CH₄, CH₃OH, and CO, or to HCOO. Furthermore, we find that formation of adsorbed H is more inhibiting selectivity than H₂ formation from adsorbed H. This shows that adsorbed H is not used to reduce CO₂, and that this process requires electrochemically active species.

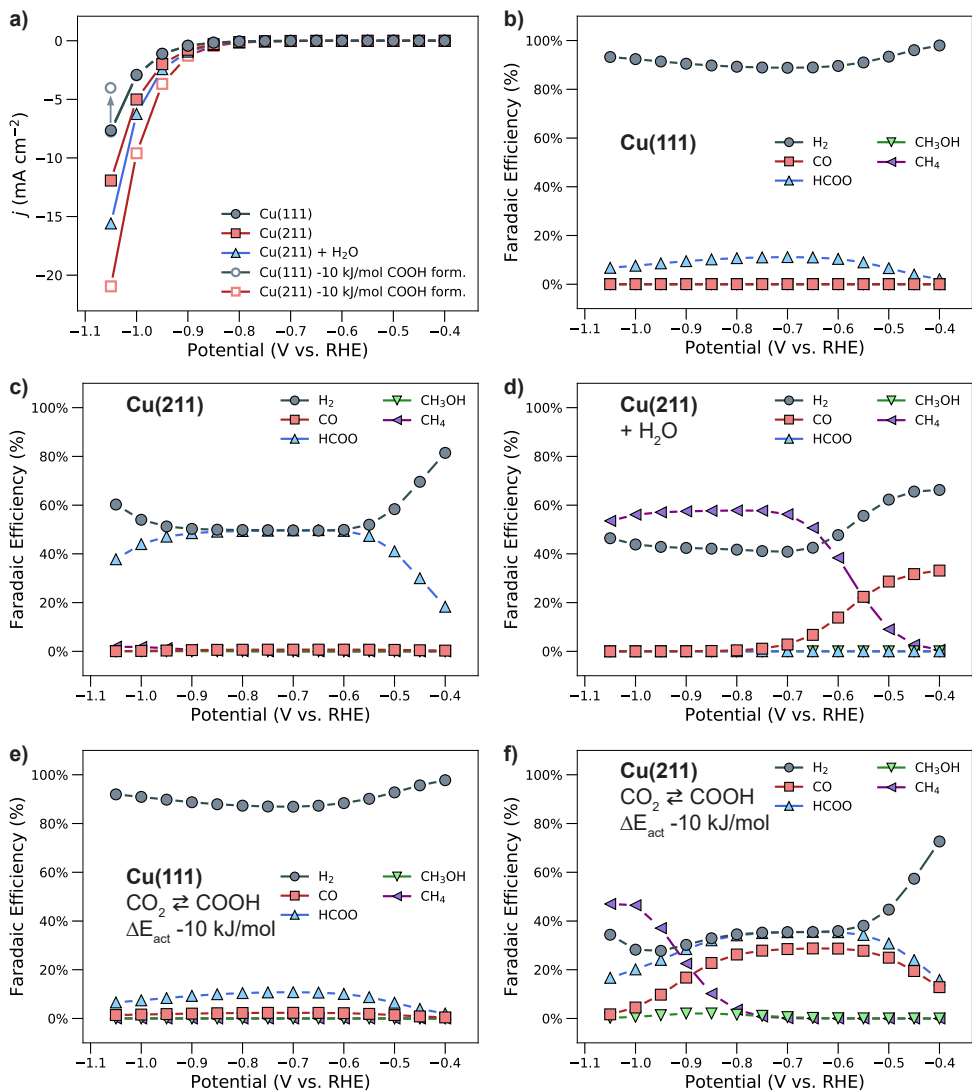


Figure 7.5: Microkinetics simulations of electrochemical CO₂ reduction on Cu(111), Cu(211) and Cu(211)+H₂O surfaces on a rotating disc electrode at 100 rpm and a bulk pH of 6.8: (a) total electrochemical current; (b-f) Faradaic efficiency of various products.

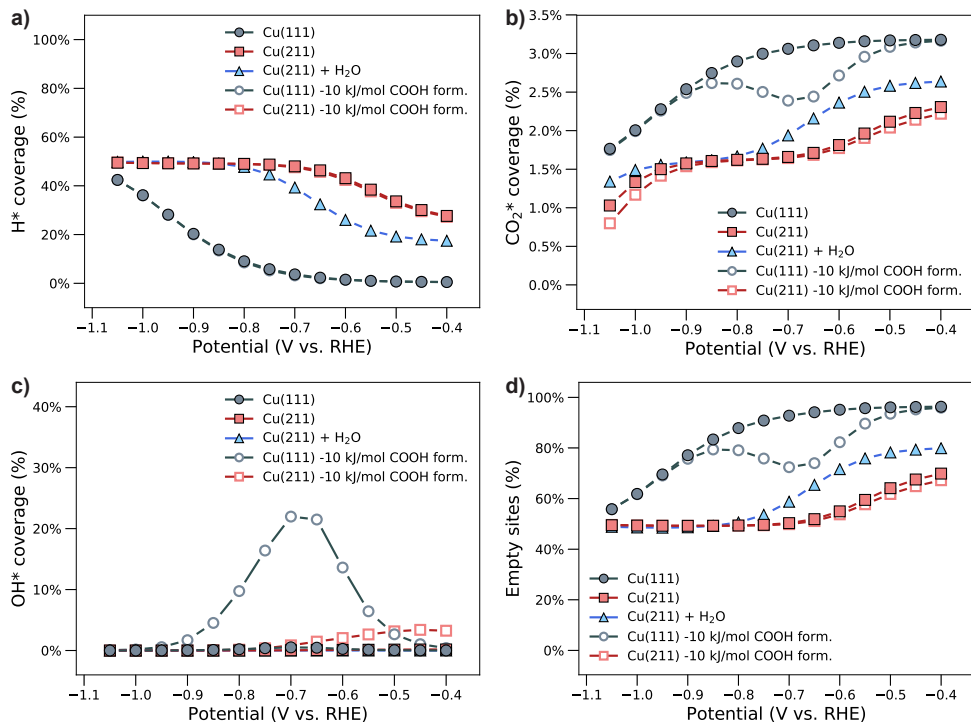


Figure 7.6: Microkinetics simulations of electrochemical CO₂ reduction on Cu(111), Cu(211) and Cu(211)+H₂O surfaces on a rotating disc electrode at 100 rpm and a bulk pH of 6.8: (a) H coverage; (b) CO₂ coverage; (c) OH coverage; (d) empty site coverage.

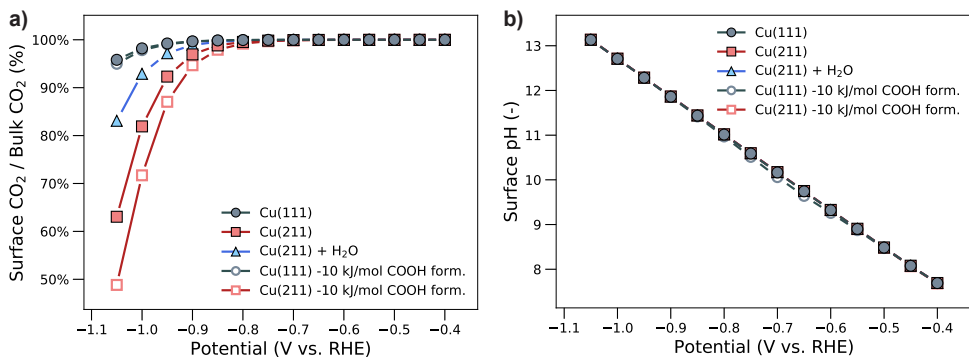


Figure 7.7: Microkinetics simulations of electrochemical CO₂ reduction on Cu(111), Cu(211) and Cu(211)+H₂O surfaces on a rotating disc electrode at 100 rpm and a bulk pH of 6.8: (a) Percentage of near-surface concentrations of CO₂ compared to bulk CO₂ concentrations; (b) local pH near the electrochemical surface.

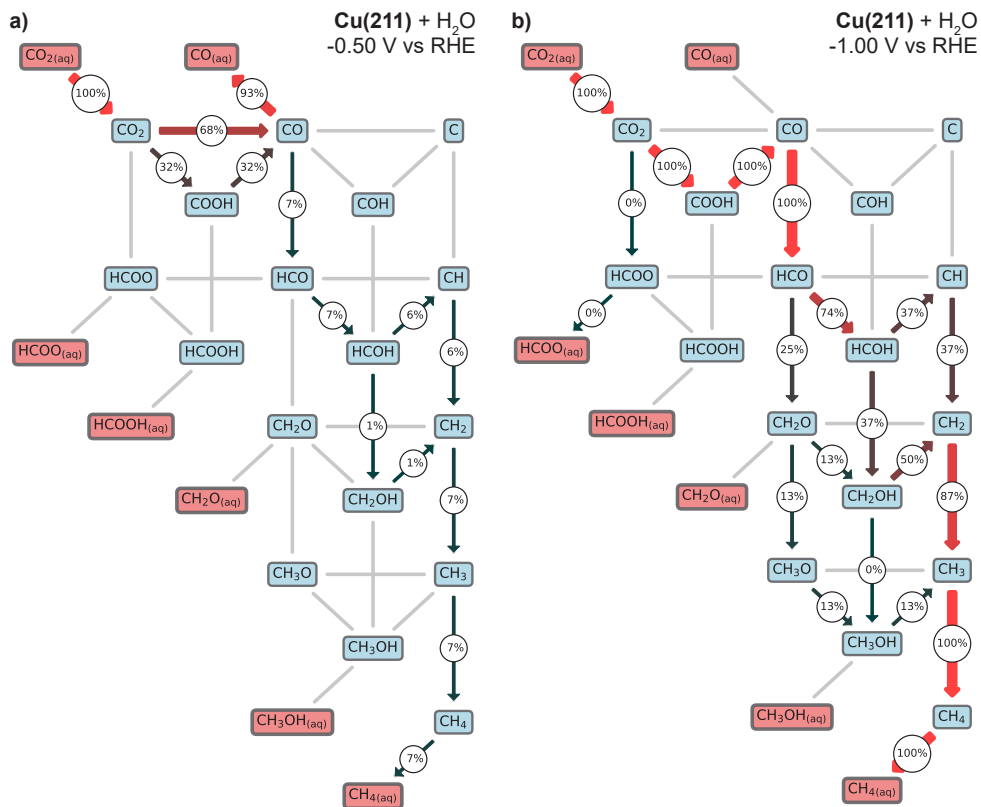


Figure 7.8: Reaction network analysis of electrochemical CO₂ reduction on the Cu(211)+H₂O surface at 100 rpm and a bulk pH of 6.8: (a) -0.5 V *vs.* RHE; (b) -1.0 V *vs.* RHE.

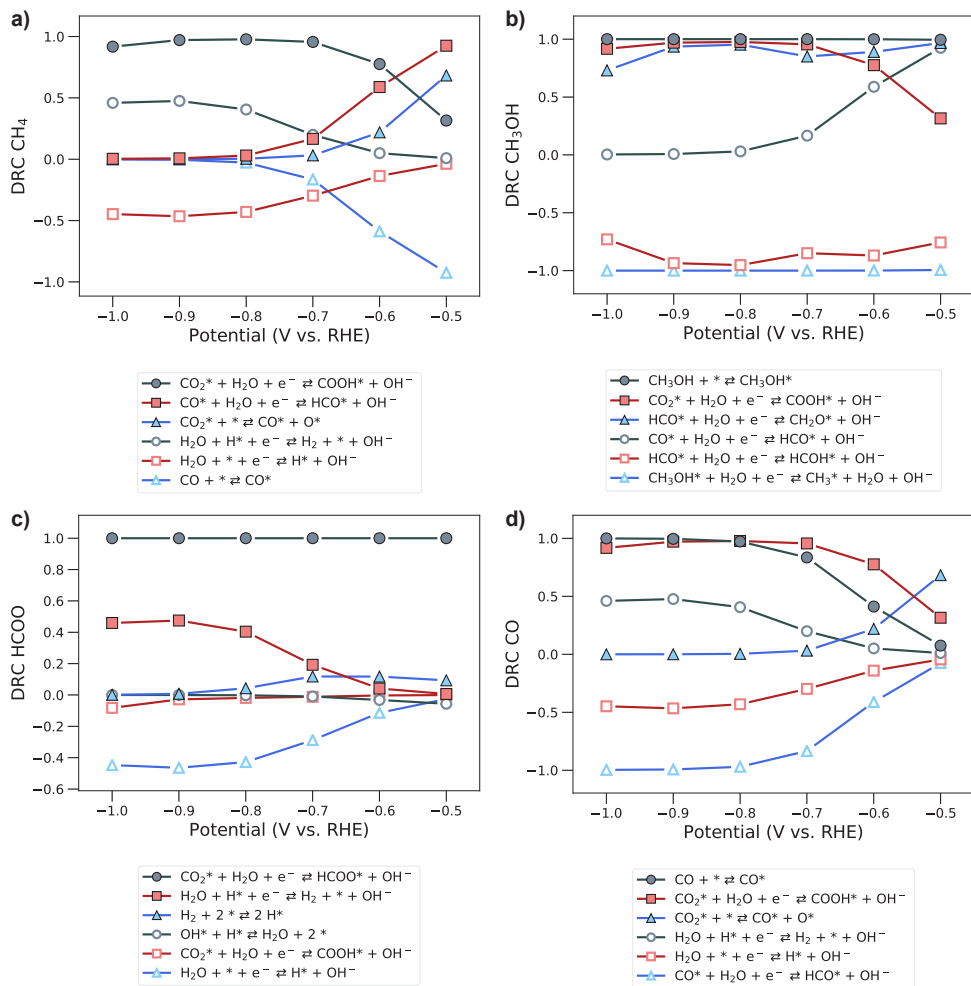


Figure 7.9: Degree of rate control for various products formed during electrochemical CO₂ reduction on the Cu(211)+H₂O surface on a rotating disc electrode at 100 rpm and a bulk pH of 6.8. (a) CH₄; (b) CH₃OH; (c) HCOO; (d) CO.

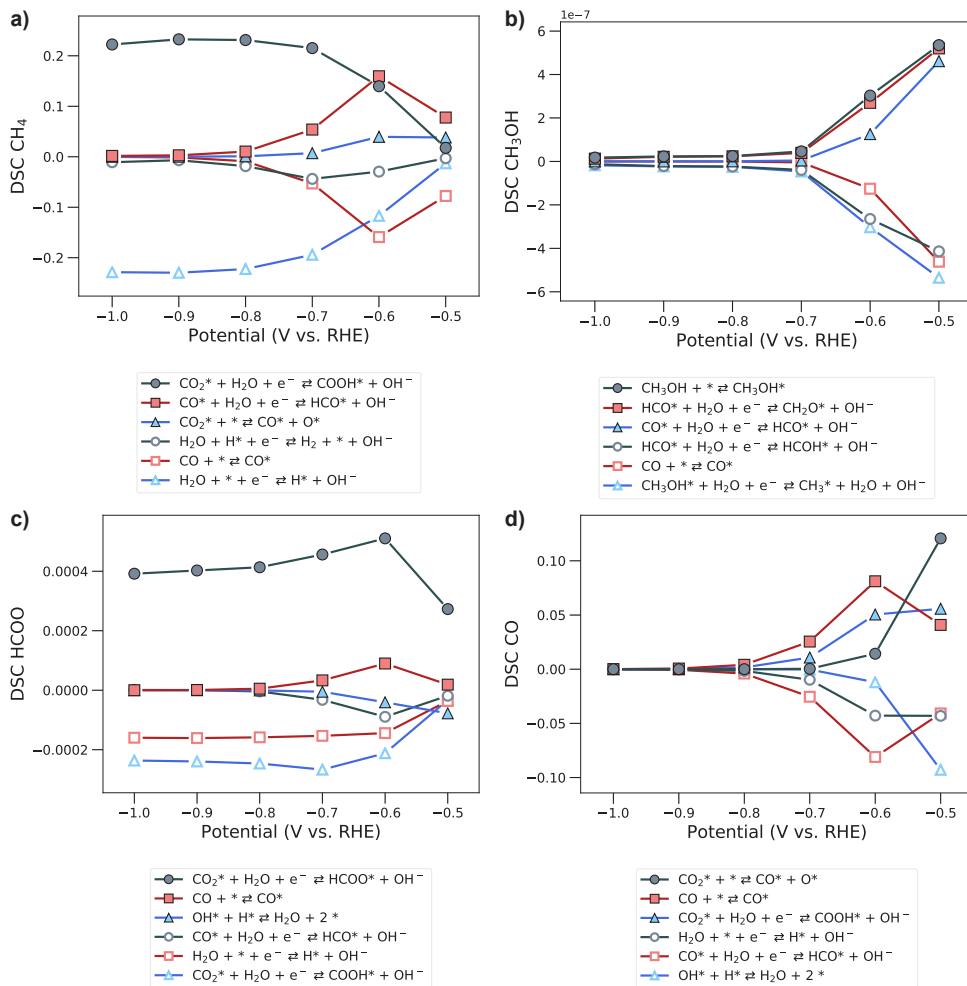


Figure 7.10: Degree of selectivity control for various products formed during electrochemical CO₂ reduction on the Cu(211)+H₂O surface on a rotating disc electrode at 100 rpm and a bulk pH of 6.8. (a) CH₄; (b) CH₃OH; (c) HCOO; (d) CO.

7.4 Conclusions

The first-principles microkinetics simulations as described herein were conducted to explain the electrochemical reduction of CO₂ into CO, HCOO(H), CH₃OH and CH₄ over a copper electrode. We took into account the Cu(111) and Cu(211) surfaces to model both terrace- and step-site topologies. The influence of the electrochemical potential on the activation barriers was taken into account in the simulations. Using this approach, we reproduced the effect of proton transport limitations to the electrode surface in a typical hydrogen evolution experiment. The resulting current density plateaus indicate that current densities at high overpotentials are the result of water reduction instead of the reduction of free protons due to the high pH occurring at the electrode surface. By including CO₂ reduction, current densities as a function of potential (*i*-*V* curves), Faradaic efficiency, and surface coverage were computed. The data show that hydrogen evolution and CO₂ reduction compete on these surfaces. The stepped Cu(211) surface is more active than the Cu(111) terrace for electrochemical CO₂ reduction. While Cu(211) still forms HCOO as the main CO₂ reduction product, the presence of a catalytic H₂O molecule (simulating the presence of an electrolyte) increases the overall rate and selectivity to the more reduced products CO and CH₄. The simulations show that this is due to a lowering of the barriers of X-OH formation. An analysis of the degrees of rate and selectivity control show that the hydrogenation step from CO₂ → COOH is critical in the formation of CO and CH₄. The simulated product distribution as a function of potential is in reasonable agreement with experiment. A small change in the barrier for COOH formation within the accuracy of DFT results in a much better correspondence. A reaction network analysis shows that CH₄ is formed mainly via the CO → HCO → HCOH → CH + OH pathway and CH_{*x*}OH species, which are potential precursors to CH₃OH, are rapidly dissociated to CH_{*x*} and H₂O in a PCET step, explaining why at high potential typically CH₄ is observed instead of CH₃OH. At high potential, CO₂ diffusion can limit the current density, which negatively affects CO₂ reduction *vs.* proton reduction.

7.5 References

- [1] M. Cokoja, C. Bruckmeier, B. Rieger, W. A. Herrmann, F. E. Kuhn, *Angew Chem Int Ed Engl* **2011**, *50*, 8510–37.
- [2] E. E. Benson, C. P. Kubiak, A. J. Sathrum, J. M. Smieja, *Chem Soc Rev* **2009**, *38*, 89–99.
- [3] G. Centi, E. A. Quadrelli, S. Perathoner, *Energy & Environmental Science* **2013**, *6*, 1711–1731.
- [4] X. Liu, J. Xiao, H. Peng, X. Hong, K. Chan, J. K. Norskov, *Nat Commun* **2017**, *8*, 15438.
- [5] M. Azuma, K. Hashimoto, M. Hiramoto, M. Watanabe, T. Sakata, *Journal of the Electrochemical Society* **1990**, *137*, 1772–1778.

- [6] N. Hoshi, H. Ito, T. Suzuki, Y. Hori, *Journal of Electroanalytical Chemistry* **1995**, *395*, 309–312.
- [7] S. Nakagawa, A. Kudo, M. Azuma, T. Sakata, *Journal of Electroanalytical Chemistry* **1991**, *308*, 339–343.
- [8] Y. H. Nagahiro Hoshi, Makiko Kato, *Journal of Electroanalytical Chemistry* **1997**, *440*, 283–286.
- [9] S. Sen, D. Liu, G. T. R. Palmore, *ACS Catalysis* **2014**, *4*, 3091–3095.
- [10] S. Rasul, D. H. Anjum, A. Jedidi, Y. Minenkov, L. Cavallo, K. Takanabe, *Angew Chem Int Ed Engl* **2015**, *54*, 2146–50.
- [11] D. Gao, H. Zhou, J. Wang, S. Miao, F. Yang, G. Wang, J. Wang, X. Bao, *J Am Chem Soc* **2015**, *137*, 4288–91.
- [12] Y. Hori, K. Kikuchi, S. Suzuki, *Chemistry Letters* **1985**, *14*, 1695–1698.
- [13] Y. Hori, K. Kikuchi, A. Murata, S. Suzuki, *Chemistry Letters* **1986**, *15*, 897–898.
- [14] Y. Hori, A. Murata, R. Takahashi, *Journal of the Chemical Society-Faraday Transactions I* **1989**, *85*, 2309–2326.
- [15] Y. Hori, H. Wakebe, T. Tsukamoto, O. Koga, *Electrochimica Acta* **1994**, *39*, 1833–1839.
- [16] N. Hoshi, M. Noma, T. Suzuki, Y. Hori, *Journal of Electroanalytical Chemistry* **1997**, *421*, 15–18.
- [17] Y. Hori, I. Takahashi, O. Koga, N. Hoshi, *Journal of Physical Chemistry B* **2002**, *106*, 15–17.
- [18] K. Hara, A. Kudo, T. Sakata, *Journal of Electroanalytical Chemistry* **1995**, *391*, 141–147.
- [19] K. P. Kuhl, T. Hatsukade, E. R. Cave, D. N. Abram, J. Kibsgaard, T. F. Jaramillo, *J Am Chem Soc* **2014**, *136*, 14107–13.
- [20] M. Bevilacqua, J. Filippi, H. A. Miller, F. Vizza, *Energy Technology* **2015**, *3*, 197–210.
- [21] R. Kortlever, J. Shen, K. J. Schouten, F. Calle-Vallejo, M. T. Koper, *J Phys Chem Lett* **2015**, *6*, 4073–82.
- [22] D. Raciti, K. J. Livi, C. Wang, *Nano Lett* **2015**, *15*, 6829–35.
- [23] J. Lee, Y. Tak, *Electrochimica Acta* **2001**, *46*, 3015–3022.
- [24] A. J. B. D. W. DeWulf, T. Jin, *J. Electrochem. Soc.* **1989**, *136*, 1686–1691.
- [25] J. J. Kim, D. P. Summers, K. W. Frese, *Journal of Electroanalytical Chemistry* **1988**, *245*, 223–244.
- [26] W. J. Durand, A. A. Peterson, F. Studt, F. Abild-Pedersen, J. K. Nørskov, *Surface Science* **2011**, *605*, 1354–1359.
- [27] C. Shi, H. A. Hansen, A. C. Lausche, J. K. Nørskov, *Phys Chem Chem Phys* **2014**, *16*, 4720–7.

- [28] R. Reske, H. Mistry, F. Behafarid, B. Roldan Cuenya, P. Strasser, *J Am Chem Soc* **2014**, *136*, 6978–86.
- [29] K. Manthiram, B. J. Beberwyck, A. P. Alivisatos, *J Am Chem Soc* **2014**, *136*, 13319–25.
- [30] R. Reske, M. Duca, M. Oezaslan, K. J. P. Schouten, M. T. M. Koper, P. Strasser, *The Journal of Physical Chemistry Letters* **2013**, *4*, 2410–2413.
- [31] C. Costentin, M. Robert, J. M. Saveant, *Chem Soc Rev* **2013**, *42*, 2423–36.
- [32] W. Tang, A. A. Peterson, A. S. Varela, Z. P. Jovanov, L. Bech, W. J. Durand, S. Dahl, J. K. Norskov, I. Chorkendorff, *Phys Chem Chem Phys* **2012**, *14*, 76–81.
- [33] Y. Hori, I. Takahashi, O. Koga, N. Hoshi, *Journal of Molecular Catalysis a-Chemical* **2003**, *199*, 39–47.
- [34] X. Zhang, J.-X. Liu, B. Zijlstra, I. A. W. Filot, Z. Zhou, S. Sun, E. J. M. Hensen, *Nano Energy* **2018**, *43*, 200–209.
- [35] P. B. Rasmussen, M. Kazuta, I. Chorkendorff, *Surface Science* **1994**, *318*, 267–280.
- [36] P. B. Rasmussen, P. M. Holmblad, T. Askgaard, C. V. Ovesen, P. Stoltze, J. K. Norskov, I. Chorkendorff, *Catalysis Letters* **1994**, *26*, 373–381.
- [37] J. Yoshihara, C. T. Campbell, *Journal of Catalysis* **1996**, *161*, 776–782.
- [38] J. Yoshihara, S. C. Parker, A. Schafer, C. T. Campbell, *Catalysis Letters* **1995**, *31*, 313–324.
- [39] Y. Hori in *Modern Aspects of Electrochemistry*, (Eds.: C. Vayenas, R. White, M. Gamboa-Aldeco), Modern Aspects of Electrochemistry, Springer New York, **2008**, Chapter Chapter 3, pp. 89–189.
- [40] M. Le, M. Ren, Z. Zhang, P. T. Sprunger, R. L. Kurtz, J. C. Flake, *Journal of the Electrochemical Society* **2011**, *158*, E45–E49.
- [41] C. W. Li, M. W. Kanan, *J Am Chem Soc* **2012**, *134*, 7231–4.
- [42] K. J. Schouten, Z. Qin, E. Perez Gallent, M. T. Koper, *J Am Chem Soc* **2012**, *134*, 9864–7.
- [43] Y. Hori, R. Takahashi, Y. Yoshinami, A. Murata, *Journal of Physical Chemistry B* **1997**, *101*, 7075–7081.
- [44] I. Takahashi, O. Koga, N. Hoshi, Y. Hori, *Journal of Electroanalytical Chemistry* **2002**, *533*, 135–143.
- [45] A. A. Peterson, J. K. Norskov, *Journal of Physical Chemistry Letters* **2012**, *3*, 251–258.
- [46] P. Hirunsit, W. Soodsawang, J. Limtrakul, *Journal of Physical Chemistry C* **2015**, *119*, 8238–8249.
- [47] K. J. P. Schouten, Y. Kwon, C. J. M. van der Ham, Z. Qin, M. T. M. Koper, *Chemical Science* **2011**, *2*, 1902–1909.

- [48] K. P. Kuhl, E. R. Cave, D. N. Abram, T. F. Jaramillo, *Energy & Environmental Science* **2012**, *5*, 7050–7059.
- [49] M. Gattrell, N. Gupta, A. Co, *Journal of Electroanalytical Chemistry* **2006**, *594*, 1–19.
- [50] Y. Hori, A. Murata, R. Takahashi, S. Suzuki, *Journal of the American Chemical Society* **1987**, *109*, 5022–5023.
- [51] L. Z. Gao, C. T. Au, *Journal of Catalysis* **2000**, *189*, 1–15.
- [52] L. N. Zhai, C. N. Cui, Y. T. Zhao, X. L. Zhu, J. Y. Han, H. Wang, Q. F. Ge, *Journal of Physical Chemistry C* **2017**, *121*, 16275–16282.
- [53] A. B. A. Reyimjan A. Sidik, *Journal of Electroanalytical Chemistry* **2002**, *528*, 69–76.
- [54] J. Rossmeisl, J. K. Nørskov, C. D. Taylor, M. J. Janik, M. Neurock, *Journal of Physical Chemistry B* **2006**, *110*, 21833–21839.
- [55] J. K. Nørskov, J. Rossmeisl, A. Logadottir, L. Lindqvist, J. R. Kitchin, T. Bligaard, H. Jónsson, *The Journal of Physical Chemistry B* **2004**, *108*, 17886–17892.
- [56] M. P. Hyman, J. W. Medlin, *Journal of Physical Chemistry B* **2005**, *109*, 6304–6310.
- [57] K. Y. Yeh, M. J. Janik, *J Comput Chem* **2011**, *32*, 3399–408.
- [58] C. D. Taylor, S. A. Wasileski, J.-S. Filhol, M. Neurock, *Physical Review B* **2006**, *73*, 165402.
- [59] A. A. Peterson, F. Abild-Pedersen, F. Studt, J. Rossmeisl, J. K. Nørskov, *Energy & Environmental Science* **2010**, *3*, 1311–1315.
- [60] T. Burdyny, W. A. Smith, *Energy & Environmental Science* **2019**, *12*, 1442–1453.
- [61] P. E. Blochl, *Phys Rev B Condens Matter* **1994**, *50*, 17953–17979.
- [62] J. P. Perdew, K. Burke, M. Ernzerhof, *Physical Review Letters* **1996**, *77*, 3865–3868.
- [63] K. J. Sun, Y. H. Zhao, H. Y. Su, W. X. Li, *Theoretical Chemistry Accounts* **2012**, *131*, 11181–11190.
- [64] G. Henkelman, B. P. Uberuaga, H. Jonsson, *Journal of Chemical Physics* **2000**, *113*, 9901–9904.
- [65] X. Nie, M. R. Esopi, M. J. Janik, A. Asthagiri, *Angew Chem Int Ed Engl* **2013**, *52*, 2459–62.
- [66] G. Rostamikia, A. J. Mendoza, M. A. Hickner, M. J. Janik, *Journal of Power Sources* **2011**, *196*, 9228–9237.
- [67] H. A. Hansen, V. Viswanathan, J. K. Nørskov, *The Journal of Physical Chemistry C* **2014**, *118*, 6706–6718.
- [68] P. Ferrin, D. Simonetti, S. Kandoi, E. Kunkes, J. A. Dumesic, J. K. Nørskov, M. Mavrikakis, *J Am Chem Soc* **2009**, *131*, 5809–15.
- [69] X. Liu, P. Schlexer, J. Xiao, Y. Ji, L. Wang, R. B. Sandberg, M. Tang, K. S. Brown, H. Peng, S. Ringe, C. Hahn, T. F. Jaramillo, J. K. Nørskov, K. Chan, *Nat Commun* **2019**, *10*, 32.

- [70] L. Wang, S. A. Nitopi, E. Bertheussen, M. Orazov, C. G. Morales-Guio, X. Liu, D. C. Higgins, K. Chan, J. K. Nørskov, C. Hahn, T. F. Jaramillo, *ACS Catalysis* **2018**, *8*, 7445–7454.
- [71] I. A. W. Filot, B. Zijlstra, E. J. M. Hensen, MKMCXX, a C++ program for constructing microkinetic models, <http://www.mkmcxx.nl/>.
- [72] I. A. Filot, R. A. van Santen, E. J. Hensen, *Angew Chem Int Ed Engl* **2014**, *53*, 12746–12750.
- [73] P. W. Atkins, J. De Paula, *Atkins' Physical chemistry*, **2014**.
- [74] H. Ooka, M. C. Figueiredo, M. T. M. Koper, *Langmuir* **2017**, *33*, 9307–9313.
- [75] M. Auinger, I. Katsounaros, J. C. Meier, S. O. Klemm, P. U. Biedermann, A. A. Topalov, M. Rohwerder, K. J. Mayrhofer, *Phys Chem Chem Phys* **2011**, *13*, 16384–94.
- [76] B. Hammer, M. Scheffler, K. W. Jacobsen, J. K. Nørskov, *Phys Rev Lett* **1994**, *73*, 1400–1403.
- [77] Ž. Šljivančanin, B. Hammer, *Physical Review B* **2002**, *65*, 085414.
- [78] J. J. Carroll, J. D. Slupsky, A. E. Mather, *Journal of Physical and Chemical Reference Data* **1991**, *20*, 1201–1209.
- [79] P. J. Feibelman, B. Hammer, J. K. Nørskov, F. Wagner, M. Scheffler, R. Stumpf, R. Watwe, J. Dumesic, *Journal of Physical Chemistry B* **2001**, *105*, 4018–4025.
- [80] A. J. Garza, A. T. Bell, M. Head-Gordon, *ACS Catalysis* **2018**, *8*, 1490–1499.
- [81] J. H. Montoya, A. A. Peterson, J. K. Nørskov, *ChemCatChem* **2013**, *5*, 737–742.
- [82] T. L. Tan, L. L. Wang, J. Zhang, D. D. Johnson, K. W. Bai, *ACS Catalysis* **2015**, *5*, 2376–2383.
- [83] E. Skúlason, V. Tripkovic, M. E. Björketun, S. Gudmundsdóttir, G. Karlberg, J. Rossmeisl, T. Bligaard, H. Jónsson, J. K. Nørskov, *The Journal of Physical Chemistry C* **2010**, *114*, 18182–18197.
- [84] D. H. Mei, L. Xu, G. Henkelman, *Journal of Catalysis* **2008**, *258*, 44–51.
- [85] S. Shetty, R. A. van Santen, *Catalysis Today* **2011**, *171*, 168–173.
- [86] I. M. Ciobica, R. A. van Santen, *Journal of Physical Chemistry B* **2003**, *107*, 3808–3812.
- [87] J. D. Goodpaster, A. T. Bell, M. Head-Gordon, *J Phys Chem Lett* **2016**, *7*, 1471–7.
- [88] C. Stegelmann, A. Andreasen, C. T. Campbell, *Journal of the American Chemical Society* **2009**, *131*, 8077–8082.
- [89] C. Stegelmann, N. C. Schiødt, C. T. Campbell, P. Stoltze, *Journal of Catalysis* **2004**, *221*, 630–649.

Appendix E

- Table E1: Energetics for non-electrochemical hydrogenation reactions
- Figure E1: Water reduction contribution to hydrogen evolution on Cu(111)
- Figure E2: Water reduction contribution to total activity on Cu(211) surfaces
- Figure E3: Effect of RDE rotation speed on Cu(211)
- Figure E4: Effect of RDE rotation speed on Cu(211) + H₂O
- Figure E5: Effect of RDE rotation speed on Cu(211) -10kJ/mol COOH
- Figure E6: Flux diagram Cu(111)
- Figure E7: Flux diagram Cu(211)
- Figure E8: Flux diagram Cu(111)-10kJ/mol COOH
- Figure E9: Flux diagram Cu(211)-10kJ/mol COOH
- Figure E10: DRC to CH₄, CH₃OH, HCOO and CO on Cu(211)
- Figure E11: DRC to CH₄, CH₃OH, HCOO and CO on Cu(211) -10kJ/mol COOH
- Figure E12: DRC to H₂ on Cu(111) and Cu(211) surfaces
- Figure E13: DSC to CH₄, CH₃OH, HCOO and CO on Cu(211)
- Figure E14: DSC to CH₄, CH₃OH, HCOO and CO on Cu(211) -10kJ/mol COOH
- Figure E15: DSC to H₂ on Cu(111) and Cu(211) surfaces
- Figure E16: Adsorbed geometries of HCOO and COOH
- Figure E17: Transition state geometries for the formation of COOH and HCOO
- Figure E18: Transition state geometries for the formation of HCO and HCOH

Table E1: Energetics for non-electrochemical hydrogenation reactions in CO₂ reduction on Cu surfaces.

Elementary reaction	Cu(111)		Cu(211)		Cu(211)+H ₂ O	
	$E_{\text{act}}^{\text{forw}}$	$E_{\text{act}}^{\text{back}}$	$E_{\text{act}}^{\text{forw}}$	$E_{\text{act}}^{\text{back}}$	$E_{\text{act}}^{\text{forw}}$	$E_{\text{act}}^{\text{back}}$
O + H ⇌ OH	96	151	100	171	84	148
OH + H ⇌ H ₂ O	143	209	145	113	100	90
C + H ⇌ CH	68	166	74	141	119	169
CH + H ⇌ CH ₂	48	88	64	84	66	105
CH ₂ + H ⇌ CH ₃	52	117	54	124	66	136
CH ₃ + H ⇌ CH ₄	74	146	90	126	98	134
CO + H ⇌ COH	123	23	121	23	105	5
CO + H ⇌ HCO	104	8	101	24	90	15
HCO + H ⇌ HCOH	67	21	59	26	54	4
HCO + H ⇌ CH ₂ O	65	72	48	61	71	82
COH + H ⇌ HCOH	111	69	131	119	150	125
HCOH + H ⇌ CH ₂ OH	67	109	51	102	48	98
CH ₂ O + H ⇌ CH ₂ OH	89	80	92	97	55	43
CH ₂ O + H ⇌ CH ₃ O	23	100	23	97	35	93
CH ₂ OH + H ⇌ CH ₃ OH	86	157	76	122	80	151
CH ₃ O + H ⇌ CH ₃ OH	107	90	74	50	79	80
COH + H ⇌ C + H ₂ O	80	29	63	28	35	15
HCOH + H ⇌ CH + H ₂ O	56	146	33	77	34	88
CH ₂ OH + H ⇌ CH ₂ + H ₂ O	80	167	70	83	60	103
CH ₃ OH + H ⇌ CH ₃ + H ₂ O	133	214	94	131	78	120
CO ₂ + H ⇌ COOH	147	79	137	113	129	116
CO ₂ + H ⇌ HCOO	133	141	127	143	144	159
COOH + H ⇌ HCOOH	135	175	212	222	148	133
HCOO + H ⇌ HCOOH	151	115	142	112	143	99
COOH + H ⇌ CO + H ₂ O	95	203	66	85	157	185

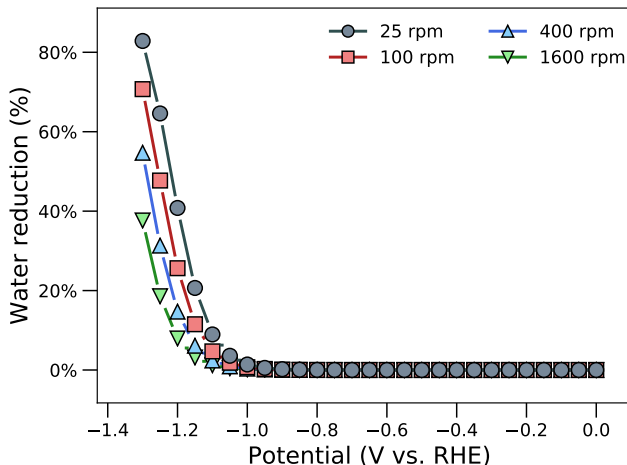


Figure E1: Contribution of the water reduction mechanism to the total activity for electrochemical hydrogen evolution for a Cu(111) surface representing a rotating disc electrode experiment in which the rotation speed was varied (298 K, pH 2.5).

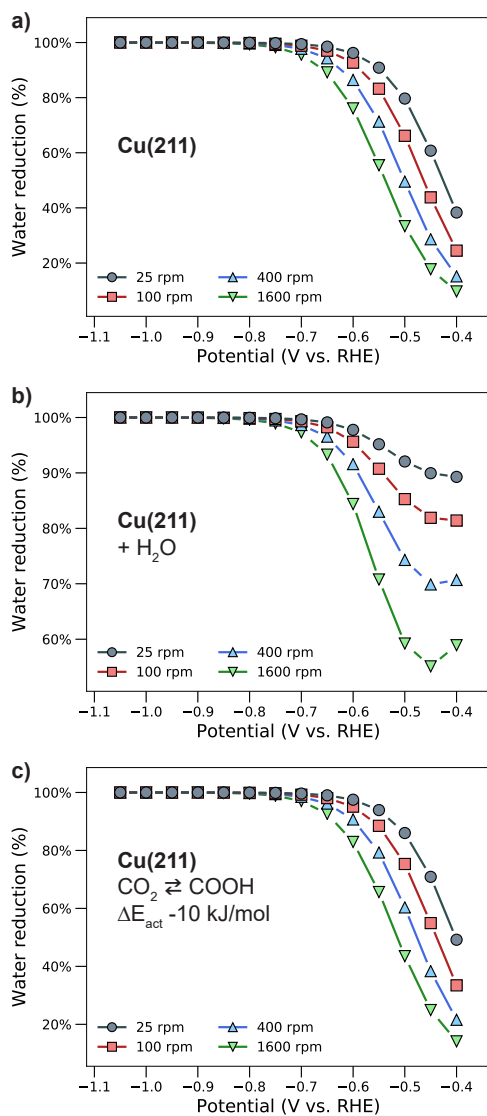


Figure E2: Contribution of the water reduction mechanism to the total activity for electrochemical CO₂ reduction on a rotating disc electrode at 100 rpm and a bulk pH of 6.8: (a) Cu(211), (b) Cu(211)+H₂O, (c) Cu(211) -10 kJ/mol COOH barrier.

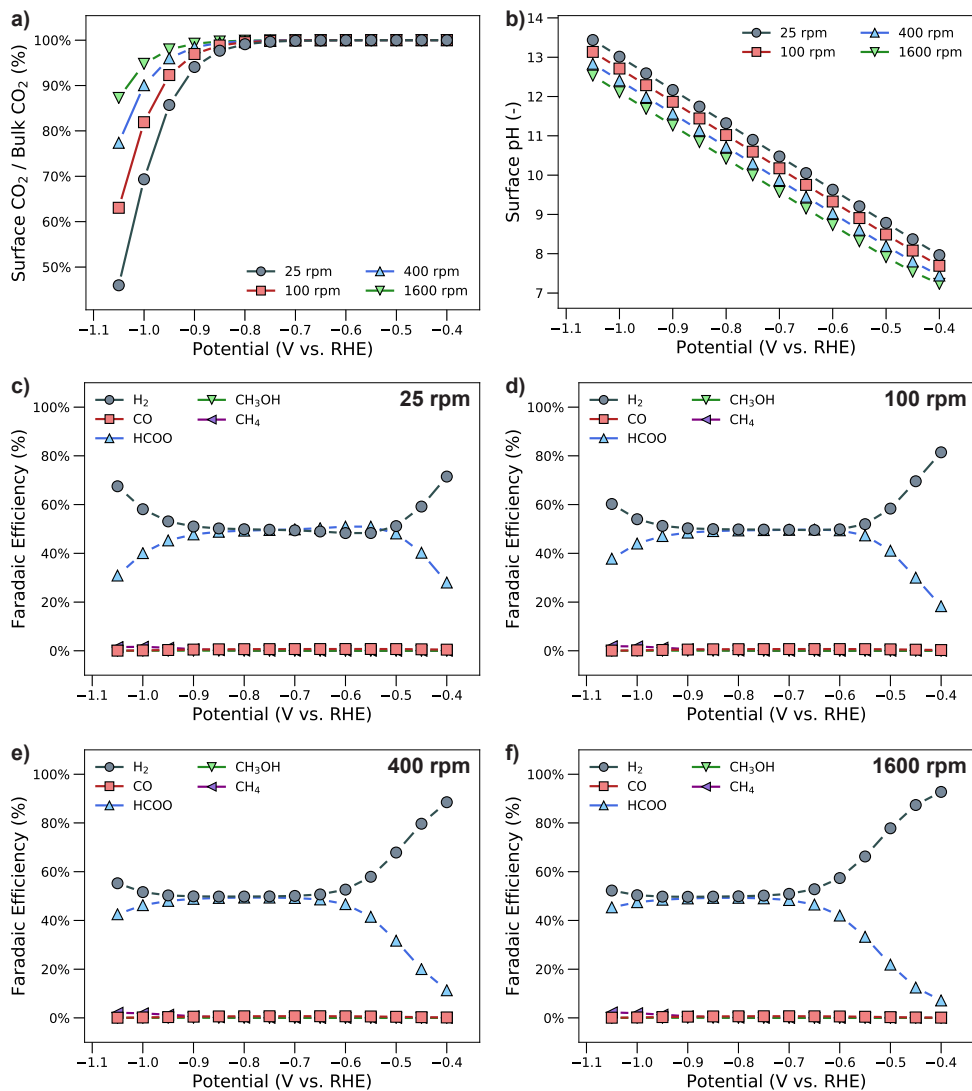


Figure E3: Simulated electrochemical CO₂ reduction on Cu(211) at a bulk pH of 6.8 as a function of RDE rotation speed: (a) Percentage of near-surface concentrations of CO₂ compared to bulk CO₂ concentrations; (b) local pH near the electrochemical surface; (c-f) Faradaic Efficiency at 25, 100, 400 and 1600 rpm.

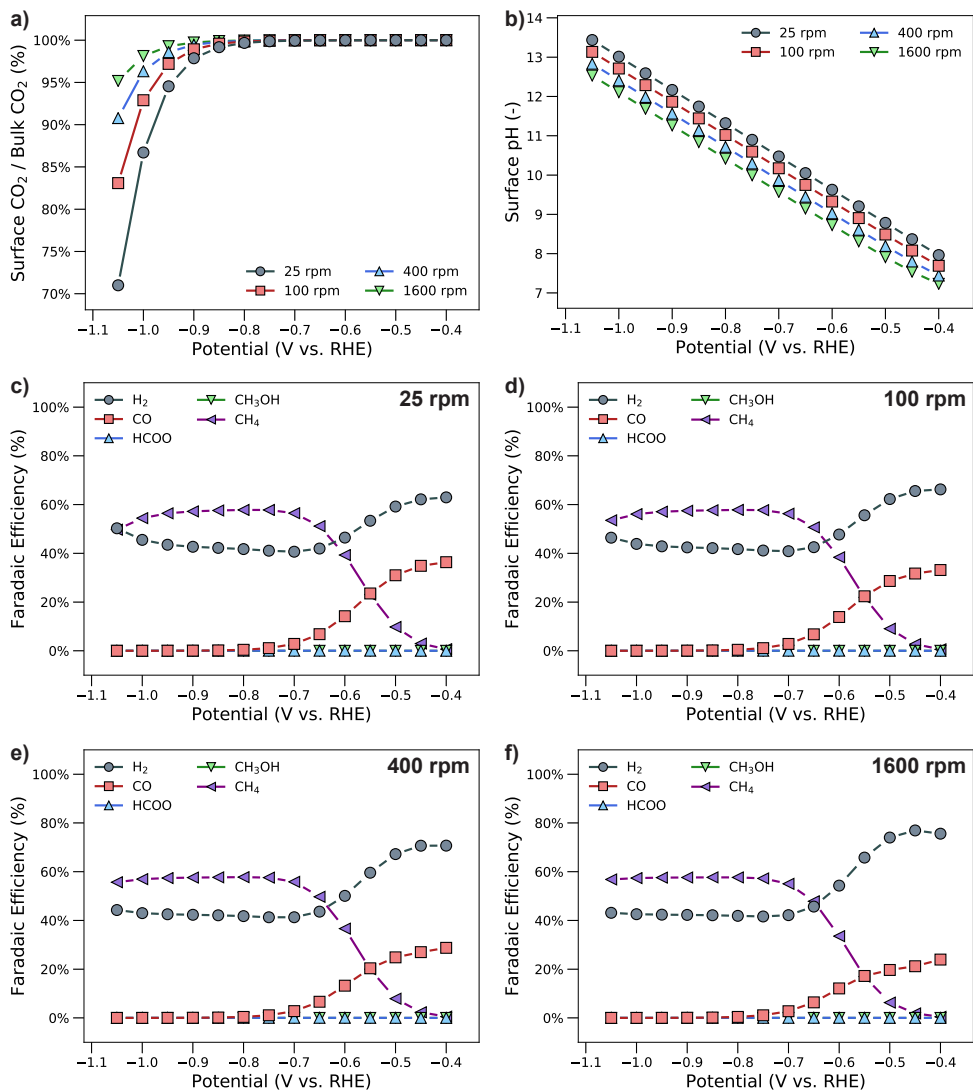


Figure E4: Simulated electrochemical CO₂ reduction on Cu(211)+H₂O at a bulk pH of 6.8 as a function of RDE rotation speed: (a) Percentage of near-surface concentrations of CO₂ compared to bulk CO₂ concentrations; (b) local pH near the electrochemical surface; (c-f) Faradaic Efficiency at 25, 100, 400 and 1600 rpm.

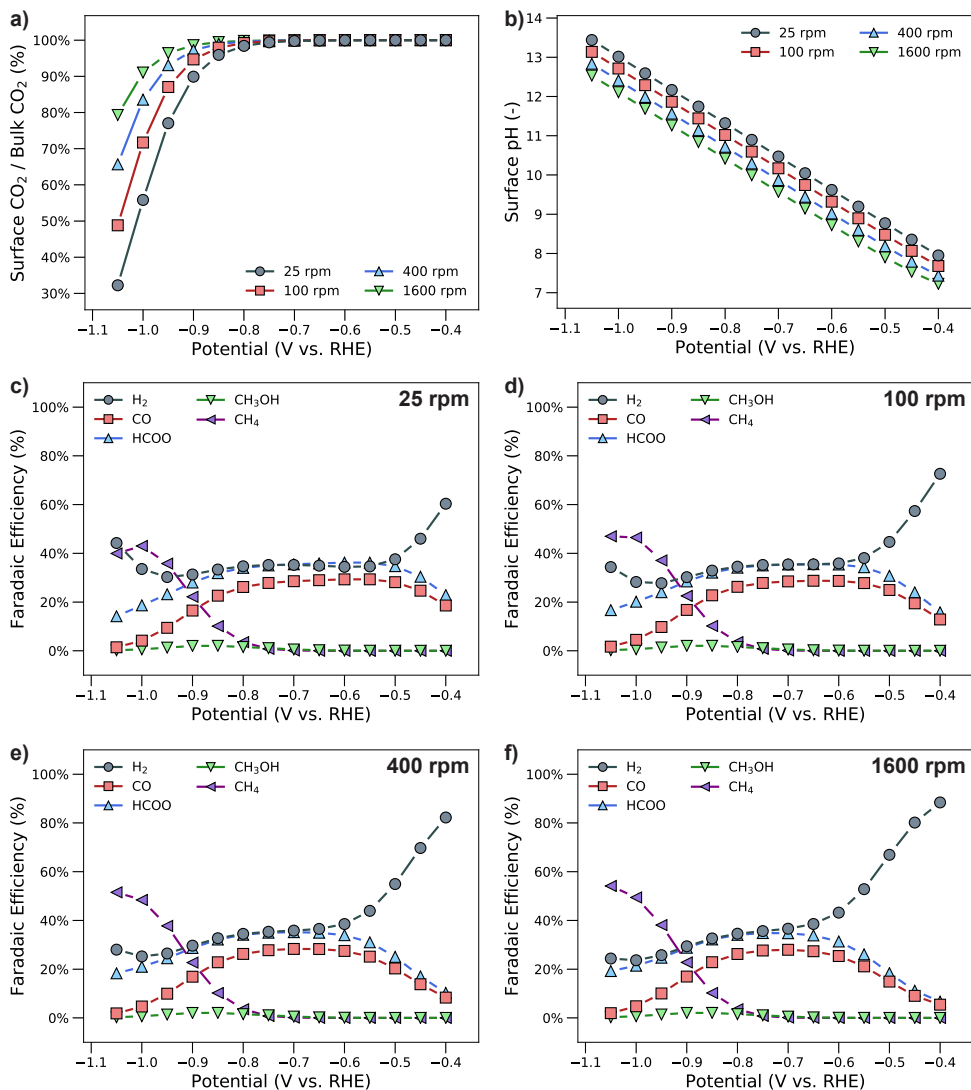


Figure E5: Simulated electrochemical CO₂ reduction on Cu(211) -10 kJ/mol COOH barrier at a bulk pH of 6.8 as a function of RDE rotation speed: (a) Percentage of near-surface concentrations of CO₂ compared to bulk CO₂ concentrations; (b) local pH near the electrochemical surface; (c-f) Faradaic Efficiency at 25, 100, 400 and 1600 rpm.

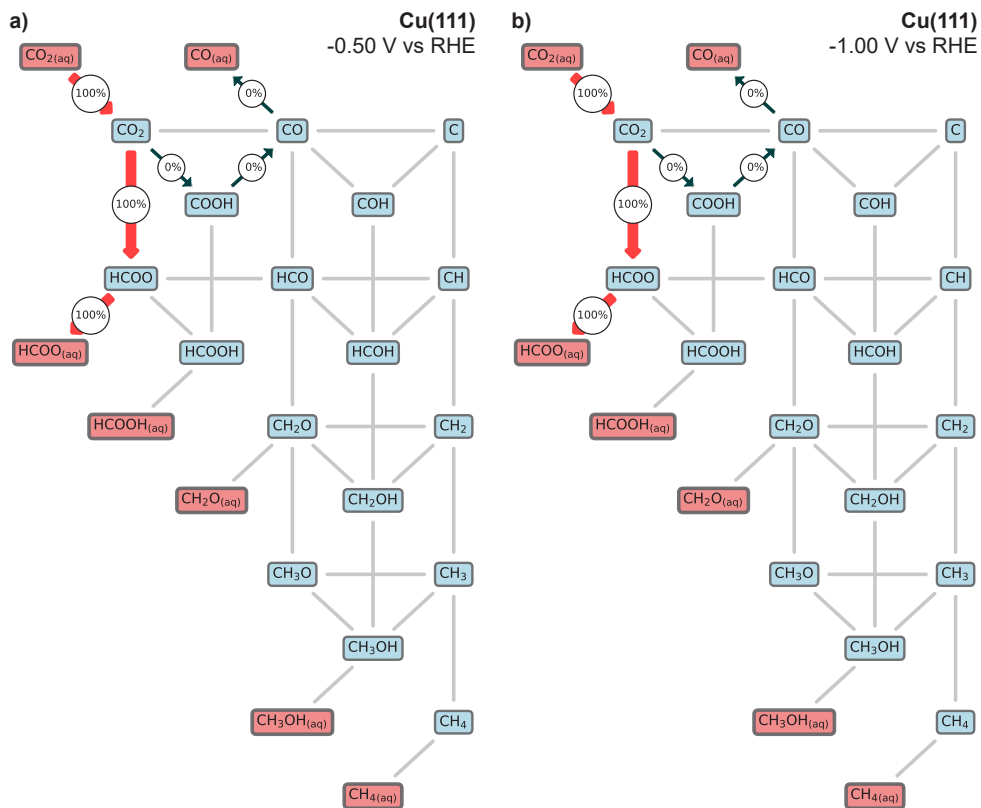


Figure E6: Flux diagram of electrochemical CO₂ reduction on the Cu(111) surface at 100 rpm and a bulk pH of 6.8: (a) -0.5 V *vs.* RHE; (b) -1.0 V *vs.* RHE.

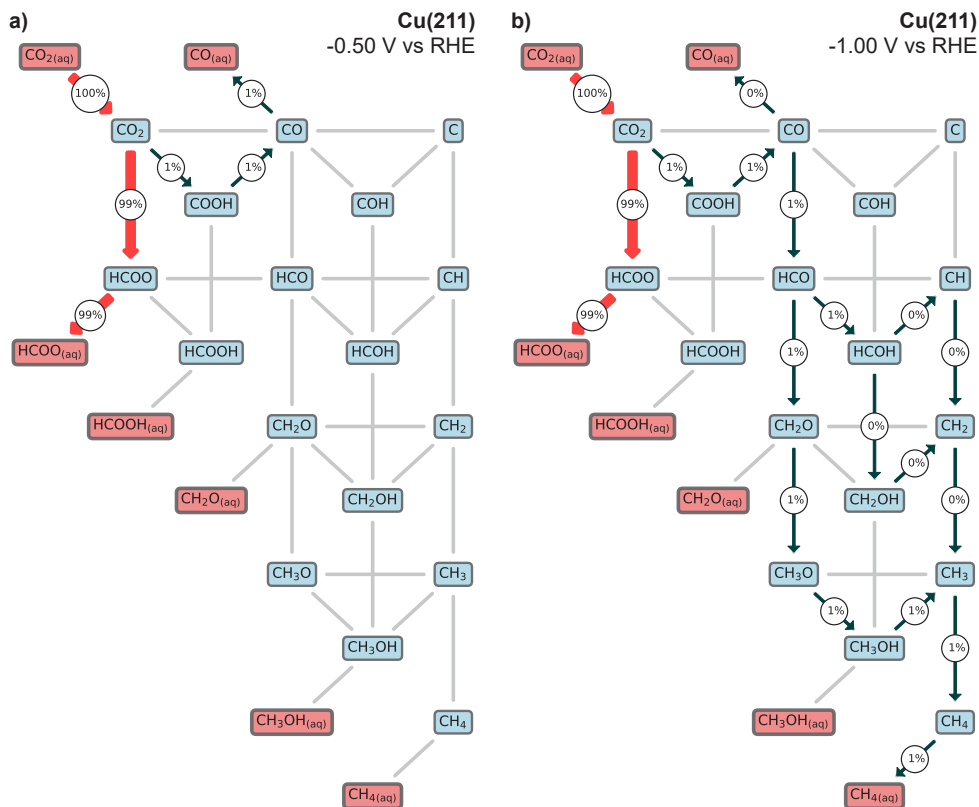


Figure E7: Flux diagram of electrochemical CO₂ reduction on the Cu(211) surface at 100 rpm and a bulk pH of 6.8: (a) -0.5 V *emphvs.* RHE; (b) -1.0 V *vs.* RHE.

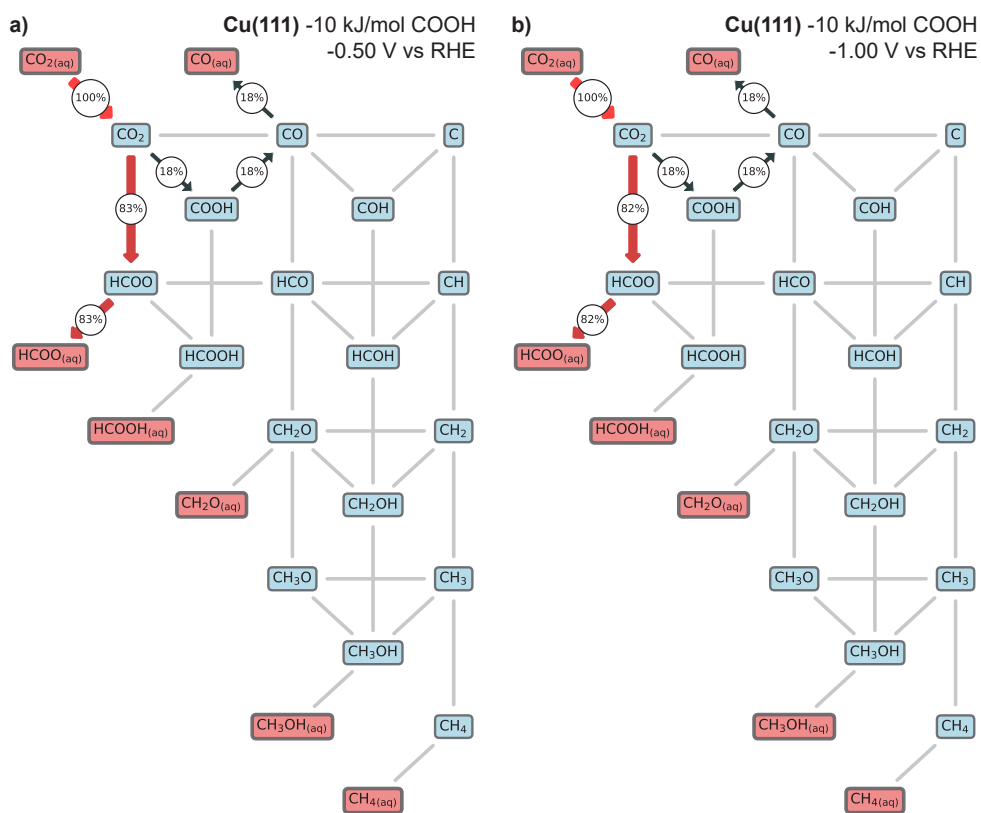


Figure E8: Flux diagram of electrochemical CO₂ reduction on the Cu(111) surface -10 kJ/mol COOH barrier at 100 rpm and a bulk pH of 6.8: (a) -0.5 V *vs.* RHE; (b) -1.0 V *vs.* RHE.

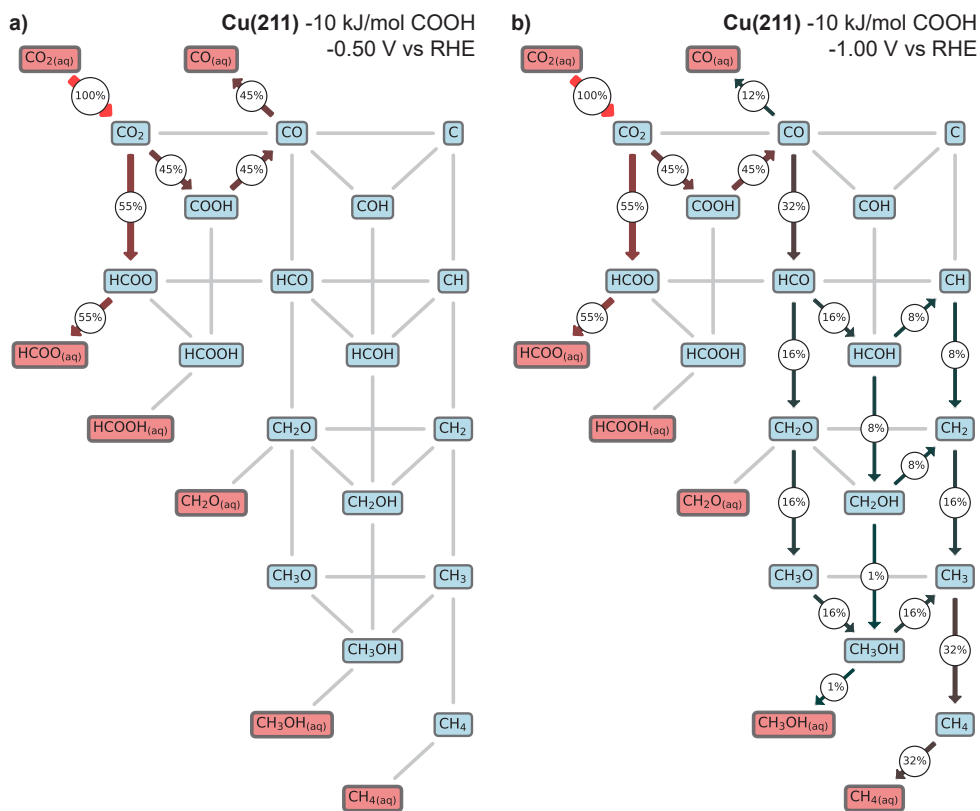


Figure E9: Flux diagram of electrochemical CO₂ reduction on the Cu(211) surface -10 kJ/mol COOH barrier at 100 rpm and a bulk pH of 6.8: (a) -0.5 V *vs.* RHE; (b) -1.0 V *vs.* RHE.

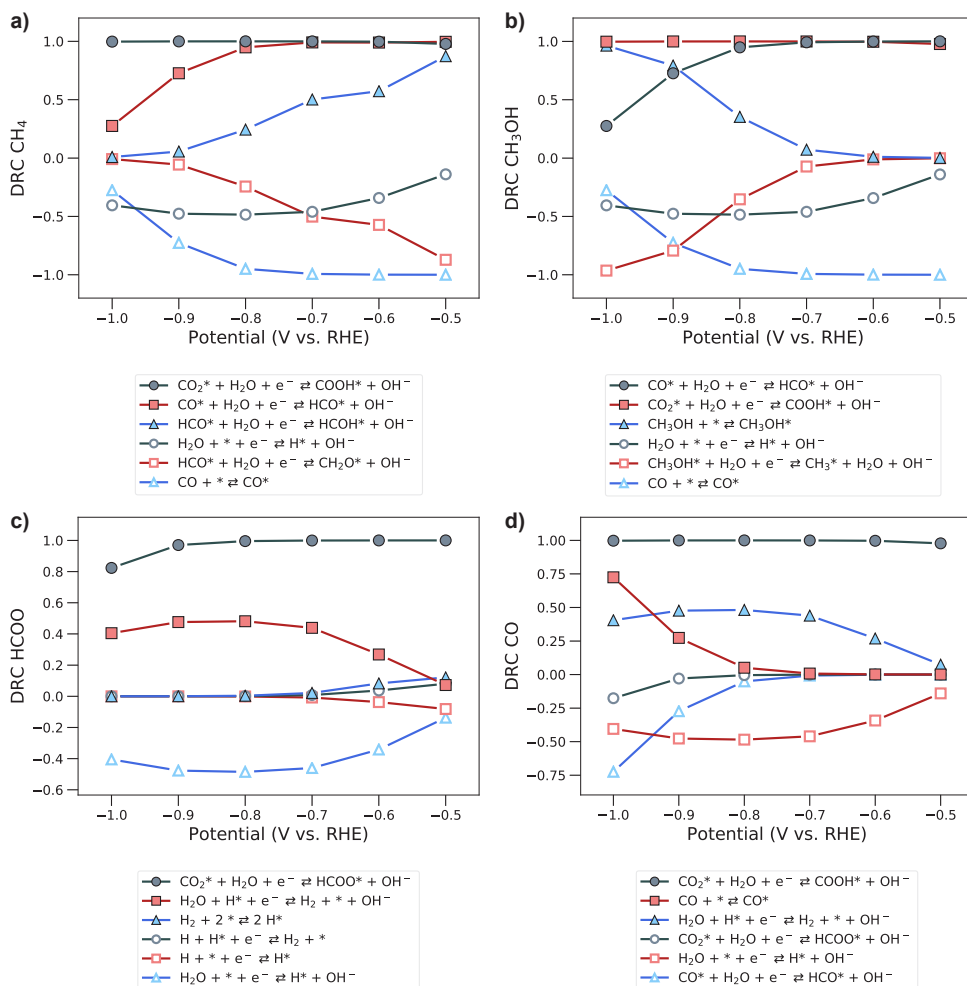


Figure E10: Degree of rate control for various products formed during electrochemical CO₂ reduction on the Cu(211) surface on a rotating disc electrode at 100 rpm and a bulk pH of 6.8. (a) CH₄; (b) CH₃OH; (c) HCOO; (d) CO.

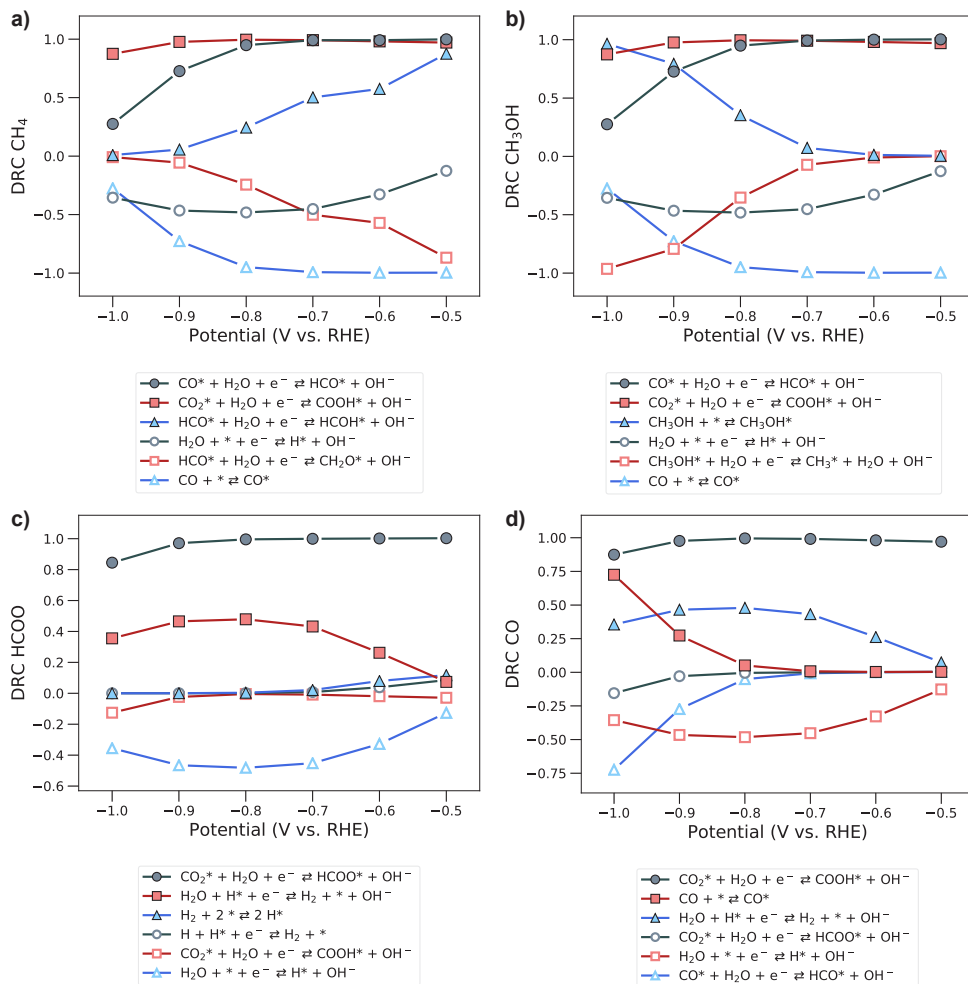


Figure E11: Degree of rate control for various products formed during electrochemical CO₂ reduction on the Cu(211) surface -10 kJ/mol COOH barrier on a rotating disc electrode at 100 rpm and a bulk pH of 6.8. (a) CH₄; (b) CH₃OH; (c) HCOO; (d) CO.

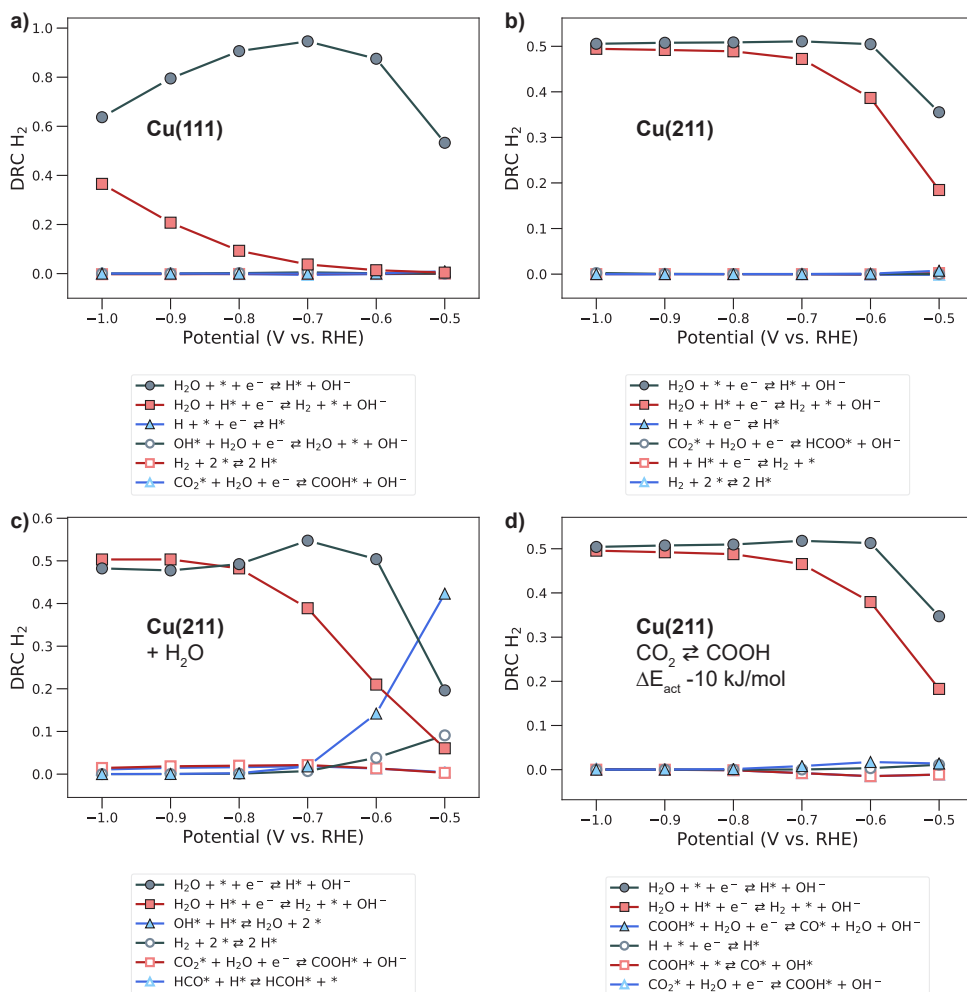


Figure E12: Degree of rate control for H₂ evolution during electrochemical CO₂ reduction on a rotating disc electrode at 100 rpm and a bulk pH of 6.8. (a) Cu(111); (b) Cu(211); (c) Cu(211)+H₂O; (d) Cu(211) -10 kJ/mol COOH barrier.

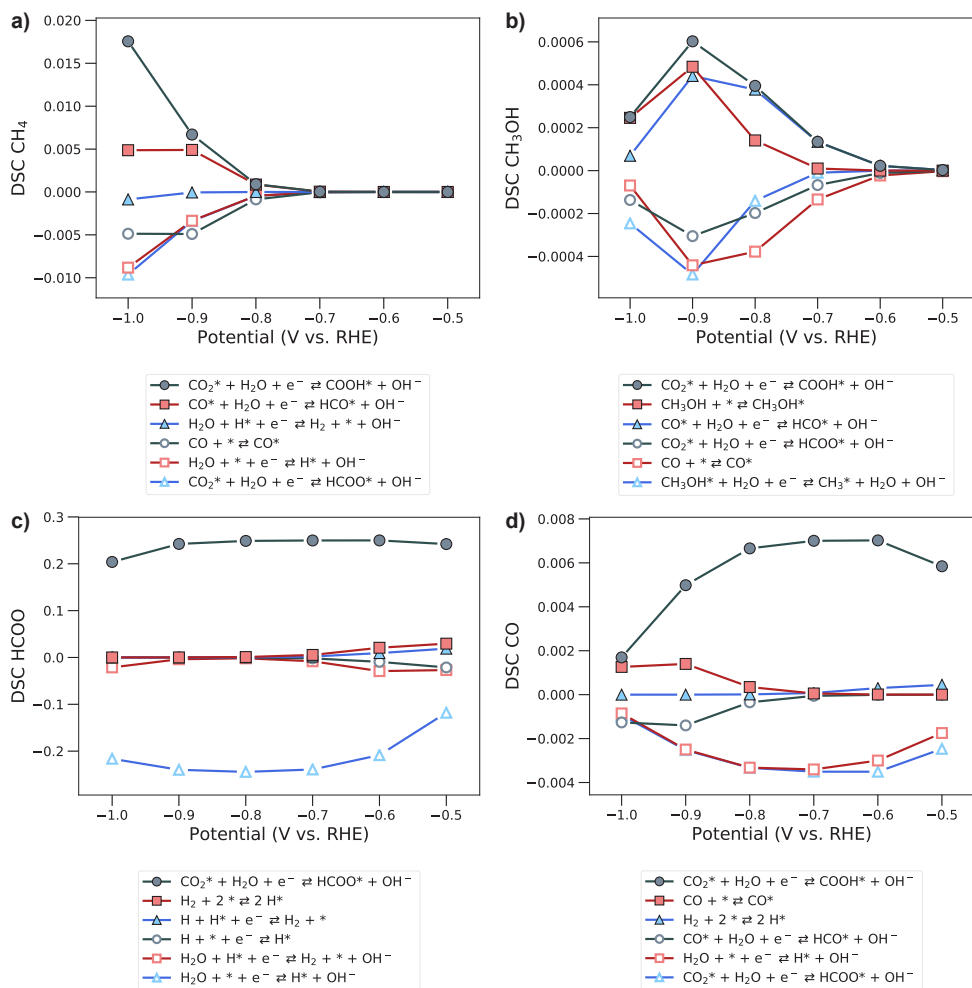


Figure E13: Degree of selectivity control for various products formed during electrochemical CO₂ reduction on the Cu(211) surface on a rotating disc electrode at 100 rpm and a bulk pH of 6.8. (a) CH₄; (b) CH₃OH; (c) HCOO; (d) CO.

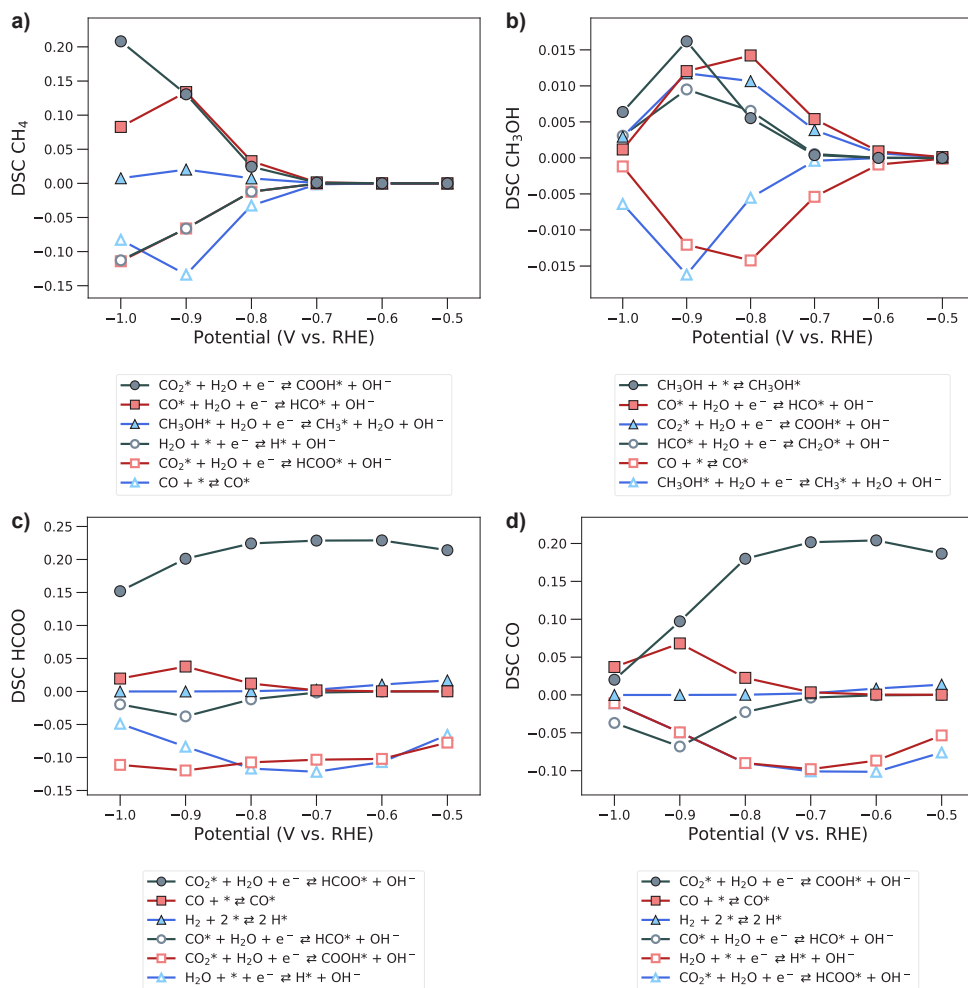


Figure E14: Degree of selectivity control for various products formed during electrochemical CO₂ reduction on the Cu(211) surface -10 kJ/mol COOH barrier on a rotating disc electrode at 100 rpm and a bulk pH of 6.8. (a) CH₄; (b) CH₃OH; (c) HCOO; (d) CO.

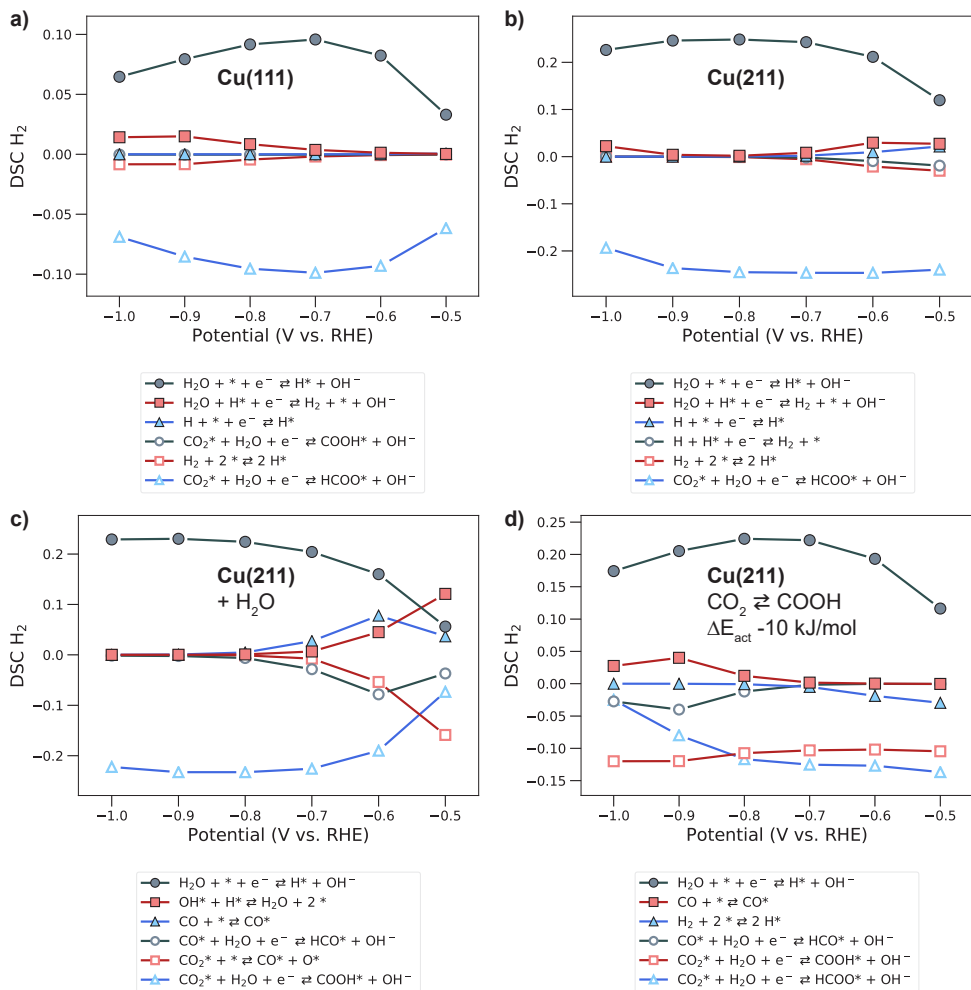


Figure E15: Degree of selectivity control for H₂ evolution during electrochemical CO₂ reduction on a rotating disc electrode at 100 rpm and a bulk pH of 6.8. (a) Cu(111); (b) Cu(211); (c) Cu(211)+H₂O; (d) Cu(211) -10 kJ/mol COOH barrier.

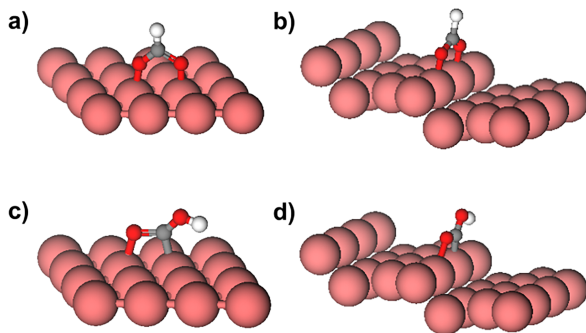


Figure E16: Geometries of (a,b) HCOO and (c,d) COOH intermediates on (a,c) Cu(111) and (b,d) Cu(211).

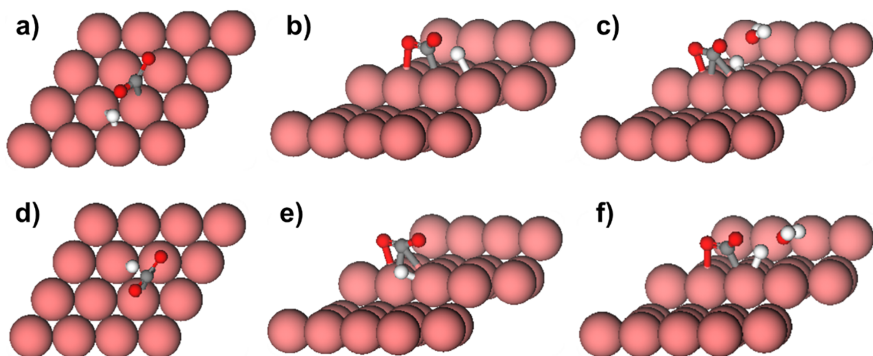


Figure E17: Transition state geometries for the formation of (a-c) COOH and (d-f) HCOO on (a, d) Cu(111), (b,e) Cu(211) and (c, f) Cu(211) in the presence of a catalytic H₂O molecule.

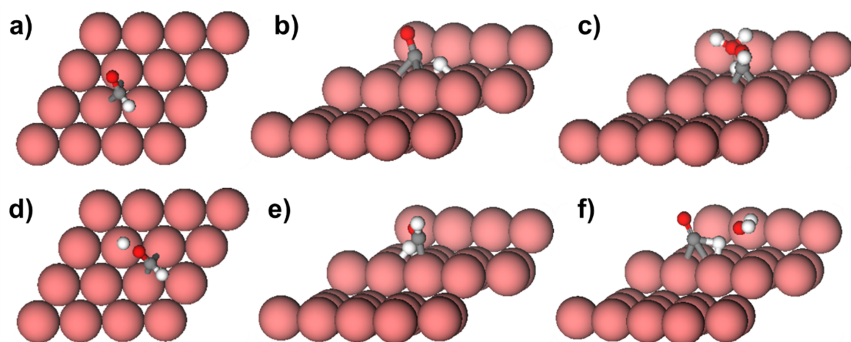


Figure E18: Transition state geometries for the formation of (a-c) HCO and (b-d) HCOH on (a, d) Cu(111), (b,e) Cu(211) and (c, f) Cu(211) in the presence of a catalytic H₂O molecule.

SUMMARY

Microkinetic Modeling of Fischer-Tropsch Synthesis on Cobalt

Climate change due to anthropogenic greenhouse gas emissions is recognized as one of the most pressing societal challenges and, accordingly, is also high on the political agenda. Burning fossil resources releases CO₂ in the atmosphere, which is linked to global warming and climate change. It is clear that only a relatively small part of all available fossil resources can be converted into CO₂ if we wish to stay below the 1.5 °C temperature rise as implemented in The Paris Agreement. Our energy system needs to undergo a transition to low-carbon technologies, of which the production of CO₂-neutral liquid transportation fuels by the Fischer-Tropsch (FT) process is one of the possible transition technologies. Iron and cobalt catalysts are already applied industrially to convert synthesis gas (CO+H₂) to valuable hydrocarbon products. The synthesis gas is currently derived from cheap coal and natural gas and should, in the future, be derived from renewable sources like biomass or CO₂ from the air. In the overall FT process these changes require fundamental understanding of the mechanisms underlying hydrocarbon formation from synthesis gas. In this thesis we have shown how density functional theory (DFT) calculations and microkinetic modeling (MKM) can be used to unravel the FT synthesis reaction to the elementary reaction step level.

In Chapter 2 we gave an overview of the computational methods used in this work and the theory behind them. We showed how elementary reaction step rates can be defined on model surfaces to describe the overall processes on real catalysts. Stable geometries of adsorbates and transition states can be computed by DFT, and MKM provides predictions of reaction rates, surface coverages, and rate- and selectivity-controlling steps.

Often, microkinetics simulations do not include lateral interactions. However, these lateral interactions have a significant influence on both the activity and selectivity of the FT reaction. Therefore, we discussed in Chapter 3 the incorporation of these effects in a mean-field microkinetic model. We found that under FT conditions the CO coverage on a cobalt catalyst surface reaches a saturation coverage well below unity. At a relevant

temperature of 500 K, we predict a maximum CO coverage in the range of 0.32 ML - 0.55 ML, which is in good correspondence to experimental results. Importantly, we found that the coverage effects are independent of the surface, indicating that inter-adsorbate repulsion is the main lateral interaction effect. To model these effects we proposed both a rigorous and a more versatile lateral interaction potential satisfying thermodynamic consistency. We then applied the more versatile potential in later Chapters to reproduce experimentally observed adsorption and desorption behavior.

In Chapter 4 we investigated CO dissociation, which is a key reaction step in the FT reaction because its rate determines the number of FT monomers available for chain growth. While the H-assisted HCO-pathway is preferred on the terrace Co(0001) surface, the corresponding overall barrier of 182 kJ/mol is too high to produce FT monomers at rates comparable to experimental turnovers. The direct CO dissociation step on the stepped Co(11 $\bar{2}$ 1) surface has a much lower barrier of 100 kJ/mol, supporting the hypothesis that step-edge sites are the active sites of CO dissociation in the FT reaction. We then investigated how the activation barrier for direct CO dissociation depends on CO coverage for step-edge and terrace cobalt sites. Whereas on terrace sites increasing coverage results in a substantial increase of the direct CO dissociation barrier, we found that this barrier is nearly independent of CO coverage for the step-edge sites on corrugated surfaces. A detailed electronic analysis showed that this difference is due to the flexibility of the adsorbed layer, minimizing Pauli repulsion during the carbon-oxygen bond dissociation reaction on the step-edge site.

Advances in transient kinetic analysis methods contribute to unraveling the complex reaction pathways of FT synthesis. However, tracing the activity and selectivity of Fischer-Tropsch catalysts to the individual events occurring at the active site remains difficult with experimental techniques. In Chapter 5 we provided simulations of transient kinetics at the scale of the active site by making use of the reaction energetics for CO hydrogenation to methane on the stepped and terrace cobalt surfaces. We investigated the hydrogen-deuterium kinetic isotope effect and simulated common steady-state and chemical isotopic transients. We confirmed that direct CO dissociation is the main pathway for breaking the C–O bond and that it occurs exclusively on step-edge sites. While the experimentally observed hydrogen-deuterium kinetic isotopic effect is often used as evidence for H-assisted CO dissociation, we showed that hydrogenation of C and O as partly rate-controlling steps provides an alternative explanation. The simulations of the chemical transients provide significant insight into the importance of the changing surface coverages and the reversibility of CO dissociation on cobalt step-edges.

In Chapter 6, we developed a microkinetic model describing also all relevant coupling and chain-hydrogenation reaction steps. We included important aspects such as lateral interactions, different chain growth mechanisms and the presence of both sites in one surface model including migration of species between them. We found that CH_x-CH_y coupling pathways relevant to the carbide mechanism have favorable barriers compared to CO dissociation, while the overall barrier for chain growth via CO insertion is much higher. Microkinetics simulations showed that the Co(11 $\bar{2}$ 1) model surface is highly active

and selective for the FT reaction with a proper chain-growth probability. Adding terrace Co(0001) sites in a dual-site model lead to a substantially higher CH₄ selectivity at the expense of the C₂₊-hydrocarbons selectivity. At typical FT conditions, chain growth occurs exclusively at step-edge sites, while additional CH₄ stems from CH and CH₃ migration from step-edge to terrace sites followed by hydrogenation. Replacing CO as a reactant by CO₂ shifts the product distribution nearly completely to CH₄ with CO as a minor by-product. The much higher H/CO coverage ratio during CO₂ hydrogenation in comparison to CO hydrogenation is causing the high CH₄ selectivity. The current results provide novel insight into the importance of a proper balance of CO and H species at the surface and the role of low-reactive terrace sites close to step-edge sites in the formation of CH₄.

Finally, Chapter 7 addressed the microkinetics simulation of the electrochemical reduction of CO₂. Electrochemical reduction of CO₂ provides an alternative pathway to store excess renewable electricity in chemical bonds. We incorporated the reaction energetics for CO₂ reduction on Cu(111) and Cu(211) determined by DFT calculations in microkinetics simulations to predict the influence of surface topology, the presence of water and possible diffusion limitations on current density-potential curves and Faradaic efficiencies. Our reaction-diffusion model could well reproduce hydrogen evolution including the effect of proton diffusion limitations and a shift of proton reduction at low potential to water reduction at high potential. We found that the stepped Cu(211) surface is more active than the Cu(111) terrace for CO₂ reduction towards HCOO(H), CO and CH₄. The presence of a catalytic H₂O molecule increases the overall rate and selectivity to products CO and CH₄. Trend-wise, the simulated product distribution follows the potential-dependent distribution observed in the experiment. At high potential, CO₂ reduction becomes increasingly diffusion-limited, which supports the need for better design of mass transfer in electrochemical reactors, which operate at high current density.

While the reaction-diffusion model shows the importance of diffusion-limitations to the catalyst surface, an open question that remains is whether diffusion limitations can occur on the catalyst surface. In particular in the context of FT catalysis, the diffusion of intermediates between active sites can be an important part of the mechanism. In this work we have assumed that diffusion of adsorbates is fast, and that the barriers for migration are not significantly influenced by surface coverage. In a mean-field microkinetic model there is no topological information other than the inclusion of different active sites. As such there is no typical distance that CH_x monomers can diffuse away from the step-edge sites before being either hydrogenated or incorporated into growing chains. Predicting the contribution of such phenomena could be done with kinetic Monte Carlo (KMC) methods, although the size of the FT network will come together with high computational complexity. Another multiscale approach that can offer additional insight into real FT catalyst behavior is the inclusion of the mean-field microkinetics in a more detailed reactor model incorporating computational fluid dynamics (CFD). Especially at industrially relevant conversions a large amount of water and high-molecular-weight waxes will be present near, on, or in the catalyst particle. The corresponding diffusion limitations could change the H₂/CO ratio near the surface and in the particle, changing both activity and selectivity.

ACKNOWLEDGMENTS

A thesis is never finished, it is just printed. I've always been a perfectionist, and releasing the final version of my thesis is a difficult moment. There is so much that could have been added, improved, or polished, but I'm proud of the end result. I've looked up some reference theses to unravel how to write a good Acknowledgments section. I found that some were very brief, some were slightly 'too honest', but most were a genuine compilation of gratitude towards friends and colleagues. Here I will attempt the latter.

The first person that I want to thank is my promoter Emiel Hensen. Emiel, I am very happy that I was able to do both my Master's graduation project in your group and also this PhD project. Your knowledge and vision have guided me and has shaped me into a better person. Sometimes it's discouraging when I send you manuscripts and I get back more corrected text than original text. Nevertheless, I've always been grateful for that feedback because it improved my work every time. I also highly value the opportunities you gave me to go to external courses and to present my work at conferences.

Another beacon of knowledge has been my co-promotor Ivo Filot. Ivo, you recruited me into the IMC group and you have thought me most of the theoretical and computational methods that I needed for finishing this thesis. Moreover, you have trained me to write good and efficient C++ programs. You have been a great academic role model and I think many new students will see you like that as well.

I want to thank also my other Committee members: prof.dr.ir Hans Kuipers, prof.dr. Atsushi Urakawa, dr.ir. Bernd Ensing, prof.dr.ir. Martin van Sint Annaland, and dr. Leendert Bezemer. I highly appreciate your efforts in reading and evaluating my dissertation and participating in the defense ceremony.

I would also like to acknowledge Bernd for organizing the Han-Sur-Lesse winter schools. I've had the privilege to attend the lectures you organized for multiple years in a row and they were invaluable in getting to where I am now.

Leendert, thank you for the useful discussions regarding my work and the many comments you had to improve my thesis. Your expertise greatly helps to put my theoretical results in

an experimental context. I also want to thank your colleagues at Shell for the feedback I got every time we would visit STCA. In particular I want to thank Sander van Bavel and Heiko Oosterbeek. We have not only collaborated during my PhD, but you have also excellently guided me during my industrial internship.

Robin and Michel, thank you for being my paranymphs during the defense. Robin, we have been office bros for a long time. I've always enjoyed our Microkinetic Modeling Mondays. Michel, I actually met you before I met Robin, but I never really knew you well until you applied for a PhD position at IMC. Now I'm happy to see you as one of my close friends.

I've had the honor to be paranymph myself a few times. Wei, Farid, Jan, thank you for being great examples of how to successfully defend one's thesis. Wei, part of my work is featured in your thesis. You had written down everything so beautifully only for me to tell you that I mixed up a few numbers in my calculation script. You had to rewrite a decent amount after I corrected my mistake. For that I am truly sorry. Farid, you are one of the kindest people I know and I am grateful to have been your paranymph. Jan, your eagerness to discuss science knows no bounds. You would have been a good paranymph for my defense if you weren't already on your way to your next challenge in Japan.

I gratefully acknowledge the many people that I could collaborate with on their publications: Ivo, Wei, Roderigh, Xue, Robin, Jin-Xun, Yaqiong, Farid, Wilbert, Min, and Charlotte. Marta and Dimitra, thank you for clearing up some questions I had regarding my simulations of electrochemical CO₂ reduction. Jan Philipp and Longfei, thank you for giving Joost and me the opportunity to design a cover for your publication. Joost, you did a tremendous job.

A common saying when doing a theoretical PhD is: "Coffee in, code out". It is therefore very important to have a nice group of people to drink coffee with. I've always enjoyed the diversity of the coffee group and I also liked the interaction with Arjan, Jos, Gijsbert and Erik from Hybrid Catalysis. Tiny, if only my code-debugging software was as good as you are for debugging experimental setups. You are also good at debugging people, as there were numerous times that you motivated me when I felt disheartened. Adelheid, thank you for correcting me whenever my remarks strayed too much from popular opinion.

The most important coffee moment is the one before 9:00 AM. I especially liked the dedicated mini-coffee group that we had for some time, consisting of Yohan, Lingqian, Robin and me. We would sit in exactly the same setup every morning and discuss actual societal issues.

Min, Evert, Jessica, and also Rudie, Ellen, Micha, Other Bart. I've seen you grow as Master's students and I hope I've been able to convey to you the importance of computational chemistry and how fun programming can be. Min, you were always so very kind, I'll never forget your stay here in Eindhoven. Evert, it was nice to cry together whenever the MKMCXX code produced segmentation faults. Jessica, your presence brought an inexhaustible source of movie trivia to our group. Rudie, I liked the strong commitment you showed whenever we had discussions. Ellen, I'm very happy to see that our collaboration has led to an amazing Master's thesis for you at Utrecht University. The beautiful publication

that has followed from it demonstrates the value of your work. Micha, I considered you to be a 'Bart in training'. You're highly intelligent and motivated, and I've seen you make considerable improvements in your soft skills. Other Bart, I'm amazed by your theoretical knowledge. You're also a PhD student now and I look forward to seeing what you can achieve. I also expect that you'll give the programming discipline in our group a big boost. I give here also a shout-out to Koen, Tom, Sven, Mariska, Cas, Roos, and Anouk, who all asked me short specific questions to which I responded with epic monologues about good programming practices. Jasper, please follow the trouble-shooting guidelines.

The best way to work on soft skills is to partake in social activities with many different people. I want to acknowledge all the connections I made within the association Prometheus. To name a few: Sandra, Peter, Tom, Patrick, Joris, Gert-Jan, Juliën, and Rim; thank you. Many thanks also to my fellow Koempels: Dannie, Ivo, Ferdinand, Yoran, Tom, Mark, Michelle, Addie, Evelien, Frank, Jolanda, Jorrick, Camiel. Thanks to every one of the pizza & karaoke crew. Michelle, I'm always amazed how good you can sing. Credit also goes to Bianca, Jerome, Francesco, and Nicolò.

I usually leave the karaoke bar a bit earlier so I can still catch a train back to Roermond. In ten years of traveling to and from Eindhoven I've endured quite a lot of delays. Luckily, I've had a few people with whom I could share the journey. I've traveled with Dannie and Jorick on many occasions. The most memorable moment will always remain that one time that us three traveled back and that Jorick had to fix his glasses due to an unplanned acrobatic entry into the F.O.R.T. Iris, whenever we met in the train you always asked how I was doing. I often expressed my uncertainty to whether I was on-schedule for getting my PhD. You always responded positively and uplifting, thank you for that. Another person I should definitely thank is Annabel. Although we never traveled together by train, you took me to Weert by car when my last train from Eindhoven to Roermond was canceled. Thank you. I should also mention here the time that Dannie picked me up in Roermond to get me to Ivo and Sandra's wedding in time. Without Dannie I would have been terribly late. Dannie, you literally go the distance for your friends; you're amazing.

Arjan, thank you for absolutely demolishing me every Friday-afternoon run. I can still remember when I first joined you, Jos, and Ivo about six years ago. I was out-of-commission after about one or two kilometers and my muscles ached for roughly a week. I've improved enormously, but I still can't keep up with you Arjan. Fortunately, we can grab a drink afterwards and replenish the lost salts with some potato chips. Therefore, also thanks to everyone involved in organizing these Friday-afternoon drinks.

My Friday-evenings are usually dedicated to playing video-games. Richard and Daphne, thank you for hosting me every time. Richard, it amazes me that after all these years the outcome of a game of FIFA is still very much unpredictable. Less unpredictable were the games of Battlefield against Vincent; I think the chances were slightly in my favor. We should really do that again some time.

The time is nearing that being with the IMC group will also be for old times' sake. I'm not the first to leave the group, so I will join a list of respectable people. To name a few whom I've had the pleasure to meet during my time at IMC: Gilbere, Andreas, Remco,

William, Iris, Dennis, Jarno, Coen and Mariët.

To all the other current and previous members of our group that I have not mentioned explicitly, thank you! Of course, there is still one person in particular that deserves my utmost gratitude. Emma, thank you for everything you have done for me from the moment I entered the group to finishing the last forms for my defense. Socially, you might be the most knowledgeable person in our group. Having a quick chat with you on good or bad days always lifted my spirits and helped me to finish this thesis.

Tot slot wil ik graag mijn ouders enorm bedanken voor alle toeverlaat gedurende mijn tijd als BSc-, MSc-, en PhD-student. Het was zeker niet altijd zonder stress. Ik heb door kunnen zetten dankzij jullie onvoorwaardelijke steun. Ontzettend bedankt!

LIST OF PUBLICATIONS

Publications within the scope of this thesis:

2020

- First-principles based microkinetic modeling of Fischer-Tropsch synthesis on cobalt
Zijlstra, B., Broos, R.J.P., Chen, W., Bezemer, G.L., Filot, I.A.W., Hensen, E.J.M.
(*in preparation*)
- First-Principles Microkinetics Simulations of Electrochemical Reduction of CO₂ over Cu Catalysts
Zijlstra, B., Zhang, X., Liu, J.-X., Filot, I.A.W., Zhou, Z., Sun, S., Hensen, E.J.M.
(*submitted*)

2019

- Coverage Effects in CO Dissociation on Metallic Cobalt Nanoparticles
Zijlstra, B., Broos, R.J.P., Chen, W., Oosterbeek, H., Filot, I.A.W., Hensen, E.J.M.
ACS Catalysis 9(8), pp. 7365-7372
- First-principles based microkinetic modeling of transient kinetics of CO hydrogenation on cobalt catalysts
Zijlstra, B., Broos, R.J.P., Chen, W., Filot, I.A.W., Hensen, E.J.M.
Catalysis Today 342, pp. 131-141

2018

- Mechanism of Carbon Monoxide Dissociation on a Cobalt Fischer-Tropsch Catalyst
Chen, W., **Zijlstra, B.**, Filot, I.A.W., Pestman, R., Hensen, E.J.M.
ChemCatChem 10(1), pp. 136-140

Publications outside the scope of this thesis:**2019**

- Understanding carbon dioxide activation and carbon-carbon coupling over nickel
Vogt, C., Monai, M., Sterk, E.B., Palle, J., Melcherts, A.E.M., **Zijlstra, B.**, Groeneveld, E., Berben, P.H., Boereboom, J.M., Hensen, E.J.M., Meirer, F., Filot, I.A.W., Weckhuysen, B.M.
Nature Communications 10, pp. 5330
- A theoretical study of the reverse water-gas shift reaction on Ni(111) and Ni(311) surfaces
Zhang, M., **Zijlstra, B.**, Filot, I.A.W., Li, F., Wang, H., Li, J., Hensen, E.J.M.
Canadian Journal of Chemical Engineering (*in Press*)
- Efficient Base-Metal NiMn/TiO₂ Catalyst for CO₂ Methanation
Vrijburg, W.L., Moioli, E., Chen, W., Zhang, M., Terlingen, B.J.P., **Zijlstra, B.**, Filot, I.A.W., Züttel, A., Pidko, E.A., Hensen, E.J.M.
ACS Catalysis 9(9), pp. 7823-7839
- Quantum-chemical-based microkinetics simulations of syngas conversion over MoS₂(100) surface
Fariduddin, F., Filot, I.A.W., **Zijlstra, B.**, Hensen, E.J.M.
Chemical Engineering Science pp. 166-183
- Theoretical Approach to Predict the Stability of Supported Single-Atom Catalysts
Su, Y.-Q., Wang, Y., Liu, J.-X., Filot, I.A.W., Alexopoulos, K., Zhang, L., Muravev, V., **Zijlstra, B.**, Vlachos, D.G., Hensen, E.J.M.
ACS Catalysis 9(4), pp. 3289-3297
- A quantum-chemical study of the CO dissociation mechanism on low-index Miller planes of θ -Fe₃C
Broos, R.J.P., Klumbers, B., **Zijlstra, B.**, Filot, I.A.W., Hensen, E.J.M.
Catalysis Today 342, pp. 152-160

2018

- Quantum-Chemical DFT Study of Direct and H- and C-Assisted CO Dissociation on the χ -Fe₅C₂ Hägg Carbide
Broos, R.J.P., **Zijlstra, B.**, Filot, I.A.W., Hensen, E.J.M.
Journal of Physical Chemistry C 122(18), pp. 9929-9938
- Optimum Particle Size for Gold-Catalyzed CO Oxidation
Liu, J.-X., Filot, I.A.W., Su, Y., **Zijlstra, B.**, Hensen, E.J.M.
Journal of Physical Chemistry C 122(15), pp. 8327-8340

- An Active Alkali-Exchanged Faujasite Catalyst for p-Xylene Production via the One-Pot Diels-Alder Cycloaddition/Dehydration Reaction of 2,5-Dimethylfuran with Ethylene
Rohling, R.Y., Uslamin, E., **Zijlstra, B.**, Tranca, I.C., Filot, I.A.W., Hensen, E.J.M., Pidko, E.A.
ACS Catalysis 8(2), pp. 760-769
- Influence of Carbon Deposits on the Cobalt-Catalyzed Fischer-Tropsch Reaction: Evidence of a Two-Site Reaction Model
Chen, W., Kimpel, T.F., Song, Y., Chiang, F.-K., **Zijlstra, B.**, Pestman, R., Wang, P., Hensen, E.J.M.
ACS Catalysis 8(2), pp. 1580-1590
- Optimum Cu nanoparticle catalysts for CO₂ hydrogenation towards methanol
Zhang, X., Liu, J.-X., **Zijlstra, B.**, Filot, I.A.W., Zhou, Z., Sun, S., Hensen, E.J.M.
Nano Energy 43, pp. 200-209

2017

- Mechanism of Cobalt-Catalyzed CO Hydrogenation: 1. Methanation
Chen, W., Pestman, R., **Zijlstra, B.**, Filot, I.A.W., Hensen, E.J.M.
ACS Catalysis 7(12), pp. 8050-8060
- Kinetic aspects of chain growth in Fischer-Tropsch synthesis
Filot, I.A.W., **Zijlstra, B.**, Broos, R.J.P., Chen, W., Pestman, R., Hensen, E.J.M.
Faraday Discussions 197, pp. 153-164

2016

- A quantum-chemical DFT study of CO dissociation on Fe-promoted stepped Rh surfaces
Filot, I.A.W., Fariduddin, F., Broos, R.J.P., **Zijlstra, B.**, Hensen, E.J.M.
Catalysis Today 275, pp. 111-118

CURRICULUM VITAE

Bart Zijlstra was born on the 29th of May, 1991 in Roermond. He followed pre-university college from 2003 to 2009 at Bisschoppelijk College Broekhin in Roermond, where he also obtained the International Baccalaureate Certificate for English A2 Higher Level. After finishing pre-university college he studied Chemical Engineering at the Eindhoven University of Technology with a Minor in Applied Physics. In 2012 he obtained his Bachelor of Science degree and he enrolled in the Chemical Engineering Master program. He carried out his graduation project within the Inorganic Materials & Catalysis (IMC) group of prof. dr. ir. Emiel Hensen. The project was co-supervised by dr. ir. Ivo Filot and focused on modeling the Fischer-Tropsch reaction on cobalt surfaces. Afterwards, Bart completed an industrial internship at the Shell Technology Centre Amsterdam (STCA) where he studied the Fischer-Tropsch reaction in a wafer reactor. In 2015 he obtained his Master of Science degree with the distinction *cum laude*. That year he returned to the Inorganic Materials & Catalysis group and started a PhD project of which the results are presented in this dissertation. He is a core developer of the C++ program MKMCXX and various Python-based analysis tools. Since 2019 he is employed as a university researcher in the IMC group.



